

https://dspace.org/

Colloidal synthesis of MoSe2, ReSe2, and SnSe2 nanomaterials and their carbon nanocomposites for applications in hydrogen evolution reactions

Ndala, Zakhele Bafana

2022
https://hdl.handle.net/10539/37146

Downloaded from a DSpace repository. https://dspace.org/



WITS
UNIVERSITY

Colloidal synthesis of $MoSe_2$, $ReSe_2$, and $SnSe_2$ nanomaterials and their carbon nanocomposites for applications in hydrogen evolution reactions

A Thesis submitted to the Faculty of Science, University of the Witwatersrand, in partial fulfilment of the requirements for the degree Doctor of Philosophy

By

Zakhele Bafana Ndala
Student no: 491384

Z. Ndala

02 August 2022

Zakhele B. Ndala

02 August 2022

Supervisor: Prof. Nosipho Moloto

Co-supervisors: Dr Siziwe Gqoba, Dr Cebisa Linganiso

Declaration

I declare that the work reported herein is my independent work, submitted at the School of Chemistry, University of the Witwatersrand, Johannesburg. This work has not been submitted for any degree or examination in any other institution of higher learning.

Z. Ndala

Zakhele B. Ndala

02 August 2022

Abstract

The work herein focuses on the synthesis of $MoSe_2$, $ReSe_2$, and $SnSe_2$ nanostructures using the colloidal method. This work is aimed to show that the colloidal method can be used to produce transition metal dichalcogenide (TMD) nanostructures with excellent catalytic activity toward the hydrogen evolution reaction (HER). Moreover, this work demonstrates that the method can be used to incorporate various techniques that are used to improve the catalytic activity of TMD nanostructures. The catalytic activity of the TMD nanostructures was improved by introducing Se vacancies, chemical doping, increasing exposure of active edge sites, and forming hybrid nanostructures with carbon nanomaterials. The colloidal method was successfully used to synthesize $MoSe_2$, $ReSe_2$, and $SnSe_2$ nanostructures. The $MoSe_2$ and $ReSe_2$ were synthesized using selenium powder as the selenium precursor and oleic acid as the solvent/surfactant. $SnSe_2$ was synthesized using selenium powder as the selenium precursor and olelyamine as the solvent/surfactant. The $MoSe_2$ and $ReSe_2$ nanostructures formed spherical structures flower-like morphologies that were composed of few-layer nanosheets. The $SnSe_2$ nanostructures formed into 2D nanoplates. The onset potential and overpotential of the $MoSe_2$ nanostructures were recorded as 108 mV and 313 mV respectively. The onset potential and overpotential of the $ReSe_2$ were measured to be 168 mV and 331 mV respectively. These materials were used as a baseline and attempts were made to improve their catalytic activity. A change in the selenium precursor from selenium powder to selenourea was shown to result in the introduction of Se vacancies in the $MoSe_2$. This in turn resulted in improved catalytic activity towards the HER, which was attributed to an increase in the number of active sites provided by the Se vacancies. The onset potential and the overpotential of the $SnSe_2$ nanostructures were measured to be 319 mV and 618 mV respectively. However, the $SnSe_2$ nanoplates were electrochemically activated through H^+ intercalation, and the catalytic performance of the nanostructures drastically improved. The electrochemically activated $SnSe_2$ nanoplates exhibited exceptional improvements in catalytic performance with an onset potential of 141 mV and an overpotential of 289 mV. The pristine $SnSe_2$ was used as a baseline and attempts were made to improve the catalytic activity of these materials.

The effect of surface functionalization of the nanostructures on their catalytic activity toward the HER was studied. Three solvents/surfactants commonly used in colloidal synthesis were studied. These were oleylamine (OLA), oleic acid (OA), and trioctylphosphine oxide (TOPO). The surfactants interacted differently with the TMD nanostructures, but a common observation

was made. The use of TOPO instead of OA which was initially used resulted in an improvement of the catalytic activity. The TOPO synthesized $ReSe_2$ nanostructures had a reduced onset potential and overpotential of 73 mV and 171 mV respectively. The TOPO synthesized $MoSe_2$ nanostructures also had a reduced onset potential and overpotential of 297 mV and 193 mV respectively. The TOPO synthesized $SnSe_2$ had improved catalytic activity with an onset potential and overpotential of 229 mV and 569 mV respectively. This improvement in the catalytic activity was attributed to the degree of passivation on the surface of the nanostructures. The computational studies on the $ReSe_2$ nanostructures showed that OA and OLA result in a high degree of passivation of the nanostructure surface compared to the TOPO, this results in the surfactants blocking more of the active sites which negatively impacts the catalytic activity. TOPO is a much bulkier surfactant, which results in a lower degree of surface passivation.

Hybrid nanostructures of the TMDs and carbon nanostructures were produced using colloidal synthesis. Pristine and nitrogen-doped reduced graphene oxide was used for the study. This was done to increase the electrical conductivity of the TMD nanostructures, which would, in turn, result in increased catalytic activity towards the HER. Few-layered $ReSe_2$ nanostructures were grown on rGO ($ReSe_2$-rGO) and N-rGO ($ReSe_2$-N-rGO). The catalytic activity of the $ReSe_2$ improved after incorporating the nanostructures on the carbon nanostructures. The $ReSe_2$-N-rGO had higher catalytic activity than the $ReSe_2$-rGO, this was attributed to the improved electrical conductivity of the N-rGO provided by the nitrogen doping. The onset potential and overpotential of $ReSe_2$-N-rGO were measured to be 115 mV and 218 mV respectively, which were much improved from pristine $ReSe_2$ nanostructures. The $SnSe_2$-N-rGO also showed some improvement in the catalytic activity of the nanostructures. However, the $MoSe_2$-N-rGO did not show any improvement and the catalytic activity worsened. This was attributed to the interaction of the $MoSe_2$ with the N-rGO nanosheets, the $MoSe_2$ nanostructures grew independently to the N-rGO nanosheets which were in stark contrast to the $ReSe_2$-N-rGO nanostructures. This limited the interaction of the $MoSe_2$ with the N-rGO and resulted in impaired catalytic activity. Alkali metal doping was used to improve the catalytic activity of $SnSe_2$ nanostructures. Potassium was used to dope the $SnSe_2$ nanostructures. The doping was confirmed using powder X-ray diffraction, X-ray fluorescence spectroscopy, and UV-vis spectroscopy. The potassium doped $SnSe_2$ nanostructure showed an improvement to the catalytic activity compared to the pristine $SnSe_2$ nanostructures. The onset potential and overpotential of the doped nanostructures were measured to be 265 mV and 385

mV respectively. This improvement was attributed to the introduction of new active sites on the $SnSe_2$ nanoplates through potassium doping. This was confirmed using the electrochemically active surface area (ECSA) which increased from 8.8 mF/cm^2 in the pristine nanostructures to 11.7 mF/cm^2 in the doped nanostructures. This work has successfully demonstrated that colloidal synthesis can be used to produce TMDs with excellent catalytic activity. The catalytic activity of some of these materials is comparable to the best catalyst of the same materials reported in the literature that are produced using other methods.

Dedication

I dedicate this work to my incredible parents Eric and Josephine Ndala

Acknowledgments

- My deepest gratitude goes to my supervisors Prof Nosipho Moloto, Dr. Siziwe Gqoba, and Dr. Cebisa Linganiso. I sincerely appreciate your guidance and advice throughout the duration of the project and the time you have spent going through all of my work. Your contribution to this work made it possible for me make it to the finish line. Special thanks to Prof Nosipho Moloto for her help and guidance in pushing to get this work published, her desire to get the work to the highest level possible kept me working harder.
- The completion of this work would not have been possible without the contribution of important collaborators such as Prof Phumlane Mdluli, Dr. Ofentse Makgae, Dr. Caren Billing, Prof Marc Humphries, and Dr. Rudolf Erasmus.
- My gratitude also goes to the School of Chemistry at the University of the Witwatersrand for providing the facilities and resources for me to successfully conduct my research. Thank you to the MMU for providing the microscopy instrumentation. I would also like to thank the national research foundation (NRF) for providing the necessary funding for this project.
- I would also like to express my deepest gratitude to all my colleagues at the Nano-Webs research group. Especially to my friends and co-collaborators Mr Ndivhuwo Shumbula, Dr Siyabonga Nkabinde, and Ms Tshwarela Kolokoto. Also, to Dr. Lerato Machogo who was a constant encouragement to all of us in the lab, and whose work has helped me frame my approach to the writing of my thesis. Special thanks to Mr Ndivhuwo Shumbula for being my close friend and partner who helped me throughout the process.
- I would like to thank the CATMAT group for their assistance and constructive criticism throughout this journey. Special thanks to Dr. Thapelo Mofokeng and Dr. Victor Mashindi for help with the electrochemical characterization. Thank you to my girlfriend and co-collaborator Ms. Thelma Majola for her help on the carbon-related work on this project and most important for her emotional and moral support.
- Most importantly, thank you to my family for their love and support, which was what kept me going. None of this would be possible without my parents and my dear brothers.

Presentations

- Oral presentation at Nanomaterials for water, energy, biomedical and sensor applications (NANO-WEBS) seminar held at the School of Chemistry, University of the Witwatersrand on the 15/05/2018.
- Oral presentation at the catalysis and materials (CATMAT) research group seminar at the School of Chemistry, University of the Witwatersrand on the 23/10/2018.
- Oral presentation at the 2018 Nanosciences Young Researchers' Symposium (NYRS) held at North West University on the 16/11/2018 (2^{nd} place prize).
- Poster presentation at the 11^{th} annual cross-faculty symposium held at the University of the Witwatersrand on the 12/10/2020 (1^{st} place prize).
- Grad-flash presentation at the 12^{th} annual cross-faculty symposium held at the University of the Witwatersrand on the 18/09/2020 (3^{rd} place prize).
- Oral presentation at the 1^{st} annual PhD seminar held at the University of the Witwatersrand on the 10/11/2020 (2^{nd} place prize).

Publications

- **Ndala, Z**.; Shumbula, N.; Nkabinde, S.; Kolokoto, T.; Nchoe, O.; Shumbula, P.; Tetana, Z. N.; Linganiso, E. C.; Gqoba, S. S.; Moloto, N., Evaluating the Effect of Varying the Metal Precursor in the Colloidal Synthesis of $MoSe_2$ Nanomaterials and Their Application as Electrodes in the Hydrogen Evolution Reaction. *Nanomaterials* 2020, *10* (9), 1786. {I did all the synthetic work, wrote and corrected the manuscript, and did most of the characterization. I did all of the data interpretation for the characterization. The supervisors (Prof Moloto, Dr. Siziwe Gqoba, and Dr. Cebisa Linganiso) conceptualized the project and made corrections to the manuscript. Dr. Poslet Shumbula assisted with the HRTEM images for the manuscript. Mr. Ndivhwuwo Shumbula, Dr. Siyabonga Nkabinde, Mr Obakeng Nchoe, and Ms. Tshwarela Kolokoto helped in discussing and interpreting the TEM and electrochemical data. Dr. Zikhona Tetyana helped with the SEM}.
- **Ndala, Z**.; Shumbula, N.; Nkabinde, S.; Kolokoto, T.; Linganiso, E. C.; Gqoba, S. S.; Moloto, N., Exploring the electrocatalytic activity of pristine and electrochemically activated $SnSe_2$ nanoplates for the hydrogen evolution reaction. Ndala, Z. B.; Shumbula, N. P.; Nkabinde, S.; Kolokoto, T.; Gqoba, S.; Linganiso, C.; Moloto, N., Electrocatalytic activity of pristine and electrochemically activated SnSe2 nanoplates for the hydrogen evolution reaction. *J. Electroanal. Chem.* **2022**, 116464. {Prof Moloto, Dr Siziwe Gqoba, and Dr cebisa Linganiso) conceptualized the project and made corrections to the manuscript. Mr. Ndivhwuwo Shumbula, Dr. Siyabonga Nkabinde, and Ms. Tshwarela Kolokoto helped in discussing and interpreting the XRD, XPS, TEM, and electrochemical data}.
- Nkabinde, S. S.; **Ndala, Z. B**.; Shumbula, N. P.; Kolokoto, T.; Nchoe, O.; Ngubeni, G. N.; Mubiayi, K. P.; Moloto, N., Delineating the role of crystallinity in the electrocatalytic activity of colloidally synthesized MoP nanocrystals. *New Journal of Chemistry* **2020,** *44* (33), 14041-14049. {I contributed to the electrochemical characterization and discussed the results with the first author}
- Gqoba, S. S.; Rodrigues, R.; Mphahlele, S. L.; **Ndala, Z**.; Airo, M.; Fadojutimi, P. O.; Hümmelgen, I. A.; Linganiso, E. C.; Moloto, M. J.; Moloto, N., Hierarchical Nanoflowers of Colloidal WS2 and Their Potential Gas Sensing Properties for Room

Temperature Detection of Ammonia. Processes 2021, 9 (9), 1491. {I contributed by conducting the SEM analysis}

Table of contents

Declaration……iii
Abstract……iv
Dedication……vii
Acknowledgements……viii
Presentations……ix
Publications……x
List of figures……..xvii
Chapter 1……xvii
Chapter 2……xvii
Chapter 3……xvii
Chapter 4……xviii
Chapter 5.1……xix
Chapter 5.2……xx
Chapter 6.1……xxi
Chapter 6.2……xxii
Chapter 7……xxii
List of tables……..xxiii
Chapter 3……xxiii
Chapter 4……xxiii
Chapter 5.1……xxiii
Chapter 5.2……xxiii
Chapter 6.1……xxiii
Chapter 6.2……xxiii
Chapter 7……xxiii
List of abbreviations……xxv
Synopsis……xxvi
Chapter 1: General background……..1
1. Introduction……1
2. Problem statement……3
3. Motivation and rationale……3
4. Aims and objectives……6
5. References……..6

Chapter 2: Literature review……10
1. Transition metal dichalcogenides……10
1.1 Crystal structure of TMDs……..10
1.2 Electronic properties of TMDs and possible applications……..11
2. Synthesis of TMDs……...12
2.1 Top-down methods……12
2.1.1 Mechanical exfoliation……..12
2.1.2 Liquid exfoliation……..13
2. Bottom-up methods……..15
2.2.1 Chemical vapor deposition (CVD)……15
2.2.2 Wet chemical methods for the synthesis of TMDs…….....17
3. Colloidal synthesis as an effective method for producing TMDs……..18
3.1 Colloidal synthetic methods for the synthesis of TMDs……..21
4. The hydrogen evolution reaction……..24
4.1 Introduction to the hydrogen evolution reaction……..24
4.2 The exploration of TMDs as effective catalysts in the HER……..30
4.3 Colloidal synthesis of TMDs for HER…….....33
5. References……34
Chapter 3: Elucidating the effect of metal and chalcogen precursor selection on the colloidal synthesis of $MoSe_2$ and $ReSe_2$ nanostructures and its impact on catalytic activity of the nanostructures towards the hydrogen evolution reaction……42
1. Introduction……..…42
2. Experimental section……43
2.1 Chemicals…….....43
2.2 Synthesis of $MoSe_2$ and $ReSe_2$ nanostructures…….....43
2.3 Characterization techniques……43
2.4 Electrochemical characterization……44
3. Results and discussion……..44
4. Conclusions……..54
5. References……55
6. Supplementary information……...…58
Chapter 4: Exploring the electrocatalytic activity of pristine and electrochemically activated $SnSe_2$ nanoplates for the hydrogen evolution reaction……61
1. Introduction……..61

2. Experimental section……62
2.1 Chemicals…….....62
2.2 Synthesis of $SnSe_2$ nanostructures……..62
2.3 Characterization techniques……62
2.4 Electrochemical characterization……63
3. Results and discussion……..63
4. Conclusions……..73
5. References……73
6. Supplementary information……..77
Chapter 5: Unravelling the effects of surface functionalization on the catalytic activity of TMD nanostructures towards the hydrogen evolution reaction……..80
Chapter 5.1: Unravelling the effects of surface functionalization on the catalytic activity of $ReSe_2$ nanostructures towards the hydrogen evolution reaction……80
1. Introduction……..80
2. Experimental section…….81
2.1 Chemicals……..81
2.2 Synthesis of $ReSe_2$ nanostructures using OLA, OA, and TOPO……...81
2.3 Characterization techniques……...82
2.4 Electrochemical characterization……...82
2.5 Computational studies……....83
3. Results and discussion…….83
4. Conclusions……...103
5. References……104
6. Supplementary information……...109
Chapter 5.2: Unravelling the effects of surface functionalization on the catalytic activity of $MoSe_2$ and $SnSe_2$ nanostructures towards the hydrogen evolution reaction……..117
1. Introduction……117
2. Experimental section…….....118
2.1 Chemicals……..……..118
2.2 Synthesis of $MoSe_2$ and $SnSe_2$ nanostructures using OLA, OA, and TOPO…..……118
2.3 Characterization techniques…….119
2.4 Electrochemical characterization…...……..119
3. Results and discussion……120
4. Conclusions……132

5. References……..132
6. Supplementary information……135
Chapter 6: The colloidal synthesis of TMD nanostructures on pristine and nitrogen-doped reduced graphene oxide for use as electrocatalysts in the hydrogen evolution reaction……141
Chapter 6.1: The colloidal synthesis of $ReSe_2$ nanostructures on pristine and nitrogen-doped reduced graphene oxide for use as electrocatalysts in the hydrogen evolution reaction.....141
1. Introduction……141
2. Experimental section……..142
2.1 Chemicals……..142
2.2 Synthesis of nanostructures……...142
2.3 Characterization techniques…….....143
2.3 Electrochemical characterization……...143
3. Results and discussion……144
4. Conclusions……156
5. References……..156
6. Supplementary information…….....159
Chapter 6.2: The colloidal synthesis of $MoSe_2$ and $SnSe_2$ nanostructures on nitrogen doped reduced graphene oxide for use as electrocatalysts in the hydrogen evolution reaction ……162
1. Introduction……162
2. Experimental…….....162
2.1 Chemicals……...162
2.2 Synthesis of nanostructures……163
2.3 Characterisation techniques……163
2.4 Electrochemical techniques……164
3. Results and discussion……164
4. Conclusions……172
5. References……..172
6. Supplementary information…….....174
Chapter 7: The catalytic activity of potassium doped $SnSe_2$ nanostructures towards the hydrogen evolution reaction……...176
1. Introduction……176
2. Experimental section……..…….. 177

2.1 Chemicals…….177
2.2 Synthesis of $SnSe_2$ nanostructures…….....177
2.3 Characterization techniques……..177
2.4 Electrochemical techniques……..178
3. Results and discussion……178
4. Conclusions……187
5. References……..187
6. Supplementary information……189
Chapter 8: Overall conclusions and recommendations……..190
8.1 Conclusions……..190
8.2 Recommendations……191

List of figures

Chapter 1

Figure 1: The hydrogen economy……..…..1

Figure 2: Crystal structure of $ReSe_2$ (a) Top view with Re chains, (b) side view……5

Chapter 2

Figure 1: Diagram depicting the structure of bulk TMDs…….....10

Figure 2: Metal coordination of 2H and 1T TMDs……...11

Figure 3: Mechanical exfoliation of graphite to produce graphene……..13

Figure 4: Liquid exfoliation methods. (a) chemical exfoliation and (b) Intercalation…….....13

Figure 5: Using shear force from a blender to exfoliate bulk TMD crystals……14

Figure 6: MOCVD synthesis of TMDs……....16

Figure 7: Hydrothermal synthesis of MoS_2/MoO_3 nanosheets for HER applications……...17

Figure 8: A graphical representation of the LaMer and Dinegar nucleation……19

Figure 9: Schematic representation of the colloidal synthesis of QDs…….....20

Figure 10: NbS_2 structure dependence on the OAc/OAm molar ratio and the amount of CS_2……23

Figure 11: Schematic representation of HER pathway…….....26

Figure 12: Trasatti volcano plot……...27

Figure 13: Volcano plots for hydrogen evolution in acidic solution……...28

Figure 14: Typical polarisation curve with the denoted region for the onset region and overpotential at 10 mA/cm^2……..……29

Figure 15: Tafel plot showing how the Tafel slope and exchange current density are extracted from the plot……..30

Figure 16: Synthetic procedure detailing the formation of MoS_2 nanosheets on the surface of rGO……...32

Figure 17: Schematic illustration of the hydrothermal synthetic process of $ReSe_2$@GO.....32

Chapter 3

Figure 1: PXRD patterns of (a) $MoSe_2$ nanostructures and (b) $ReSe_2$ nanostructures. Raman spectra of (c) $MoSe_2$ nanostructures, and (d) $ReSe_2$ nanostructures……45

Figure 2: TEM images of (a-b) $MoSe_2$, (c-d) $MoSe_2$-Sel, (e-f) $ReSe_2$, and (g-h) $ReSe_2$-Sel**.**……47

Figure 3: TEM images of the $MoSe_2$ nanostructures at (a) 15 min, (b) 30 min, (c) 60 min, and (d) 90 min. TEM images of the $ReSe_2$ nanostructures at (e) 15 min, (f) 30 min, (g) 60 min, and (h) 90 min……..48
Figure 4: Schematic representation of the formation of flower-like microsphere……..49
Figure 5: (a) Polarisation curves, (b) Tafel plots, (c) Cdl plots, and (d) Nyquist plots of the $MoSe_2$ and $ReSe_2$ nanostructures……..50
Figure S1: Deconvoluted A_{1g} peak from the Raman spectrum of $MoSe_2$-Sel……...58
Figure S2: Powder patterns of the $MoSe_2$ and $ReSe_2$ at 15 min, 30 min, 60 min, and 90 min (d)…….59
Figure S3: Particle size distribution for flower-like $MoSe_2$ microspheres……....59
Figure S4: CV curves of (a) $MoSe_2$, (b) $MoSe_2$-Sel, $ReSe_2$, and (d) $ReSe_2$-Sel……....60

Chapter 4

Figure 1: (a) PXRD patterns of $SnSe_2$ nanomaterials and (b) Raman spectrum of $SnSe_2$ nanomaterials. High-resolution XPS spectra of (c) Sn 3d state and (d) Se 3d state……64
Figure 2: TEM (a) and SEM (b) images of $SnSe_2$ nanostructures…….....65
Figure 3: (a) Polarisation curves of $SnSe_2$ nanoplates and Pt/C. (b) Tafel plots of $SnSe_2$ nanoplates and Pt/C……..65
Figure 4: (a) Polarisation curves for the $SnSe_2$ nanoplates after every 200 scans. (b) Chronoamperometry curve for the $SnSe_2$ nanoplates at 620 mV applied potential and 300 min time scale. (c) Tafel plots of the $SnSe_2$, A-$SnSe_2$, and Pt/C. (d) Nyquist plots of the $SnSe_2$ and A-$SnSe_2$……67
Figure 5: Intercalation of H^+ cations in the internal structure of the $SnSe_2$……69
Figure 6: (a) cyclic voltammogram of the $SnSe_2$ nanostructures in 0.5 M H_2SO_4. (b) PXRD patterns of the pristine and A-$SnSe_2$ nanostructures. (c) Shift of the (001) peak due to proton intercalation……..70
Figure 7: (a) Cdl plots the $SnSe_2$ nanostructures before and after activation. (b) Raman spectra of the $SnSe_2$ nanostructures before and after activation. (c) XPS spectra of the $SnSe_2$ nanostructures before and after activation…….....72
Figure S1: Chronoamperometry curve for the $SnSe_2$ nanoplates at 620 mV vs RHE applied potential and 15 hr time scale……77
Figure S2: Polarisation curves showing the pre-feature in the initial scan……77
Figure S3: (a) Polarisation curves for $SnSe_2$ in 0.5 M KOH. (b) Polarisation curves showing the stability of the $SnSe_2$ nanoplates after a 1000 LSV scans……78

Figure S4: CV curves at 20, 40, 60, 80, and 100 mV/s for $SnSe_2$ (a) and activated $SnSe_2$ (b)…….78
Figure S5: TEM image of the electrochemically activated $SnSe_2$ nanoplates……78

Chapter 5.1

Figure 1: PXRD patterns for $ReSe_2$ nanostructures synthesized using the three specified surfactants. Oleylamine ($ReSe_2$-OLA), oleic acid ($ReSe_2$-OA), and trioctylphosphine oxide ($ReSe_2$-TOPO)……..84
Figure 2: High-resolution XPS spectra of $ReSe_2$-OLA (a and b), $ReSe_2$-OA (c and d), and $ReSe_2$-TOPO (e and f)……...85
Figure 3: Crystal structure of $ReSe_2$, viewed perpendicular to the basal plane, with the a and b axes and their respective crystal planes…….91
Figure 4: Adsorption isotherm of the surfactants on the $ReSe_2$ nanostructures indicating the average loading of the surfactant molecules per cell on the two crystal planes……...92
Figure 5: Density of state of (a) $ReSe_2$ cleaved along the {010} surface, (c) $ReSe_2$ cleaved along the {100}; supercell structures for (b) $ReSe_2$ cleaved along the {010} surface, (d) $ReSe_2$ cleaved along the {100}…….....93
Figure 6: Supercell and density of state of the optimized cleaved crystal of $ReSe_2$, where Density of state of (a) $ReSe_2$-TOPO, (d) $ReSe_2$-OLA, (g) $ReSe_2$-OA; optimized structure of (b) $ReSe_2$-TOPO, (e) $ReSe_2$-OLA, (h) $ReSe_2$-OA; and (c) Top vi (c) $ReSe_2$-TOPO, (f) $ReSe_2$-OLA, (i) $ReSe_2$-OA…….94
Figure 7: TEM images of the (a) $ReSe_2$-OLA (c) $ReSe_2$-OA and (e) $ReSe_2$-TOPO nanostructures. The HRTEM images of the images are shown in (b) $ReSe_2$-OLA, (d) $ReSe_2$-OA, and (f) $ReSe_2$-TOPO……..96
Figure 8: HAADF-STEM image and elemental mapping of the (a) $ReSe_2$-OLA, (b) $ReSe_2$-OA, and (c) $ReSe_2$-TOPO nanostructures…….98
Figure 9: (a) Polarisation curves of $ReSe_2$ nanostructures, 20% Pt/C and glassy carbon (b) Tafel plots of the nanostructures synthesized with the various surfactants and that of 20% Pt/C. (c) C_{dl} plots of the $ReSe_2$ nanostructures (d) Anodic peaks due to the surface oxidation of the $ReSe_2$ nanostructures. (e) Nyquist plots of the $ReSe_2$ nanostructures. (f) Polarisation curves of the $ReSe_2$-TOPO nanostructures initially and after 1000 cycles……...99
Figure S1: Structure of the surfactants and their respective head groups……109
Figure S2: XPS survey spectra of (a) $ReSe_2$-OLA, (b) $ReSe_2$-OA, and $ReSe_2$-TOPO……110

Figure S3: (a) N1s spectrum of $ReSe_2$-OLA, (b) C1s spectrum of $ReSe_2$-OA, and (c) O1s spectrum of $ReSe_2$-OA……....111
Figure S4: FTIR spectra of free surfactant and capped nanomaterials for (a) $ReSe_2$-OLA, (b) $ReSe_2$-OA, and (c) $ReSe_2$-TOPO……....112
Figure S5: The 1H NMR spectra of capped nanomaterials and their free surfactants for (a) $ReSe_2$-OLA, (b) $ReSe_2$-OA, and $ReSe_2$-TOPO……...113
Figure S6: Band structures of $ReSe_2$ clusters where (a) un-cleaved layer and (b) cleaved layer along the {010} surface……...114
Figure S7: HRTEM images of the $ReSe_2$-TOPO nanomaterials……...114
Figure S8: EDX spectra for the $ReSe_2$ nanomaterials (a) $ReSe_2$-OLA, (b) $ReSe_2$-OA, and $ReSe_2$-TOPO……..115
Figure S9: CV for the $ReSe_2$ nanomaterials (a) $ReSe_2$-OLA, (b) $ReSe_2$-OA and (c) $ReSe_2$-TOPO……116

Chapter 5.2

Figure 1: (a) PXRD patterns of $MoSe_2$. (b) Raman spectra of $MoSe_2$ nanostructures. (c) PXRD patterns of $SnSe_2$ nanostructures. (d) Raman spectra of $SnSe_2$ nanostructures……120
Figure 2: TEM images of (a) $MoSe_2$-OA, (b) $MoSe_2$-OLA, (c) $MoSe_2$-TOPO, (d) $SnSe_2$- OLA, (e) $SnSe_2$-OA, and (f) $SnSe_2$-TOPO……125
Figure 3: Schematic representation of the rod formation……...126
Figure 4: (a) Polarisation curves of $MoSe_2$ nanostructures. (b) Polarisation curves of the $SnSe_2$ nanostructures. (c) Tafel plots of $MoSe_2$ nanostructures. (d) Tafel plots of $SnSe_2$ nanostructures……127
Figure 5: (a) C_{dl} plots of the $MoSe_2$ nanostructures. (b) Cdl plots of the $SnSe_2$ nanostructures. (c) Nyquist plots of the $MoSe_2$ nanomaterials. (d) Nyquist plots of the $SnSe_2$ nanostructures……129
Figure S1: Structure of the solvents (a) oleylamine, (b) oleic acid, and (c) trioctylposphine oxide……...135
Figure S2: FTIR spectra of (a) OLA, $MoSe_2$-OLA, and $SnSe_2$-OLA. (b) OA, $MoSe_2$-OA, and $SnSe_2$-OA. (c) TOPO, $MoSe_2$-TOPO, and $SnSe_2$-TOPO……...136
Figure S3: NMR spectra of (a) OLA and $MoSe_2$-OLA, (b) OA and $MoSe_2$-OA, (c) TOPO and $MoSe_2$-TOPO, (d) OLA and $SnSe_2$-OLA, (e) OA and $SnSe_2$-OA, (f) TOPO and $SnSe_2$-TOPO……137

Figure S4: TEM images of the (a) $SnSe_2$-OA rod-like nanostructures and (b) curling in the $SnSe_2$-TOPO nanoplates……138
Figure S5: CV curves for the stability studies of (a) $MoSe_2$-OLA, (b) $MoSe_2$-OA and (c) $MoSe_2$-TOPO. CV curves for the stability of studies of (a) $SnSe_2$-OLA, $SnSe_2$-OA, and $SnSe_2$-TOPO……139
Figure S6: Polarisation curves for the stability studies of (a) $MoSe_2$-OLA, (b) $MoSe_2$-OA and (c) $MoSe_2$-TOPO. Polarisation curves for the stability of studies of (a) $SnSe_2$-OLA, $SnSe_2$-OA, and $SnSe_2$-TOPO……....140

Chapter 6.1

Figure 1: PXRD patterns of (a) rGO and N-rGO. (b) PXRD shows the shift of the (002) in rGO and N-rGO. (c) the PXRD pattern of the $ReSe_2$ and the nanocomposites (d) Raman spectra of the rGO and N-rGO……....144
Figure 2: (a) Deconvoluted XPS spectrum of the N 1s peak. (b) Graphical representation of the types of nitrogen defects introduced. (c) High-resolution XPS spectrum of Re. (d) High-resolution XPS spectrum of Se……..147
Figure 3: TEM images of (a) $ReSe_2$ nanoflowers, (b) rGO, (c) N-rGO, (d) $ReSe_2$-rGO, and (e) $ReSe_2$-N-rGO……148
Figure 4: Decomposition profiles of (a) rGO and N-rGO, (c) rGO and $ReSe_2$-rGO, (d) N-rGO and $ReSe_2$-N-rGO. (b) derivative decomposition profile of rGO and N-rGO…….....150
Figure 5: Adsorption- desorption isotherms of (a) $ReSe_2$, (b) $ReSe_2$-rGO, and (c) $ReSe_2$-N-rGO……151
Figure 6: (a) Polarisation curves of the $ReSe_2$ nanostructures and their nanocomposites. (b) Tafel plots of the $ReSe_2$ nanostructures and nanocomposites. (c) Cdl plots of the $ReSe_2$ nanostructures and nanocomposites. (d) Nyquist plots of the $ReSe_2$ nanostructures and nanocomposites. (e) Irreversible surface oxidation profile of $ReSe_2$-rGO and $ReSe_2$-N-rGO. (f) Stability studies of the $ReSe_2$ nanostructures and nanocomposites…….153
Figure S1: XPS survey scan of (a) rGO and (b) N-rGO……..159
Figure S2: C1s XPS spectrum of (a) rGO and (b) N-rGO……159
Figure S3: XPS survey spectra of (a) $ReSe_2$-rGO and (b) $ReSe_2$-N-rGO…….160
Figure S4: Adsorption-desorption isotherm of (a) rGO and (b) N-rGO……...160
Figure S5: C_{dl} plots of (a) $ReSe_2$, (b) $ReSe_2$-rGO, and (b) $ReSe_2$-N-rGO……161

Chapter 6.2

Figure 1: PXRD patterns of (a) $MoSe_2$-N-rGO and (b) $SnSe_2$-N-rGO. Raman spectra of (c) $MoSe_2$-N-rGO and (d) $SnSe_2$-N-rGO…….165

Figure 2: TGA profiles of (a) $MoSe_2$-N-rGO and (b) $SnSe_2$-N-rGO……166

Figure 3: TEM images of (a) $MoSe_2$, (b) $SnSe_2$, (c) N-rGO, (d) $MoSe_2$-rGO, and (e) $SnSe_2$-N-rGO…….167

Figure 4: Adsorption- desorption isotherms of (a) $MoSe_2$, (b) $MoSe_2$-rGO, (c) $SnSe_2$, and (d) $SnSe_2$-N-rGO……..168

Figure 5: (a) Polarisation curves of the $MoSe_2$, $SnSe_2$ nanostructures and their N-rGO nanocomposites. (b) Tafel plots of the $MoSe_2$, $SnSe_2$ nanostructures and N-rGO nanocomposites. (c) Cdl plots of $MoSe_2$, $SnSe_2$, $MoSe_2$-N-rGO, and $SnSe_2$-N-rGO. (d) Nyquist plots of $MoSe_2$, $SnSe_2$, $MoSe_2$-N-rGO, and $SnSe_2$-N-rGO…….170

Figure S1: TEM image of $SnSe_2$ nanoplates on N-rGO nanosheets…….174

Figure S2: Adsorption- desorption isotherms of N-rGO……...175

Chapter 7

Figure 1: (a) PXRD patterns of pristine and doped $SnSe_2$ nanostructures, (b) Shift of the (001) peak after doping, (c) Raman spectra of the pristine and doped $SnSe_2$ nanostructures, and (d) the shift in the A_{1g} peak of the doped nanostructures……...179

Figure 2: XPS spectra of Sn^{4+} and Se^{2-} respectively for (a-b) $SnSe_2$, (c-d) $SnSe_2$-K1, and (e-f) $SnSe_2$-K2……180

Figure 3: TEM and SEM images of $SnSe_2$ nanostructures (a-b) $SnSe_2$, (c-d) $SnSe_2$-K1, (e-f) $SnSe_2$-K2……182

Figure 4: (a) Polarisation curves of the pristine and doped $SnSe_2$ nanostructures, (b) Tafel plots, (c) C_{dl} plots, and (d) Nyquist plots of the pristine and doped $SnSe_2$ nanostructures…183

Figure 5: The stability studies of (a) $SnSe_2$ (b) $SnSe_2$-K1, and (c) $SnSe_2$-K2……..186

Figure S1: Cyclic voltammetry curves of (a) $SnSe_2$, (b) $SnSe_2$-K1, and $SnSe_2$- K2. (d) Tauc plot of the pristine and doped $SnSe_2$ nanostructures……..189

List of Tables

Chapter 3

Table 1: Comparison of the catalytic activity of the as-synthesized $MoSe_2$ and $ReSe_2$ and their literature counterparts……...53

Chapter 4

Table 1: Electrocatalytic parameters of the $SnSe_2$ nanoplates before and after electrochemical activation……..68

Chapter 5.1

Table 1: Summary of the bonding configuration and elemental composition data…….86

Table 2: FTIR assignments for OLA, OA, and TOPO and the $ReSe_2$ nanostructures……88

Table 3: NMR assignments for free surfactants and capped nanostructures……...89

Table 4: Comparison of the catalytic performance of the synthesized nanostructures and other $ReSe_2$ nanostructures in literature……...103

Chapter 5.2

Table 1: Assignments of the FTIR peaks in the free surfactants and capped nanostructures……122

Table 2: Assignments of the 1H NMR peaks in the free surfactants and capped nanostructures……123

Table 3: Comparison of the catalytic performance of the synthesized nanostructures and other $MoSe_2$ and $SnSe_2$ nanostructures in literature…….....131

Chapter 6.1

Table 1: Summary of the elemental composition of rGO and N-rGO……..146

Table 2: Summary of the C 1s assignments and composition……...146

Table 3: Comparison of the catalytic activity of the as-synthesized $ReSe_2$, the hybrid nanostructures, and their literature counterparts…...…….155

Chapter 6.2

Table 1: Comparison of the catalytic activity of the as-synthesized $MoSe_2$, $SnSe_2$, the hybrid nanostructures, and their literature counterparts…….171

Chapter 7

Table 1: Summary of the peak binding energies and atomic compositions of the pristine and doped $SnSe_2$ nanostructures……...181

Table 2: Electrocatalytic parameters of the pristine and doped $SnSe_2$ nanoplates before and after electrochemical activation……..187

List of abbreviations

BET- Brunauer- Emmett-Teller

CV- Cyclic voltammetry

CVD- Chemical vapor deposition

DFT – Density functional theory

EDX – Energy dispersive X-ray spectroscopy

EIS- Electrical impedance spectroscopy

FTIR- Fourier transform infrared spectroscopy

HAADF – High-angle dark-field imaging

HRTEM - High-resolution transmission electron microscopy

NMR - Nuclear magnetic resonance

OA - Oleic acid

OLA - Oleylamine

PXRD - Powder X-ray diffraction

SEM - Scanning electron microscopy

TEM - Transmission electron microscopy

TGA -Thermogravimetric analysis

TMD - Transition metal dichalcogenide

TOPO- Trioctylphosphine oxide

UV-Vis - Ultraviolet-visible spectroscopy

XPS - X-ray photoelectron spectroscopy

XRF - X-ray fluorescence spectroscopy

Synopsis

Transition metal dichalcogenides (TMDs) have garnered a lot of interest due to the interesting properties they exhibit in their monolayer and few-layer forms. They have been explored in various applications such as sensors, batteries, supercapacitors, and electrocatalysis. These materials have become increasingly popular as candidate electrocatalysts in the hydrogen evolution reaction (HER). This reaction is used for the production of green hydrogen, which can be used as a clean and efficient energy carrier to replace fossil fuels. This reaction has been conducted using the rare, expensive, and precious metal platinum as a catalyst, which negatively affects the economic feasibility of this process, hence the need for novel electrocatalysts made using TMDs. This will eventually lead to a demand in the large-scale synthesis of these materials for these types of applications. This work aimed to synthesize $MoSe_2$, $ReSe_2$, and $SnSe_2$ nanomaterials using a facile colloidal method, for the purpose of using these materials as electrocatalysts in the hydrogen evolution reaction (HER). The study demonstrated that the strategies used to improve the catalytic activity of TMDs could be applied using the colloidal method. The outline of the thesis is therefore shown below:

Chapter 1: This chapter gives a brief introduction to the hydrogen economy, and one of the biggest challenges facing the large-scale synthesis of green hydrogen. It motivates the use of TMDs as a possible solution to this problem and identifies a method by which these TMD could be produced at a large-scale in the future.

Chapter 2: This chapter provides a general background on TMDs. It also details various techniques that have been used for the synthesis of these materials and any advancements that have been made in this area. A background into the colloidal synthesis of semiconductor nanostructures and TMDs are provided. A detailed introduction into the HER, the use of TMD nanostructures as electrocatalysts in the HER, and the characterization of these nanostructures in this application.

Chapter 3: This chapter focuses on the synthesis of $MoSe_2$ and $ReSe_2$ nanostructures. The work demonstrates that the choice of both the metal and selenium precursor plays a vital role in the properties of the synthesized nanostructures. This method showed that an understanding of the effect of the precursor on the nucleation and growth processes in synthesis could help produce nanostructures with similar structural properties. These materials will act as a baseline

and the subsequent chapters will focus on improving the catalytically activity of the nanostructures.

Chapter 4: This chapter has been published in the Journal of Electroanalytical Chemistry (*J. Electroanal. Chem.* **2022**, 116464). This chapter focuses on the synthesis and electrochemical characterisation of $SnSe_2$ nanostructures. In this work, the catalytic activity of $SnSe_2$ nanoplates towards the HER was evaluated. $SnSe_2$ nanoplates were synthesized and found to be rather poor catalysts for the HER. However, it was also found that the $SnSe_2$ undergoes electrochemical activation after several LSV scans. This phenomenon was found to be due to proton intercalation in between the layers of the nanoplates which has been known to result in a drastic increase in the catalytic performance of TMDs towards the HER. This work also serves as a baseline to further evaluate the performance of modified $SnSe_2$ catalyst in subsequent chapters.

Chapter 5.1: This work focuses on the surface functionalization of $ReSe_2$ nanostructures during colloidal synthesis and its effect on the catalytic activity of the nanostructures towards the HER. Three common surfactants (oleylamine, oleic acid, and trioctylphosphine oxide) were used to synthesize $ReSe_2$ nanostructures. These surfactants were able to bind to the surface of the nanostructures during synthesis. This work demonstrated that the choice of surfactant could result in excellent catalytic activity. Provided the surfactant chosen allowed for the growth of nanosheets with a high density of active edges and that, the surfactant does not highly passivate the surface of the nanostructures.

Chapter 5.2: This work follows from **chapter 5.1** and evaluates the effect of surface functionalization on the catalytic activity of $MoSe_2$ and $SnSe_2$ nanostructures.

Chapter 6.1: This work focuses on the growth of $ReSe_2$ on reduced graphene oxide (rGO) and nitrogen-doped reduced graphene oxide (N-rGO). This was done to study how colloidal synthesis could be used to produce TMD and carbon nanostructure hybrid nanomaterials. This is also a good strategy to improve the catalytic activity of TMDs by increasing the electron conductivity of the nanostructures through the use of rGO and N-rGO as carbon supports.

Chapter 6.2: This work carries on from **chapter 6.1**. The work focuses on growing $MoSe_2$ and $SnSe_2$ nanostructures on N-rGO. N-rGO was chosen because it improved the catalytic activity more effectively than rGO in **chapter 6.1**.

Chapter 7: This work focuses on the potassium doping of $SnSe_2$ nanostructures to improve their catalytic activity towards the HER. It has been theorized using computational models that the alkali metal doping of $SnSe_2$ can activate the otherwise inert basal plane of the nanostructures towards the HER. This work sought to investigate whether these claims had any merit.

Chapter 8: Overall conclusions of the study and recommendations.

Chapter 1: General background

1. Introduction

As the global population has increased, there is a greater demand for energy, which has led to an increase in the use of fossil fuels to meet these energy needs. Unfortunately, this has also led to an increase in CO_2 emissions, which the scientific community has agreed is one of the greatest contributors to climate change. Studies have shown that if the rise in global temperature increases to 2 °C in the next dozen years, this could spell catastrophe for the planet.[1-2] This has led to renewed efforts in the race to find a clean and efficient way of producing energy that is not detrimental to our environment. The 'hydrogen economy' is an energy system that uses hydrogen gas as a clean, efficient, and low-polluting energy carrier as opposed to fossil fuels. The system relies on the use of renewable energy to produce hydrogen gas, the hydrogen gas can be used to power industries, transportation, homes, etc. as shown in **Fig.1**.[3]

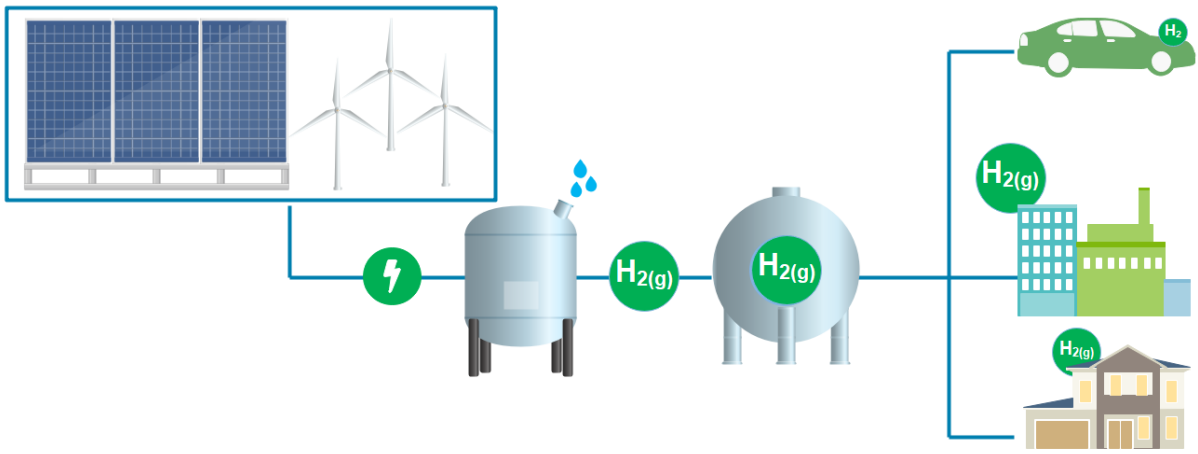


Figure 1: The hydrogen economy.

This hydrogen gas would drastically reduce CO_2 emissions because the only by-product would be water and heat.[4] The global hydrogen demand is estimated to increase by 30% in 2040. Hydrogen gas can be generated by electrolysis through the hydrogen evolution reaction (HER). The HER is an electrocatalytic process that is conducted with the use of platinum as a catalyst. Unfortunately, the use of platinum which is a scarce and expensive noble metal makes the HER an economically unfavorable process.[5-6] Cheap and abundant catalysts are required as alternatives to platinum to drive down the cost of hydrogen production. Transition metal

dichalcogenides have been identified as potential alternatives to platinum as a catalyst for the HER.

Layered transition metal dichalcogenides (TMDs) are 2D materials that have the general formula MX_2 where M is a transition metal (M = Mo, W, Nb, Ti, Ta, Re) and X is a chalcogen (X= S, Se, Te). A single layer is comprised of a transition metal that is covalently bonded to chalcogen atoms. The configuration of a single layer takes that of a sandwiched structure where the metal layer is sandwiched between two chalcogen layers (X-M-X). These single layers stack together to make the bulk crystal which is held together by weak van der Waals forces. The monolayer and few-layer counterparts of these materials exhibit interesting and exotic electronic, optical, and catalytic properties that are dependent on thickness, composition, and crystal structure.[7-8] There are various TMDs that have been found to have excellent catalytic activity towards the HER. TMDs such as MoS_2, $MoSe_2$, and VS_2 have particularly shown quite compelling catalytic activity towards the HER.[9-11] A study into the catalytic activity of these materials has shown that the active sites for the HER on these materials are the edge sites while the basal plane remains largely inert.[12] Thus, the strategies for improving the catalytic activity of TMDs to rival that of Pt have focused on improving the exposure of the active edge sites.[13-15] However, there have been increased efforts in using various other strategies to improve the performance of these materials. It has been shown that the basal plane of these materials can be activated by introducing defects.[16-17] Other methods have also been shown to increase the catalytic activity of TMDs such as phase engineering, chemical doping, and formation of hybrid nanostructures.[18-20]

These TMDs were initially synthesized using mechanical exfoliation, which is a top-down method that has been used to remove a monolayer of the TMDs from the bulk crystal.[21] However, this method is only suited to produce these materials at a lab-scale and cannot be scaled up for large-scale production. The large-scale synthesis of these materials is the most pressing problem in producing these materials for commercial applications.[22-23] Various methods are being developed for the large-scale synthesis of TMDs such as liquid exfoliation, metal-organic chemical vapor deposition (MOCVD), and hydrothermal synthesis.[24-26] Colloidal synthesis has also been shown to be an effective method to synthesize TMDs.[27-28] Colloidal synthesis was initially developed to synthesize high-quality and monodispersed quantum dots (QDs), the method has recently been adapted to the synthesis of TMD nanostructures. It has proven to be an effective way of synthesizing TMDs with the potential

for synthesis of these materials at a large-scale. The method has also been shown to synthesize TMD nanostructures with tuneable properties. Properties such as the thickness, phase, and interlayer spacing can be controlled by varying certain reaction parameters such as the temperature, solvent/capping agent, and precursors.[29-31]

In this work, the synthesis of various TMDs using colloidal synthesis was explored. Specifically, the synthesis of TMD nanostructures for applications as electrocatalysts in the HER. This work shows how the colloidal synthesis can be used to tune the properties of TMDs in order to increase the catalytic activity of the TMD nanostructures towards the HER. The method has been used to introduce defects such as Se vacancies, to increase the exposure of the active edge sites using various solvents/capping agents, doping using alkali metals, and formation of hybrid materials using carbonaceous materials.

2. Problem statement

The advent of TMDs as novel nanostructures for applications in various applications such as transistors, biosensors, batteries, and electrocatalysis will lead to a sizeable demand for these nanostructures for commercial applications. TMDs have particularly shown impressive performance as electrocatalysts in the HER reaction. Considering that the demand for hydrogen will increase by over 30% in 2030, the demand for large-scale production of TMD nanostructures for hydrogen production will surely increase.[32] Unfortunately, the current methods available at this time are not yet suitable to produce these materials on a large-scale. Moreover, the synthetic methods that need to be developed would need to be adaptable and versatile in order to synthesize various TMDs that can suit very particular circumstances. Developing synthetic methods that carry all these characteristics has proven to be a daunting task. Certainly, when looking at the progress of graphene in the last couple of years, it is easy to see how crucial viable and economically feasible production methods can be to the large-scale application of advanced materials. Thus, the development of suitable methods for the industrial production of TMDs is of paramount importance to prevent these materials from encountering the same issues as graphene.

3. Motivation and rationale

In an effort to try and meet the increasing demand for hydrogen many countries have intensified their funding into various hydrogen initiatives. Several G8 countries have invested heavily in the hydrogen economy and fuel cell technology. The French government in June 2018 unveiled

a $117 million plan in support for the technology, while countries like Germany which is a front leader in the technology continued to invest more money in fuel cells projects by green-lighting an investment of $110 million into funding 20 research labs that focus on this technology.[33] Some countries like South Korea and Japan have invested heavily in the development of public and private automobiles that utilize hydrogen as a source of fuel. South Africa has also begun investing heavily in this technology. From an R&D perspective, the country has set-up the development and innovation strategy on hydrogen called (HySA). The South African minister of energy stated that the department aimed to "stimulate and guide innovation along the value chain of hydrogen and fuel cell technologies".[34] The president of South Africa Mr. Cryil Ramaphosa has announced the "hydrogen valley", which will aim to pull together and integrate all hydrogen initiatives to form an integrated system. Certainly, these advocate for the development of methods that will allow for the synthesis of viable catalysts for the HER. The colloidal synthesis has certainly been shown to be a viable solution for the synthesis of novel TMD electrocatalysts. This work explores the use of this method to improve the catalytic activity of the methods through the introduction of defects, chemical doping, increasing the number of active sites, and forming nanohybrid materials with carbon nanostructures. This work will demonstrate the ability of these methods to incorporate all the methods that are available to increase the catalytic activity of TMDs towards the HER.

3.1 Motivation for selecting $MoSe_2$, $ReSe_2$, and $SnSe_2$ as subject TMDs

$MoSe_2$ is one of the most explored TMDs after MoS_2 and WS_2. It has been found to be an interesting material in various applications including electrocatalysis. $MoSe_2$ has been investigated substantially for application as an electrocatalyst in the HER, and some promising results have been reported on this material. Colloidal synthesis of $MoSe_2$ nanostructures for HER applications has already been undertaken by the author of this Ph.D. thesis. The synthetic methods used in the synthesis of $MoSe_2$ were used for the synthesis of $ReSe_2$ nanostructures which was the second TMD that was to be studied.[31] This was done to determine whether these synthetic methods could be used to synthesize other TMDs with similar properties. **Chapter 3** in this thesis shows how the understanding of nucleation and growth characteristics of $MoSe_2$ in colloidal synthesis can be used to synthesize more obscure TMDs such as $ReSe_2$ using the same methods. $MoSe_2$ was also used as a benchmark to determine whether colloidal synthesis can be used to produce TMD nanostructure that can compete with $MoSe_2$ synthesized using other methods. $ReSe_2$ has emerged as one of the most interesting in the TMD family of materials. It has been shown to crystallize in the uncommon distorted 1T phase. The structure

contains diamond-shaped Re_4 chains along the b[010] direction as shown in **Fig.2(a)** that are due to the stabilization of the valance electrons in the Re atoms. The $ReSe_2$ exhibits a low symmetry crystal lattice which results in anisotropic optical and electronic properties.[35] Due to the distorted 1T structure shown in **Fig.2(b)**, bulk $ReSe_2$ possesses weak interlayer coupling which results in the bulk structure acting like electronically and vibrationally decoupled monolayers.

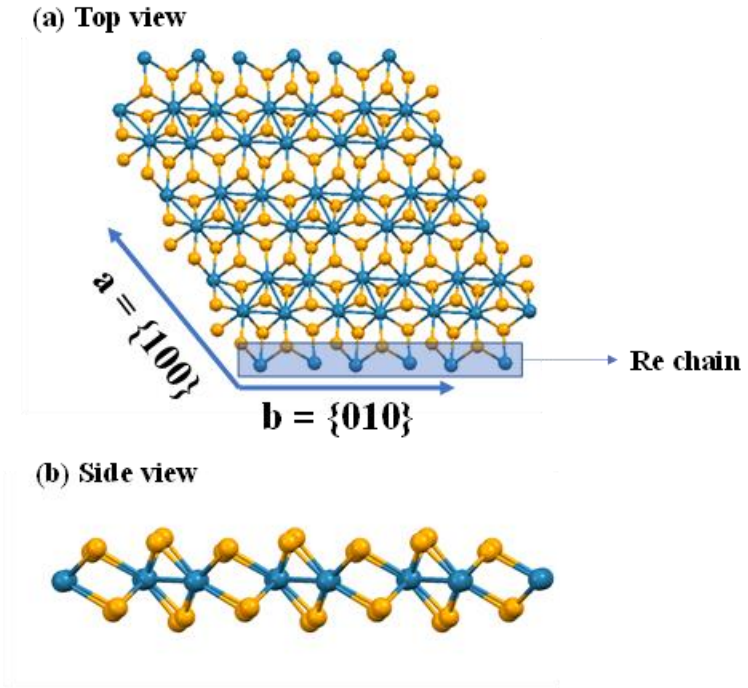


Figure 2: Crystal structure of $ReSe_2$ (a) Top view with Re chains, (b) side view.

Due to these interesting properties, there has been increasing interest in $ReSe_2$ nanostructures for various applications. Interest in using these materials as electrocatalysts in the HER has grown steadily and reports on its impressive catalytic activity have begun to crop up.[35-37] Colloidal synthesis could certainly be used to investigate any interesting TMD nanostructures and to improve the catalytic activity of these nanostructures. Another group of TMD nanostructures that have gone largely unexplored is the group IVA TMD nanostructures. $SnSe_2$ is notable among the group IVA TMDs, it has been shown to be an excellent material in applications like batteries and photo-catalysis.[38-39] There has been relatively no exploration of $SnSe_2$ nanostructures in HER applications. However, there have been various computational studies that have explored the possible catalytic activity of $SnSe_2$ nanostructures towards the HER. These studies have alluded that the $SnSe_2$ nanostructures could have poor catalytic activity towards HER on both the basal plane and the edge sites.[40] The edge sites have better

catalytic activity compared to the basal plane. The computational studies have also shown that the catalytic activity of the materials can be improved through the introduction of defects and alkali metal doping. In this thesis, the gap of knowledge between the computational studies and the experimental data was addressed.

4. Aims and objectives

The aim of this work was primarily to demonstrate how colloidal synthesis can be used to synthesize TMD nanostructures with high catalytic activity towards the HER. This work was also aimed at showing that colloidal synthetic techniques could be adapted to incorporate all the strategies used to increase the catalytic activities of TMDs such as introducing defects, chemical doping, increasing exposure of the active edge sites, and forming hybrid nanostructures with carbon nanostructures.

As such the following objectives were identified:

- Synthesize $MoSe_2$, $ReSe_2$, and $SnSe_2$ nanostructures using colloidal synthesis.
- Demonstrate how colloidal synthesis can be used to alter the morphology of TMDs to increase the exposure of active edge sites.
- Investigate how precursor selection affects the structure and properties of TMD nanostructures.
- Evaluate the effect of surface functionalization on the catalytic activity of colloidally synthesized TMDs.
- Produce transition metal dichalcogenide and reduced graphene oxide nanocomposites that have superior catalytic activity.
- To demonstrate how these synthetic methods can be used to dope $SnSe_2$ with K^+ in order to increase its catalytic activity towards the HER.

5. References

1. Buis, A., A Degree of Concern: Why Global Temperatures Matter. *NASA's Glob Clim Chang Website* 2019, *19*.

2. Bongaarts, J., Intergovernmental panel on climate change special report on global warming of 1.5° C Switzerland: IPCC, 2018. Wiley Online Library: 2019.

3. Dou, Y.; Sun, L.; Ren, J.; Dong, L., Opportunities and future challenges in hydrogen economy for sustainable development. In *Hydrogen Economy*, Elsevier: 2017; pp 277-305.

4. Morgan, T., The hydrogen economy: A non-technical review. 2006.

5. Parsons, R., The rate of electrolytic hydrogen evolution and the heat of adsorption of hydrogen. *J. Chem. Soc. Faraday Trans.* 1958, *54*, 1053-1063.

6. Neyerlin, K.; Gu, W.; Jorne, J.; Gasteiger, H. A., Study of the exchange current density for the hydrogen oxidation and evolution reactions. *J. Electrochem. Soc.* 2007, *154* (7), B631-B635.

7. Xia, J.; Yan, J.; Shen, Z. X., Transition metal dichalcogenides: structural, optical and electronic property tuning via thickness and stacking. *FlatChem* **2017,** *4*, 1-19.

8. Zhao, Y.; Zhang, Z.; Ouyang, G., Band shift of 2D transition-metal dichalcogenide alloys: size and composition effects. *Appl. Phys. A* **2018,** *124* (4), 1-9.

9. Masurkar, N.; Thangavel, N. K.; Arava, L. M. R., CVD-grown $MoSe_2$ nanoflowers with dual active sites for efficient electrochemical hydrogen evolution reaction. *ACS appl. Mater. Interfaces* **2018,** *10* (33), 27771-27779.

10. Liu, X.; Liu, L.; Wu, Y.; Wang, Y.; Yang, J.; Wang, Z., Rosette-like MoS_2 nanoflowers as highly active and stable electrodes for hydrogen evolution reactions and supercapacitors. *RSC Adv.* **2019,** *9* (24), 13820-13828.

11. Qu, Y.; Shao, M.; Shao, Y.; Yang, M.; Xu, J.; Kwok, C. T.; Shi, X.; Lu, Z.; Pan, H., Ultra-high electrocatalytic activity of VS_2 nanoflowers for efficient hydrogen evolution reaction. *J. Mater. Chem. A.* **2017,** *5* (29), 15080-15086.

12. Prabhu, P.; Jose, V.; Lee, J.-M., Design strategies for development of TMD-based heterostructures in electrochemical energy systems. *Matter* **2020,** *2* (3), 526-553.

13. Zhou, Q.; Zhao, G.; Rui, K.; Chen, Y.; Xu, X.; Dou, S. X.; Sun, W., Engineering additional edge sites on molybdenum dichalcogenides toward accelerated alkaline hydrogen evolution kinetics. *Nanoscale* **2019,** *11* (2), 717-724.

14. Tsai, C.; Abild-Pedersen, F.; Nørskov, J. K., Tuning the MoS_2 edge-site activity for hydrogen evolution via support interactions. *Nano lett.* **2014,** *14* (3), 1381-1387.

15. Wan, Y.; Zhang, Z.; Xu, X.; Zhang, Z.; Li, P.; Fang, X.; Zhang, K.; Yuan, K.; Liu, K.; Ran, G., Engineering active edge sites of fractal-shaped single-layer MoS_2 catalysts for high-efficiency hydrogen evolution. *Nano Energy* **2018,** *51*, 786-792.

16. Yang, Y.-Q.; Zhao, C.-X.; Bai, S.-Y.; Wang, C.-P.; Niu, C.-Y., Activating MoS_2 basal planes for hydrogen evolution through the As doping and strain. *Phys. Lett. A* **2019,** *383* (24), 2997-3000.

17. Kwon, H.; Bae, D.; Jun, H.; Ji, B.; Won, D.; Lee, J.-H.; Son, Y.-W.; Yang, H.; Cho, S., Basal-plane catalytic activity of layered metallic transition metal ditellurides for the hydrogen evolution reaction. *Appl. Sci.* **2020,** *10* (9), 3087.

18. Chhowalla, M.; Voiry, D.; Yang, J.; Shin, H. S.; Loh, K. P., Phase-engineered transition-metal dichalcogenides for energy and electronics. *MRS Bull.* **2015,** *40* (7), 585-591.
19. Yang, S. Z.; Gong, Y.; Manchanda, P.; Zhang, Y. Y.; Ye, G.; Chen, S.; Song, L.; Pantelides, S. T.; Ajayan, P. M.; Chisholm, M. F., Rhenium-doped and stabilized MoS_2 atomic layers with basal-plane catalytic activity. *Adv. Mater.* **2018,** *30* (51), 1803477.
20. Kamila, S.; Mohanty, B.; Samantara, A. K.; Guha, P.; Ghosh, A.; Jena, B.; Satyam, P. V.; Mishra, B.; Jena, B. K., Highly active 2D layered MoS_2-rGO hybrids for energy conversion and storage applications. *Sci. Rep.* **2017,** *7* (1), 1-13.
21. Huang, Y.; Pan, Y.-H.; Yang, R.; Bao, L.-H.; Meng, L.; Luo, H.-L.; Cai, Y.-Q.; Liu, G.-D.; Zhao, W.-J.; Zhou, Z., Universal mechanical exfoliation of large-area 2D crystals. *Nat. commun.* **2020,** *11* (1), 1-9.
22. Song, X.; Guo, Z.; Zhang, Q.; Zhou, P.; Bao, W.; Zhang, D. W., Progress of Large-Scale Synthesis and Electronic Device Application of Two-Dimensional Transition Metal Dichalcogenides. *Small* **2017,** *13* (35), 1700098.
23. Bubnova, O., 2D materials grow large. *Nat. nanotechnol.* **2021,** *16* (11), 1179-1179.
24. Nguyen, D.-T.; Ting, H.-A.; Su, Y.-H.; Hofmann, M.; Hsieh, Y.-P., Additive-Enhanced Exfoliation for High-Yield 2D Materials Production. *Nanomaterials* **2021,** *11* (3), 601.
25. Lee, D. H.; Sim, Y.; Wang, J.; Kwon, S.-Y., Metal–organic chemical vapor deposition of 2D van der Waals materials—The challenges and the extensive future opportunities. *Appl. Mater.* **2020,** *8* (3), 030901.
26. Yang, J.; Voiry, D.; Ahn, S. J.; Kang, D.; Kim, A. Y.; Chhowalla, M.; Shin, H. S., Two-dimensional hybrid nanosheets of tungsten disulfide and reduced graphene oxide as catalysts for enhanced hydrogen evolution. *Angew. Chem.* **2013,** *125* (51), 13996-1399.
27. Li, W.; Wei, X.; Dong, H.; Ou, Y.; Xiao, S.; Yang, Y.; Xiao, P.; Zhang, Y., Colloidal Synthesis of NbS_2 Nanosheets: From Large-Area Ultrathin Nanosheets to Hierarchical Structures. *Front. Chem.* **2020,** *8*, 189.
28. Meerbach, C.; Klemmed, B.; Spittel, D.; Bauer, C.; Park, Y. J.; Hübner, R.; Jeong, H. Y.; Erb, D.; Shin, H. S.; Lesnyak, V., General colloidal synthesis of transition-metal disulfide nanomaterials as electrocatalysts for hydrogen evolution reaction. *ACS Appl. Mater. Interfaces* **2020,** *12* (11), 13148-13155.
29. Yarema, O.; Perevedentsev, A.; Ovuka, V.; Baade, P.; Volk, S.; Wood, V.; Yarema, M., Colloidal phase-change materials: synthesis of monodisperse GeTe nanoparticles and quantification of their size-dependent crystallization. *Chem. Mater.* **2018,** *30* (17), 6134-6143.

30. Machogo, L. F.; Sithole, R. K.; Phao, N.; Kolokoto, T.; Gqoba, S. S.; Mlambo, M.; Moloto, M. J.; Shumbula, P. M.; Mdluli, P. S.; Moloto, N., Probing the structure and functionalized surface of colloidal AuSe. *Mater. Sci. Eng. B.* **2021,** *263*, 114878.

31. Ndala, Z.; Shumbula, N.; Nkabinde, S.; Kolokoto, T.; Nchoe, O.; Shumbula, P.; Tetana, Z. N.; Linganiso, E. C.; Gqoba, S. S.; Moloto, N., Evaluating the Effect of Varying the Metal Precursor in the Colloidal Synthesis of $MoSe_2$ Nanomaterials and Their Application as Electrodes in the Hydrogen Evolution Reaction. *Nanomaterials* **2020,** *10* (9), 1786

32. Simone Liedtke , "*Hydrogen demand to rise to 140m tonnes in 2030*", mining weakly, accessed (05-02-2022), https://www.miningweekly.com/article/hydrogen-demand-to-rise-to-140m-tonnes-in-2030-2021-11-17/rep_id:3650.

33. Jason Deign, 2019, "*10 Countries Moving Toward a Green Hydrogen Economy"*, gtm, accessed (12-14-2021), https://www.greentechmedia.com/articles/read/10-countries-moving-towards-a-green-hydrogen-economy.

34. Martin Creamer, "*South Africa playing key role in hydrogen economy – Minister",* engineering weekly, accessed (12-14-2021) *https://www.engineeringnews.co.za/article/south-africa-playing-key-role-in-hydrogen-economy-minister-2021-03-24*.

35. Jiang, S.; Zhang, Z.; Zhang, N.; Huan, Y.; Gong, Y.; Sun, M.; Shi, J.; Xie, C.; Yang, P.; Fang, Q., Application of chemical vapor–deposited monolayer $ReSe_2$ in the electrocatalytic hydrogen evolution reaction. *Nano Res.* **2018,** *11* (4), 1787-1797.

36. Kwon, I. S.; Kwak, I. H.; Ju, S.; Kang, S.; Han, S.; Park, Y. C.; Park, J.; Park, J., Adatom Doping of Transition Metals in $ReSe_2$ Nanosheets for Enhanced Electrocatalytic Hydrogen Evolution Reaction. *ACS nano* **2020,** *14* (9), 12184-12194.

37. Luxa, J.; Marvan, P.; Lazar, P.; Sofer, Z., Chalcogenide vacancies drive the electrocatalytic performance of rhenium dichalcogenides. *Nanoscale* **2019,** *11* (31), 14684-14690.

38. Cheng, Y.; Huang, J.; Cao, L.; Xie, H.; Wang, Y.; Wang, Y.; Wu, H.; Xi, S.; Li, J., Structure-controlled $SnSe_2$ nanosheets as high performance anode material for lithium ion batteries. *Ionics* **2020,** *26* (6), 2855-2862.

39. Li, J.; Zhao, H.; Lei, Y.; Yang, Q.; Zheng, Z., Synthesis and Photocatalytic Properties of $SnSe_2$/Se Heterojunction Films. *Nano* **2018,** *13* (04), 1850045.

40. Inamdar, A. N.; Som, N. N.; Pratap, A.; Jha, P. K., Hydrogen evolution and oxygen evolution reactions of pristine and alkali metal doped $SnSe_2$ monolayer. *Int. J. Hydrog. Energy.* **2020,** *45* (37), 18657-18665.

Chapter 2: Literature review

1. Transition metal dichalcogenides

Transition metal dichalcogenides are layered materials much like graphite. They have the general formula MX_2 where M is a transition metal (M = Mo, W, Nb, Ti, Ta, Re) and X is a chalcogen (X= S, Se, Te). TMDs include layered materials such as MoS_2, WSe_2, and $NbSe_2$. Bulk TMDs have very diverse properties; MoS_2 and WS_2 exhibit semiconductor properties, HfS_2 behaves like an insulator and VSe_2 is a semi-metal. $NbSe_2$ and TaS_2 can even exhibit low-temperature phenomena such as superconductivity.[1-3] Much like graphite, these materials can be exfoliated to obtain 2D atomic crystals of the materials. These 2D atomic crystals exhibit interesting properties due to confinement effects. Bulk MoS_2 for example has an indirect band-gap but the 2D atomic crystal has a direct band-gap of ~ 1.8 eV and has a calculated carrier mobility of ~ 410 $cm^2V^{-1}s^{-1}$.[4-5] This has led to an increase in research of TMD 2D atomic crystals.

1.1 Crystal structure of TMDs

The material is composed of atomically thin layers that comprise a layer of transition metal atoms arranged in a graphite-like hexagonal structure that is sandwiched between two layers of chalcogen atoms.[6] The transition metal is bonded to the chalcogen in a trigonal prismatic co-ordination. The intra-layer M-X bonds are covalent bonds while the layers themselves are held together by weak van der Waals forces, the distance between the layers is 6.5 Å. A representation of the structure of a TMD such as MoS_2 is shown in **Fig.1**.[6]

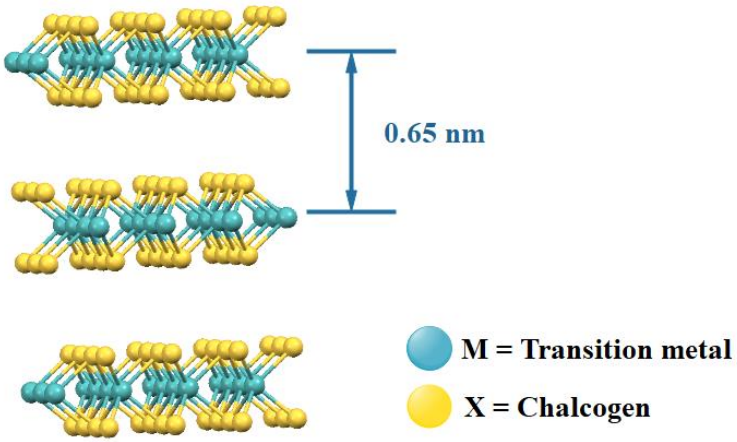


Figure 1: Diagram depicting the structure of bulk TMDs.[8]

The individual layers are comprised of three layers, a metal layer that is sandwiched between the two chalcogen layers. The transition metal adopts a +4 oxidation state and the chalcogen has an oxidation state of -2. The transition metal is covalently bonded to six chalcogen atoms and the chalcogen is bonded to three metal atoms. The length of the M-M bonds ranges between 3.15 Å and 4.03 Å depending on the size of the chalcogen and the metal itself.[7] The co-ordination of the metal in the TMD can either be octahedral or trigonal prismatic as shown in **Fig.2**. The TMD has three different polytypes which is a specific type of polymorphism. The three polytypes are 1T, 2H, and 3R where T= tetragonal, H = Hexagonal, and R = Rhombohedral. The numbers indicate the number of layers in the stacking sequence.[7] The most common phases are the 2H and 1T phases, which are shown in **Fig.2**. The 2H phase TMDs are normally semiconducting while 1T phase TMDs have metallic character.

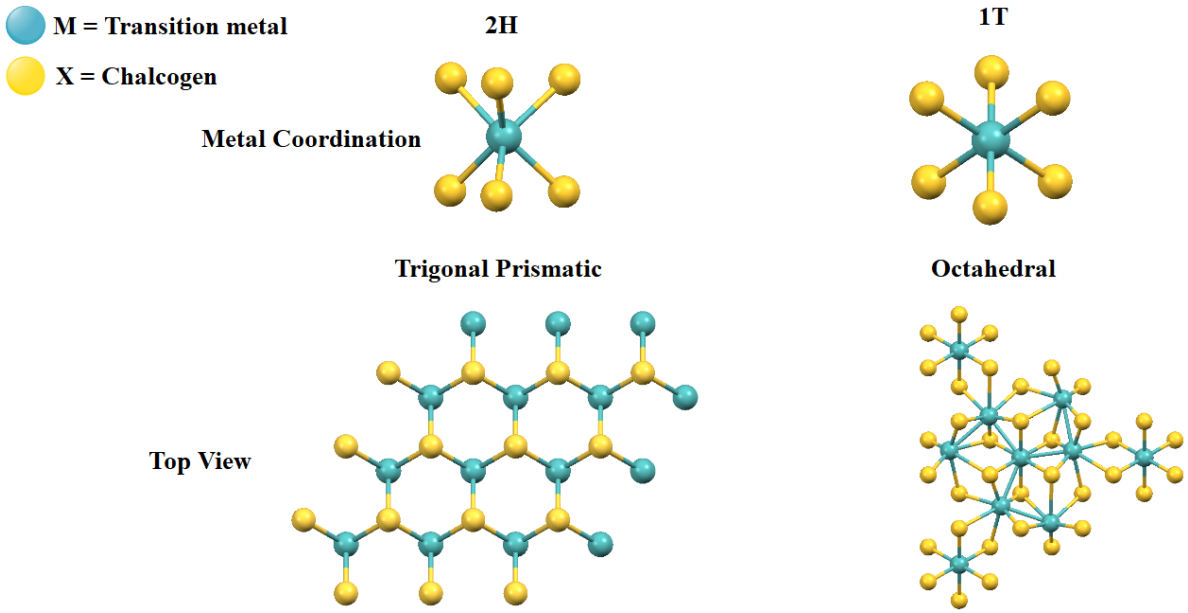


Figure 2: Metal coordination of 2H and 1T TMDs.

1.2 Electronic properties of the 2D atomic crystals of TMDs and possible applications

The transition from bulk TMDs to monolayer sheets gives rise to interesting changes in the electronic properties of the materials. These changes in the electronic properties could be due to changes in the degree of quantum confinement in the nanosheets, interlayer coupling, and symmetry elements.[8] In TMDs such as MoS_2 it is observed that the material switches from having an indirect band-gap in the bulk structure to having a direct band-gap in 2D atomic crystals. This phenomenon is also observed in WX_2 TMDs as well. The change to a direct band-gap has major implications with regard to the application of these materials in

optoelectronics, sensors, and photonics.[8] TMDs are being considered by researchers to be good candidate materials for use in FET, the materials are ideal because they have sub-nanometer thickness, they have a band-gap in the 1-2 eV range which is crucial to achieving high on/off ratios. The thickness of the material can reduce short-channel effects and power dissipation which are important parameters in transistor miniaturization.[10] Transistor miniaturization is an important factor for the use of semiconductor materials in digital devices. Another important aspect in 2D nanomaterials is the carrier mobility.

2. Synthesis techniques for TMDs

TMDs were initially synthesized using mechanical exfoliation after successful synthesis of graphene using the same method. The method involves physically removing a single layer of material from the bulk crystal using scotch tape. The method was used to produce high-quality monolayer and few-layer TMDs. Unfortunately, the method can only be used for lab-scale purposes. The mechanical exfoliation has been classified as a top-down method of synthesis which are methods that break down the bulk TMD materials into mono or few-layer TMDs. Bottom-up methods are the opposite of top-down methods in that the nanostructures are built up atom by atom in order to form the monolayer or few-layer nanostructures. The large-scale industrial synthesis of these materials is crucial for the commercial application of these materials. Finding "top-down" and "bottom-up" methods that can be used to produce TMDs at large-scale remains one of the largest challenges in this area. This is not surprising considering this challenge has also been a bottleneck problem that has affected the commercial application of graphene. In this section of the literature review, the traditional methods that have been utilized to synthesize these materials and any advancements in adapting these methods for large-scale synthesis were explored. More importantly, an introduction into the use of colloidal synthesis of these materials was delved into and the amazing benefits of this method have been explored.

2.1 Top-down methods

2.1.1 Mechanical exfoliation

Mechanical exfoliation was the first method used for the synthesis of graphene which was the first reported stable monolayer 2D crystal. Novoselov and Geim were able to isolate a monolayer of graphene by using scotch tape to strip the layer from bulk graphite.[11] A schematic representation of the scotch-tape method is shown in **Fig.3.**

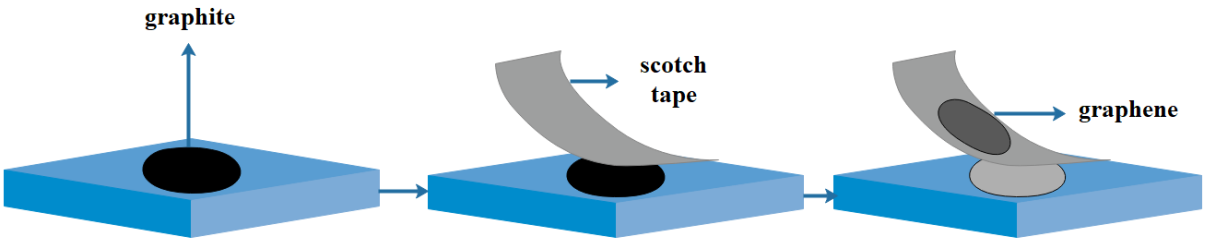


Figure 3: Mechanical exfoliation of graphite to produce graphene.

This method was extremely effective in producing lab-scale monolayer 2D crystals for research purposes. Unfortunately, this method was not suited for large-scale production of 2D materials.

2.1.2 Liquid exfoliation

Another "top-down" method useful for synthesizing TMDs is liquid exfoliation. Liquid exfoliation uses foreign species such as ions, inorganic molecules, organic molecules, and metal atoms to induce expansion that weakens the weak van der Waals force between two adjacent layers.[12-13] This process allows for the exfoliation of bulk layered materials to few-layered and monolayer TMDs. Liquid exfoliation can be conducted in two processes which are intercalation and chemical exfoliation as shown in **Fig.4**.

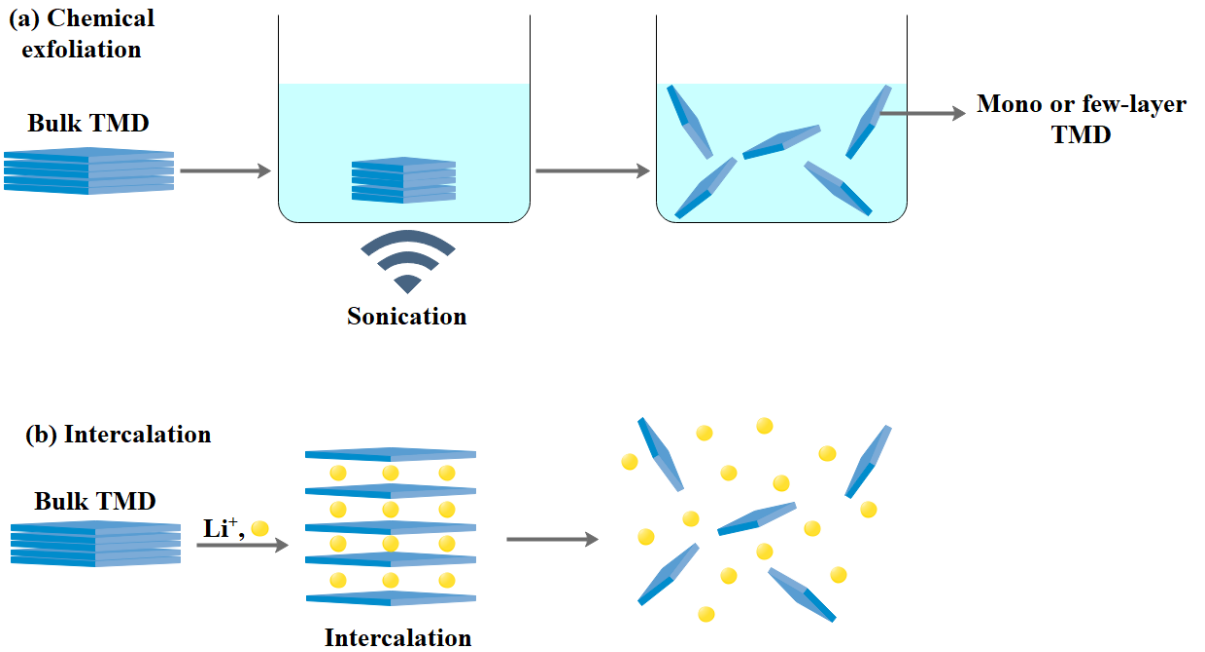


Figure 4: Liquid exfoliation methods. (a) chemical exfoliation and (b) Intercalation.

Intercalation involves introducing charged ions into the space between the layers of a layered bulk crystal in order to cause expansion of the interlayer spacing. This results in the decoupling

of the layers while maintaining the individual sheets.[13] Chemical exfoliation involves the use of high-intensity ultrasound waves (sonication) with a suitable solvent to decouple the TMD layers. Liquid exfoliation has been a popular method for the possible synthesis of TMDs at a large-scale, the method has various advantages such as allowing for various species doping, tuneable properties, controlled process, simple operation, and high yield.[14-17] Chemical exfoliation and intercalation still have major challenges that impair their ability to produce TMDs at large scale applications. The challenges of using liquid exfoliation include the inability to control the lateral sizes of the nanosheets produced and the difficulty of obtaining a high yield of monolayer nanosheets.[12,13,18,19] The challenges of using intercalation methods include the production of side products such as Li_2S if the process is not strictly controlled and the time required for complete exfoliation can at times be excessively long.[12,13,20] There have been significant developments in such areas to circumvent the challenges associated with liquid exfoliation. Coleman *et al.* have designed innovative ways to potentially produce TMD nanomaterials at a large-scale.[21] The group has used a shear-exfoliation method for the large-scale production of MoS_2 nanosheets. The process was conducted using an aqueous surfactant solution and a kitchen blender as shown in **Fig.5**.



Figure 5: Using shear force from a blender to exfoliate bulk TMD crystals.[21]

They evaluated the dependence of the dimensions of the nanosheets on the processing parameters. They found that the nanosheets concentration and dimensions were dependant on the mixing parameters which were the MoS_2 concentration, the mixing time, the liquid volume, and the rotor speed. Through the optimization of these parameters, the group was able to obtain production rates as high as 1.3 mg/min. The nanosheet concentration was found to be heavily dependent on the surfactant concentration and so was the nanosheet lateral size and thickness. For example, higher surfactant concentration resulted in smaller flake sizes while lower surfactant concentration resulted in larger flakes. The dimensions of the nanosheets could be

controlled during the shear exfoliation to lateral sizes between 40-220 nm and layer thickness between 2-12 layers.[21] The relatively high production rate and reliable control of the physical properties of the nanomaterials make this production method a good candidate for large-scale production of TMDs. They have also shown that this method can be applied to other 2D materials like boron nitride and WS_2. There have also been hybrid exfoliation methods that have shown promise in the large-scale synthesis of TMDs. Wong *et al.* developed a method to produce TMDs at a large-scale using low energy ball milling and sonication.[22] The ball milling is able to cleave the layers of the TMDs into 2D nanosheets from the top/bottom and edges of the TMD surfaces using shearing force and compression force. The subsequent exfoliation through sonication further breaks down the larger crystallites into smaller crystallites. The 2D nanosheets could be dispersed in aqueous solutions in high concentrations, 1.2 mg/L for boron nitride (BN), 0.8 mg/L for MoS_2, and 0.9 mg/L for graphene. The nanosheets were stabilized with a sodium dodecyl sulphate (SDS) – water solution, the solution allowed for the fabrication of 2D material papers by vacuum filtration. This method shows great potential for fabricating 2D materials-based devices.

2.2 Bottom-up methods

2.2.1 Chemical vapor deposition (CVD)

There have been various "bottom-up methods that can have been explored for the large-scale synthesis of TMDs, one of which is chemical vapor deposition (CVD). CVD has been identified as the most likely synthesis method for realizing high-quality large-area 2D TMDs at a low cost. There are various CVD methods that have recently been developed for large-scale synthesis of TMDs including atmospheric pressure CVD (APCVD), low-pressure CVD (LPCVD), plasma-assisted CVD (PECVD), and the most common and widely used metalorganic CVD (MOCVD).[23-26] In MOCVD, the metal and chalcogen precursors are vaporized and transported into a reaction chamber using a carrier gas.[27] The TMD film is grown from the bottom-up on a substrate as the metal precursor reacts with the chalcogen precursor as shown in **Fig.6**.

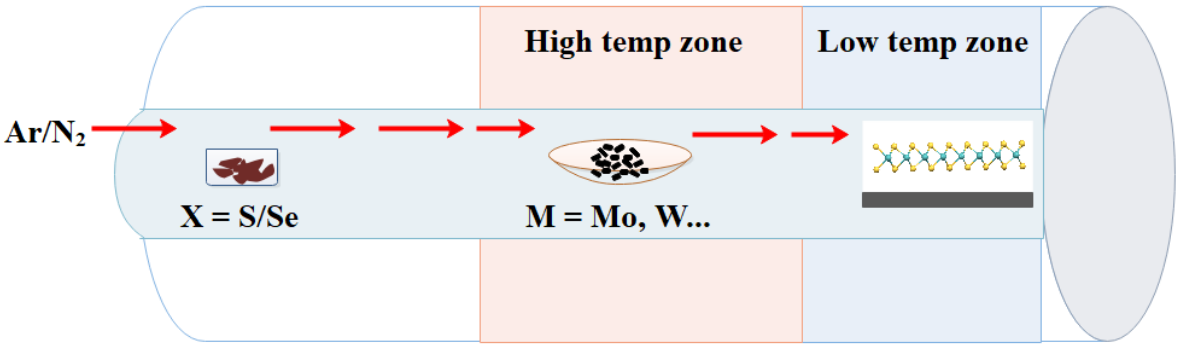


Figure 6: MOCVD synthesis of TMDs.

The choice of precursor is one of the most crucial aspects of the MOCVD approach. The precursors are normally chosen due to their stability at room temperature and have adequate vapour pressure at the desired temperature. The precursors have to also decompose in such a way that eliminates any chance of side products. Since the precursors can be highly volatile and flammable, special safety precautions need to be taken when conducting the experiments.[27] However, MOCVD has various advantages that can be exploited compared to CVD. (i) Controlling the gas flow-rate, allows for the control of the thickness and composition of the thin TMD layer, (ii) The ability to quickly change the gas composition is beneficial for the growth of heterojunctions and multiple structures, (iii) Since the precursors are easy to vaporize and exist as gases in the reaction chamber they can mix more uniformly and the formed film can thus also be more uniform.[27,28,29] There are several other parameters to consider in MOCVD but the most crucial are normally noted as temperature, precursor flow, synthesis atmosphere, etc. MOCVD has been widely utilized for the synthesis of wafer-thin TMDs for some time. For example, Kang *et al.* were able to synthesize wafer-thin films of MoS_2 and WS_2 using MOCVD.[30] Kang *et al.* used molybdenum hexacarbonyl and tungsten hexacarbonyl as the metal precursors and dimethyl sulfide was used as the sulphur precursor. The group used a long-time growth method which took ~ 26 hrs to produce a continuous wafer-thin film. Many of the major challenges with MOCVD are also being addressed such as carbon contamination when using precursors such as dimethyl sulfide. Lin et al. have shown the H_2Se can be used as an alternative when producing WSe_2. The use of H_2Se is preferable to the use of diethyl selenium to prevent the formation of amorphous carbon. Furthermore, to address the issue of long growth times Esarawan *et al.* used a liquid precursor for molybdenum which was bis(tertbulymido) molybdenum and H_2S gas to form a 2-inch MoS_2 thin film within 4 mins.[31]

2.2.2 Wet-chemical methods for synthesis of TMDs

Wet chemical methods have gained significant popularity for potential use as large-scale synthesis methods to produce TMDs. They have gained such popularity because of the possibility of modifying the properties of these materials during the growth process. Solution-based methods also offer an advantage in that the materials can be easily processed once synthesized without having to pry them from a substrate. Considering that most production methods such as roll-to-roll methods are solution-based methods, the need for the large-scale production methods of TMDs in solution is justified.[32-35] Liquid-phase exfoliation as already mentioned has been demonstrated as a possible solution-based technique for the large-scale production of TMDs. Another possible method is hydrothermal synthesis.[36-39] Hydrothermal synthesis refers to the synthesis of nanostructured materials in sealed vessels at high temperatures and pressure conducted in water. Fan *et al.* were among the first to successfully synthesize nanocrystalline MoS_2 and $MoSe_2$ using the hydrothermal method. They were able to synthesize nanocrystalline amorphous MoS_2 and $MoSe_2$ that were 4 nm and 7 nm respectively, the synthesis was conducted using Na_2MoO_4 as the Mo precursor and $Na_2S_2O_3$/Na_2SeSO_3 as the sulfur/selenium sources.[40] The amorphous nanocrystals were annealed at 350 °C for 9 hrs, this resulted in the formation of MoS_2 and $MoSe_2$ in the 2H phase. Duraisamy *et al.* have developed a one-step hydrothermal method for the synthesis of a 3D network of self-assembled metallic MoS_2/MoO_3 nanosheets as shown in **Fig.7**.[41]

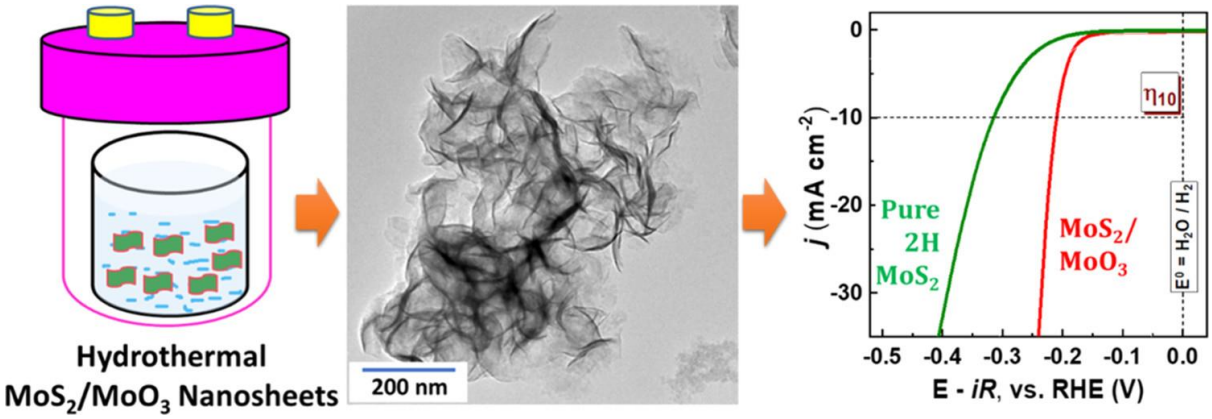


Figure 7: Hydrothermal synthesis of MoS_2/MoO_3 nanosheets for HER applications.[41]

The synthesis was conducted using α-MoO_3 as the metal precursor and thiourea as the sulfur source. Modulation of the α-MoO_3/thiourea ratio and reaction temperature allowed for the synthesis of a 3D network consisting of 1T/2H-MoS_2 and 1T-MoS_2/MoO_3 nanoscale heterostructures. These nanostructures were shown to be excellent electrocatalysts for the hydrogen evolution reaction.

3. Colloidal synthesis as an effective method producing TMDs

Colloidal synthesis techniques entail the formation of colloids which are crystals or crystalline nanoclusters that are made up of a few hundred or a few thousand atoms. The atoms agglomerate to form the colloids which are dispersed in some solvent.[42-43] Chemical techniques such as chemical reduction, thermal decomposition, and sol-gel are used to produce the atoms needed for the formation of the colloids from various precursors.[43] Thermal decomposition is a popular approach that is used for the synthesis of semiconductor nanocrystals, this approach utilizes organometallic precursors that are thermally decomposed in an organic solvent at elevated temperatures. Chestoney *et al.* were among the first to use this method to synthesize crystalline group II-VI semiconductor nanocrystals in 1986.[44] However, the nanocrystals synthesized were not monodispersed. Bawendi *et al.* were able to adapt the method to form monodispersed semiconductor nanocrystals by using a method he termed the "hot-injection" method.[45] The hot injection method is the rapid injection of organometallic precursors into a hot solvent, this results in the formation of homogeneous nuclei that in turn result in the formation of monodispersed nanocrystals. This method was adapted specifically for the synthesis of quantum dots (QDs), which are semiconductor nanocrystals with sizes of a few nanometres (<10nm). These nanocrystals have interesting and exotic properties compared to their bulk counterparts, this difference in optical and electronic properties is brought about by quantum confinement effects in the small nanocrystals. The "hot injection" approach was developed to form QDs with monodispersed nanocrystals and to have control over the sizes of the nanocrystals. The mechanism by which this is accomplished can be understood using the theoretical principles of nucleation and growth nanocrystals developed by LaMer and Dinger in the 1950s.[46-47] They suggest homogeneous nucleation where there is a burst of nucleation after supersaturation that leads to the formation of many nuclei of the same size.[46-47] The subsequent growth of the nuclei occurs without the formation of new nuclei. The process can be described in three stages as depicted in **Fig.8**: (i) The increase of monomer concentration in solution due to the decomposition of precursor, the concentration of monomer increases until the solution reaches critical supersaturation of monomer concentration (C_s); (ii) The saturation will increase until it reaches a level C_{min}, at this point the energy barrier for nucleation is overcome which leads to rapid nucleation (burst nucleation); (iii) Burst nucleation leads to a drastic drop in monomer concentration which results in a drop in the supersaturation level, the nucleation process then stops.

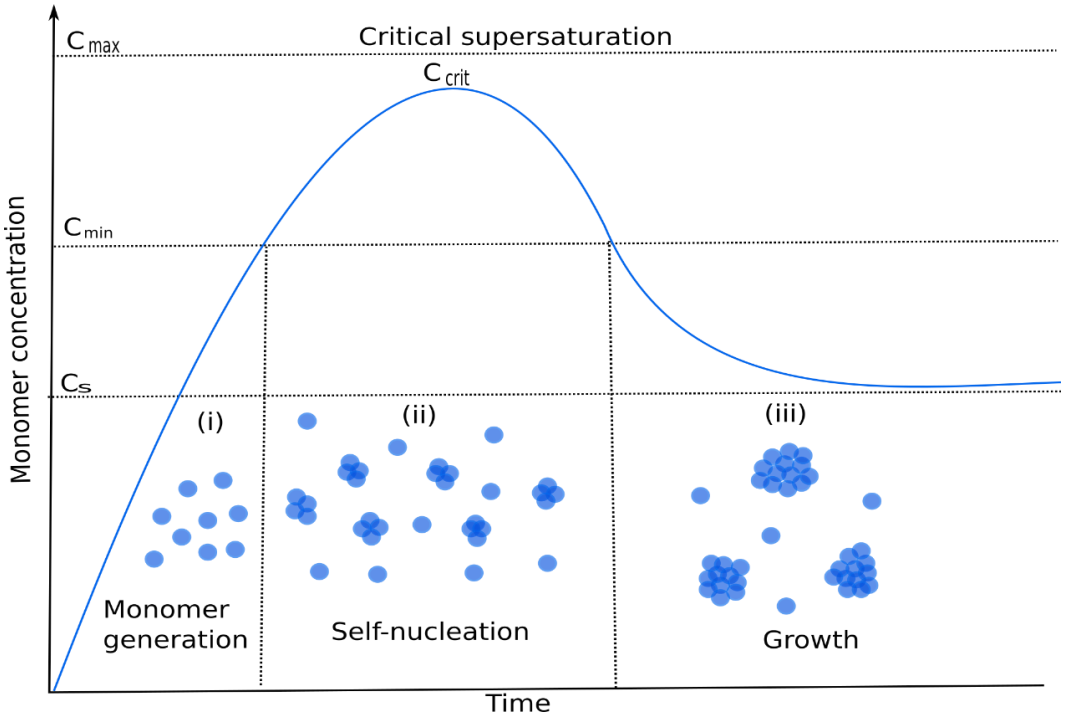


Figure 8: A graphical representation of the LaMer and Dinegar nucleation.

The nuclei then begin to grow due to the diffusion of the monomer to the nucleation site. In the context of the "hot injection" method, the rapid or "burst" nucleation occurs when the organometallic precursor is injected into the hot organic solvent. Once nucleation occurs, a diffusion-controlled process occurs that regulates the size of the nanoparticles. This process ensures that larger nuclei grow slower than larger nuclei, which induces a size focusing effect that results in monodispersed nanostructures. When the nuclei begin to grow and Ostwald ripening occurs, the smaller nuclei are dissolved into solution because they are less stable than the larger nuclei.[48] After dissolution, the smaller nuclei attach to the larger nuclei which leads to an increase in the size of the nanoparticles. This phenomenon works in tandem with the nucleation process to ensure the narrow size distribution of semiconductor nanocrystals. A schematic representation of the synthesis of QDs is shown in **Fig.9.**

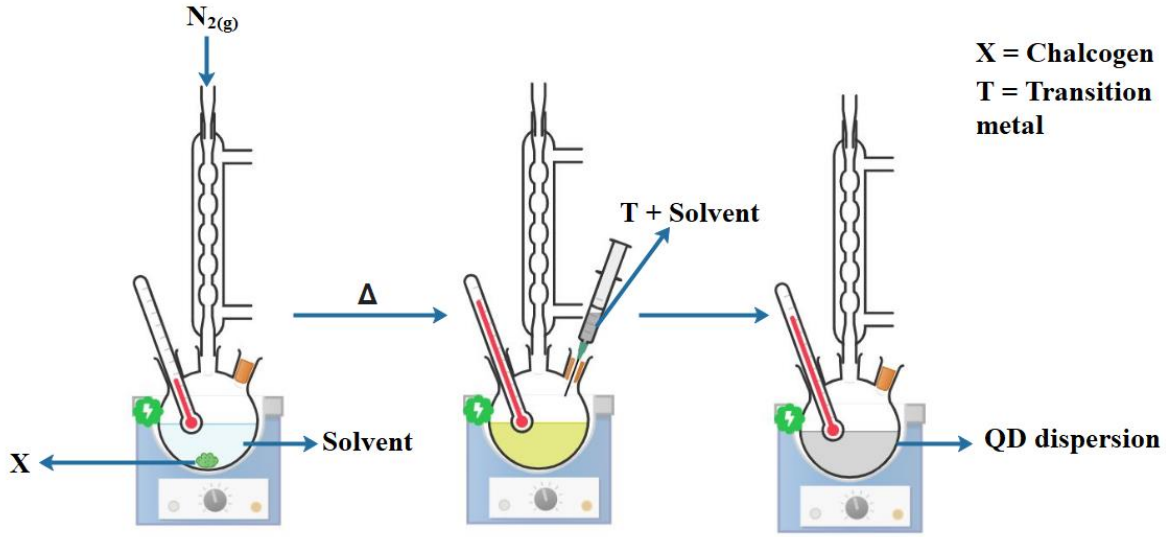


Figure 9: Schematic representation of the colloidal synthesis of QDs.

In a typical synthetic procedure, the chalcogen (X=S, Se, Te) is dissolved in a suitable solvent and put into a three-neck round bottom flask. The flask is degassed with $N_{2(g)}$ using a Schlenk line, after which the temperature of the reaction mixture is increased. The solvent can also act as a reducing agent which can reduce the chalcogen into its reactive monomer (X^{2-}). The metal precursor is then dissolved in the same solvent, and the solution is injected into the reaction mixture at the required temperature. The semiconductor nanostructures are formed and then subsequently washed by centrifugation in a suitable solvent. This method has become extremely popular not just due to the ability to have precise control over the size of the synthesized nanostructures, but it can be used to control other properties such as phase and morphology.[49-52] This precise control over the structural properties of nanostructures has been achieved through the modulation of the experimental conditions such as the temperature, precursor selection, solvent/surfactant, and mole ratio of precursors.[53-55] A quick look at the influence of some of the different parameters is discussed as follows.

Influence of precursor selection on the nucleation and growth of semiconductor nanostructures: The selection of suitable precursors for colloidal synthesis is one of the most important parameters to consider when designing a synthetic method. The colloidal synthesis relies on the formation of free monomer for nucleation and growth of nanostructures to occur. How quickly that monomer is made available and how quickly that monomer will react to begin the nucleation process influences the size and shape of the nanostructures synthesized.[56-57] The precursor must undergo a chemical process that will allow for the release of free monomer into

the reaction solution. Thermal decomposition is used to break down precursors to release the required monomer. The precursor is normally a metal salt or a metal complex. The monomer required in this case is the metal itself. The rate of decomposition of the metal precursor and the reactivity of the monomer are determined by the accompanying ligands on the metal precursor.

Influence of temperature on nucleation and growth the semiconductor nanostructures: Temperature plays a vital role in the decomposition of the metal precursor. The rate at which the metal precursor is decomposed determines the rate at which the reactive metal monomer is made available for nucleation and growth.[58-59] the temperature can affect the kinetics of the nanocrystal growth and it also acts on the formation of the ligand assemblies which are another important shape control parameter.

Influence of solvent selection on the nucleation and growth of the semiconductor nanostructures: In colloidal synthesis, the reactions are normally conducted in organic solvents which can also act as capping agents that bind to the surface of the nanoparticles to stabilize the nanoparticles, to prevent the nanoparticles from aggregating to form larger clusters and to protect the surface from oxidation.[60-62] The solvents/capping agents can also be used to control the size and shape of the nanoparticles synthesized. A crucial aspect of the colloidal synthetic methods is the potential for scale-up. It has been shown that these methods can be scaled-up for the synthesis of semiconductor nanostructures at a large-scale. Commercial companies such as *Nanosys* and *Nanoco* which were founded by Pioneers in the synthesis of QD nanostructures or their students have used various modified versions of the colloidal synthesis methods to produce nanostructures at a large-scale. Considering that TMDs have a similar chemical configuration to QDs, namely the combination of a chalcogen and a transition metal. Many researchers have begun to utilize colloidal synthetic methods to synthesize various TMDs. In fact, even *Nanoco* has recently released various patents on the synthesis of TMDs using such methods which suggests a notable commercial interest in producing TMDs in this manner.[63-64]

3.1 Colloidal synthetic methods for the synthesis of TMDs

In the search for synthetic techniques that can potentially produce TMDs at a large scale, colloidal synthesis methods such as “hot-injection” have begun to garner some significant interest in recent years.[65-67] These methods have been shown to be quite effective in the

synthesis of highly crystalline TMDs. Apart from the desire to develop a scalable method for the synthesis of TMDs, colloidal synthesis can allow for the synthesis of TMD materials with tunable properties through judicious selection of precursors and solvents/capping agents together with the optimization of reaction conditions such as concentration and temperature.[68] These methods have also resulted in a unique understanding of the formation of these materials in solution and the structure-property relationships that arise through the manipulation of the structural properties of these materials during synthesis.[68] In 2012 Cheon *et al.* reported on the development of a generalized synthetic protocol for the synthesis of various TMDs such as TiS_2, $TiSe_2$, ZrS_2, $ZrSe_3$, HfS_2, $HfSe_3$, VS_2, VSe_2, NbS_2, $NbSe_2$, TaS_2, and $TaSe_2$ nanocrystals.[69] They initially developed the method for the synthesis of TiS_2 and $TiSe_2$ nanocrystals, but they were able to extend the method to the synthesis of the various TMDs already mentioned. Cheon *et al.* demonstrated that the choice of chalcogen precursor is essential in the synthesis of 2D layered TMD nanocrystals. They found that the use of elementals sulfur in the synthesis of TiS_2 nanocrystals resulted in materials that were poor in size, shape, and crystallinity. This is due to the creation of highly reactive radicals from elemental S that promote degradation of the structural integrity of the 2D layered nanocrystals. The group has also shown that the lateral size of the nanocrystals can be controlled by adjusting the reactant concentration. Through this work, Cheon *et al.* demonstrated that colloidal synthesis is an effective strategy for the synthesis of various TMDs and also demonstrated the effect that the reaction parameters have on the properties of the synthesized TMDs. Mansouri *et al.* have also demonstrated the control of shape and dimensionality of NbS_2 nanostructures using ligand-directed colloidal synthesis protocols.[70] The group has shown that the choice of solvent/capping agent used can affect the structural properties of these nanostructures. They were able to synthesize NbS_2 using CS_2 as the sulfur source, $NbCl_5$ as the niobium source, and oleylamine (OAm) as the solvent. The CS_2 was injected into a mixture of OAm and $NbCl_5$ in a three-neck round bottom flask at 300 °C. This reaction resulted in the formation of monolayer nanosheets. The addition of oleic acid (OAc) as a complementary solvent to OAm resulted in shape confined 2D nanostructures with small lateral sizes. The ratio of OAm and OAc was shown to greatly affect the structural properties of the nanostructures. A ratio of OAm/OAc above 0.6 resulted in ultrathin nanosheets with reduced lateral size. However, the OAm/OAc ratio of 0.3 resulted in single-crystalline hexagonal plates with a thickness of 9.5 nm and a lateral size of 106 nm. The concentration of the CS_2 was shown to affect the structure of the nanostructures, an increase in the concentration of CS_2 without the addition of OAc resulted in the formation of multilayer NbS_2 nanosheets along with a flowerlike structure. A further

increase in the concentration of CS_2 resulted in the formation of 1D nanorods with a hexagonal cross-section. A schematic representation of these changes is shown in **Fig.10**.

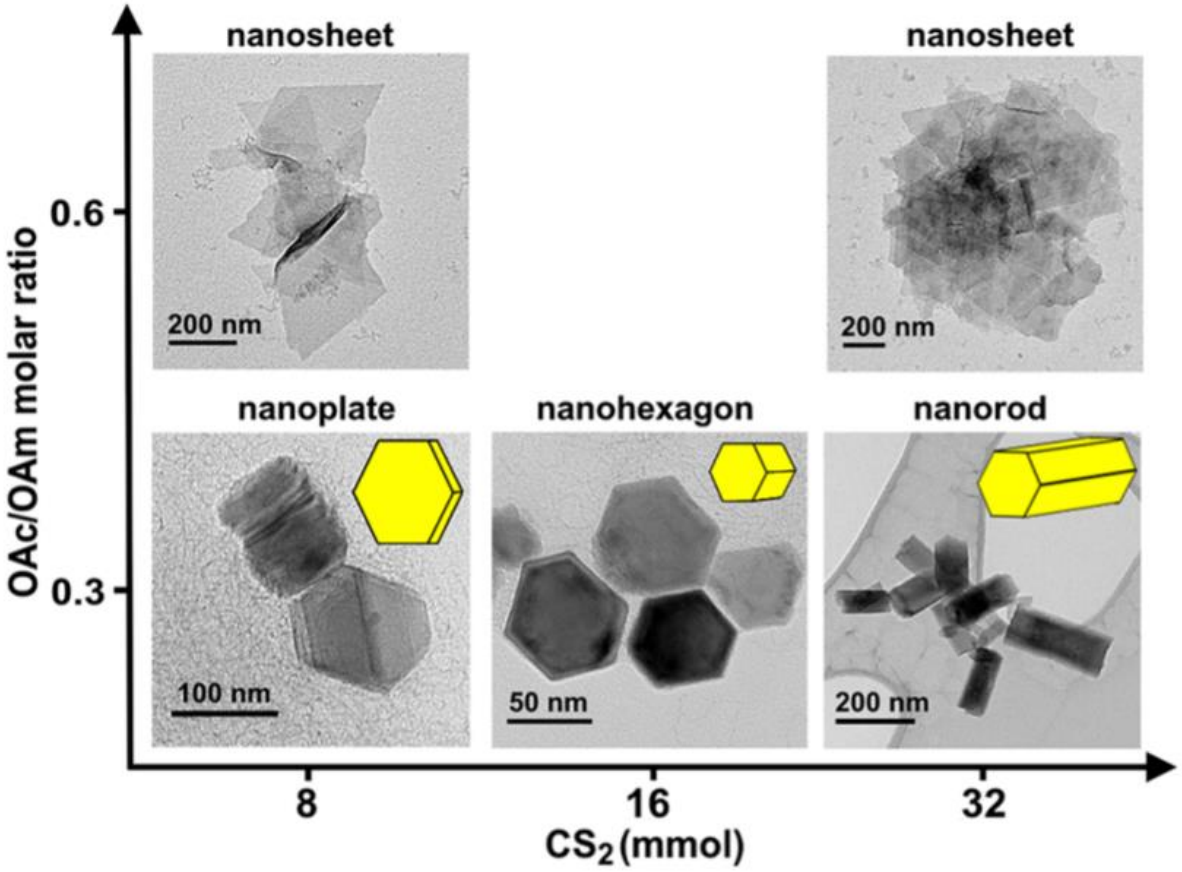


Figure 10: NbS_2 structure dependence on the OAc/OAm molar ratio and the amount of CS_2.

When the coordination solvent OAm is replaced with the non-coordinating solvent 1-octadacene (ODE), in the synthesis procedure that resulted in nano hexagons. The morphology turns into 0D nanospheres with an average size of 24 nm. Jung *et al.* have investigated the effect of using different capping agents in the synthesis of WSe_2 and $MoSe_2$ nanomaterials.[71] They found that the use of amine ligands allows for control of the lateral dimensions of the $MoSe_2$ nanosheets as the amine ligand preferentially bind to the edge sites and inhibits lateral growth. The use of ligands such as oleyl alcohol which contain hydroxyl groups are able to preferentially binds to the basal plane of the nanosheets which inhibits vertical growth leading to the formation of monolayer nanomaterials. Interestingly enough Guo *et al.* have investigated the effect of oleylamine (OAm) and oleic acid (OA).[72] The group synthesized the nanomaterial using OAm only, OA only and a 1:1 mixture of OA and OAm. They found out that the use of oleylamine resulted in ultrathin nanosheets that were superimposed to form a nanonetwork.

The use of oleic acid on the other hand resulted in the formation of a nanoflower like morphology. These results contradict the results reported by Jung *et al*. The use of a capping agent with a hydroxyl group may not be a sure way of obtaining monolayer nanosheets. Liu *et al*. have shown that it is possible to use colloidal synthesis to selectively synthesize stable 1T` phase dominated $WS_2$ nanostructures.[73] The $WS_2$ nanostructures were found to be a mixture of 1T` and 2H phases with the 1T` being the dominating phase. The 1T` phase was confirmed using high-resolution transmission electron microscopy (HRTEM), the WS_2 was shown to be dominated by distorted 1T phase structure with a feature of a zig-zag chain of W atoms. X-ray photoelectron spectroscopy (XPS) was used to determine the ratio of the 1T` and 2H phases of the $WS_2$ nanostructures, it was determined that the 1T` phase was dominating with 66.4 % while the 2H phase was minor with a 5.8% contribution. The 1T phase of TMDs is sought after as it is the more electron-conducting polytype compared to the semiconducting 2H phase. It is very popular for applications that require high electron conductivity such as electrocatalysis.

4. The hydrogen evolution reaction

4.1 Introduction to the hydrogen evolution reaction

In recent years there has been a drive to consider hydrogen as a clean and efficient energy carrier. As an energy carrier hydrogen could be a secondary energy source that would be used to generate, move, store and deliver energy in a usable form.[74] Hydrogen is a high efficiency, clean (low polluting) energy carrier that can be utilized for power generating, heating, and transportation.[74] Hydrogen would be an important energy alternative to fossil fuels. Hydrogen exists on earth as a constituent of compounds such as water, coal, and other various hydrocarbons. Hydrogen is thus produced by converting these compounds to hydrogen. Steam reforming is used to convert hydrocarbons to hydrogen and electrolysis is used to produce hydrogen from water.[75-76] steam reforming involves the conversion of methanol to hydrogen gas by reacting it with steam at high temperatures. This is currently the cheapest way to produce hydrogen but unfortunately, this method produces greenhouse gases that contribute to global warming.[76] Electrolysis is a method used to produce hydrogen by passing an electric current through water to split water into hydrogen and oxygen. The process does not produce any greenhouse gases because the electricity used can be from sunlight or other renewable energy sources.[77] The water splitting process can be described as two half-reactions: the hydrogen evolution reaction and the oxygen evolution reaction. The hydrogen evolution reactions involve the reduction of protons (H^+) at the cathode to produce hydrogen.[77] The process is shown below:

$$2H_{(aq)}^{+} + 2e^{-} \rightarrow H_{2(g)}$$

The oxygen evolution reaction involves the oxidation of water molecules at the anode to produce oxygen. The process is shown below:

$$2H_2O_{(l)} \rightarrow O_{2(l)} + 4H_{(aq)}^{+} + 4e^{-}$$

The overall water splitting reaction is:

$$2H_2O_{(l)} \rightarrow O_{2(g)} + 2H_{2(g)}$$

The HER is the reaction of interest as this is where the production of hydrogen actually occurs. The HER can be done using an acidic electrolyte such as sulphuric acid instead of water because it is easier to reduce a proton than it is to reduce a water molecule. The HER is an electrocatalytic process, which means a catalyst is needed to accelerate the hydrogen production process. Unfortunately, platinum has thus far been the best performing catalyst for the HER. Pt is a scarce and expensive metal which is the reason why the electrocatalytic production of hydrogen is still an expensive process.[78-80] Hence the need to develop catalysts made from earth-abundant and cheap metals. The electrocatalytic production in acidic media has three possible reaction pathways:

(Volmer step) $H_3O^{+} + e^{-} + M \rightleftharpoons M\text{-}H + H_2O,$ *(3)*

(Heyrovsky step) $M\text{-}H + H_3O^{+} + e^{-} \rightleftharpoons H_2 + H_2O + M,$ *(4)*

(Tafel step) $2M\text{-}H \rightleftharpoons H_2 + 2M,$ *(5)*

The initial reaction is the Volmer reaction which involves the adsorption of a proton (H^{+}) on the surface of the electrode and combination with an electron to form an adsorbed hydrogen atom. The reaction can then proceed either through a desorption step (Heyrovsky step), or a recombination step (Tafel step). A schematic representation of this process is shown in **Fig.11.**

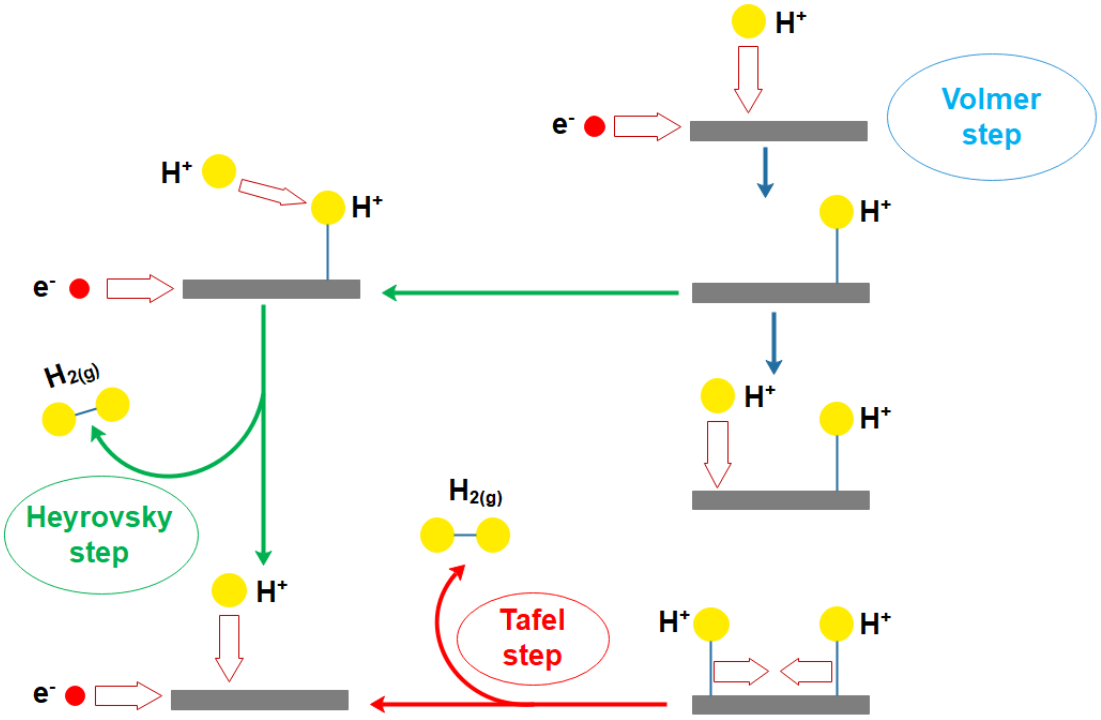


Figure 11: Schematic representation of HER pathway.

The hydrogen adsorption has been regarded theoretically as the rate-limiting step of the HER. The free energy of hydrogen adsorption (ΔG_H) has been regarded as the theoretical descriptor for the catalytic activity of materials towards the HER.[81-82] In an ideal catalyst, the ΔG_H should be thermo-neutral ($\Delta G_H = 0$), this is to ensure that the hydrogen does not bind too strongly or weakly to the surface of the catalyst. A positive value for the ΔG_H ($\Delta G_H > 0$) indicates low kinetics of hydrogen absorption, and a negative value for ΔG_H ($\Delta G_H < 0$) indicates low kinetics of hydrogen molecule release. In other words, a positive ΔG_H indicates weak binding of the hydrogen which would limit the overall rate of reaction and a negative ΔG_H indicates strong binding of the hydrogen to the catalyst and the desorption step of the reaction will limit the overall reaction rate. Investigating the ΔG_H of various metals gives rise to the Trasatti "volcano" relationship, which is observed when the HER exchange current density of different metals is plotted against the adsorption energy of a hydrogen atom on these metals as shown in **Fig.12**.[83]

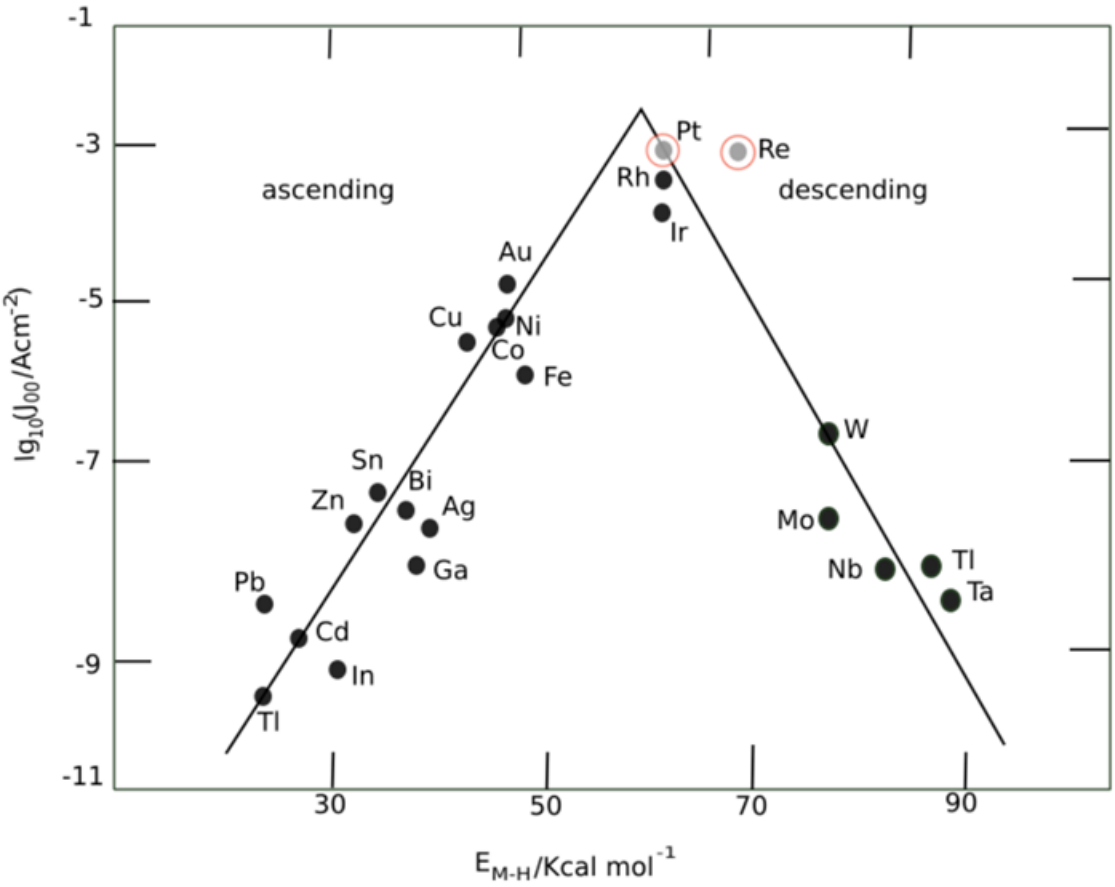


Figure 12: Trasatti volcano plot.

This volcano plot was put together by Trasatti in 1987, he put it together using the energy of hydride formation because the experimental and theoretical data for the hydrogen adsorption had not been available at the time. Unfortunately, the descending part of the plot used metals that had an oxidized top layer. This would certainly reduce the reaction rate of hydrogen adsorption by several orders of magnitude. An updated version of the plot has been developed using new information. A modern version of the hydrogen volcano plot in acidic media is shown in **Fig.13**.[84]

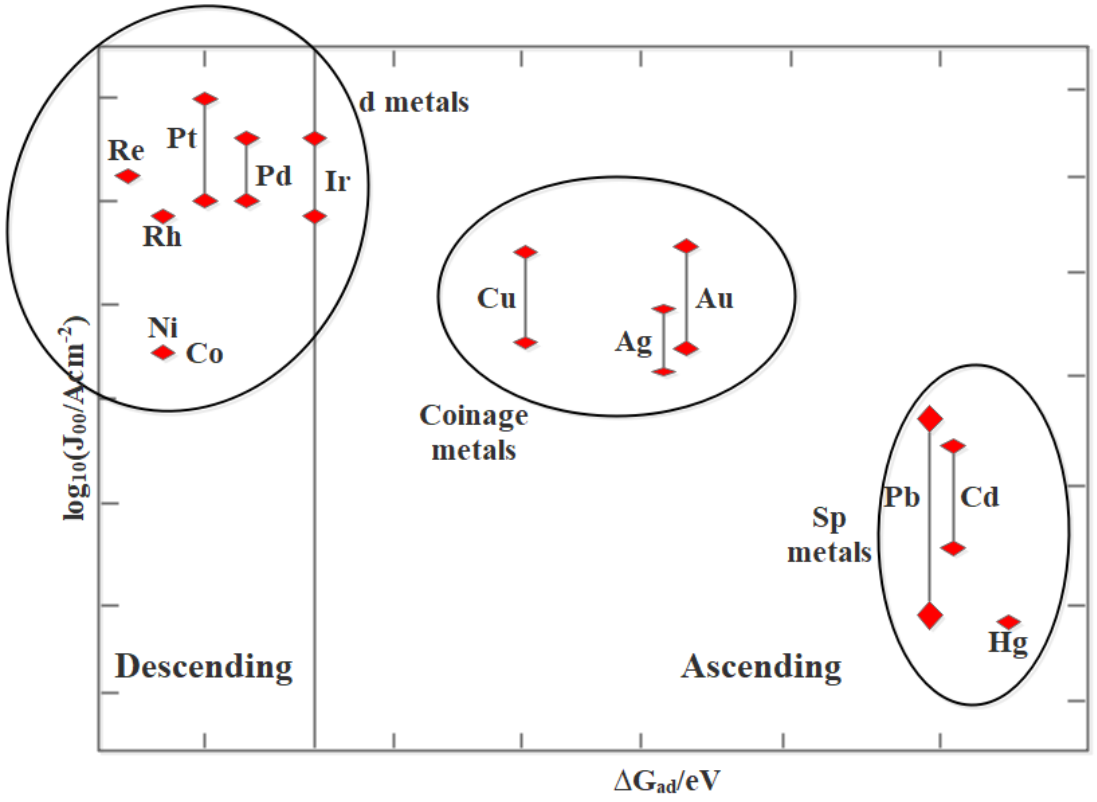


Figure 13: Volcano plots for hydrogen evolution in acidic solution.

The catalytic performance of any potential catalysts towards the HER is evaluated using electrochemical methods. There are several key parameters that are evaluated to assess the catalytic performance of materials such as the onset potential, the overpotential at a specified current density, Tafel slope, exchange current density, charge transfer resistance, and the stability of the catalyst in acidic media.[85-86] The parameters can be evaluated using various electrochemical methods such as linear sweep voltammetry (LSV), cyclic voltammetry (CV), chronoamperometry, and electrochemical impedance spectroscopy (EIS). A brief description of the most important parameters is discussed below:

These parameters include:

(i) Overpotential at 10 $mAcm^{-2}$: The overpotential is the difference between the applied potential and the thermodynamically determined potential for an electrochemical reaction. A useful way to compare catalysts is to report the overpotential needed to reach a specified current density.[87] One that is been found useful is the overpotential needed to reach 10 $mAcm^{-2}$. This current density corresponds to the working current density of the most competitive cost-

competitive PEC (photoelectrochemical water splitting) system. This parameter can be evaluated using the LSV as shown in **Fig.14**.

(ii) Onset potential: The onset potential is the overpotential at which the catalytic current is first observed. This parameter can also be evaluated using the LSV as shown in **Fig.14**.[85]

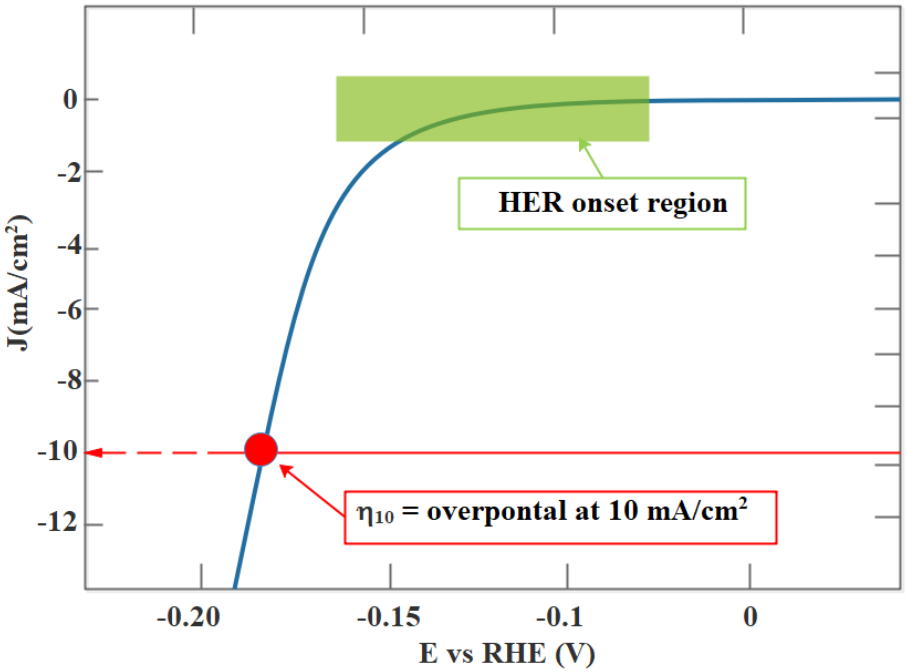


Figure 14: Typical polarisation curve with the denoted region for the onset region and overpotential at 10 mA/cm^2.

(iii) Tafel slope: The kinetics of the HER is strongly dependant on the electrochemical potential given by the Butler-Volmer (B-V) equations as shown in equation 1.[88]

$$J = J_0(-e^{-\frac{\alpha F\eta}{RT}} + e^{\frac{(1-\alpha)nF\eta}{RT}}) \quad (1)$$

Where J is the current density, J_0 is the exchange current density, α is the charge transfer coefficient, F is Faraday's constant, R is the gas constant, T is the temperature, n is the number of electrons, and η is the overpotential. When the overpotential is sufficiently large (η > 0.05), the B-V equation can be simplified as the Tafel equation:

$$\eta = a + b\log J = \frac{-2.3RT}{\alpha nF}\log J_0 + \frac{2.3RT}{\alpha nF}\log J \quad (2)$$

The equation shows a linear relationship between the overpotential and logJ, the slope of this equation is defined as the Tafel slope. The Tafel plot is the overpotential plotted against logJ, which can be obtained directly from the LSV curves. An example of a Tafel plot is given in **Fig.15**. The gradient of this plot gives the Tafel slope. The Tafel slope can be understood as

the sensitivity of the electric current response to an applied potential. It can be used to provide insights into the mechanism and rate-determining step of the catalyst surface.

(iv) Exchange current density: is the current density at the equilibrium potential and reflects the inherent nature of the catalyst. The exchange current density can be obtained from the Tafel plot, it is obtained via the intersection of the extrapolated linear part of the Tafel plot to the X-axis ($\log J_0 = a$) as shown in **Fig.15**.[85]

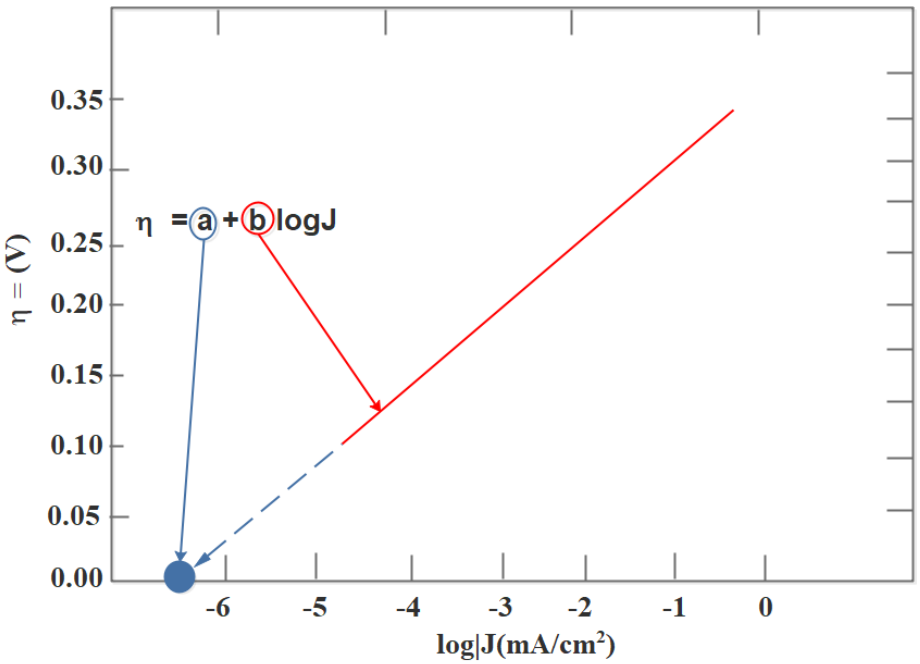


Figure 15: Tafel plot showing how the Tafel slope and exchange current density are extracted from the plot.

(v) Stability: This describes the ability of the catalyst to retain its activity after being subjected to numerous degradation cycles.

4.2 The exploration of TMDs as effective catalysts in the HER

Bulk MoS_2 was the first TMD to be investigated as an electrocatalyst for HER in 1977.[89] The material was found to be an inefficient catalyst due to its high Tafel slope (692 mV) and the large internal resistance in the bulk structure of the material. In 2005 Hinnemann *et al.* calculated that the free energy of adsorption of hydrogen on the edge sites of MoS_2 was comparable to that of the adsorption of hydrogen on Pt.[90] The edge sites of MoS_2 were thus considered to be the active sites for the electrocatalytic production of H_2 in the HER. This was then experimentally verified by a number of researchers such as Chorkendorff *et al.* Chorkendorff *et al.* was able to show using MoS_2 that was deposited on an Au substrate that

the exchange current density was proportional to the length of the edge sites of the MoS_2.[91] There was no such correlation for the sites in the basal plane of the material. This proved that the edge sites of the MoS_2 were the catalytically active sites which was a phenomenon not observed in bulk MoS_2. This then rejuvenated efforts to improve the catalytic activity of MoS_2 by maximizing exposure of the edge sites of the material. This was demonstrated to be one of the many strategies to increase the catalytic activity of TMD nanostructures. This represents one of the many strategies that have been employed to increase the catalytic activities of TMDs. These strategies are discussed as follows.

Maximizing exposure of TMD edge sites: Jaramillo et al. were able to maximize the exposure of the edge by creating a bicontinuous highly ordered network of MoS_2 nanosheets with nanoscale pores.[92] This was done by electrodepositing Mo on a porous Si template which was then subsequently sulphurised with H_2S to form the MoS_2. This structure was able to expose a large number of edge sites which resulted in excellent catalytic activity with an onset potential of -0.2 to -0.5 V vs RHE and a Tafel slope of 50 mV per dec. Tan *et al.* fabricated a constant 3D MoS_2 monolayer by using a gold 3D curved surface as a template.[93] The $MoSe_2$ supported on 3D nanoporous gold substrate exhibited a low overpotential of 226 mV and Tafel slope of 46 mV/dec. The excellent catalytic activity was attributed to the formation of out-of-plane strains that arise from the synthesis of the MoS_2 films on the 3D gold substrate.

Phase changes from 2H to 1T TMDs: There is another approach that has been shown to improve the electrocatalytic activity of MoS_2. Several researchers such as Jin *et al.* have reported that the metastable 1T phase of MoS_2 is more catalytically active than the more stable 2H phase.[94] This has been partly attributed to the decreased charge transfer resistance and better electron transport in the 1T phase. Some researchers suggest that the basal plane of the materials is also active for HER in the 1T phase which results in improved catalytic activity. It is still unclear why the 1T phase is more catalytically active than the 2H phase but it has been reported to have a Tafel slope that is 5-15 mV lower than that of 2H MoS_2.

Forming hybrid structures between TMDs and carbon nanostructures: One other strategy to improve the catalytic activity of TMDs is to increase the electron transport between the TMDs and the electrode. This can be done by making composites of the TMDs with a highly conductive material such as a carbon material. Reports have identified graphene-based carbon materials as the most suitable for this purpose. It was thought that the chemical and electrical

coupling effects, the electrical conductivity and the high surface area of graphene would certainly increase the HER activity of MoS_2.[95] Li *et al*. proved this in 2011 using a MoS_2/rGO composite, the composite was made using a solvothermal method.[95] The method resulted in MoS_2 particles that were uniformly dispersed on the surface of the rGO nanosheets as shown in **Fig.16**.

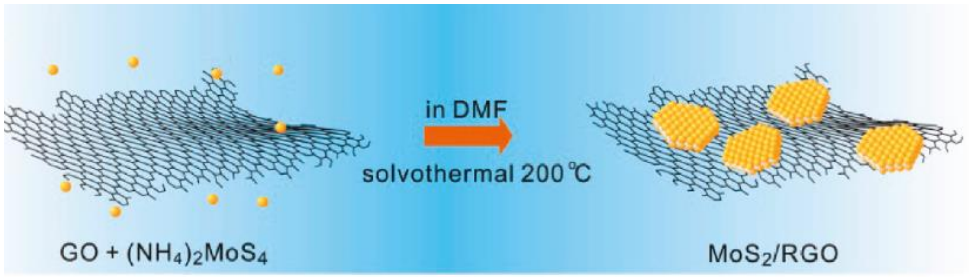


Figure 16: Synthetic procedure detailing the formation of MoS_2 nanosheets on the surface of rGO.[95]

Yan *et al.* employed a similar strategy in the synthesis of perpendicularly anchored $ReSe_2$ nanoflakes on graphene oxide.[96] The hybrid nanostructure was produced using hydrothermal synthesis. In this process, Se powder was mixed with N_2H_2 to form a homogeneous solution which was subsequently mixed with a solution consisting of NH_4ReO_4 and exfoliated GO nanosheets. The solution was stirred and ultrasonicated before being subjected to hydrothermal synthesis in a Teflon-lined reactor at 160 °C. The synthetic procedure was represented in schematic form as shown in **Fig.17**.

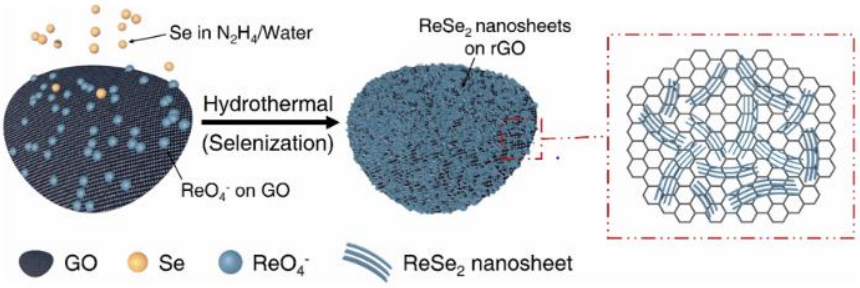


Figure 17: Schematic illustration of the hydrothermal synthetic process of $ReSe_2$@GO.[96]

The $ReSe_2$ nanoflakes were successfully anchored on rGO which provided a growing platform for the few-layered $ReSe_2$ nanoflakes. The vertical growth of the $ReSe_2$ on the rGO through the C-O-Re anchor was able to result in the maximal exposure of the edge/corner sites of $ReSe_2$. As a result, the overpotential and Tafel slope of the $ReSe_2$@rGO (145.3 mV and 40.7 mV/dec respectively) were much improved compared to those of the pristine $ReSe_2$ (183 mV and 76.2 mV/dec).

4.3 Colloidal synthesis of TMDs for HER

Since it has been shown that TMDs could be viable candidates as electrocatalysts in the HER. This validates the need to develop scalable methods for the synthesis of TMDs as electrocatalysts in the HER. There have recently been increased efforts in the colloidal synthesis of TMDs for HER applications. Eychmuller *et al.* have developed a straightforward, and low-cost general colloidal synthesis method for the production of various TMDs such as MoS_2, WS_2, NiS_x, FeS_x, and VS_2.[97] They were able to synthesize MoS_2 nanostructures with onset potentials as low as 149 mV, and small Tafel slope of 46 mV/dec. They also discovered that introducing Co as a dopant in the structure of MoS_2 increases the catalytic activity of MoS_2. The $Co_xMo_{1-x}S_2$ catalyst was shown to have an onset potential of 134 mV and a Tafel slope of 55 mV/dec. Yang *et al.* have also developed a fats strategy to synthesize scalable hierarchical ultrathin $MoSe_{2-x}$ ($x \sim 0.74$) nanosheets. The $MoSe_{2-x}$ nanosheets were found to be Mo rich with Se vacancies. The nanosheets had a small overpotential of 170 mV and a Tafel slope of 98 mV/dec. The high catalytic activity was attributed to the high concentration of Se vacancies. Zhou *et al.* were able to develop a facile strategy for the precise control of the lateral sizes and layer number of MoS_2 and WS_2 nanosheets.[98] They were able to synthesize small lateral dimension MS_2 (M=Mo, W) nanosheets with sizes of 15 to 40 nm. The nanosheets have well-controlled odd layer numbers such as 1,3 and 5 layers. The lateral sizes of the nanostructures could be altered by changing the mole ratio of the Mo and S in the MoS_2 nanosheets while the number of layers could be controlled by employing a multi-injection approach to the synthesis. The MoS_2 nanosheets exhibited a small overpotential of 100 mV and a Tafel slope of 52 mV/dec and the WS_2 nanosheets exhibited an overpotential of 80 mV and a Tafel slope of 46 mV/dec. The nanosheets were also found to be quite stable, even after 500 cycles the observed current density remains almost unchanged. Even more unusual TMDs have been explored for HER applications through colloidal synthesis. Zhao *et al.* were able to synthesize hexagonal $RuSe_2$ (h-$RuSe_2$) nanosheets that were a mixture of 2H and 1T through a facile bottom-up colloidal method. The h-$RuSe_2$ had a low overpotential of 119 mV and a Tafel slope of 139 mV/dec in alkaline media. The exceptional activity of the $RuSe_2$ was attributed to the enhanced adsorption free energies of H_2O ($\Delta G_{H_2O^*}$), the optimized adsorption free energies of H (ΔG_{H^*}), and the improved conductivity.[99] Bar-Sadan *et al.* have shown that colloidal synthesis can be used to introduce Mn dopants in $MoSe_2$ nanostructures in order to improve the catalytic activity of the nanomaterials.[100] The group was able to dope the $MoSe_2$ nanostructures with 1.7% and 2.4 % Mn concentration. The increase in dopant concentration resulted in better catalytic performance. The overpotential improved from 225 mV in pristine $MoSe_2$ to 167 mV in 2.4 %

Mn-doped nanostructures. A Tafel slope of 60 mV/dec was measured for the 2.4 % Mn-doped $MoSe_2$ nanostructured which was much improved from the Tafel slope of the pristine $MoSe_2$ at 83 mV/dec. The increased catalytic activity of the doped $MoSe_2$ was attributed to Se vacancies that are created through the Mn doping.

5. References

1. Han, S. A.; Bhatia, R.; Kim, S.-W., Synthesis, properties and potential applications of two-dimensional transition metal dichalcogenides. *Nano Converg.* 2015, 2 (1), 17.

2. Sipos, B.; Kusmartseva, A. F.; Akrap, A.; Berger, H.; Forró, L.; Tutǐs, E., From Mott state to superconductivity in 1T-TaS_2. *Nat. Mater*. 2008, 7 (12), 960.

3. Gordon, R.; Yang, D.; Crozier, E.; Jiang, D.; Frindt, R., Structures of exfoliated single layers of WS_2, MoS_2, and $MoSe_2$ in aqueous suspension. *Phys. Rev. B* 2002, 65 (12), 125407

4. Mak, K. F.; Shan, J., Photonics and optoelectronics of 2D semiconductor transition metal dichalcogenides. *Nat. Photon.* 2016, 10 (4), 216-226.

5. Bernardi, M.; Ataca, C.; Palummo, M.; Grossman, J. C., Optical and electronic properties of Two-Dimensional layered materials. *Nanophotonics* 2017, 6 (2), 479-493.

6. Lv, R.; Robinson, J. A.; Schaak, R. E.; Sun, D.; Sun, Y.; Mallouk, T. E.; Terrones, M., Transition metal dichalcogenides and beyond: synthesis, properties, and applications of single- and few-layer nanosheets. *Acc. Chem. Res*. 2014, 48 (1), 56-64.

7. Chhowalla, M.; Shin, H. S.; Eda, G.; Li, L.-J.; Loh, K. P.; Zhang, H., The chemistry of two-dimensional layered transition metal dichalcogenide nanosheets. *Nat. Chem.* 2013, 5 (4), 263-275.

8. Kang, M.; Kim, B.; Ryu, S. H.; Jung, S. W.; Kim, J.; Moreschini, L.; Jozwiak, C.; Rotenberg, E.; Bostwick, A.; Kim, K. S., Universal mechanism of band-gap engineering in transition-metal dichalcogenides. *Nano letters* **2017,** *17* (3), 1610-1615.

9. Liu, J.; Liu, H.; Wang, J.; Sheng, H.; Tang, G.; Zhang, J.; Bai, D., Optical and electronic properties of dichalcogenides WX_2 (X= S, Se, and Te) monolayers under biaxial strain. *Phys. B: Condens. Matter* **2019,** *568*, 18-24.

10. Radamson, H. H.; He, X.; Zhang, Q.; Liu, J.; Cui, H.; Xiang, J.; Kong, Z.; Xiong, W.; Li, J.; Gao, J., Miniaturization of CMOS. *Micromachines* **2019,** *10* (5), 293.

11. Novoselov, K. S.; Geim, A. K.; Morozov, S. V.; Jiang, D.-e.; Zhang, Y.; Dubonos, S. V.; Grigorieva, I. V.; Firsov, A. A., Electric field effect in atomically thin carbon films. *science* **2004,** *306* (5696), 666-669.

12. Huo, C.; Yan, Z.; Song, X.; Zeng, H., 2D materials via liquid exfoliation: a review on fabrication and applications. *Sci. bull.* **2015,** *60* (23), 1994-2008.
13. Zhang, Q.; Mei, L.; Cao, X.; Tang, Y.; Zeng, Z., Intercalation and exfoliation chemistries of transition metal dichalcogenides. *J. Mater. Chem. A* **2020,** *8* (31), 15417-15444.
14. Manamela, L.; Fru, J. N.; Kyesmen, P. I.; Diale, M.; Nombona, N., Electrically Enhanced Transition Metal Dichalcogenides as Charge Transport Layers in Metallophthalocyanine-Based Solar Cells. *Front. Chem.* **2020**, 1163.
15. Velusamy, D. B.; Kim, R. H.; Cha, S.; Huh, J.; Khazaeinezhad, R.; Kassani, S. H.; Song, G.; Cho, S. M.; Cho, S. H.; Hwang, I., Flexible transition metal dichalcogenide nanosheets for band-selective photodetection. *Nat. Commun.* **2015,** *6* (1), 1-11.
16. Nguyen, D.-T.; Ting, H.-A.; Su, Y.-H.; Hofmann, M.; Hsieh, Y.-P., Additive-Enhanced Exfoliation for High-Yield 2D Materials Production. *Nanomaterials* **2021,** *11* (3), 601.
17. Backes, C.; Hanlon, D.; Szydlowska, B. M.; Harvey, A.; Smith, R. J.; Higgins, T. M.; Coleman, J. N., Preparation of liquid-exfoliated transition metal dichalcogenide nanosheets with controlled size and thickness: a state of the art protocol. *J. Vis. Exp.* **2016,** (118), e54806.
18. Nicolosi, V.; Chhowalla, M.; Kanatzidis, M. G.; Strano, M. S.; Coleman, J. N., Liquid exfoliation of layered materials. *Science* **2013,** *340* (6139), 1226419.
19. Niu, L.; Coleman, J. N.; Zhang, H.; Shin, H.; Chhowalla, M.; Zheng, Z., Production of two-dimensional nanomaterials via liquid-based direct exfoliation. *Small* **2016,** *12* (3), 272-293.
20. Yazyev, O. V.; Kis, A., MoS_2 and semiconductors in the flatland. *Mater. Today* **2015,** *18* (1), 20-30.
21. Varrla, E.; Backes, C.; Paton, K. R.; Harvey, A.; Gholamvand, Z.; McCauley, J.; Coleman, J. N., Large-scale production of size-controlled MoS_2 nanosheets by shear exfoliation. *Chem. Mater.* **2015,** *27* (3), 1129-1139.
22. Yao, Y.; Lin, Z.; Li, Z.; Song, X.; Moon, K.-S.; Wong, C.-p., Large-scale production of two-dimensional nanosheets. *J. Mater. Chem.* **2012,** *22* (27), 13494-13499.
23. Meng, L.; Hu, S.; Yan, W.; Feng, J.; Li, H.; Yan, X., Controlled synthesis of large scale continuous monolayer WS_2 film by atmospheric pressure chemical vapor deposition. *Chem. Phys. Lett.* **2020,** *739*, 136945.
24. Yang, P.; Zou, X.; Zhang, Z.; Hong, M.; Shi, J.; Chen, S.; Shu, J.; Zhao, L.; Jiang, S.; Zhou, X., Batch production of 6-inch uniform monolayer molybdenum disulfide catalyzed by sodium in glass. *Nat. Commun.* **2018,** *9* (1), 1-10.

25. Ahn, C.; Lee, J.; Kim, H. U.; Bark, H.; Jeon, M.; Ryu, G. H.; Lee, Z.; Yeom, G. Y.; Kim, K.; Jung, J., Low-temperature synthesis of large-scale molybdenum disulfide thin films directly on a plastic substrate using plasma-enhanced chemical vapor deposition. *Adv. Mater.* **2015,** *27* (35), 5223-5229.

26. Kalanyan, B.; Kimes, W. A.; Beams, R.; Stranick, S. J.; Garratt, E.; Kalish, I.; Davydov, A. V.; Kanjolia, R. K.; Maslar, J. E., Rapid wafer-scale growth of polycrystalline 2H-MoS_2 by pulsed metal–organic chemical vapor deposition. *Chem. Mater.* **2017,** *29* (15), 6279-6288.

27. Lee, D. H.; Sim, Y.; Wang, J.; Kwon, S.-Y., Metal–organic chemical vapor deposition of 2D van der Waals materials—The challenges and the extensive future opportunities. *Appl. Mater.* **2020,** *8* (3), 030901.

28. Cohen, A.; Patsha, A.; Mohapatra, P. K.; Kazes, M.; Ranganathan, K.; Houben, L.; Oron, D.; Ismach, A., Growth-etch metal–organic chemical vapor deposition approach of WS_2 atomic layers. *ACS nano* **2020,** *15* (1), 526-538.

29. Okada, M.; Okada, N.; Chang, W.-H.; Endo, T.; Ando, A.; Shimizu, T.; Kubo, T.; Miyata, Y.; Irisawa, T., Gas-source CVD growth of atomic layered WS_2 from WF_6 and H_2S precursors with high grain size uniformity. *Sci. Rep.* **2019,** *9* (1), 1-10.

30. Cun, H.; Macha, M.; Kim, H.; Liu, K.; Zhao, Y.; LaGrange, T.; Kis, A.; Radenovic, A., Wafer-scale MOCVD growth of monolayer MoS_2 on sapphire and SiO_2. *Nano Res.* **2019,** *12* (10), 2646-2652.

31. Seravalli, L.; Bosi, M., A Review on Chemical Vapour Deposition of Two-Dimensional MoS_2 Flakes. *Materials* **2021,** *14* (24), 7590.

32. Wang, D.; Xie, T.; Li, Y., Nanocrystals: Solution-based synthesis and applications as nanocatalysts. *Nano Res.* **2009,** *2* (1), 30-46.

33. Morse, J., Nanofabrication technologies for roll-to-roll processing. **2012**.

34. Hu, Q.; Tuck, C.; Wildman, R.; Hague, R., Application of nanoparticles in manufacturing. *Handbook of Nanoparticles; Aliofkhazraei, M., Ed.; Springer International Publishing: Cham, Switzerland* **2016**, 1219-1278.

35. Jung, M.; Kim, J.; Koo, H.; Lee, W.; Subramanian, V.; Cho, G., Roll-to-roll gravure with nanomaterials for printing smart packaging. *J. Nanosci. Nanotechnol.* **2014,** *14* (2), 1303-1317.

36. Chaudhary, N.; Khanuja, M.; Islam, S., Hydrothermal synthesis of MoS_2 nanosheets for multiple wavelength optical sensing applications. *Sens. Actuator A: Phys.* **2018,** *277*, 190-198.

37. Wang, Z.; Yue, H. Y.; Yu, Z. M.; Yao, F.; Gao, X.; Guan, E. H.; Zhang, H. J.; Wang, W. Q.; Song, S. S., One-pot hydrothermal synthesis of $MoSe_2$ nanosheets spheres-reduced

graphene oxide composites and application for high-performance supercapacitor. *J. Mater. Sci.: Mater Electron.* **2019,** *30* (9), 8537-8545.

38. Cao, S.; Liu, T.; Hussain, S.; Zeng, W.; Peng, X.; Pan, F., Hydrothermal synthesis of variety low dimensional WS_2 nanostructures. *Mater. Lett.* **2014,** *129*, 205-208.

39. Fang, W.; Zhao, H.; Xie, Y.; Fang, J.; Xu, J.; Chen, Z., Facile hydrothermal synthesis of VS_2/graphene nanocomposites with superior high-rate capability as lithium-ion battery cathodes. *ACS Appl. Mater. Interf.* **2015,** *7* (23), 13044-13052.

40. Fan, R.; Chen, X.; Chen, Z., A novel route to obtain molybdenum dichalcogenides by hydrothermal reaction. *Chem. Lett.* **2000,** *29* (8), 920-921.

41. Duraisamy, S.; Ganguly, A.; Sharma, P. K.; Benson, J.; Davis, J.; Papakonstantinou, P., One-Step Hydrothermal Synthesis of Phase-Engineered MoS_2/MoO_3 Electrocatalysts for Hydrogen Evolution Reaction. *ACS Appl. Nano Mater.* **2021,** *4* (3), 2642-2656.

42. Pellegrino, T.; Kudera, S.; Liedl, T.; Muñoz Javier, A.; Manna, L.; Parak, W. J., On the development of colloidal nanoparticles towards multifunctional structures and their possible use for biological applications. *Small* 2005, 1 (1), 48-63.

43. Wang, Y.; Xia, Y., Bottom-up and top-down approaches to the synthesis of monodispersed spherical colloids of low melting-point metals. *Nano lett.* 2004, 4 (10), 2047-2050.

44. Chestnoy, N.; Harris, T. D.; Hull, R.; Brus, L. E., Luminescence and photophysics of cadmium sulfide semiconductor clusters: the nature of the emitting electronic state. *J. Phys. Chem.* **1986,** *90* (15), 3393-3399.

45. Murray, C.; Norris, D. J.; Bawendi, M. G., Synthesis and characterization of nearly monodisperse CdE (E=sulfur, selenium, tellurium) semiconductor nanocrystallites. Journal of the American *Chem. Soc*. 1993, 115 (19), 8706-8715.

46. LaMer, V. K.; Dinegar, R. H., Theory, production and mechanism of formation of monodispersed hydrosols. *J. Am. Chem. Soc.* 1950, 72 (11), 4847-4854.

47. Polte, J., Fundamental growth principles of colloidal metal nanoparticles–a new perspective. CrystEngComm 2015, 17 (36), 6809-6830.

48. WZ, O., Ostwald ripening. *Phys. Chem.* **1900,** *34*, 495-503.

49. De Nolf, K.; Capek, R. K.; Abe, S.; Sluydts, M.; Jang, Y.; Martins, J. C.; Cottenier, S.; Lifshitz, E.; Hens, Z., Controlling the size of hot injection made nanocrystals by manipulating the diffusion coefficient of the solute. *J. Am. Chem. Soc.* **2015,** *137* (7), 2495-2505.

50. Mirbagheri, N.; Engberg, S.; Crovetto, A.; Simonsen, S. B.; Hansen, O.; Lam, Y. M.; Schou, J., Synthesis of ligand-free CZTS nanoparticles via a facile hot injection route. *Nanotechnology* **2016,** *27* (18), 185603.

51. Bade, B. R.; Rondiya, S. R.; Jadhav, Y. A.; Kamble, M. M.; Barma, S. V.; Jathar, S. B.; Nasane, M. P.; Jadkar, S. R.; Funde, A. M.; Dzade, N. Y., Investigations of the structural, optoelectronic and band alignment properties of Cu_2ZnSnS_4 prepared by hot-injection method towards low-cost photovoltaic applications. *J. Alloys Compd.* **2021,** *854*, 157093.

52. Kulpa-Greszta, M.; Tomaszewska, A.; Dziedzic, A.; Pązik, R., Rapid hot-injection as a tool for control of magnetic nanoparticle size and morphology. *RSC Adv.* **2021,** *11* (34), 20708-20719.

53. Deng, C.; Fu, B.; Li, L.; Wang, Y.; Yang, L., Influence of Sulfur Precursor Solutions on Crystallinity of $CuInS_2$ Nanocrystals Fabricated with Hot-Injection Method. *J. Nanosci. Nanotechnol.* **2020,** *20* (7), 4533-4536.

54. McCarthy, S.; Ratkic, R.; Purcell-Milton, F.; Perova, T. S.; Gun'ko, Y., Adaptable surfactant-mediated method for the preparation of anisotropic metal chalcogenide nanomaterials. *Sci. Rep.* **2018,** *8* (1), 1-10.

55. Lokhande, A.; Gurav, K.; Jo, E.; He, M.; Lokhande, C.; Kim, J. H., Towards cost effective metal precursor sources for future photovoltaic material synthesis: CTS nanoparticles. *Opt. Mater.* **2016,** *54*, 207-216

56. van Embden, J.; Chesman, A. S.; Jasieniak, J. J., The heat-up synthesis of colloidal nanocrystals. *Chem. Mater.* 2015, 27 (7), 2246-2285.

57. Ndala, Z.; Shumbula, N.; Nkabinde, S.; Kolokoto, T.; Nchoe, O.; Shumbula, P.; Tetana, Z. N.; Linganiso, E. C.; Gqoba, S. S.; Moloto, N., Evaluating the Effect of Varying the Metal Precursor in the Colloidal Synthesis of $MoSe_2$ Nanomaterials and Their Application as Electrodes in the Hydrogen Evolution Reaction. *Nanomaterials* **2020,** *10* (9), 1786.

58. Baletto, F.; Ferrando, R., Structural properties of nanoclusters: Energetic, thermodynamic, and kinetic effects. Reviews of modern physics 2005, 77 (1), 371

59. Chauhan, H.; Kumar, Y.; Deka, S., New synthesis of two-dimensional CdSe/CdS core@ shell dot-in-hexagonal platelet nanoheterostructures with interesting optical properties. *Nanoscale* 2014, 6 (17), 10347-10354.

60. Sperling, R. A.; Parak, W., Surface modification, functionalization and bioconjugation of colloidal inorganic nanoparticles. *Philos. Trans. Royal Soc. A: Math. Phys. Eng. Sci.* 2010, 368 (1915), 1333-1383.

61. Bakshi, M. S., How surfactants control crystal growth of nanomaterials. *Cryst. Growth Des.* 2015, 16 (2), 1104-1133.

62. Machogo, L. F.; Sithole, R. K.; Phao, N.; Kolokoto, T.; Gqoba, S. S.; Mlambo, M.; Moloto, M. J.; Shumbula, P. M.; Mdluli, P. S.; Moloto, N., Probing the structure and functionalized surface of colloidal AuSe. *Mater. Sci. Eng. B* **2021,** *263*, 114878.
63. Daniels, S., Synthesis of luminescent 2D layered materials using an amine-met al complex and a slow sulfur-releasing precursor. Google Patents: 2021.
64. Daniels, S.; Pickett, N. L., Template-assisted synthesis of 2D nanosheets using nanoparticle templates. Google Patents: 2020.
65. Liu, Y.; Zhong, Q.; Chen, K.; Zhou, J.; Yang, X.; Chen, W., Morphologies controllable synthesis of MoS2 by hot-injection method: from quantum dots to nanosheets. *J. Mater. Sci. Mater. Electron.* **2017,** *28* (18), 13633-13637.
66. Savjani, N.; Lewis, E. A.; Bissett, M. A.; Brent, J. R.; Dryfe, R. A.; Haigh, S. J.; O'Brien, P., Synthesis of Lateral Size-Controlled Monolayer 1 H-MoS_2@ Oleylamine as Supercapacitor Electrodes. *Chem. Mater.* **2016,** *28* (2), 657-664.
67. Scarfiello, R.; Cesari, A.; Altamura, D.; Masi, S.; Nobile, C.; Balzano, F.; Giannini, C.; Grillo, V.; Tavabi, A. H.; Dunin-Borkowski, R. E., Mechanistic insight into the formation of colloidal WS_2 nanoflakes in hot alkylamine media. *Nanoscale adv.* **2019,** *1* (7), 2772-2782.
68. Sun, Y.; Terrones, M.; Schaak, R. E., Colloidal Nanostructures of Transition-Metal Dichalcogenides. *Acc. Chem. Res.* **2021,** *54* (6), 1517-1527.
69. Jeong, S.; Yoo, D.; Jang, J.-t.; Kim, M.; Cheon, J., Well-defined colloidal 2-D layered transition-metal chalcogenide nanocrystals via generalized synthetic protocols. *J. Am. Chem. Soc.* **2012,** *134* (44), 18233-18236.
70. Mansouri, A.; Semagina, N., Colloidal synthesis protocol of shape-and dimensionally-controlled transition-metal chalcogenides and their hydrodesulfurization activities. *ACS Appl. Nano Mater.* **2018,** *1* (9), 4408-4412
71. Jung, W.; Lee, S.; Yoo, D.; Jeong, S.; Miró, P.; Kuc, A.; Heine, T.; Cheon, J., Colloidal synthesis of single-layer MSe_2 (M= Mo, W) nanosheets via anisotropic solution-phase growth approach. *J. Am. Chem. Soc.* **2015**, 137 (23), 7266-7269.
72. Guo, W.; Chen, Y.; Wang, L.; Xu, J.; Zeng, D.; Peng, D.-L., Colloidal synthesis of $MoSe_2$ nanonetworks and nanoflowers with efficient electrocatalytic hydrogen-evolution activity. Electrochim. Acta **2017**, 231, 69-76.
73. Liu, Z.; Li, N.; Su, C.; Zhao, H.; Xu, L.; Yin, Z.; Li, J.; Du, Y., Colloidal synthesis of 1T'phase dominated WS_2 towards endurable electrocatalysis. *Nano Energy* **2018,** *50*, 176-181.
74. Mazloomi, K.; Gomes, C., Hydrogen as an energy carrier: prospects and challenges. Renew. Sust. Energ. Rev. **2012**, 16 (5), 3024-3033.

75. Tsou, J., The Greening Economy. Race, Poverty & the Environment 2006, 13 (1), 51-55.
76. Ashcroft, A.; Cheetham, A. K.; Green, M., Partial oxidation of methane to synthesis gas using carbon dioxide. *Nature* **1991**, 352 (6332), 225-226.
77. Parsons, R., The rate of electrolytic hydrogen evolution and the heat of adsorption of hydrogen. *J. Chem. Soc., Faraday trans.* **1958**, 54, 1053-1063.
78. Pan, Y.; Lin, Y.; Liu, Y.; Liu, C., A novel CoP/MoS 2-CNTs hybrid catalyst with Pt-like activity for hydrogen evolution. *Catal. Sci. Technol.* **2016,** *6* (6), 1611-1615.
79. Shinde, S.; Sami, A.; Kim, D.-H.; Lee, J.-H., Nanostructured SnS-N-doped graphene as an advanced electrocatalyst for the hydrogen evolution reaction. *Chem. Commun.* **2015,** *51* (86), 15716-15719.
80. Pan, H., Metal dichalcogenides monolayers: novel catalysts for electrochemical hydrogen production. *Sci. Rep.* **2014,** *4* (1), 1-6.
81. Seo, B.; Jung, G. Y.; Sa, Y. J.; Jeong, H. Y.; Cheon, J. Y.; Lee, J. H.; Kim, H. Y.; Kim, J. C.; Shin, H. S.; Kwak, S. K., Monolayer-precision synthesis of molybdenum sulfide nanoparticles and their nanoscale size effects in the hydrogen evolution reaction. *ACS nano* **2015,** *9* (4), 3728-3739.
82. Hakala, M.; Kronberg, R.; Laasonen, K., Hydrogen adsorption on doped MoS_2 nanostructures. *Sci. Rep.* **2017,** *7* (1), 1-13.
83. Trasatti, S., Electrocatalysis by oxides—attempt at a unifying approach. *J. Electroanal. Chem. Interf. Electrochem.* **1980,** *111* (1), 125-131.
84. Quaino, P.; Juarez, F.; Santos, E.; Schmickler, W., Volcano plots in hydrogen electrocatalysis–uses and abuses. *Beilstein. J. Nanotechnol.* **2014,** *5* (1), 846-854.
85. Benck, J. D.; Hellstern, T. R.; Kibsgaard, J.; Chakthranont, P.; Jaramillo, T. F., Catalyzing the hydrogen evolution reaction (HER) with molybdenum sulfide nanomaterials. *ACS Catal.* **2014,** *4* (11), 3957-3971.
86. Prabhu, P.; Jose, V.; Lee, J.-M., Design strategies for development of TMD-based heterostructures in electrochemical energy systems. *Matter* **2020,** *2* (3), 526-553.
87. McCrory, C. C.; Jung, S.; Ferrer, I. M.; Chatman, S. M.; Peters, J. C.; Jaramillo, T. F., Benchmarking hydrogen evolving reaction and oxygen evolving reaction electrocatalysts for solar water splitting devices. *J. Am. Chem. Soc.* **2015,** *137* (13), 4347-4357.
88. Fang, Y.-H.; Liu, Z.-P., Tafel kinetics of electrocatalytic reactions: from experiment to first-principles. *ACS Catal.* **2014,** *4* (12), 4364-4376.
89. 21. Tributsch, H.; Bennett, J., Electrochemistry and photochemistry of MoS_2 layer crystals. I. *J. Electroanal. Chem. Interf. Electrochem.* **1977**, 81 (1), 97-111.

90. Hinnemann, B.; Moses, P. G.; Bonde, J.; Jørgensen, K. P.; Nielsen, J. H.; Horch, S.; Chorkendorff, I.; Nørskov, J. K., Biomimetic hydrogen evolution: MoS_2 nanoparticles as catalyst for hydrogen evolution. *J. Am. Chem. Soc.* **2005**, 127 (15), 5308-5309.

91. Jaramillo, T. F.; Jørgensen, K. P.; Bonde, J.; Nielsen, J. H.; Horch, S.; Chorkendorff, I., Identification of active edge sites for electrochemical H_2 evolution from MoS_2 nanocatalysts. *science* **2007**, 317 (5834), 100-102.

92. Kibsgaard, J.; Chen, Z.; Reinecke, B. N.; Jaramillo, T. F., Engineering the surface structure of MoS_2 to preferentially expose active edge sites for electrocatalysis. *Nat. Mater.* **2012**, 11 (11), 963.

93. Tan, Y.; Liu, P.; Chen, L.; Cong, W.; Ito, Y.; Han, J.; Guo, X.; Tang, Z.; Fujita, T.; Hirata, A., Monolayer MoS_2 films supported by 3D nanoporous metals for high-efficiency electrocatalytic hydrogen production. *Adv. Mater.* **2014,** *26* (47), 8023-8028.

94. Lukowski, M. A.; Daniel, A. S.; Meng, F.; Forticaux, A.; Li, L.; Jin, S., Enhanced hydrogen evolution catalysis from chemically exfoliated metallic MoS_2 nanosheets. *J. Am. Chem. Soc.* **2013**, 135 (28), 10274-10277.

95. Ran, N.; Sun, B.; Qiu, W.; Song, E.; Chen, T.; Liu, J., Identifying metallic transition-metal dichalcogenides for hydrogen evolution through multilevel high-throughput calculations and machine learning. *J. Phys. Chem. Lett.* **2021**, 12 (8), 2102-2111.

96. Yan, Y.; Xu, S.; Li, H.; Selvam, N. C. S.; Lee, J. Y.; Lee, H.; Yoo, P. J., Perpendicularly anchored $ReSe_2$ nanoflakes on reduced graphene oxide support for highly efficient hydrogen evolution reactions. *Chem. Eng. Sci.* **2021,** *405*, 126728.

97. Meerbach, C.; Klemmed, B.; Spittel, D.; Bauer, C.; Park, Y. J.; Hübner, R.; Jeong, H. Y.; Erb, D.; Shin, H. S.; Lesnyak, V., General colloidal synthesis of transition-metal disulfide nanomaterials as electrocatalysts for hydrogen evolution reaction. *ACS Appl. Mater. Interf.* **2020,** *12* (11), 13148-13155.

98. Zhou, M.; Zhang, Z.; Huang, K.; Shi, Z.; Xie, R.; Yang, W., Colloidal preparation and electrocatalytic hydrogen production of MoS_2 and WS_2 nanosheets with controllable lateral sizes and layer numbers. *Nanoscale* **2016,** *8* (33), 15262-15272.

99. Zhao, Y.; Cong, H.; Li, P.; Wu, D.; Chen, S.; Luo, W., Hexagonal $RuSe_2$ nanosheets for highly efficient hydrogen evolution electrocatalysis. *Angew. Chem.* **2021,** *133* (13), 7089-7093.

100. Kuraganti, V.; Jain, A.; Bar-Ziv, R.; Ramasubramaniam, A.; Bar-Sadan, M., Manganese doping of MoSe2 promotes active defect sites for hydrogen evolution. *ACS appl. Mater. Interf.* **2019,** *11* (28), 25155-25162.

Chapter 3: Elucidating the effect of metal and chalcogen precursor selection on the colloidal synthesis of $MoSe_2$ and $ReSe_2$ nanostructures and its impact on the catalytic activity of the nanostructures towards the hydrogen evolution reaction

1. Introduction

Transition metal dichalcogenides (TMDs) are a class of layered materials with the general formula MX_2, where M is a transition metal and X is a chalcogen (X=S, Se, or Te). The materials have been shown to have extraordinary properties when in their monolayer to few-layer forms. Due to these incredible properties, these materials have been widely explored for various applications such as in sensors, energy storage devices, photovoltaic cells, and electrocatalysis.[3-6] The greatest challenge to the commercial application of these materials is the development of scalable synthetic methods that can produce these materials at a large-scale. Colloidal synthetic techniques are becoming increasingly popular due to their ability to produce highly crystalline TMDs using relatively simple synthetic procedures. The methods also have the added benefit of being scalable and also allow for control of the properties of the nanomaterials synthesized.[13-14] However, there are still some challenges that need to be addressed in the colloidal synthesis of TMDs. There is still debate on whether colloidal synthesis protocols can be developed for the production of various TMDs, even the members of the TMD family that are more obscure.[15] The more pressing debate is whether these synthetic protocols can be used to synthesize TMDs with similar structural and catalytic properties.[15,16] $MoSe_2$ has been one of the most extensively explored TMDs, it has been found to be a rather versatile material that can be utilized in various applications.[17-18] $ReSe_2$ on the other hand has only recently garnered a lot of interest due to its uncommon distorted 1T crystal configuration and low symmetry crystal lattice, which results in interesting electronic and optical properties.[19] This work focuses on the colloidal synthesis of $MoSe_2$ and $ReSe_2$ nanostructures. More importantly, this work demonstrates how colloidal synthetic protocols can be used to synthesize various TMD nanostructures with similar structural properties. This was done using a specific selection of the metal precursors used for the synthesis of the $MoSe_2$ and $ReSe_2$ nanostructures. The selenium precursor was varied from selenium powder to selenourea to

demonstrate how impactful precursor selection is to the properties of the synthesized nanostructures. The selection of the chalcogen precursor has been shown to greatly affect the size, morphology, and phase of nanostructured materials including TMDs.[15] This constitutes an interesting study on how the choice of metal and chalcogen precursor affects the nucleation and growth of TMD nanostructures. The catalytic activity of the $MoSe_2$ and $ReSe_2$ nanostructures towards the HER was also evaluated, as well as any changes to the catalytic activity of the $MoSe_2$ and $ReSe_2$ nanostructures due to precursor selection.

2. Experimental section

2.1 Chemicals

Molybdic acid (H_2MoO_4, 85%), Ammonium perrhanate (NH_4ReO_4, 99.98%), selenium powder (Se, 99.99%), selenourea (CH_4N_2Se, 98%), oleic acid ($C_{18}H_{34}O_2$, 90%) were purchased from Sigma-Aldrich and used as received without purification.

2.2 Synthesis of $MoSe_2$ and $ReSe_2$ nanomaterials

The selenium powder (Se, 0.559 mmol) or selenourea (CH_4N_2Se, 2.49 mmol) was added into a three-neck round bottom flask containing oleic acid ($C_{18}H_{34}O_2$, 20 ml) at room temperature. The temperature was increased to 220 ºC to thermally reduce the Se to Se^{2-} with the help of the solvent, which also acted as a reducing agent. Once all the Se was reduced, a mixture molybdic acid (H_2MoO_4, 0.15 mmol) or ammonium perrhenate (NH_4ReO_4, 0.186 mmol) and the solvent/surfactant was added into the reaction mixture. The temperature was then raised to 330 ºC and the reaction was run for 120 min. The nanoparticles formed were then washed with ethanol and toluene using a centrifuge and then left to dry.

2.3 Characterization techniques

The phase purity, crystallinity and preferred crystal orientation of the products were examined by using PXRD on a Bruker MeasSrv (D2-205530)/D2-205530 diffractometer using secondary graphite monochromated CoKα radiation (λ 1.78897 Å) at 30 kV/30 mA). Measurements were taken using a glancing angle of incidence detector at an angle of 2°, for 2θ values over 10 - 70° in steps of 0.026° with a step time of 37 s and at a temperature of 25 °C. Raman spectroscopy (J-Y T64000 micro-Raman spectrometer, Horiba Jobin-Yvon, Ltd., Stanmore, UK) equipped with a liquid nitrogen cooled charge coupled device detector. All samples were measured after excitation with a laser wavelength of 514.5 nm. The sample sizes and morphologies were determined by the transmission electron microscopy (TEM) carried out on a FEI Tecnai T12

TEM microscopy operated at an acceleration voltage of 200 kV with a beam spot size of 20 - 100 nm in TEM mode. HRTEM images were obtained from a JEOL JEM-2100 microscopy with a LAB6 filament and an EDS detector, operated at 200 kV. The SEM images were obtained with the high-resolution FEI Nova Nanolab 600 at 30 kV. The total surface area and pore volume of the nanomaterials were ascertained using a Micromeritics TriStar Surface Area and Porosity Analyzer (Micromeritics Instrument Corp., Norcross, GA, USA).

2.4 Electrochemical characterization

The electrochemical measurements were carried out on a BASi epsilon E2 (1231). All measurements were carried out in 0.5 M H_2SO_4 using a three-electrode system. A Ag/AgCl electrode was used as the reference electrode, platinum wire was used as the counter electrode. A modified glassy carbon electrode with 3 mm diameter was used as the working electrode. The ink or fresh dispersion of the sample was prepared by dispersing 5.0 mg of the $MoSe_2$ nanomaterials with 0.5 mg carbon black and 40 µl of nafion solution (5 wt%) in a 1 ml mixture of water and isopropanol at a 3:1 ratio. The solution was then sonicated for 30 min and ~ 5 µl of the ink was drop-casted onto the glassy carbon electrode. The electrode was allowed to dry at room temperature. The linear sweep voltammograms were obtained at a scan rate of 2 mVs^{-1} and the cyclic voltammograms were obtained at a potential range of 0.2 – 0.6 V vs RHE. A 20% Pt/C catalyst was used for comparison. The Impedance spectroscopy studies were conducted on a Biologic SP 300, the measurements were done at a potential of -200 mV vs RHE and it was done at a frequency range between 0.01 Hz and 100 kHz.

3. Results and discussion

Powder X-ray diffraction (PXRD) was used to confirm the synthesis of $MoSe_2$ and $ReSe_2$ nanostructures. PXRD was also used to determine the crystallinity, phase, and composition of the nanostructures. The powder diffraction patterns confirm the formation of $MoSe_2$ (JCPDS card no: 03-065-3999) and $ReSe_2$ (JCPDS card no: 01-065-4275) nanostructures. The diffraction peaks for $MoSe_2$ are shown in **Fig.1(a)** at 14.6°, 37.06°, 44.44°, and 66.0°. These diffraction peaks correspond to the lattice planes (002), (100), (103), (105), and (110). The diffraction peaks for $ReSe_2$ as shown in **Fig.1(b)** are observed at 13.7°, 31.9°, 35.2°, 42.6°, 47.1, and 55.2°. These diffraction peaks correspond to the lattice planes (001), (1-22), (-220), (012), (003) and (1-42). The PXRD analysis shows that the $MoSe_2$ nanostructures have crystallized in the 2H hexagonal phase, and the $ReSe_2$ nanostructures have crystallized in the distorted 1T phase triclinic system with P-1 space group. The (002) peak in the $MoSe_2$

diffractogram arises due to the stacking of the layers into multilayer nanosheets.[20] The same is true for the (001) peak in $ReSe_2$ nanostructures.[21] The appearance of these peaks suggests that the nanostructures consist of few-layered nanosheets and not monolayer sheets.

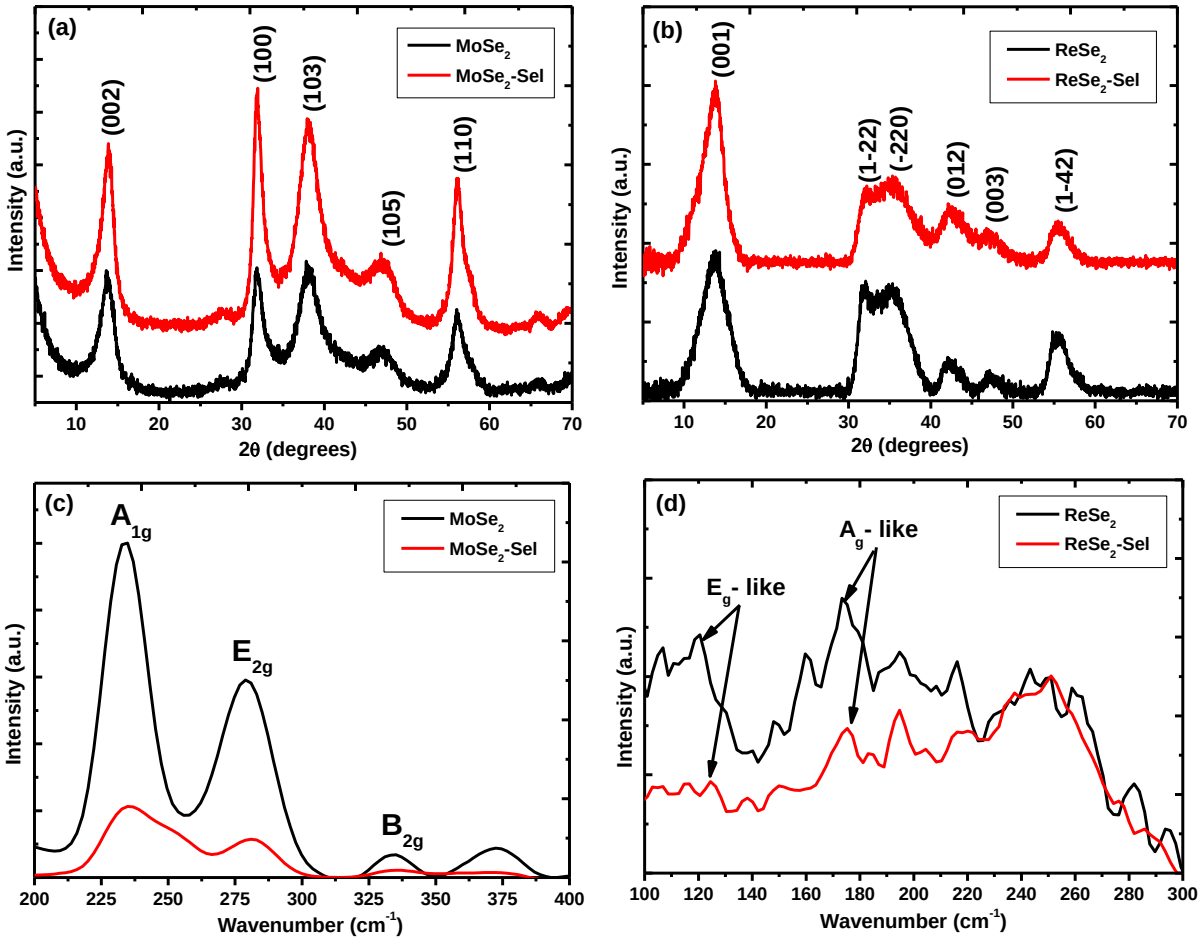


Figure 1: PXRD patterns of (a) $MoSe_2$ nanostructures and (b) $ReSe_2$ nanostructures. Raman spectra of (c) $MoSe_2$ nanostructures, and (d) $ReSe_2$ nanostructures.

The PXRD analysis also indicates that the use of selenourea instead of elemental selenium as the Se precursor does not result in any changes in the phase of the $MoSe_2$ and $ReSe_2$ nanostructures. The diffractograms from the nanostructures synthesized using both Se precursors were matched to the same JCPDS card no. All the peaks identified in the diffractogram of the nanostructures synthesized with elemental selenium were also identified in the nanostructures synthesized using selenourea without any major shifts in the peak positions.

The Raman spectrum of $MoSe_2$ has two main characteristic peaks which are the out of plane A_{1g} and the in-plane E^1_{2g}, the mono or few-layered nanostructures are identified by the shift in the position of these characteristic peaks from their positions in the bulk material which are 242 cm^{-1} and 285 cm^{-1} for A_{1g} and E^1_{2g} respectively.[22] The A_{1g} has red-shifted from the bulk to 237 cm^{-1} as shown in **Fig.1(c)**. The Raman spectrum shows that both peaks have red-shifted from their positions in the bulk material, this confirms that the nanosheets produced are indeed few-layer.[23] There is one other characteristic peak observed in the Raman spectrum, the B^1_{2g} which has been shown to not appear in monolayer nanosheets or in the bulk material. This peak only appears for few-layer nanosheets with a layer number between 2-5 layers. The appearance of the B^1_{2g} peak at ~350 cm^{-1} also confirms that the nanosheets are indeed few-layered.[23] The A_{1g} peak in Raman spectrum of $MoSe_2$ nanostructures synthesized using selenourea ($MoSe_2$-Sel) shows a shoulder peak that appears to have overlapped with the A_{1g}. Upon deconvolution of the A_{1g} peak, the position of the shoulder peak was measured to be at 250 cm^{-1} as shown in **Fig.S1**. This peak has been shown to be due to defects caused by Se vacancies in the $MoSe_2$ nanocrystals.[24] This indicates that using selenourea as a Se precursor introduces more defects into the nanostructures. The Raman spectrum of $ReSe_2$ has been known to be feature rich, having a number of peaks between 100 – 400 cm^{-1} as shown in **Fig.1(d)**. The peaks are non-degenerate and are thought to be caused by the low crystal symmetry of the $ReSe_2$.[25] However, the $ReSe_2$ has two characteristic Raman modes namely the in-plane E_g-like and out-of-plane A_g-like peaks at 124 cm^{-1} and 174 cm^{-1} respectively.[25] However, the characteristic peaks for the in-plane E_g-like and the out-of-plane A_g-like have been observed at 121 cm^{-1} and 175 cm^{-1} respectively. This further confirms the formation of $ReSe_2$ nanostructures as concluded in the PXRD. The analysis is also true for the nanostructures synthesized using selenourea ($ReSe_2$-Sel), the A_g-like and the E_g-like were observed at 124 cm^{-1} and 175 cm^{-1} respectively. The selection of selenourea as a selenium precursor also results in the formation of $ReSe_2$ nanostructures.

Transmission electron microscopy (TEM) was used to determine the morphology of the nanostructures. The TEM images of $MoSe_2$ and $ReSe_2$ are shown in **Fig.2**. The TEM images in **Fig.2(a) and (b)** show the formation of $MoSe_2$ microspheres. These seem to be 3D microspheres with a diameter of 230 +/- 30 nm. The particle size distribution is shown in **Fig.S3**. The edges of the microspheres seem to suggest that $MoSe_2$ nanosheets have grown from the dense central core that is observed from the microspheres. This gives the microspheres an almost flower-like morphology.

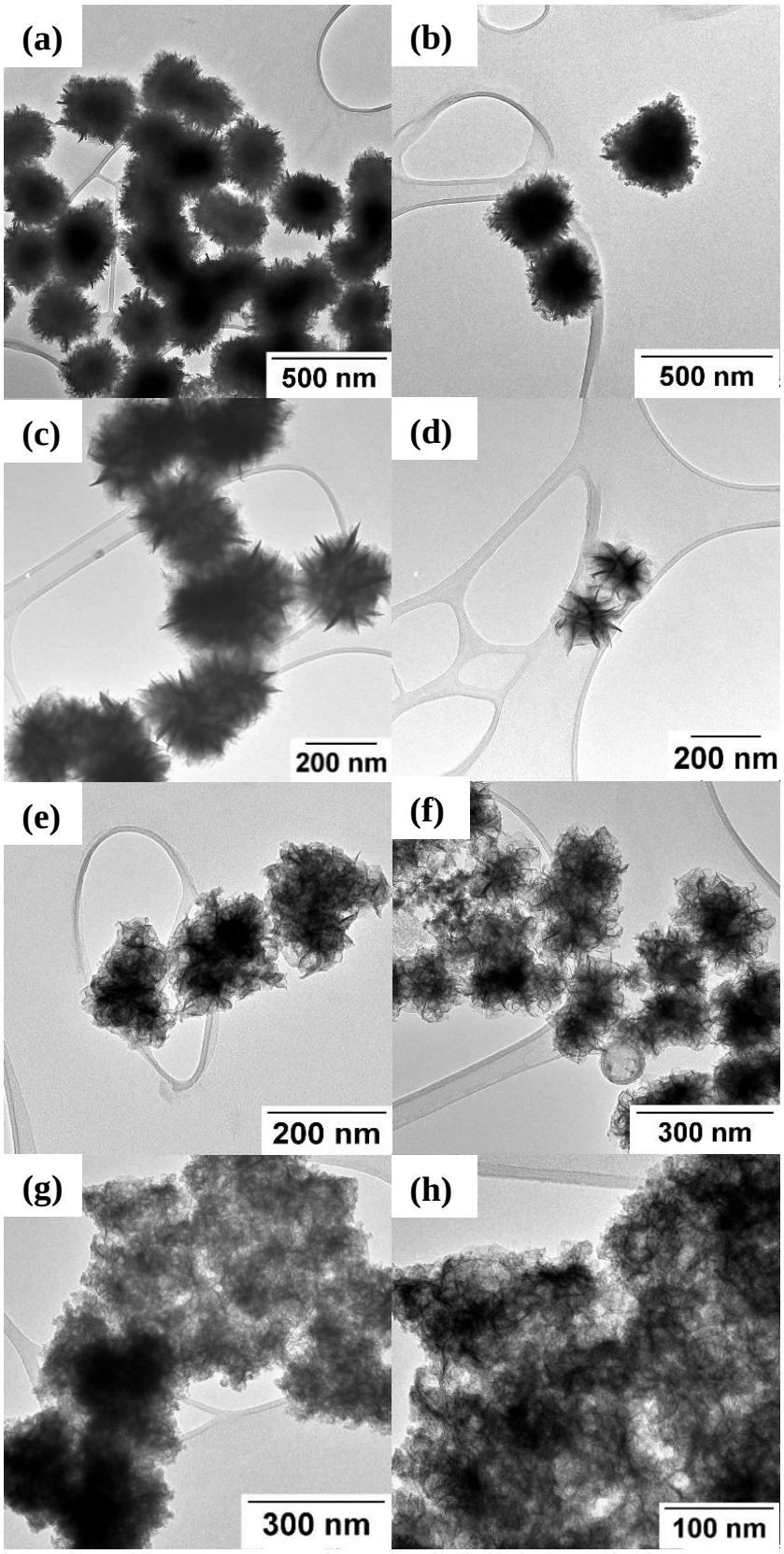


Figure 2: TEM images of (a-b) $MoSe_2$, (c-d) $MoSe_2$-Sel, (e-f) $ReSe_2$, and (g-h) $ReSe_2$-Sel.

The formation of the microspheres can be tracked using TEM by obtaining images of the as-synthesized nanostructures at various stages of the reaction. TEM images of the $MoSe_2$ nanostructures were taken at 15 min, 30 min, 60 min, and 90 min as shown in **Fig.3(a-d)**. The time study shows that the microspheres begin to form quickly after the metal precursor is added, such that the flowers-like nanostructures can be identified 15 min after the reaction has begun (15 min after the metal precursor is added). The formation of these flower-like microspheres has been discussed in a previous publication.[27] The molybdic acid decomposes to form the molybdic anion (MoO_4^{2-}) which acts as the metal monomer which then reacts with the Se^{2-} to form the $MoSe_4^{2-}$ intermediate. This intermediate is then thermally converted to $MoSe_2$ as the Mo (VI) is reduced to Mo (IV).[26-27] This is shown in the PXRD patterns of the nanostructures at the various reaction times, the PXRD pattern at 15 min shows some unidentified peaks which could be due to the intermediate as shown in **Fig.S2(a).** These peaks are phased out 30 min into the reaction.

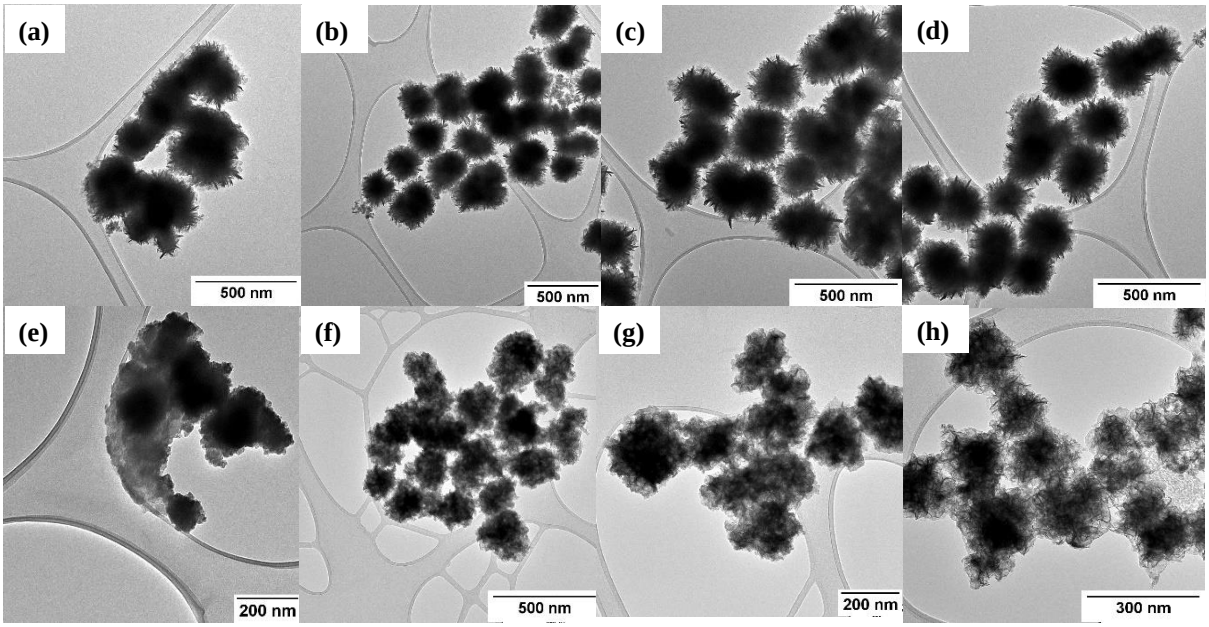


Figure 3: TEM images of the $MoSe_2$ nanostructures at (a) 15 min, (b) 30 min, (c) 60 min, and (d) 90 min. TEM images of the $ReSe_2$ nanostructures at (e) 15 min, (f) 30 min, (g) 60 min, and (h) 90 min.

The use of selenourea as the selenium precursor does not change the morphology of the nanomaterials as they also form flower-like microspheres as shown in **Fig.2(c and d)**. The TEM images of the $ReSe_2$ nanostructures also show that they form into flower-like microspheres as shown in **Fig.2(e)**. The individual nanosheets that comprise that flower-like

microsphere can clearly be observed from the TEM image of the individual nanoflowers at **Fig.2(f)**. The formation of the $ReSe_2$ nanostructures were also tracked using the TEM images of the nanostructures at various reaction times. The TEM images of the $ReSe_2$ nanostructures taken at 15, 30, 60 and 90 min are shown in **Fig.3(e-h)**. The TEM image of the $ReSe_2$ nanostructures sampled at 15 min shown in **Fig.3(e)**, the image shows that the nanostructures begin as a flocculate with dense central cores. As the reaction proceeds, the intermediate is consumed to form the nanosheets that grow from the dense central core. The growth of the flower-like microspheres progresses from 30 to 90 min as shown in **Fig.3(f-h)**. A schematic representation of the process is shown in **Fig.4**.

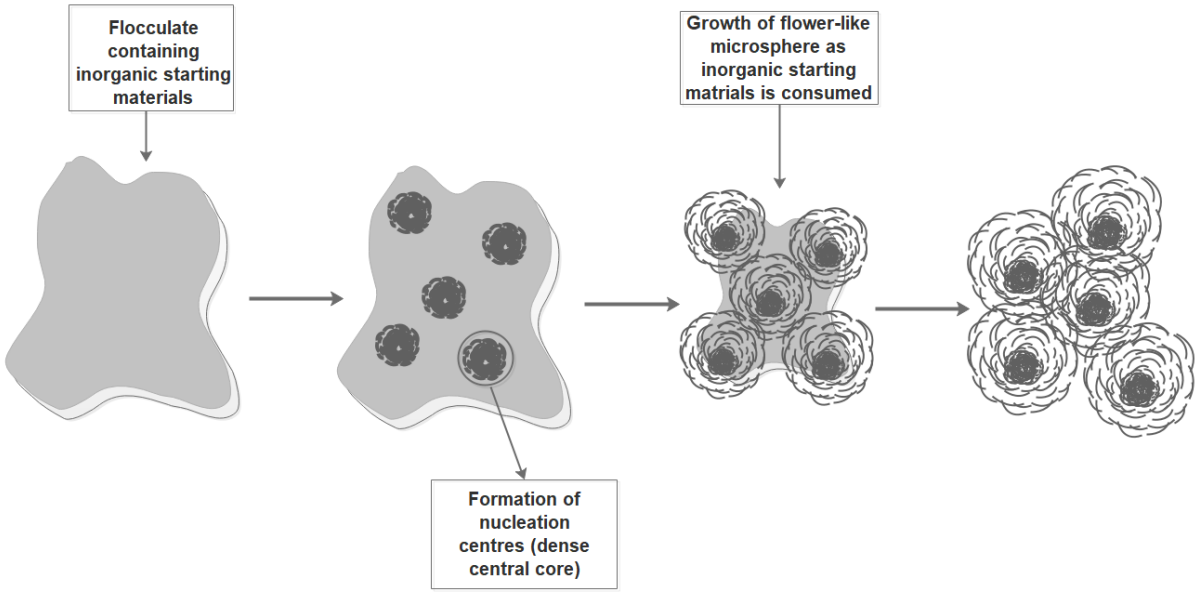


Figure 4: Schematic representation of the formation of flower-like microsphere.

This shows that the synthetic procedure used can reproduce the morphology of the nanostructures. The morphology of the $ReSe_2$ nanostructures also formed flower-like microspheres due to similar choices in the metal precursor. Ammonium perrhenate (NH_4ReO_4) was chosen as the metal precursor because of its similarity to molybdic acid. Specifically, the decomposition of ammonium perrhenate has been shown to result in the formation of ReO_4^{2-}.[21] This indicates that the decomposition of the metal precursor proceeds in the same manner as that of molybdic acid. The decomposition of the ammonium perrhenate forms the ReO_4^{2-} monomer which can react with the Se^{2-} monomer to form the $ReSe_4^{2-}$ intermediate. The intermediate then converts to the $ReSe_2$ as the Re(VI) reduces to Re(IV). The diffractograms for the nanostructures at various time periods are shown on **Fig.S2(b).** However, the use of

selenourea to synthesize the $ReSe_2$ alters the morphology of the nanostructures. The use of selenourea results in the formation of a large area flocculate that is composed of overlapping nanosheets small lateral dimension nanosheets as shown in **Fig.2(g and h)**. The catalytic activity of these nanostructures towards the HER was evaluated using various electrochemical techniques. These methods can be used to determine various key parameters that are used to evaluate the performance of electrocatalysts towards the HER. These parameters include the onset potential, overpotential at 10 mA/cm^2 (η_{10}), Tafel slope, exchange current density (J_0), and the charge transfer resistance (R_{ct}). Linear sweep voltammetry (LSV) is an electrochemical technique where one applies a potential on the working electrode at a certain scan rate and measures the current response. These LSV or polarisation curves can be used to determine the onset potential, overpotential, Tafel slope, and the exchange current density. The polarisation curves of the $MoSe_2$ and $ReSe_2$ nanostructures is shown in **Fig.5(a).**

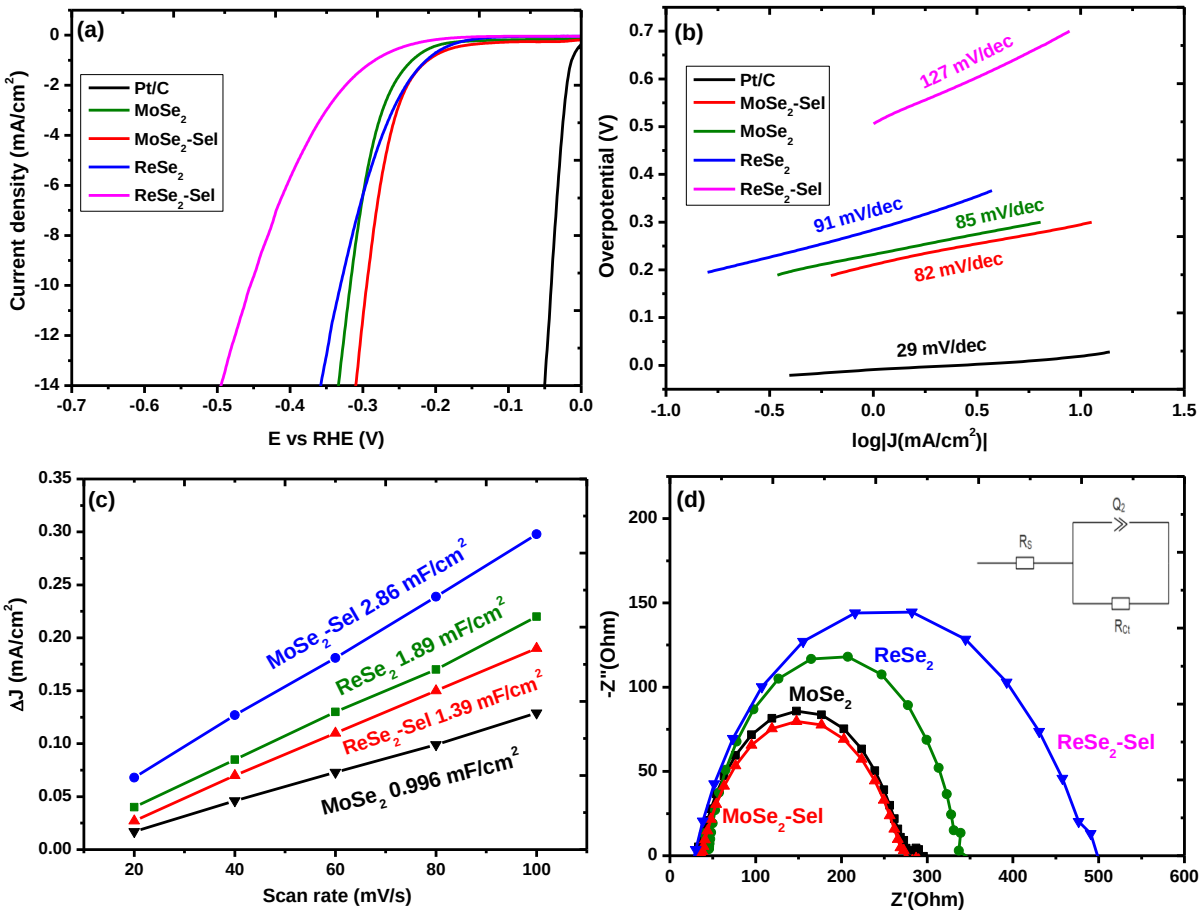


Figure 5: (a) Polarisation curves, (b) Tafel plots, (c) Cdl plots, and (d) Nyquist plots of the $MoSe_2$ and $ReSe_2$ nanostructures.

The first parameter evaluated using the polarisation curves was the onset potential. Which can be defined as the overpotential at which catalytic current is first observed. A low onset potential is ideal as it represents a low overpotential needed to initiate the reaction. The $MoSe_2$ nanostructures had the lowest onset potentials, the $MoSe_2$ and the $MoSe_2$-Sel had an onset potential of 108 mV and 116 mV respectively. The $ReSe_2$ nanostructures had a comparable onset potential of 168 mV, while the $ReSe_2$ synthesized using selenourea had an onset potential that was significantly higher at 220 mV. An interesting observation is that all the nanostructures with a flower-like morphology had comparable onset potential. This trend continues for the rest of the parameters. The overpotential is another crucial property to consider, this parameter is normally reported at a specified current density. The specified current density was 10 mA/cm^2, which is the working current density for the most cost-competitive photoelectrochemical cell (PEC).[28] This is then reported as the overpotential at a current density of 10 mA/cm^2 (η_{10}). The lower the η_{10} the better the performance of the catalyst. The η_{10} of the $MoSe_2$ and $MoSe_2$-Sel was measured to be 319 mV and 294 mV respectively. The η_{10} of the $ReSe_2$ and $ReSe_2$-Sel was measured to be 331 mV and 456 mV respectively. The η_{10} of all the nanostructures were comparable except for that of the $ReSe_2$-Sel which is significantly higher.

The kinetics of the HER is strongly dependent on the electrochemical potential given by the Butler-Volmer (B-V) equations as shown in equation 1.[29]

$$J = J_0(-e^{-\frac{\alpha F\eta}{RT}} + e^{\frac{(1-\alpha)nF\eta}{RT}}) \quad (1)$$

Where J is the current density, J_0 is the exchange current density, α is the charge transfer coefficient, F is Faraday's constant, R is the gas constant, T is the temperature, n is the number of electrons, and η is the overpotential. When the overpotential is sufficiently large ($\eta > 0.05$), the B-V equation can be simplified as the Tafel equation:

$$\eta = a + blogJ = \frac{-2.3RT}{\alpha nF} logJ_0 + \frac{2.3RT}{\alpha nF} logJ \quad (2)$$

The equation shows a linear relationship between the overpotential and logJ, the slope of this equation is defined as the Tafel slope. The Tafel slope can be determined by plotting the Overpotential against logJ, which can be obtained directly from the LSV curves. The Tafel slope can be described as the measure of the sensitivity of the current density to the changes in the overpotential. In HER, the Tafel slope can be used to determine the rate-determining step and the HER reaction pathway. The HER in acidic media has three possible reaction pathways:

(Volmer step) $H_3O^+ + e^- + M \rightleftharpoons M\text{-}H + H_2O$, (3)

(Heyrovsky step) $M\text{-}H + H_3O^+ + e^- \rightleftharpoons H_2 + H_2O + M$, (4)

(Tafel step) $2M\text{-}H \rightleftharpoons H_2 + 2M$, (5)

The initial reaction is the Volmer reaction which involves the adsorption of a proton (H^+) on the surface of the electrode and combination with an electron to form an adsorbed hydrogen atom. The reaction can then proceed either through a desorption step (Heyrovsky step), or a recombination step (Tafel step).[29] The Tafel plots of the nanostructures are shown in **Fig.5(b)**. The Tafel slopes of the $MoSe_2$, $MoSe_2$-Sel, and $ReSe_2$ nanostructures were determined to be 85 mV/dec, 81 mV/dec, and 91 mV/dec respectively. This indicates that the rate-determining step for the HER using these catalysts is the Heyrovsky step which means the reaction proceeds under the Volmer-Heyrovsky pathway. The Tafel slope of the $ReSe_2$-Sel nanostructures was determined to be 127 mV/dec, which indicates that the Volmer step is the rate-determining step for the HER using this catalyst. Another important parameter to evaluate the performance of the catalysts towards the HER is the exchange current density (i_0). The exchange current density can be described as the rate of oxidation and reduction at an equilibrium reaction expressed in terms of current density. The higher the exchange current density, the better the catalyst. The exchange current density of $MoSe_2$, $MoSe_2$-Sel, and $ReSe_2$ was determined to be 0.58 mA/cm^2, 0.61 mA/cm^2, and 0.61 mA/cm^2. The comparable values of the exchange current densities for these materials are not surprising as all the other parameters seems to be comparable as well.[30] However, the exchange current density of the $ReSe_2$-Sel was found to be 0.51 mA/cm^2 which was the lowest recorded exchange current density. This trend is observed in all the other parameters as well. It seems changing the selenium precursor for the synthesis of $ReSe_2$ to selenourea changes the results in a morphology that does not maximise the exposure of the active sites which impairs the catalytic activity.

The electrochemical double layer (C_{dl}) can be used to estimate the electrochemically active surface area (ECSA), this is because the C_{dl} is linearly proportional to the ECSA.[31] The C_{dl} can be determined using cyclic voltammetry (CV), the current response observed in the CV curves in the potential range of 0.2 to 0.6 V vs RHE are shown in **Fig.S4**. The estimation is done by plotting ΔJ (J_a-J_c) vs the scan rate at 0.41 V vs RHE which is shown in **Fig.5(c)**, in this linear plot the slope is the C_{dl}. The ECSA of the $MoSe_2$ and $MoSe_2$-Sel were measured to be 0.998 mF/cm^2 and 2.86 mF/cm^2 respectively. The increase in the ECSA of the $MoSe_2$-Sel was attributed to the introduction of Se vacancies in the structure of the $MoSe_2$ nanostructures. The $ReSe_2$ had an ECSA of 1.85 mF/cm^2. The ECSA of $ReSe_2$-Sel was measured at 1.39 mF/cm^2. The ECSA of the $ReSe_2$-Sel was higher than that of the $MoSe_2$ nanostructures which was

unexpected considering the $MoSe_2$ had superior catalytic activity. These discrepancies may be due to the inability of the C_{dl} to differentiate between the surface area on the basal plane and that of the edge sites and its inability to measure the inherent activity of the active edge sites. The $MoSe_2$ may have a lower ECSA but more catalytically active edge sites. The charge transfer kinetics of the nanostructures was determined using electrochemical impedance spectroscopy (EIS). The EIS results were represented in the form of Nyquist plots which are shown in **Fig.5(d)**. The Nyquist plots were fitted to the equivalent circuit that is shown as an insert in **Fig.5(b)**. Where R_s is the solution resistance, Q_2 is the constant phase element and R_{ct} is the charge transfer resistance. The Nyquist plots have a distinct semi-circle shape but the semi-circles are depressed which is why the constant phase element is used instead of the ideal double-layer capacitor.[32] The R_{ct} which gives information about the charge transfer kinetics for $MoSe_2$ and $MoSe_2$-Sel flower-like nanostructures was found to be 247 Ω and 235 Ω respectively. These values are quite comparable keeping with the trend of the other electrochemical parameters for these materials. The R_{ct} value for the $ReSe_2$ flower-like nanostructures was 286 Ω which is also comparable with the other $MoSe_2$ flower-like nanostructures as expected. The exception was the R_{ct} value of the $ReSe_2$-Sel nanostructures which was found to be 460 Ω. This is in keeping with the other electrochemical parameters which allude to the $ReSe_2$-Sel being the worst performing catalyst which may be due to its different morphology as compared to the other catalysts. [33] A comparison of the catalytic activity of the as-synthesized $MoSe_2$ and $ReSe_2$ nanostructures and their counterparts synthesized with other methods is shown in **Table 1**. The electrochemical characterization of the nanostructures compared was conducted in 0.5 M H_2SO_4.

Table 1: Comparison of the catalytic activity of the as-synthesized $MoSe_2$ and $ReSe_2$ and their literature counterparts

HER catalyst	Synthesis method	η_{10} (mV)	Tafel slope (mV/dec)	Onset potential (mV)	Ref
$MoSe_2$ nanosheets	Hydrothermal	305	69	171	**34**
$MoSe_2$ nanoflowers	CVD	220	61	170	**35**
$MoSe_2$ nanosheets	Colloidal	340	80	182	**27**
$MoSe_2$ nanoflowers	Colloidal	301	73	156	**27**

$MoSe_2$	Colloidal	319	85	108	**This work**
$MoSe_2$-Sel	Colloidal	294	81	102	**This work**
$ReSe_2$ Flower-shaped	CVD	270	76	-	19
$ReSe_2$ nanosheets	colloidal	143	62	-	36
$ReSe_2$ microspheres	Hydrothermal	-	68	80	31
$ReSe_2$	exfoliation	239	138	-	37
$ReSe_2$	Electrochemical treatment	430	130	-	38
$ReSe_2$	Colloidal	331	91	168	**This work**
$ReSe_2$-Sel	Colloidal	456	127	220	**This work**

The catalytic activity of the as-synthesized $MoSe_2$ nanostructures was comparable to the $MoSe_2$ nanostructures synthesized using similar methods. However, the performance was slightly lower than that of $MoSe_2$ nanostructures synthesized using other methods. The performance of the as-synthesized nanostructures was comparable to the performance of the nanostructures synthesized using other methods and in some instances, it performed better. The $MoSe_2$ and $ReSe_2$ nanostructures synthesized in this chapter were used as a baseline, and the performance of the catalysts was improved using various methods in the subsequent chapter as per the aim of this project.

4. Conclusions

In summary, the $MoSe_2$ and $ReSe_2$ nanostructures were successfully synthesized using the colloidal method. The $MoSe_2$ and $ReSe_2$ nanostructures which were synthesized using the same method shared similar structural properties. For instance, the nanostructures of both TMDs formed in a spherical/flower-like morphology. The tracking of the nucleation and growth of the nanostructures showed that the mechanism by which these materials grow is quite similar which is what led to the observed structural similarities. This work demonstrated that the choice of metal precursor can help in forming TMDs with similar properties. A change in the selenium precursor also played a crucial role in determining the properties of the as-synthesized

nanostructures. The use of selenourea as opposed to selenium powder in the synthesis of $MoSe_2$ nanostructures led to the formation of Se vacancies in the structure of the nanostructures. In the synthesis of the $ReSe_2$ nanostructures, the use of selenourea resulted in a change of the morphology of the as-synthesized nanostructures. The $MoSe_2$, $MoSe_2$-Sel, and $ReSe_2$ had comparable catalytic activity towards the HER, while the $ReSe_2$-Sel had much poorer catalytic activity. This indicates that TMDs with similar structural properties may exhibit comparable catalytic activity towards the HER.

5. References

1. Chaves, A.; Azadani, J. G.; Alsalman, H.; da Costa, D. R.; Frisenda, R.; Chaves, A.; Song, S. H.; Kim, Y. D.; He, D.; Zhou, J., Bandgap engineering of two-dimensional semiconductor materials. *npj 2D Mater. Appl.* **2020,** *4* (1), 1-21.

2. Kang, M.; Kim, B.; Ryu, S. H.; Jung, S. W.; Kim, J.; Moreschini, L.; Jozwiak, C.; Rotenberg, E.; Bostwick, A.; Kim, K. S., Universal mechanism of band-gap engineering in transition-metal dichalcogenides. *Nano lett.* **2017,** *17* (3), 1610-1615.

3. Singh, S.; Deb, J.; Sarkar, U.; Sharma, S., $MoSe_2$ crystalline nanosheets for room-temperature ammonia sensing. *ACS Appl. Nano Mater.* **2020,** *3* (9), 9375-9384.

4. Wu, Y.-C.; Liu, W.-R., Few-layered $MoSe_2$ ultrathin nanosheets as anode materials for lithium ion batteries. *J. Alloys Compd.* **2020,** *813*, 152074.

5. Akama, T.; Okita, W.; Nagai, R.; Li, C.; Kaneko, T.; Kato, T., Schottky solar cell using few-layered transition metal dichalcogenides toward large-scale fabrication of semitransparent and flexible power generator. *Sci. Rep.* **2017,** *7* (1), 1-10.

6. Tian, S.; Tang, Q., Activating transition metal dichalcogenide monolayers as efficient electrocatalysts for the oxygen reduction reaction via single atom doping. *J. Mater. Chem. C* **2021,** *9* (18), 6040-6050.

7. Zurutuza, A.; Marinelli, C., Challenges and opportunities in graphene commercialization. *Nat. Nanotechnol.* ***2014,*** *9 (10), 730-734.*

8. Millard, T. S.; Genco, A.; Alexeev, E. M.; Randerson, S.; Ahn, S.; Jang, A.-R.; Shin, H. S.; Tartakovskii, A. I., Large area chemical vapour deposition grown transition metal dichalcogenide monolayers automatically characterized through photoluminescence imaging. *npj 2D Mater. Appl.* **2020,** *4* (1), 1-9.

9. Mandyam, S. V.; Kim, H. M.; Drndić, M., Large area few-layer TMD film growths and their applications. *J. Physics: Materials* **2020,** *3* (2), 024008.

10. Zhang, L.; Chen, C.; Zhou, J.; Yang, G.; Wang, J.; Liu, D.; Chen, Z.; Lei, W., TMD Nanosheets: Solid Phase Exfoliation for Producing Dispersible Transition Metal Dichalcogenides Nanosheets. *Adv. Funct. Mater.* **2020,** *30* (45), 2070294.

11. Coogan, Á.; Gun'ko, Y. K., Solution-based "bottom-up" synthesis of group VI transition metal dichalcogenides and their applications. *Mater. Adv.* **2021**.

12. Zhang, X.; Ma, G.; Wang, J., Hydrothermal synthesis of two-dimensional MoS_2 and its applications. *Tungsten* **2019,** *1* (1), 59-79.

13. Sun, Y.; Terrones, M.; Schaak, R. E., Colloidal Nanostructures of Transition-Metal Dichalcogenides. *Acc. Chem. Res.* **2021,** *54* (6), 1517-1527.

14 van der Stam, W.; Akkerman, Q. A.; Ke, X.; van Huis, M. A.; Bals, S.; de Mello Donega, C., Solution-Processable Ultrathin Size-and Shape-Controlled Colloidal Cu_2–xS Nanosheets. *Chem. Mater.* **2014,** *27* (1), 283-291.

15. Jeong, S.; Yoo, D.; Jang, J.-t.; Kim, M.; Cheon, J., Well-defined colloidal 2-D layered transition-metal chalcogenide nanocrystals via generalized synthetic protocols. *J. Am. Chem. Soc.* **2012,** *134* (44), 18233-18236.

16. Geisenhoff, J.Q.; Tamura, A.K.; Schimpf, A. Using ligands to control reactivity, size and phase in the colloidal synthesis of WSe_2 nanocrystals. *Chem. Commun.* **2019**, *55*, 8856–8859.

17. Zhang, C.; Chen, X.; Peng, Z.; Fu, X.; Lian, L.; Luo, W.; Zhang, J.; Li, H.; Wang, Y.; Zhang, D., Phosphine-free synthesis and shape evolution of $MoSe_2$ nanoflowers for electrocatalytic hydrogen evolution reactions. *CrystEngComm* **2018,** *20* (18), 2491-2498.

18. Mao, B.; Bao, T.; Yu, J.; Zheng, L.; Qin, J.; Yin, W.; Cao, M., One-pot synthesis of $MoSe_2$ hetero-dimensional hybrid self-assembled by nanodots and nanosheets for electrocatalytic hydrogen evolution and photothermal therapy. *Nano Res.* **2017,** *10* (8), 2667-2682.

19. Jiang, S.; Zhang, Z.; Zhang, N.; Huan, Y.; Gong, Y.; Sun, M.; Shi, J.; Xie, C.; Yang, P.; Fang, Q., Application of chemical vapor–deposited monolayer $ReSe_2$ in the electrocatalytic hydrogen evolution reaction. *Nano Res.* **2018,** *11* (4), 1787-1797.

20. Gao, M.-R.; Chan, M. K.; Sun, Y., Edge-terminated molybdenum disulfide with a 9.4-Å interlayer spacing for electrochemical hydrogen production. *Nature communications* **2015,** *6*, 7493, 1-8.

21. Li, J.; Zhou, Q.; Yuan, C.; Cheng, P.; Hu, X.; Huang, W.; Gao, X.; Wang, X.; Jin, M.; Nötzel, R., Direct growth of vertically aligned $ReSe_2$ nanosheets on conductive electrode for electro-catalytic hydrogen production. *J. Colloid Interface Sci.* **2019,** *553*, 699-704.

22. Niu, L.; Li, K.; Zhen, H.; Chui, Y. S.; Zhang, W.; Yan, F.; Zheng, Z., Salt-Assisted High-Throughput Synthesis of Single-and Few-Layer Transition Metal Dichalcogenides and Their Application in Organic Solar Cells. *Small* **2014,** *10* (22), 4651-4657.

23. Tonndorf, P.; Schmidt, R.; Böttger, P.; Zhang, X.; Börner, J.; Liebig, A.; Albrecht, M.; Kloc, C.; Gordan, O.; Zahn, D. R., Photoluminescence emission and Raman response of monolayer MoS_2, $MoSe_2$, and WSe_2. *Opt. express* **2013,** *21* (4), 4908-4916.

24. Mahjouri-Samani, M.; Liang, L.; Oyedele, A.; Kim, Y.-S.; Tian, M.; Cross, N.; Wang, K.; Lin, M.-W.; Boulesbaa, A.; Rouleau, C. M., Tailoring vacancies far beyond intrinsic levels changes the carrier type and optical response in monolayer $MoSe_{2-x}$ crystals. *Nano lett.* **2016,** *16* (8), 5213-5220.

25. Jariwala, B.; Voiry, D.; Jindal, A.; Chalke, B. A.; Bapat, R.; Thamizhavel, A.; Chhowalla, M.; Deshmukh, M.; Bhattacharya, A., Synthesis and characterization of ReS_2 and $ReSe_2$ layered chalcogenide single crystals. *Chem. Mater.* **2016,** *28* (10), 3352-3359.

26. Ghosh, S.; Srivastava, C.; Nath, S.; Celis, J.-P., Simple formation of nanostructured molybdenum disulfide thin films by electrodeposition. *Int. J. Electrochem* **2013,** *2013, 1-8*.

27. Ndala, Z.; Shumbula, N.; Nkabinde, S.; Kolokoto, T.; Nchoe, O.; Shumbula, P.; Tetana, Z. N.; Linganiso, E. C.; Gqoba, S. S.; Moloto, N., Evaluating the Effect of Varying the Metal Precursor in the Colloidal Synthesis of $MoSe_2$ Nanomaterials and Their Application as Electrodes in the Hydrogen Evolution Reaction. *Nanomaterials* **2020,** *10* (9), 1786.

28. Zeng, M.; Li, Y., Recent advances in heterogeneous electrocatalysts for the hydrogen evolution reaction. *J. Mater. Chem. A* **2015,** *3* (29), 14942-14962.

29. Fang, Y.-H.; Liu, Z.-P., Tafel kinetics of electrocatalytic reactions: from experiment to first-principles. *ACS Catalysis* **2014,** *4* (12), 4364-4376.

30. Jaramillo, T. F.; Jørgensen, K. P.; Bonde, J.; Nielsen, J. H.; Horch, S.; Chorkendorff, I., Identification of active edge sites for electrochemical H_2 evolution from MoS2 nanocatalysts. *science* **2007,** *317* (5834), 100-102.

31. Qi, F.; Wang, X.; Zheng, B.; Chen, Y.; Yu, B.; Zhou, J.; He, J.; Li, P.; Zhang, W.; Li, Y., Self-assembled chrysanthemum-like microspheres constructed by few-layer $ReSe_2$ nanosheets as a highly efficient and stable electrocatalyst for hydrogen evolution reaction. *Electrochimica Acta* **2017,** *224*, 593-599.

32. Liu, X.; Liu, L.; Wu, Y.; Wang, Y.; Yang, J.; Wang, Z., Rosette-like MoS_2 nanoflowers as highly active and stable electrodes for hydrogen evolution reactions and supercapacitors. *RSC advances* **2019,** *9* (24), 13820-13828.

33. Henckel, D. A.; Lenz, O. M.; Krishnan, K. M.; Cossairt, B. M., Improved HER catalysis through facile, aqueous electrochemical activation of nanoscale WSe_2. *Nano letters* **2018,** *18* (4), 2329-2335.

34. Masurkar, N.; Thangavel, N. K.; Arava, L. M. R., CVD-grown $MoSe_2$ nanoflowers with dual active sites for efficient electrochemical hydrogen evolution reaction. *ACS appl. Mater. Interfaces* **2018,** *10* (33), 27771-27779.

35. Zhang, L.; Wang, T.; Sun, L.; Sun, Y.; Hu, T.; Xu, K.; Ma, F., Hydrothermal synthesis of 3D hierarchical $MoSe_2$/$NiSe_2$ composite nanowires on carbon fiber paper and their enhanced electrocatalytic activity for the hydrogen evolution reaction. *J. Mater. Chem A.* **2017,** *5* (37), 19752-19759.

36. Kwon, I. S.; Kwak, I. H.; Ju, S.; Kang, S.; Han, S.; Park, Y. C.; Park, J.; Park, J., Adatom Doping of Transition Metals in $ReSe_2$ Nanosheets for Enhanced Electrocatalytic Hydrogen Evolution Reaction. *ACS nano* **2020,** *14* (9), 12184-12194.

37. Wang, R.; Han, J.; Xu, P.; Gao, T.; Zhong, J.; Wang, X.; Zhang, X.; Li, Z.; Xu, L.; Song, B., Dual-Enhanced Doping in $ReSe_2$ for Efficiently Photoenhanced Hydrogen Evolution Reaction. *Adv. Sci.* **2020,** *7* (9), 2000216.

38. Luxa, J.; Marvan, P.; Lazar, P.; Sofer, Z., Chalcogenide vacancies drive the electrocatalytic performance of rhenium dichalcogenides. *Nanoscale* **2019,** *11* (31), 14684-14690.

6. Supplementary information

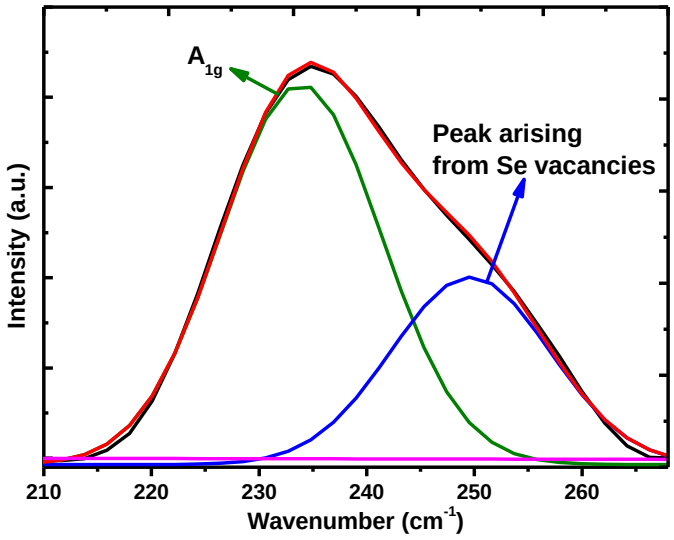


Figure S1: Deconvoluted A_{1g} peak from the Raman spectrum of $MoSe_2$-Sel.

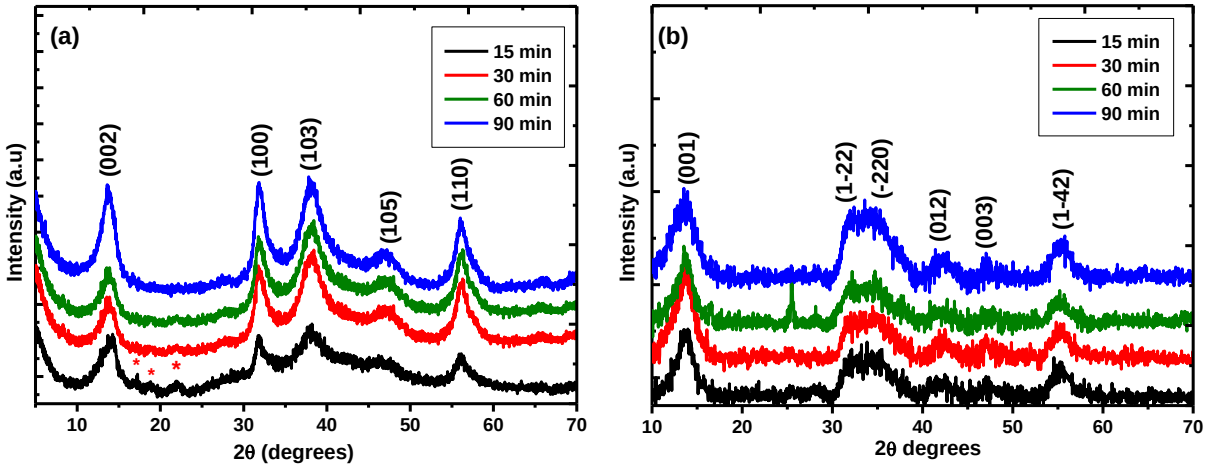


Figure S2: Powder XRD patterns of the $MoSe_2$ and $ReSe_2$ at 15 min, 30 min, 60 min, and 90 min (d).

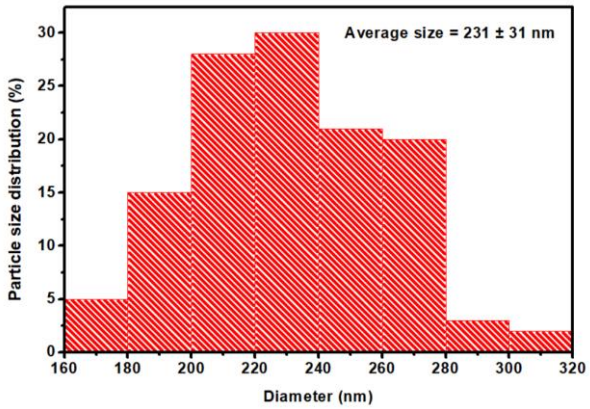


Figure S3: Particle size distribution histogram for flower-like $MoSe_2$ microspheres at 90 min.

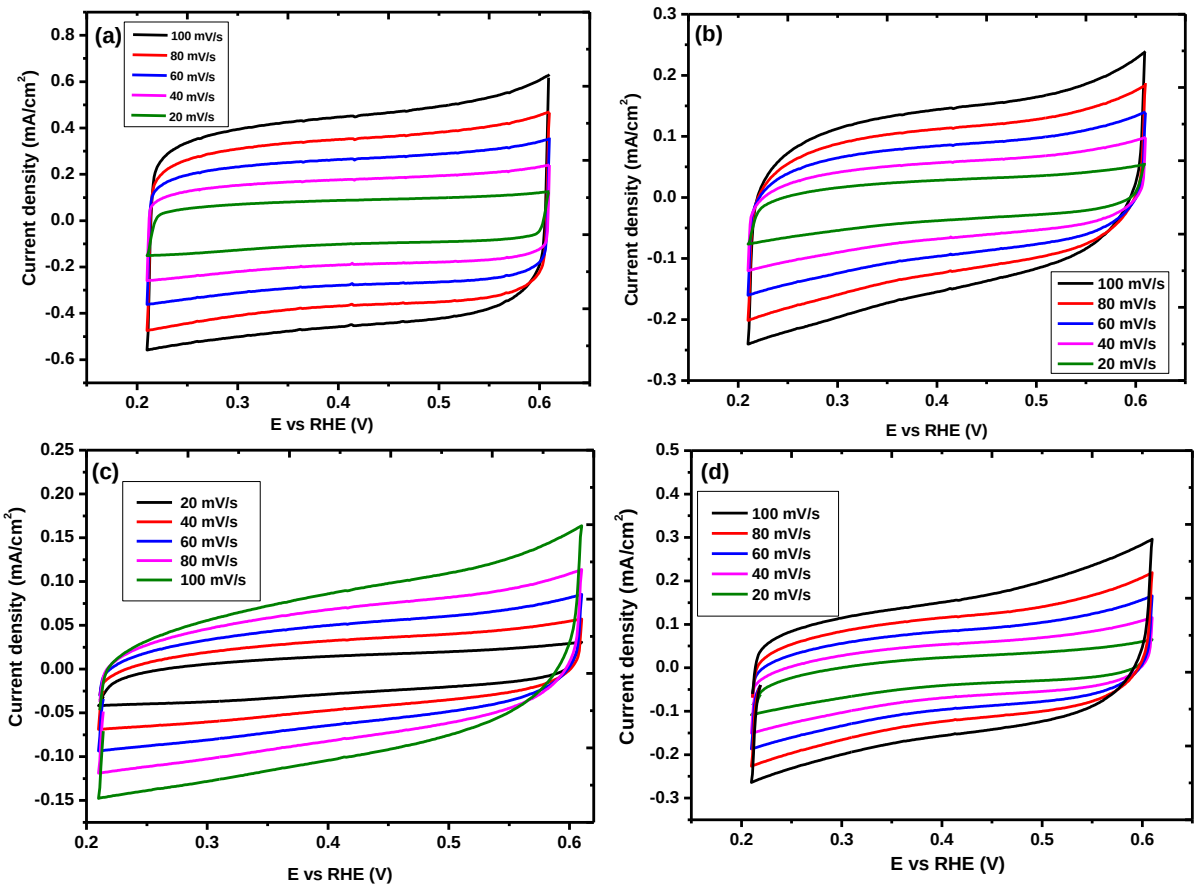


Figure S4: CV curves of (a) $MoSe_2$, (b) $MoSe_2$-Sel, $ReSe_2$, and (d) $ReSe_2$-Sel.

Chapter 4: Exploring the electrocatalytic activity of pristine and electrochemically activated $SnSe_2$ nanoplates for the hydrogen evolution reaction

1. Introduction

Transition metal dichalcogenides (TMDs) have been widely explored as potential electrocatalysts for the hydrogen evolution reaction. The hydrogen evolution reaction (HER) is the electrocatalytic reaction used to produce hydrogen gas, which can be used as a clean (low polluting) energy carrier.[1] The 2D materials have been explored as potential replacements to platinum as the electrocatalyst in HER, due to the expensive and scarce nature of the precious metal which renders it commercially unfavorable.[2-3] There are various TMDs that have been extensively studied for HER application with very promising results, these include MoS_2, $MoSe_2$, VS_2, and NbS_2.[4-7] Much of the work has thus far focused on improving the catalytic performance of TMDs, this has been attempted through increasing the number of active sites, using the more conductive 1T polymorph instead of the semiconducting 2H, making carbon composites that increase the conductivity, and electrochemical activation.[8-11] However, this level of attention has not been extended to group IVA chalcogenides. Notable among these is $SnSe_2$ whose structural and electronic properties have been studied for use in dye-sensitized solar cells, photocatalysis, and battery applications.[12-14] It is also worth noting that there have been several computational studies that have been conducted in evaluating the possible application of group IVA TMD nanostructures including $SnSe_2$ in HER.[15-17] Inamdar *et al.* have investigated the possible use of pristine and alkali metal doped $SnSe_2$. They have discovered that the favorable sites for hydrogen adsorption in $SnSe_2$ are the edge sites, their studies have also suggested that doping with alkali metals such as calcium can drastically improve the catalytic activity of $SnSe_2$ towards the HER.[15]

In this work, the electrochemical performance of colloidally synthesized $SnSe_2$ nanostructures towards the HER has been evaluated in order to bridge the knowledge gap between the computational studies and the experimental work. To improve its catalytic performance, electrochemical activation was performed. Electrochemical activation through proton intercalation has been shown to result in a drastic improvement in the catalytic activity of

TMDs towards the HER.[18-19] This phenomenon has been reported in various TMDs but to our knowledge, this work is the first time it is reported for $SnSe_2$ nanostructures.

2. Experimental

2.1 Materials

Tin(IV) chloride ($SnCl_4$, 98%), selenium powder (Se, 99.99%) and oleylamine (70%) were purchased from Sigma Aldrich and used as received without purification.

2.2 Synthesis of $SnSe_2$ nanoplates

Selenium powder (0.051 mmol) was added into the three-neck round bottom flask containing the solvent/surfactant (20 mL) at room temperature. The temperature was increased to 220 °C to thermally reduce the Se to Se^{2-} with the help of the solvent, which also acts as a reducing agent. Once all the Se was reduced, $SnCl_4$ (0.017 mmol) was added to the reaction mixture. The temperature was then raised to 300 °C and the reaction was run for 60 min. The nanoparticles formed were then washed with ethanol and toluene and then left to dry at room temperature.

2.3 Characterization

The phase purity, crystallinity, and preferred crystal orientation of the products were examined by using PXRD on a Bruker MeasSrv (D2-205530)/D2-205530 diffractometer using secondary graphite monochromated CuKα radiation (λ 1.5406 Å) at 30 kV/10 mA). Measurements were taken using a glancing angle of incidence detector at an angle of 2°, for 2θ values over 10 - 70° in steps of 0.026° with a step time of 37 s and at a temperature of 25 °C. The crystallite size was determined using the DIFFRACT.EVA V6 software. The Raman spectra were obtained using the MacroRAM (Horiba Jobin-Yvon, Ltd., Stanmore, UK) spectrophotometer which was fitted with a CCD detector that was cooled at -50 °C. All samples were measured after excitation with a laser wavelength of 785 nm. The XPS measurements were obtained using a Thermo ESCAlab 250Xi with Al kα photon source (1486.7 eV). The sample morphology was determined using transmission electron microscopy (TEM) carried out on an FEI Tecnai T12 TEM microscope operated at an acceleration voltage of 120 kV with a beam spot size of 20 - 100 nm in TEM mode**.** The SEM images were obtained using a Carl Zeiss mA 10 high-vacuum microscope, the SEM was operated at 20 keV.

2.4 Electrochemical characterization

The electrochemical measurements were carried out on a BASi Epsilon E2 (1231). All measurements were carried out in 0.5 M H_2SO_4 using a three-electrode system. A Ag/AgCl electrode was used as the reference electrode, a platinum wire was used as the counter electrode. A modified glassy carbon electrode with 3 mm diameter was used as the working electrode. The ink or fresh dispersion of the sample was prepared by dispersing 5.0 mg of the $SnSe_2$ nanomaterials with 0.5 mg carbon black and 40 µl of Nafion solution (5 wt%) in a 1 ml mixture of water and isopropanol at a 3:1 ratio. The solution was then sonicated for 30 min and ~ 5 µl of the ink was drop-casted onto the glassy carbon electrode. The electrode was allowed to dry at room temperature. The linear sweep voltammograms were obtained at a scan rate of 2 mVs^{-1} and the cyclic voltammograms were obtained at a potential range of 0.2 – 0.5 V vs RHE at 100 mVs^{-1}. A 20% Pt/C catalyst was used for comparison. The Impedance spectroscopy studies were conducted on a Biologic SP 300, the measurements were done at a potential of -200 mV vs RHE and a frequency range between 0.1 Hz and 100 kHz. The PXRD and Raman spectroscopy of the electrochemically activated $SnSe_2$ was obtained by depositing the ink on a 1 cm x 1 cm glassy carbon substrate to create the working electrode. After 1000 LSV scans were conducted on the working electrode, the PXRD diffractogram and Raman spectrum of the electrochemically activated $SnSe_2$ nanostructures were obtained.

3. Results and discussion

The phase, composition, and crystallinity of the $SnSe_2$ nanostructures were confirmed using powder X-ray diffraction (PXRD). The powder diffractogram of the $SnSe_2$ nanostructures is shown in **Fig.1(a)**. The powder diffraction pattern confirms the formation of $SnSe_2$ nanostructures (JCPDS card no: 01-089-0340). The $SnSe_2$ crystallized in a hexagonal unit cell and a P-3m1 space group. The intense peak found at $2\theta \approx 14°$, corresponds to the (001) lattice plane and is associated with the growth of the crystal along the c-axis. This indicates that multi-layer $SnSe_2$ nanostructures were formed as opposed to monolayer nanostructures.[20] Raman spectroscopy was also used to investigate the structural properties of the $SnSe_2$ nanostructures. The typical Raman spectrum of $SnSe_2$ has two characteristic peaks, the in-plane E_g vibrational mode, and the out-of-plane A_{1g} vibrational mode. The Raman spectrum of the synthesized $SnSe_2$ nanostructures is shown in **Fig.1(b)**. The spectrum shows the A_{1g} peak at 181 cm^{-1} and the E_g peak at 115 cm^{-1}. This confirms the formation of $SnSe_2$ nanostructures. The position of the E_g can offer information about the polytype of the $SnSe_2$ (2H or 1T). For 2H-$SnSe_2$ the position of the E_g is located at approximately 108 cm^{-1}. The position of the E_g peak is normally

located at approximately 118 cm^{-1} for 1T-$SnSe_2$.[20] The E_g peak for the as-synthesized $SnSe_2$ was located at 115 cm^{-1} which suggests that the nanomaterials crystallized in the 1T polytype.

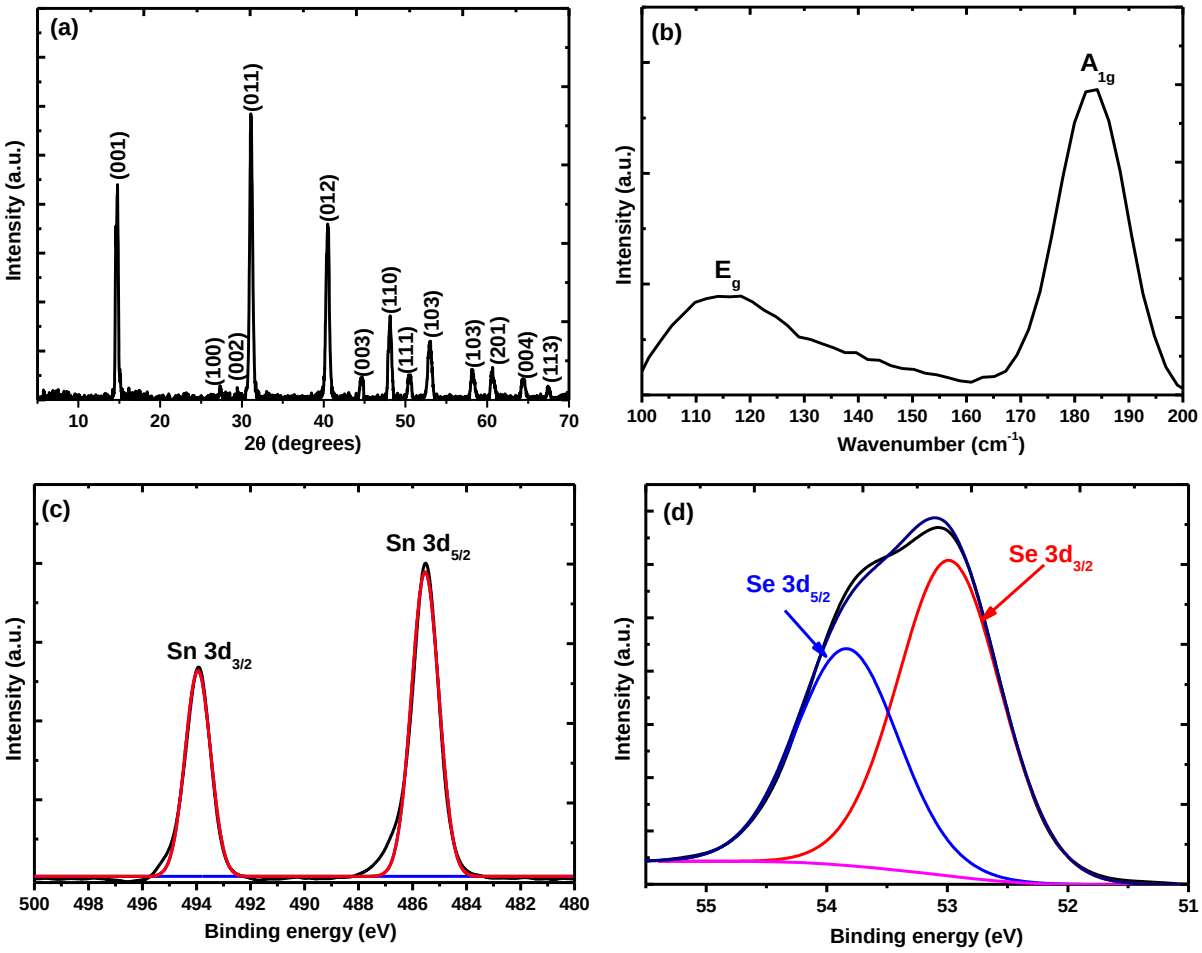


Figure 1: (a) PXRD patterns of $SnSe_2$ nanomaterials and (b) Raman spectrum of $SnSe_2$ nanomaterials. High resolution XPS spectra of (c) Sn 3d state and (d) Se 3d state.

X-ray photoelectron spectroscopy (XPS) was used to evaluate the bonding configuration and elemental composition of the $SnSe_2$ nanostructures. The peaks of interest for Sn 3d and Se 3d are shown in **Fig.1(c) and (d)**, respectively. The characteristic peak of Sn (IV) which are Sn $3d_{3/2}$ and Sn $3d_{5/2}$ are located at 493.9 eV and 485.5 eV, respectively.[21] This shows that Sn is in the Sn^{4+} state. The characteristic peaks of Se which are Se $3d_{3/2}$ and Se $3d_{5/2}$ are located at 53.8 eV and 53.0 eV, respectively.[21] The two characteristic peaks correspond to the $3d_{5/2}$ and $3d_{3/2}$ core level peaks of Se^{2-}. The analysis of the XPS spectrum shows the formation of $SnSe_2$ nanostructures. Electron microscopy was used to further analyze the structure and morphology of the $SnSe_2$ nanostructures. The TEM and SEM images of $SnSe_2$ are shown in **Fig.2(a) and (b)**, respectively. The TEM and SEM images show that the $SnSe_2$ nanostructures have formed

into nanoplates of various shapes. The images show the formation of 2D hexagonal nanoplates, along with semi-spherical nanoplates.

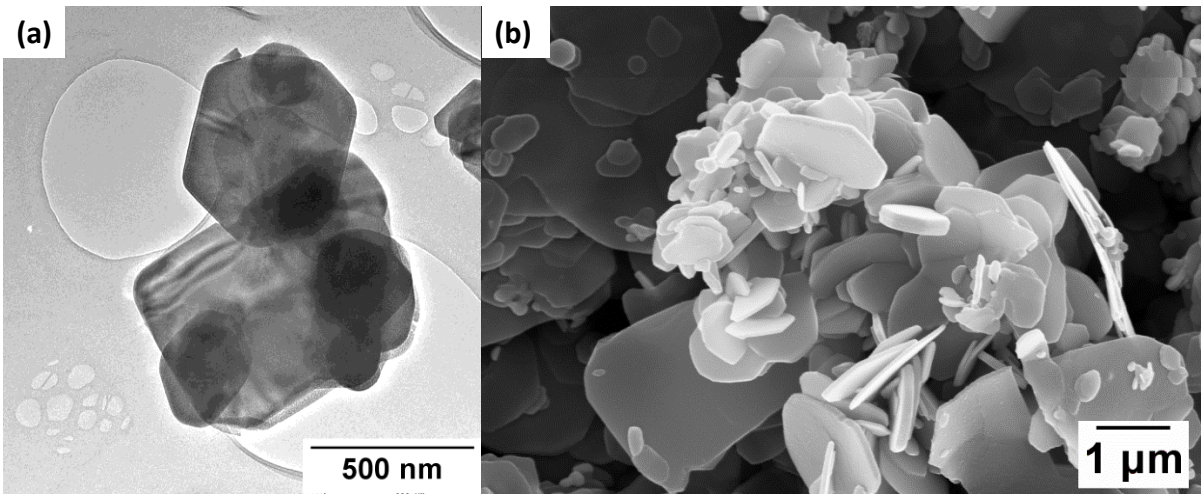


Figure 2: TEM (a) and SEM (b) images of $SnSe_2$ nanostructures.

The electrocatalytic performance of the $SnSe_2$ nanoplates towards the HER was investigated using various electrochemical methods. Linear sweep voltammetry (LSV) was used to determine some of the crucial parameters used in evaluating electrocatalyst performance in the HER. A Pt/C electrocatalyst which is the best performing commercial catalyst for HER was used as a standard and reference catalyst. The LSV or polarisation curves of the $SnSe_2$ nanoplates are shown in **Fig.3(a)**.

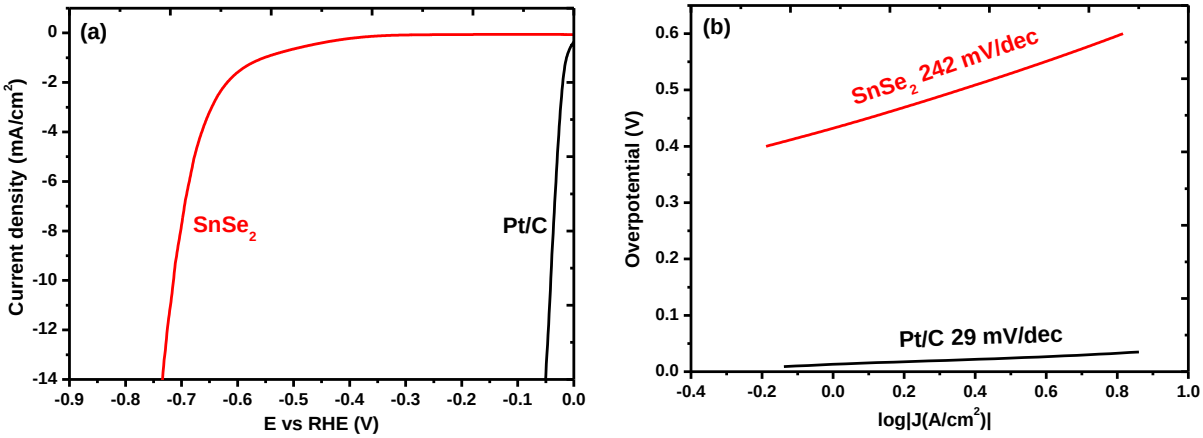


Figure 3: (a) Polarisation curves of $SnSe_2$ nanoplates and Pt/C. (b) Tafel plots of $SnSe_2$ nanoplates and Pt/C.

This LSV curve was used to determine the onset potential and overpotential at 10 mA/cm^2 (η_{10}). The onset potential which is the potential at which catalytic current is first observed was measured to be 390 mV. The catalyst can also be evaluated by determining the overpotential needed to reach a specified current density, the current that is normally used is 10 mA/cm^2

which is the operating current density for a cost-competitive photoelectrochemical cell.[22] The overpotential of the $SnSe_2$ nanoplates was measured to be 618 mV. The Tafel plot shown in **Fig.3(c)** provides the Tafel slope and the means to determine the exchange current density. The kinetics of the HER are strongly dependant on the electrochemical potential given by the Butler-Volmer (B-V) equations as shown in equation 1.[23]

$$J = J_0(-e^{-\frac{\alpha F\eta}{RT}} + e^{\frac{(1-\alpha)nF\eta}{RT}}) \quad (1)$$

Where J is the current density, J_0 is the exchange current density, α is the charge transfer coefficient, F is Faraday's constant, R is the gas constant, T is the temperature, n is the number of electrons, and η is the overpotential. When the overpotential is sufficiently large ($\eta > 0.05$), the B-V equation can be simplified as the Tafel equation:

$$\eta = a + blogJ = \frac{-2.3RT}{\alpha nF} logJ_0 + \frac{2.3RT}{\alpha nF} logJ \quad (2)$$

The equation shows a linear relationship between the overpotential and logJ, the slope of this equation is defined as the Tafel slope. The Tafel slope can be determined by plotting the overpotential against logJ. The Tafel slope can be used to determine the rate-determining step and the HER reaction pathway.[23] The HER in acidic media has three possible reaction pathways:

(Volmer step) $H_3O^+ + e^- + M \rightleftharpoons M\text{-}H + H_2O$, (3)

(Heyrovsky step) $M\text{-}H + H_3O^+ + e^- \rightleftharpoons H_2 + H_2O + M$, (4)

(Tafel step) $2M\text{-}H \rightleftharpoons H_2 + 2M$, (5)

The initial reaction is the Volmer reaction which involves the adsorption of a proton (H^+) on the surface of the electrode and combination with an electron to form an adsorbed hydrogen atom. The reaction can then proceed either through a desorption step (Heyrovsky step), or a recombination step (Tafel step). The Tafel slope was obtained from the Tafel plot (over-potential vs log |current density|) which was obtained by replotting the LSV curve. The Tafel slope of the $SnSe_2$ was determined to be 242 mV/dec which suggests that the Volmer step is the rate-determining step. The exchange current density (J_0) is an important kinetic parameter that is used to evaluate the performance of the electrocatalyst. It represents the rate of electron transfer at zero overpotential and is represented in the form of current density. The exchange current density can be determined from the Tafel plot by using the Tafel equation ($logJ_o=a$), where a is the intercept of the Tafel plot. The higher the exchange current density, the better the catalytic performance.[24] The exchange current density of the $SnSe_2$ was determined to be 0.297 mA/cm^2. The stability of the nanostructures was evaluated by running a 1000 continuous LSV scans. The polarisation curves show that the catalytic activity of the nanostructures

drastically increases over repeated LSV scans. An LSV scan was recorded after every 200 scans. The onset potential and overpotential of the $SnSe_2$ nanoplates decreases drastically over the first 400 LSV scans, the decrease then stabilizes between 800 to a 1000 LSV scans. The chronoamperometry profile of the $SnSe_2$ nanoplates is shown **Fig.4(b)**. The applied potential was 620 mV vs RHE which is the overpotential required to reach 10 mA/cm^2 for this catalyst that was determined using the initial polarization curve. When the constant potential was applied, the current density rapidly increased. The increase in the current density can be observed even after 10 hrs as shown in **Fig.S1**. The drastic increase in current density under a constant overpotential further confirms the activation of the $SnSe_2$ nanoplates towards HER over time.[11] These observations indicate that the $SnSe_2$ is electrochemically activated after continuous LSV scans. The electrocatalytic parameters for evaluating the $SnSe_2$ nanoplates were recorded after a 1000 LSV scans (after electrochemical activation). Therefore, the parameter measurements were for the electrochemically activated $SnSe_2$ nanoplates (A-$SnSe_2$).

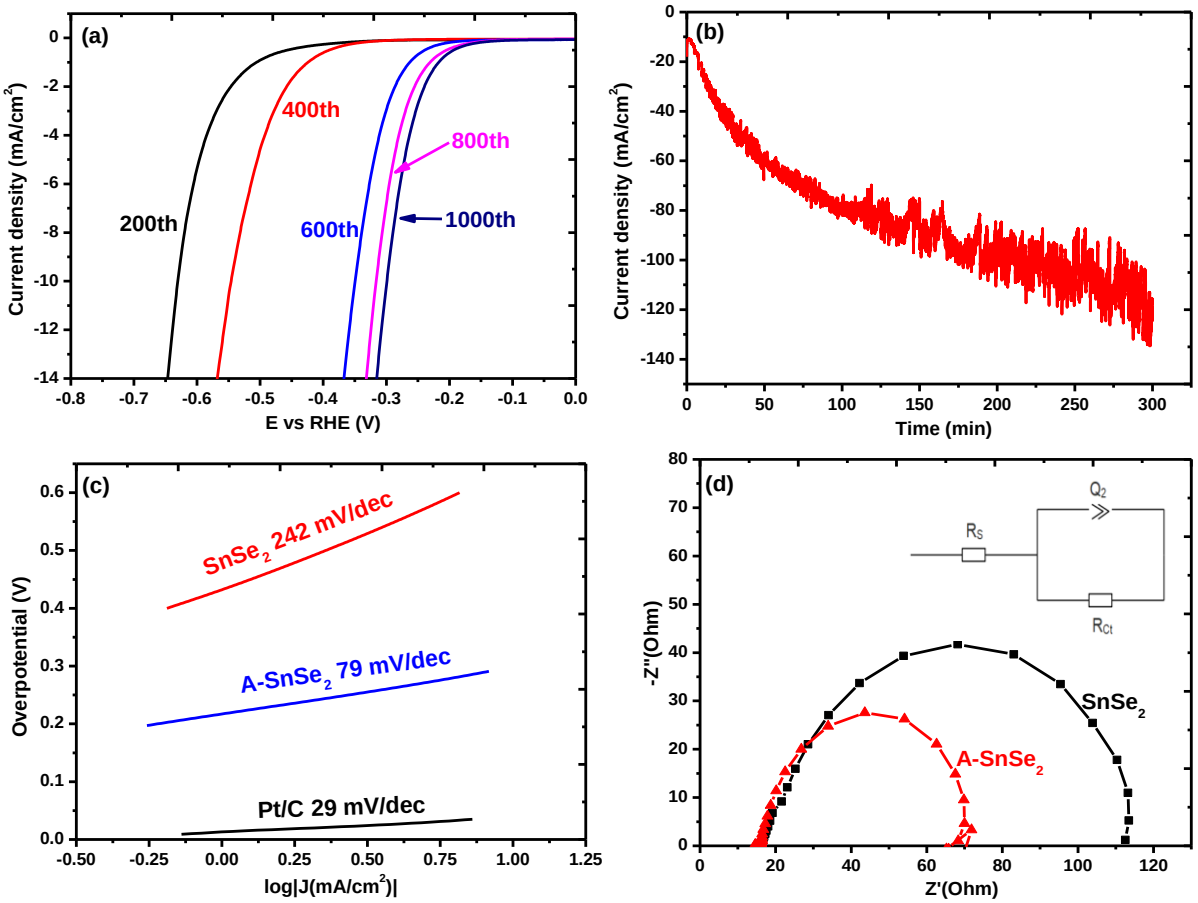


Figure 4: (a) Polarisation curves for the $SnSe_2$ nanoplates after every 200 scans. (b) Chronoamperometry curve for the $SnSe_2$ nanoplates at 620 mV vs RHE applied potential and 300 min time scale. (c) Tafel plots of the $SnSe_2$, A-$SnSe_2$, and Pt/C. (d) Nyquist plots of the $SnSe_2$ and A-$SnSe_2$.

A summary of the electrocatalytic parameter is shown in Table 1.

Table 1: Electrocatalytic parameters of the $SnSe_2$ nanoplates before and after electrochemical activation.

Electrocatalytic parameters	**$SnSe_2$**	**A-$SnSe_2$**
Onset potential	390 mV	141 mV
η_{10}	618 mV	289 mV
Tafel slope	242 mV/dec	79 mV/dec
J_0	0.297 mA/cm^2	0.607 mA/cm^2
R_{ct}	90 Ω	52 Ω

The decrease in the onset potential and overpotential clearly indicates a very drastic increase in the catalytic activity of the A-$SnSe_2$ nanoplates compared to the pristine $SnSe_2$ nanoplates. The decrease in the Tafel slope indicates that there was a change in the rate-limiting step of the HER on the electrochemically activated $SnSe_2$ nanoplates. The Tafel plot of the A-$SnSe_2$ is shown in **Fig.4(c)**. The Tafel slope of A-$SnSe_2$ suggests that the rate-limiting step is the Heyrovsky step and the HER occurs under the Volmer-Heyrovsky pathway. On the pristine $SnSe_2$ nanoplates the Volmer step was the rate-limiting step. These changes in the reaction mechanism suggest that the manner in which the hydrogen atoms interact with the surface of the nanostructures has changed. The J_0 also experiences a drastic increase in the electrochemically activated $SnSe_2$ plates, which suggests that the rate of reaction has improved quite remarkably. Electrochemical impedance spectroscopy (EIS) was used to evaluate the electron transport properties of the electrocatalyst. The equivalence circuit fitted to the Nyquist plots is shown as the insert in **Fig.4(d)**. The solution resistance is represented as R_s, the constant phase element is represented as Q_2, and the charge transfer resistance is represented as R_{ct}. The Nyquist plots also showcase the improvements in the performance of the activated catalyst. There was a significant reduction in the R_{ct} of the nanostructures from 90 Ω in the non-activated catalyst to 52 Ω in the activated catalyst. This denotes a notable improvement in the charge-transfer processes of the HER in the electrochemically activated catalyst. This increase in the performance of the catalyst may be due to proton intercalation. It has been shown that the catalytic performance of TMDs towards the HER can drastically improve due the intercalation H^+ ions between the layers of the TMD nanosheets.[19] This has been shown to occur after repeated LSV scans, which are normally conducted when evaluating the stability of the

catalysts in acidic media.[18] The Intercalated protons have been shown to cause the enhancement of the catalytic activity by improving the electrical conductivity and enabling favourable hydrogen adsorption. This phenomenon has been shown to occur in some but not all TMDs and has not yet been recorded in $SnSe_2$ nanostructures. A schematic representation of the intercalation of H^+ ions into the layers of TMDs is shown in **Fig.5**.

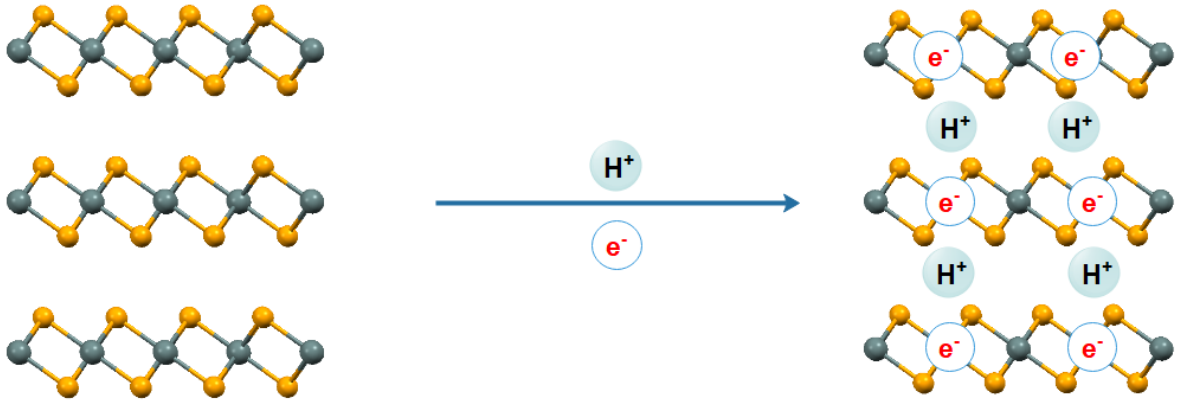


Figure 5: Intercalation of H^+ cations in the internal structure of the $SnSe_2$.

To confirm whether this improvement in the catalytic activity is due to proton intercalation, further electrochemical characterisation was conducted. The initial LSV curve of the $SnSe_2$ nanoplates is shown in **Fig.S2**, the LSV curve shows a reduction peak at ~ -500 mV vs RHE. This reduction peak has been observed in the polarisation curves of other TMDs that are reported in the literature.[19] This reduction peak has been attributed to the intercalation of cations in the internal structure of TMDs. In this case, the peak is attributed to the intercalation of H^+ ions into the layers of the $SnSe_2$ nanoplates. The reduction peak can be described as a pre-feature because it is not observed in the second scan, this also suggests that the H^+ intercalation may be a complete and irreversible process which has also been alluded to in literature.[19] Cyclic voltammetry was used to further investigate this pre-feature and the initial CV curve of the $SnSe_2$ nanoplates is shown in **Fig.6(a)**. The CV curve also shows a reduction peak at ~ 0.478 V vs RHE. The reverse scan shows two smaller peaks at -0.346 V vs RHE and -0.129 V vs RHE. These peaks were attributed to slight proton de-intercalation that occurred in a two-step process.[25] This phenomenon has been previously reported specifically for proton intercalation. The coulombic efficiency of the system was measured to be 43%. This indicates that the process is not fully irreversible.[25] The large peak at ~ 0.616 V vs RHE was attributed to the surface oxidation of the $SnSe_2$ nanoplates.[26] In the second scan, the peak attributed to intercalation is not observed. The same is true for the peaks attributed to the de-intercalation,

this further confirms that the peaks on the reverse scan for the initial CV were related to the reduction peak and were due to slight de-intercalation of protons on the $SnSe_2$ nanoplates.

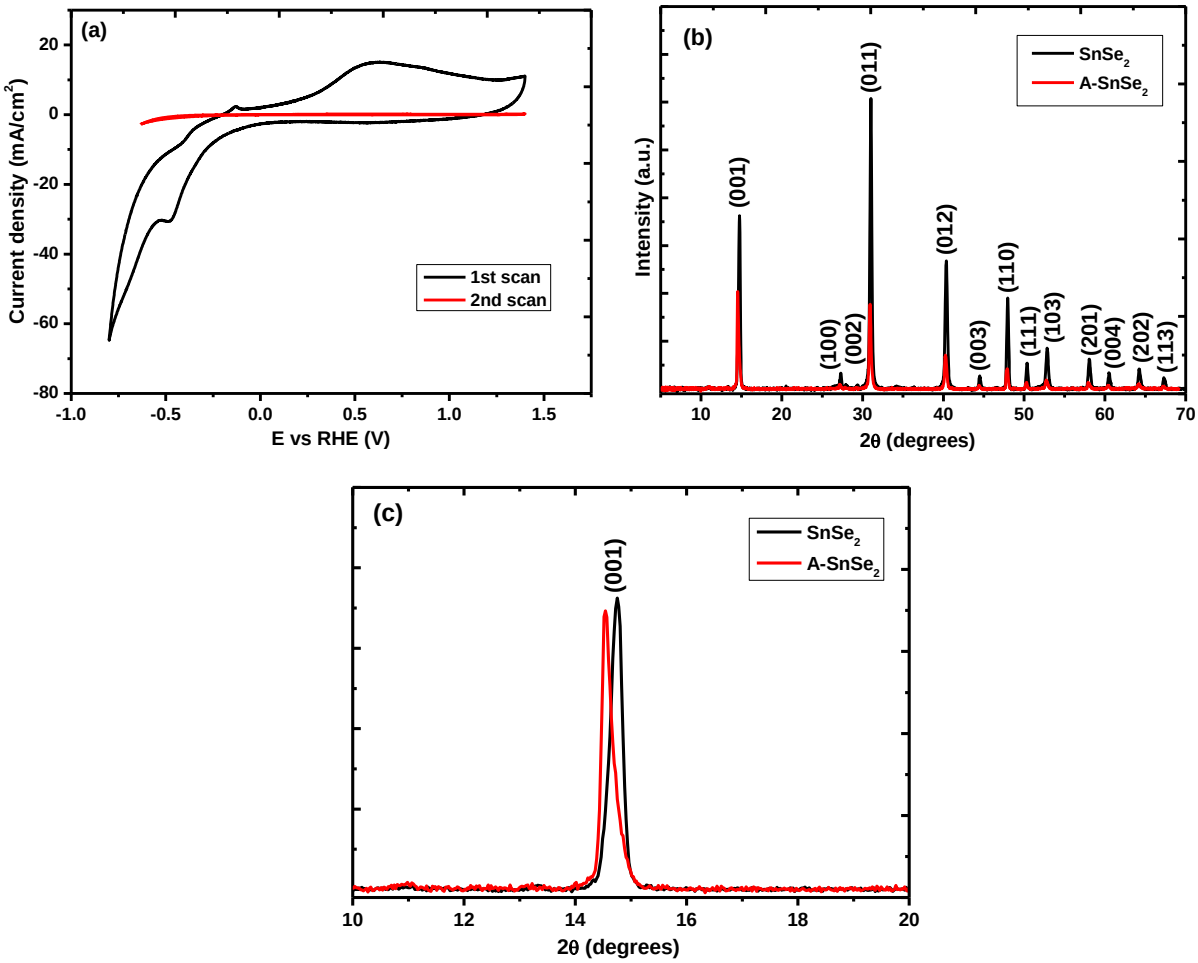


Figure 6: (a) cyclic voltammogram of the $SnSe_2$ nanostructures in 0.5 M H_2SO_4. (b) PXRD patterns of the pristine and A-$SnSe_2$ nanostructures. (c) Shift of the (001) peak due to proton intercalation.

In order to definitively determine whether this phenomenon was due to cation intercalation, the LSV scan was conducted in 0.5 M KOH. The pre-feature was also observed in a 0.5 M KOH electrolyte as shown in **Fig.S3**, this signifies the intercalation of K^+ into the internal structure of the $SnSe_2$ nanoplates. This shows that the $SnSe_2$ can accommodate other cations which is in line with what is reported about other TMDs in literature.[19] However, the use of KOH as an electrolyte does not result in an improvement to the catalytic properties of the nanostructures towards the HER. The catalytic performance does not improve in alkaline media because there aren't enough hydrogen ions to induce the activation.[18] This shows that the improved catalytic activity only occurs in H_2SO_4, which further supports that it is due to proton intercalation.

PXRD was also used to study proton intercalation in the activated $SnSe_2$ nanostructures. The powder pattern of the A-$SnSe_2$ showed no changes in phase or composition as compared to the pristine $SnSe_2$, as shown in **Fig.6(b)**. There are also no new peaks that arise from the electrochemical activation, this indicates that the improved catalytic activity was not due to some other chemical species that was formed during the electrochemical treatment. However, there was an increase in the size of the $SnSe_2$ nanoplates along the c-axis. The crystallite size along the c-axis was determined using the Debye-Scherrer equation. This was determined to be 23.7 nm in $SnSe_2$ and 54.3 nm in A-$SnSe_2$. The increase in the thickness of the nanoplates was due to the expansion of the interlayer spacing that is brought about by intercalation of the H^+ ions in the internal structure of the $SnSe_2$.[27-28] The (001) peak also shifted from a 2Θ value of 14.75° to a 2Θ value of 14.51° as shown in **Fig.6(c)**, this further confirms an expansion in the layers of the $SnSe_2$ nanoplates due to proton intercalation.[29]

To further confirm that the enhanced catalytic activity was indeed due to the electrochemical activation, other possibilities need to be eliminated. For example, the increased catalytic activity can at times be due to an increase in number of active sites.[30] New active sites can be created during the electrochemical treatment of the catalyst. One way of determining whether new active sites have been introduced is to determine the electrochemically active surface area (ECSA) before and after activation. The ECSA can be estimated using the electrochemical double layer (C_{dl}) of the nanostructures which has been shown to scale with the ECSA.[31] The C_{dl} has been determined by conducting cyclic voltammetry (CV) measurements at different scan rates. The CV curves are used to obtain ΔJ (J_{anodic}-$J_{cathodic}$) at a potential of 0.315 V vs RHE as shown in **Fig.S4**. The ΔJ is plotted against the scan rate which results in a linear plot that was used to determine the gradient, the gradient is equivalent to the C_{dl}. The C_{dl} plots are shown in **Fig.7(a)**.

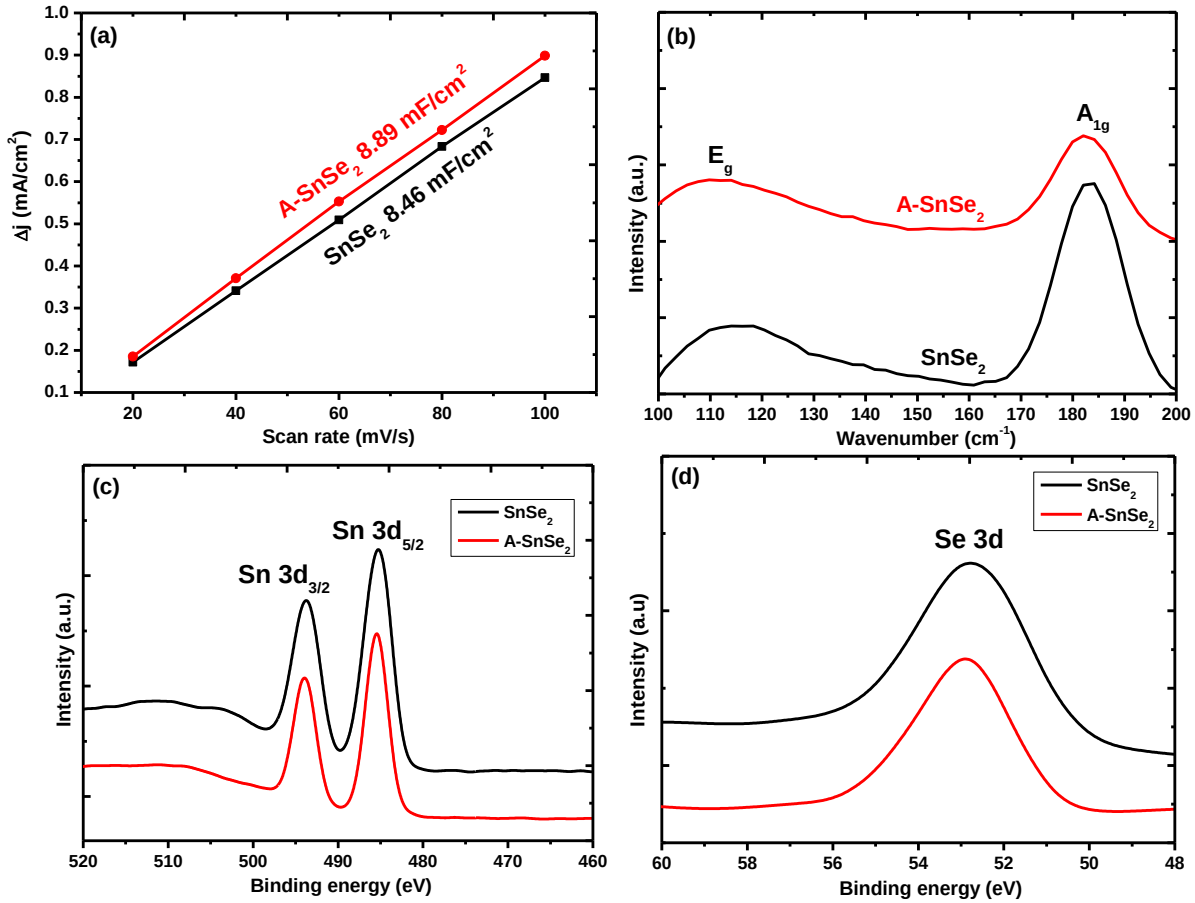


Figure 7: (a) C_{dl} plots the $SnSe_2$ nanostructures before and after activation. (b) Raman spectra of the $SnSe_2$ nanostructures before and after activation. (c) XPS spectra of the $SnSe_2$ nanostructures before and after activation.

The C_{dl} of $SnSe_2$ and A-$SnSe_2$ were found to be virtually identical at 8.46 mF/cm^2 and 8.89 mF/cm^2 respectively. This suggests that the enhanced activity was not due to an increase in the surface area or the introduction of fresh active sites.[32-33] In some instances, an enhancement in the catalytic activity may be due to changes in the phase of the $SnSe_2$ nanostructures. For instance, a transition from the 2H to the 1T phase.[34-35] To rule out any changes in phase, the Raman spectrum of the electrochemically activated catalyst were obtained. The Raman spectrum of the A-$SnSe_2$ is shown in **Fig.7(c)**, the spectrum shows the characteristic E_g and A_{1g} peaks. The position of the E_g is measured at 115 cm^{-1} for the A-$SnSe_2$ which was only slightly red-shifted from the un-activated $SnSe_2$ (114 cm^{-1}). The position of the E_g in the spectrum of activated $SnSe_2$ still suggests a 1T polymorph for the $SnSe_2$. According to the Raman spectrum, there are no changes in the phase of the nanomaterials. XPS was conducted on the $SnSe_2$ catalyst before and after electrochemical activation. The XPS spectra of the pristine and electrochemically activated $SnSe_2$ are shown in **Fig.7(c and d)**. The atomic

composition of the pristine and activated $SnSe_2$ is shown in **Table S1(a and b)** respectively. There is no significant change in the Se/Sn ratio of the pristine and activated catalysts. This indicates no formation of new active sites for HER through the formation of Se vacancies. This result shows that the electrochemical activation does not occur due to an increase in the number of active sites. This was corroborated by the analysis of the ECSA of the pristine and electrochemically activated $SnSe_2$ nanostructures, there is no significant increase in the ECSA of the activated catalyst which would indicate the formation of new active sites.[32-33] The TEM image of the A-$SnSe_2$ shown in **Fig.S5** also confirms that there are no changes in the morphology of the nanomaterials as compared to the un-activated sample. This analysis rules out any structural changes to the activated $SnSe_2$ which corroborates all earlier analyses that the activation was indeed due to proton intercalation.

4. Conclusions

In this work, the catalytic activity of colloidally synthesized $SnSe_2$ nanoplates towards the HER was evaluated. The catalytic performance of the $SnSe_2$ nanoplates was determined to be quite poor as they were characterized by a relatively high overpotential, high onset potential, low exchange current density, and a high Tafel slope. However, the $SnSe_2$ nanostructures underwent electrochemical activation through the intercalation of H^+ ions into their internal structure. The electrochemically activated nanostructures showed a drastic improvement in the catalytic activity upon continuous voltage sweeps, which is characteristic of electrochemically activated TMDs. The electrochemically activated catalyst was evaluated using CV and PXRD, which confirmed that the $SnSe_2$ nanostructures were activated by proton intercalation. Further evaluation of the electrochemical and structural properties of the activated catalyst indicated that the origin of the enhancement was not due to any changes in the structural or electrochemical properties of the nanostructures. Analysis of the XPS and ECSA revealed that the activation of the $SnSe_2$ nanoplates towards the HER was not due to the formation of any defects in the nanostructures as well. This work clearly shows that the poor catalytic activity of colloidally synthesized $SnSe_2$ nanoplates can be drastically improved through electrochemical activation.

5. References

1. Penner, S., Steps toward the hydrogen economy. *Energy* **2006,** *31* (1), 33-43.

2. Yang, J.; Mohmad, A. R.; Wang, Y.; Fullon, R.; Song, X.; Zhao, F.; Bozkurt, I.; Augustin, M.; Santos, E. J.; Shin, H. S., Ultrahigh-current-density niobium disulfide catalysts for hydrogen evolution. *Nat. Mater.* **2019,** *18* (12), 1309-1314.

3. Nkabinde, S. S.; Mwonga, P. V.; Mpelane, S.; Ndala, Z. B.; Kolokoto, T.; Shumbula, N. P.; Nchoe, O.; Maphanga, R. R.; Ozoemena, K. I.; Mubiayi, K. P., Phase-dependent electrocatalytic activity of colloidally synthesized WP and α-WP_2 electrocatalysts for hydrogen evolution reaction. *New. J. Chem.* **2021,** *45* (34), 15594-15606.

4. Lai, B.; Singh, S. C.; Bindra, J.; Saraj, C.; Shukla, A.; Yadav, T.; Wu, W.; McGill, S.; Dalal, N.; Srivastava, A., Hydrogen evolution reaction from bare and surface-functionalized few-layered MoS_2 nanosheets in acidic and alkaline electrolytes. *Mater. Today Chem.* **2019,** *14*, 100207.

5. Kwon, I. S.; Kwak, I. H.; Debela, T. T.; Abbas, H. G.; Park, Y. C.; Ahn, J.-p.; Park, J.; Kang, H. S., Se-rich $MoSe_2$ nanosheets and their superior electrocatalytic performance for hydrogen evolution reaction. *ACS nano.* **2020,** *14* (5), 6295-6304.

6. Qu, Y.; Shao, M.; Shao, Y.; Yang, M.; Xu, J.; Kwok, C. T.; Shi, X.; Lu, Z.; Pan, H., Ultra-high electrocatalytic activity of VS_2 nanoflowers for efficient hydrogen evolution reaction. *J. Mater. Chem. A.* **2017,** *5* (29), 15080-15086.

7. Gopalakrishnan, D.; Lee, A.; Thangavel, N. K.; Arava, L. M. R., Facile synthesis of electrocatalytically active NbS_2 nanoflakes for an enhanced hydrogen evolution reaction (HER). *Sustain. Energy Fuels.* **2018,** *2* (1), 96-102.

8. Li, Y.; Wang, L.; Zhang, S.; Dong, X.; Song, Y.; Cai, T.; Liu, Y., Cracked monolayer 1T MoS_2 with abundant active sites for enhanced electrocatalytic hydrogen evolution. *Catal. Sci. Technol.* **2017,** *7* (3), 718-724.

9. Huang, Y.; Sun, Y.; Zheng, X.; Aoki, T.; Pattengale, B.; Huang, J.; He, X.; Bian, W.; Younan, S.; Williams, N., Atomically engineering activation sites onto metallic 1T-MoS_2 catalysts for enhanced electrochemical hydrogen evolution. *Nat. Commun.* **2019,** *10* (1), 1-11.

10. Zhou, J.; Xiao, H.; Zhou, B.; Huang, F.; Zhou, S.; Xiao, W.; Wang, D., Hierarchical MoS_2–rGO nanosheets with high MoS_2 loading with enhanced electro-catalytic performance. *Appl. Surf. Sci.* **2015,** *358*, 152-158.

11. McGlynn, J. C.; Dankwort, T.; Kienle, L.; Bandeira, N. A.; Fraser, J. P.; Gibson, E. K.; Cascallana-Matías, I.; Kamarás, K.; Symes, M. D.; Miras, H. N., The rapid electrochemical activation of $MoTe_2$ for the hydrogen evolution reaction. *Nat. Commun.* **2019,** *10* (1), 1-9.

12. Ramasamy, P.; Manivasakan, P.; Kim, J., Phase controlled synthesis of SnSe and $SnSe_2$ hierarchical nanostructures made of single crystalline ultrathin nanosheets. *CrystEngComm* **2015,** *17* (4), 807-813.

13. Li, J.; Zhao, H.; Lei, Y.; Yang, Q.; Zheng, Z., Synthesis and Photocatalytic Properties of $SnSe_2$/Se Heterojunction Films. *Nano* **2018,** *13* (04), 1850045.

14. Cheng, Y.; Huang, J.; Cao, L.; Xie, H.; Wang, Y.; Wang, Y.; Wu, H.; Xi, S.; Li, J., Structure-controlled $SnSe_2$ nanosheets as high performance anode material for lithium ion batteries. *Ionics* **2020,** *26* (6), 2855-2862.

15. Inamdar, A. N.; Som, N. N.; Pratap, A.; Jha, P. K., Hydrogen evolution and oxygen evolution reactions of pristine and alkali metal doped $SnSe_2$ monolayer. *Int. J. Hydrog. Energy.* **2020,** *45* (37), 18657-18665.

16. Fan, Y.; Wang, J.; Zhao, M., Spontaneous full photocatalytic water splitting on 2D $MoSe_2$/$SnSe_2$ and WSe_2 /$SnSe_2$ vdW heterostructures. *Nanoscale* **2019,** *11* (31), 14836-14843.

17. Wu, Q.; Wei, W.; Lv, X.; Huang, B.; Dai, Y., Computational screening of defective group IVA monochalcogenides as efficient catalysts for hydrogen evolution reaction. *J. Phys. Chem. C* **2019,** *123* (18), 11791-11797.

18. Li, G.; Zhang, D.; Yu, Y.; Huang, S.; Yang, W.; Cao, L., Activating MoS_2 for pH-universal hydrogen evolution catalysis. *J. Am. Chem. Soc.* **2017,** *139* (45), 16194-16200.

19. Henckel, D. A.; Lenz, O. M.; Krishnan, K. M.; Cossairt, B. M., Improved HER catalysis through facile, aqueous electrochemical activation of nanoscale WSe_2. *Nano Lett.* **2018,** *18* (4), 2329-2335.

20. Zhang, Y.; Shi, Y.; Wu, M.; Zhang, K.; Man, B.; Liu, M., Synthesis and surface-enhanced Raman scattering of ultrathin $SnSe_2$ nanoflakes by chemical vapor deposition. *Nanomaterials* **2018,** *8* (7), 515.

21. Mukhokosi, E. P.; Krupanidhi, S. B.; Nanda, K. K., Bandgap engineering of hexagonal $SnSe_2$ nanostructured thin films for infra-red photodetection. *Sci. Rep.* **2017,** *7* (1), 1-10.

22. Zeng, M.; Li, Y., Recent advances in heterogeneous electrocatalysts for the hydrogen evolution reaction. *J. Mater. Chem. A.* **2015,** *3* (29), 14942-14962.

23. Murthy, A. P.; Theerthagiri, J.; Madhavan, J., Insights on Tafel constant in the analysis of hydrogen evolution reaction. *J. Phys. Chem. C.* **2018,** *122* (42), 23943-23949.

24. Yang, J.; Mohmad, A. R.; Wang, Y.; Fullon, R.; Song, X.; Zhao, F.; Bozkurt, I.; Augustin, M.; Santos, E. J.; Shin, H. S., Ultrahigh-current-density niobium disulfide catalysts for hydrogen evolution. *Nat. Mater.* **2019,** *18* (12), 1309-1314.

25. Buchheit, A.; Teßmer, B.; Muñoz-Castro, M.; Bracht, H.; Wiemhöfer, H. D., Electrochemical Proton Intercalation in Vanadium Pentoxide Thin Films and its Electrochromic Behavior in the near-IR Region. *ChemistryOpen* **2021,** *10* (3), 340-346.

26. Benck, J. D.; Hellstern, T. R.; Kibsgaard, J.; Chakthranont, P.; Jaramillo, T. F., Catalyzing the hydrogen evolution reaction (HER) with molybdenum sulfide nanomaterials. *ACS Catal.* **2014,** *4* (11), 3957-3971

27. Miu, E. V.; Mpourmpakis, G.; McKone, J. R., Predicting the Energetics of Hydrogen Intercalation in Metal Oxides Using Acid–Base Properties. *ACS Appl. Mater. Interfaces* **2020,** *12* (40), 44658-44670.

28. Liu, X.; Euchner, H.; Zarrabeitia, M.; Gao, X.; Elia, G. A.; Groß, A.; Passerini, S., Operando pH measurements decipher H^+/Zn^{2+} intercalation chemistry in high-performance aqueous Zn/δ-V_2O_5 batteries. *ACS Energy Lett.* **2020,** *5* (9), 2979-2986.

29. Zhao, Q.; Liu, L.; Yin, J.; Zheng, J.; Zhang, D.; Chen, J.; Archer, L. A., Proton Intercalation/De-Intercalation Dynamics in Vanadium Oxides for Aqueous Aluminum Electrochemical Cells. *Angew. Chem. Int. Ed.* **2020,** *59* (8), 3048-3052.

30. Beermann, V.; Kühl, S.; Strasser, P., Tuning the catalytic oxygen reduction reaction performance of Pt-Ni octahedral nanoparticles by acid treatments and thermal annealing. *J. Electrochem. Soc.* **2018,** *165* (15), J3026.

31. Qi, F.; Wang, X.; Zheng, B.; Chen, Y.; Yu, B.; Zhou, J.; He, J.; Li, P.; Zhang, W.; Li, Y., Self-assembled chrysanthemum-like microspheres constructed by few-layer $ReSe_2$ nanosheets as a highly efficient and stable electrocatalyst for hydrogen evolution reaction. *Electrochim. Acta.* **2017,** *224*, 593-599.

32. Yin, Y.; Han, J.; Zhang, Y.; Zhang, X.; Xu, P.; Yuan, Q.; Samad, L.; Wang, X.; Wang, Y.; Zhang, Z., Contributions of phase, sulfur vacancies, and edges to the hydrogen evolution reaction catalytic activity of porous molybdenum disulfide nanosheets. *J. Am. Chem. Soc.* **2016,** *138* (25), 7965-7972.

33. Kwon, H.; Ji, B.; Bae, D.; Lee, J.-H.; Park, H. J.; Kim, Y.-M.; Son, Y.-W.; Yang, H.; Cho, S., Role of anionic vacancy for active hydrogen evolution in WTe_2. *Appl. Surf. Sci.* **2020,** *515*, 145972.

34. Kim, H.-U.; Kim, M.; Seok, H.; Park, K.-Y.; Moon, J.-Y.; Park, J.; An, B.-S.; Jung, H. J.; Dravid, V. P.; Whang, D., Realization of Wafer-Scale 1T-MoS_2 Film for Efficient Hydrogen Evolution Reaction. *ChemSusChem* **2021,** *14* (5), 1344-1350.

35. Ndala, Z.; Shumbula, N.; Nkabinde, S.; Kolokoto, T.; Nchoe, O.; Shumbula, P.; Tetana, Z. N.; Linganiso, E. C.; Gqoba, S. S.; Moloto, N., Evaluating the Effect of Varying the Metal

Precursor in the Colloidal Synthesis of $MoSe_2$ Nanomaterials and Their Application as Electrodes in the Hydrogen Evolution Reaction. *Nanomaterials* **2020,** *10* (9), 1786.

6. Supplementary Information

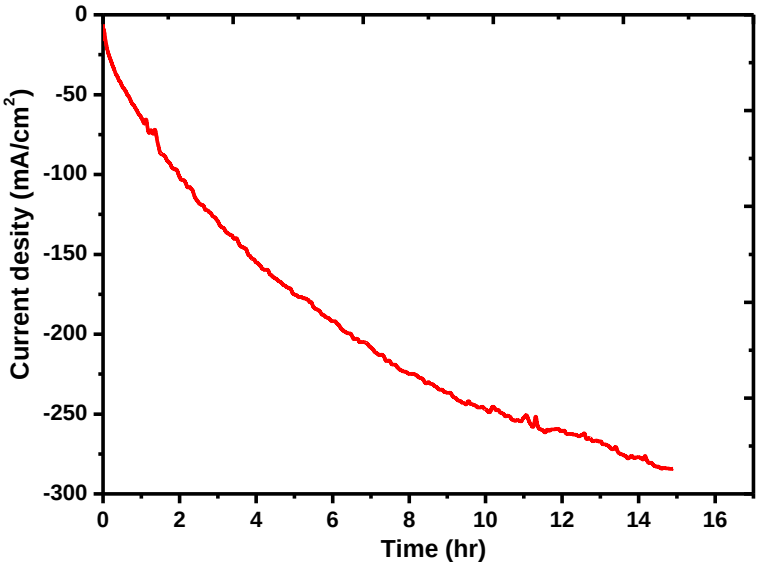


Figure S1: Chronoamperometry curve for the $SnSe_2$ nanoplates at 620 mV applied potential and 15 hr time scale.

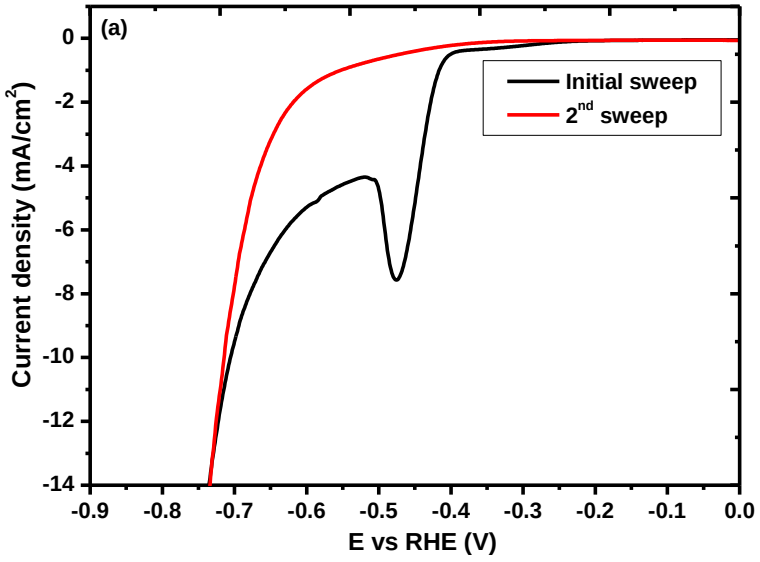


Figure S2: Polarization curves showing the pre-feature in the initial scan for $SnSe_2$ in H_2SO_4.

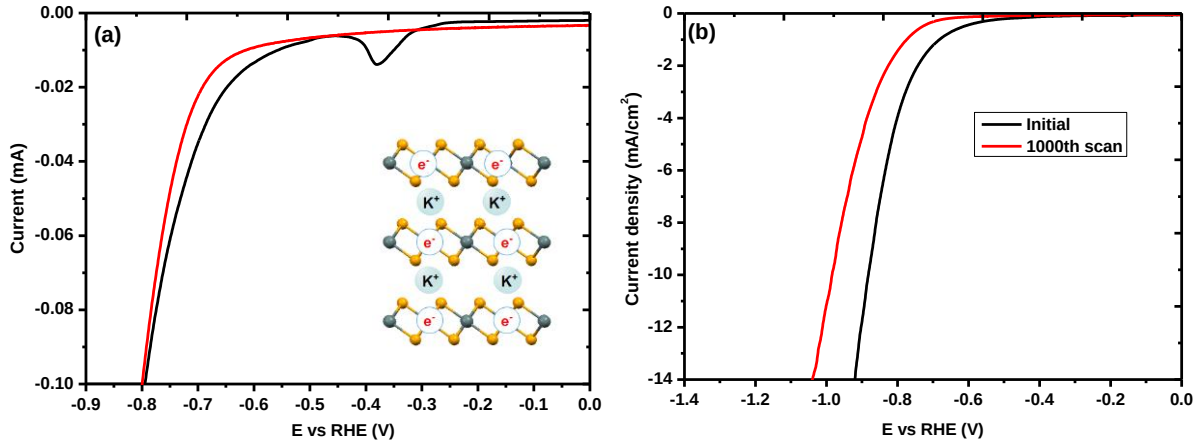


Figure S3: (a) Polarization curves for $SnSe_2$ in 0.5 M KOH. (b) Polarization curves showing the stability of the $SnSe_2$ nanoplates after a 1000 LSV scans.

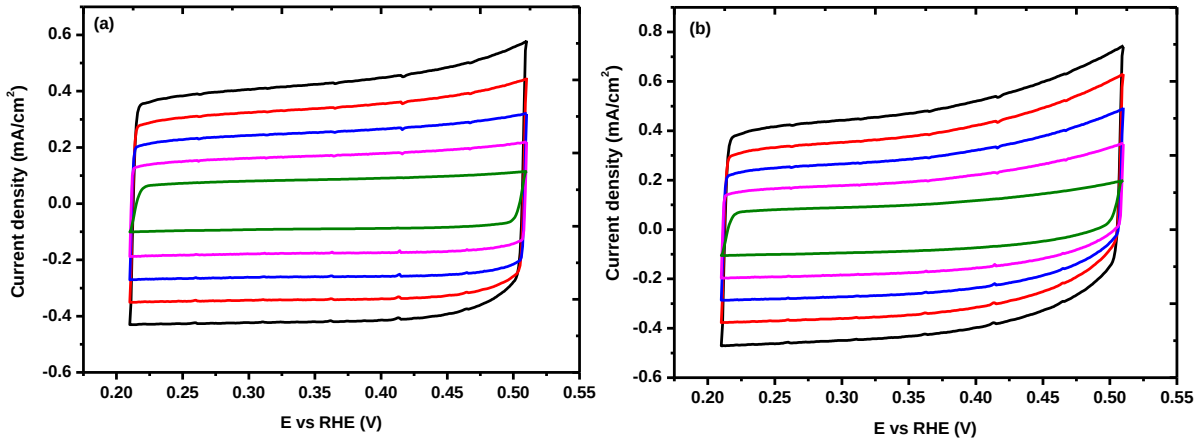


Figure S4: CV curves at 20, 40, 60, 80 and 100 mV/s for $SnSe_2$ (a) and activated $SnSe_2$ (b).

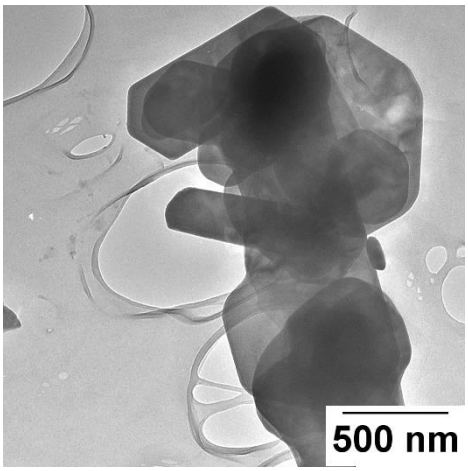


Figure S5: TEM image of the electrochemically activated $SnSe_2$ nanoplates.

Table S1: Atomic composition of (a) $SnSe_2$ (b) electrochemically activated $SnSe_2$.

(a)

Name	Peak BE	Atomic %
C 1s	285.0	38.7
F 1s	689.2	28.1
O 1s	533.0	25.7
Se	55.2	5.3
Sn	496.6	2.2

(b)

Name	Peak BE	Atomic %
C 1s	285.0	37.6
F 1s	689.2	26.7
O 1s	533.0	28.7
Se	55.2	4.9
Sn	496.6	2.1

Chapter 5: Unravelling the effects of surface functionalization on the catalytic activity of TMD nanostructures towards the hydrogen evolution reaction

Chapter 5.1: Unravelling the effects of surface functionalization on the catalytic activity of $ReSe_2$ nanostructures towards the hydrogen evolution reaction

1. Introduction

Hydrogen gas has gained immense interest as a pollution-free and highly efficient alternative to fossil fuels as an energy carrier. The desire to overturn the effects of fossil fuels on the environment is projected to result in a significant increase in demand for hydrogen gas.[1] Due to this foreseeable increase in the demand for hydrogen, methods used to produce hydrogen have been in the spotlight. The hydrogen evolution reaction (HER) is the half-reaction of water electrolysis that results in the formation of hydrogen gas, and it is the most pollution-free and efficient way to produce hydrogen gas at a large-scale.[2] Unfortunately, the HER is facilitated using scarce and expensive noble metals such as platinum which hinders its commercial application.[3] Transition metal dichalcogenides (TMDs) such as MoS_2, $MoSe_2$, and NbS_2 have been considered as alternatives to platinum due to their excellent catalytic activity towards the HER.[4-6] One of the more recently explored TMDs $ReSe_2$ has also shown impressive electrocatalytic performance towards the HER.[7-8] This has been attributed to some of its unique structural properties such as its distorted 1T crystal structure and weak interlayer coupling.[9] The active sites for the HER in $ReSe_2$ have been identified as the edge sites as with many of the prominent TMDs, and there have been efforts to increase the exposure of the active edge sites of the $ReSe_2$ using various synthetic techniques.[10-11]

Solution-based synthetic techniques such as colloidal synthesis have become rather popular for synthesizing TMDs because of their relative simplicity and potential to produce these materials at a large scale.[12] The most enticing property of these methods is their versatility and, ability to control the properties of the synthesized nanostructures by varying the reaction parameters.[13-14] The solvents/surfactants used in these reactions perform the crucial role of stabilizing and

functionalizing the synthesized nanostructures; they have also been shown to help direct and control the growth of nanostructures in the synthesis of TMD nanostructures.[15-16] The solvents are normally long-chained hydrocarbons that can preferentially bind to certain crystal facets on the surface of nanostructures through various functional groups (e.g. -NH_2, -OH, -COOH, and P=O) to produce a certain size, shape, and phase of the nanostructures.[17-18] This property can be exploited to produce nanostructures with favourable structural properties that may result in maximal exposure of the active edge sites of TMDs. The functionalization of nanostructures by these surfactants has been known to have advantageous properties in various applications.[20-21] Unfortunately, from an electrocatalysis standpoint these surfactants can also impede electrocatalytic reactions by blocking active sites.[19,22] Thus, it is essential to select a solvent/surfactant that results in maximal exposure of the active edge sites without impeding the catalytic processes of the HER. To the best of our knowledge, extensive work that seeks to identify solvents/surfactants for $ReSe_2$ nanostructures has not been undertaken. Therefore, this work focuses on identifying such solvents by investigating the functionalization of $ReSe_2$ nanostructures with three common solvents used in colloidal synthesis: oleylamine, oleic acid, and trioctylphosphine oxide.

2. Experimental section

2.1 Materials

Ammonium perrhenate (NH_4ReO_4, 99.98%), selenium powder (Se, 99.99%), oleylamine (OLA, 70%), oleic acid (OA, 90%), trioctylphosphine oxide (TOPO, 90%) were all purchased from Sigma Aldrich and used as received without purification.

2.2 Synthesis of $ReSe_2$ nanostructures using OLA, OA, and TOPO

The $ReSe_2$ nanostructures were synthesized using three different solvents/surfactants in three separate reactions. The structures of the surfactants used, and their denoted head groups are shown in **Fig.S1**. Oleylamine has an amine head group, oleic acid has a carbonyl head group, and trioctylphosphine oxide has the P=O head group. The procedure was kept the same on all occasions except for the solvent used. The selenium powder (Se, 0.932 mmol) was added into the three-neck round bottom flask containing the solvent/surfactant (20 ml) at room temperature. The flask was then degassed for 20 min. The temperature was increased to 220 ^oC to thermally reduce the Se to Se^{2-} with the help of the solvent, which also acted as a reducing agent. Once all the Se was reduced, a mixture of ammonium perrhenate (NH_4ReO_4, 0.372 mmol) and the solvent was added into the reaction mixture. The temperature was then raised

to 330 ºC and the reaction was run for 120 min. The nanoparticles formed were then washed with ethanol and toluene using a centrifuge and then left to dry.

2.3 Characterization of the nanostructures

The phase purity, crystallinity, and space group of the products were examined using powder X-ray diffraction (PXRD) on a Bruker MeasSrv D2-205530 diffractometer using secondary graphite monochromated CuKα radiation (λ 1.5406 Å) at 30 kV/10 mA. Measurements were taken using a glancing angle of incidence detector at an angle of 2°, for 2θ values over 10 - 90° in steps of 0.026° with a step time of 37 s and at a temperature of 25 °C. The X-ray photoelectron spectroscopy (XPS) measurements of the powder samples were obtained using a Thermo ESCAlab 250Xi with Al kα photon source (1486.7 eV), X-ray power of 300W, X-ray spot size of 900 µm, pass energy (survey) of 100 eV, pass energy (20 eV), and pressure of $<10^{-8}$ mBar. The sample morphologies were determined using transmission electron microscopy (TEM) on an FEI Tecnai T12 microscope operated at an acceleration voltage of 120 kV. High-resolution imaging was performed on a Cs aberration-corrected Hitachi HF-3300S environmental transmission electron microscope (ETEM) operated at 300 kV. The ETEM was equipped with an SDD X-MaxN 80T system from Oxford Instruments for energy dispersive X-ray (EDX) measurements. EDX spectra were analysed using the Aztec software. The TEM and HRTEM samples were prepared by sonicating a spatula tip of the sample in ethanol and drop-casting that dispersion on a lacey carbon Cu grid. The nanostructures' total surface area and pore volume were ascertained using a Micromeritics TriStar 3000 Surface Area and Porosity Analyzer. Analysis of organic solvents used was established using the Bruker TENSOR 27 Fourier Transform Infrared (FTIR) spectrophotometer, ATR mode was used for the analysis. Nuclear magnetic resonance (NMR) was conducted using a 500 MHz Bruker AVANCE III, the samples were run using $CDCl_3$ as a solvent at 300 K.

2.4 Electrochemical studies

The electrochemical measurements were carried out on a BASi epsilon E2. All measurements were carried out in 0.5 M H_2SO_4 using a three-electrode system. A Ag/AgCl electrode was used as the reference electrode, a platinum wire was used as the counter electrode, and a modified glassy carbon electrode with a 3 mm diameter was used as the working electrode. The ink or fresh dispersion of the sample was prepared by dispersing 5.0 mg of the $ReSe_2$ with 0.5 mg carbon black and 40 µl of Nafion solution (5 wt%) in a 1 ml mixture of water and isopropanol at a 3:1 ratio. The solution was then sonicated for 30 min and ~ 5 µl of the ink was

drop-casted onto the glassy carbon electrode. The electrode was allowed to dry at room temperature. The linear sweep voltammograms were obtained at a scan rate of 2 mVs^{-1} and the cyclic voltammograms were obtained at a potential range of 0.2 – 0.6 V vs RHE at 100 mVs^{-1} scan rate. The measured potentials vs Ag/AgCl were converted to the reversible hydrogen electrode (RHE) scale according to the Nernst equation:

$$E_{RHE} = E_{Ag/AgCl} + 00059\ pH + E^{0}_{Ag/AgCl} \quad (1)$$

Where E_{RHE} is the converted potential vs RHE, $E^{0}_{Ag/AgCl}$ = 0.210 V at 25 °C. The Impedance spectroscopy studies were conducted on a Biologic SP 300, and the measurements were done at a potential of -200 mV vs RHE and a frequency range between 0.1 Hz and 100 kHz.

2.5 Computational studies

All studied nanoclusters were built using Material Studio 2016 (MS) software package (Accelrys Inc., San Diego, CA, USA). The vacuum thickness size of 20 Å was constructed for all studied $ReSe_2$ nanostructure systems. The DMol 3 was employed to determine the efficiency of molecular adsorption of oleylamine (OLA), oleic acid (OA), and trioctylphosphine oxide (TOPO) on two crystal planes, namely {100} and {010} of the $ReSe_2$ nanostructures in the gas phase according to DFT computations. The applications of DMol 3 modules for free molecules, the general gradient approximation (GGA) functional correlations, Perdew–Burke– Ernzerh (PBE) exchange, the pseudo-conserving norm, and the DNP base set were used. A smearing value of 0.05 Ha was used in the calculation to achieve accurate electronic convergence. To achieve satisfactory and accurate results, the real space global orbital cut-off radius of 4.4 Å was used. The local density of state and partial density of states were calculated with 12 empty bands with k-point set to medium.

3. Results and discussion

The PXRD was used to confirm the synthesis of $ReSe_2$ nanostructures and to also determine the crystallinity, phase, and composition of the as-synthesized $ReSe_2$ nanostructures. The diffraction peaks as shown in **Fig.1** are observed at 13.7°, 31.9°, 35.2°, 42.6°, 47.1, and 55.2°. These diffraction peaks correspond to the lattice planes (001), (1-22), (-220), (012), (003), and (1-42). The PXRD confirms that the $ReSe_2$ nanostructures have crystallized in the distorted 1T phase triclinic system with P-1 space group (JCPDS card no: 01-065-4275). The broad nature of the diffraction peaks as shown in **Fig.1** is indicative of nanosized materials.[23]

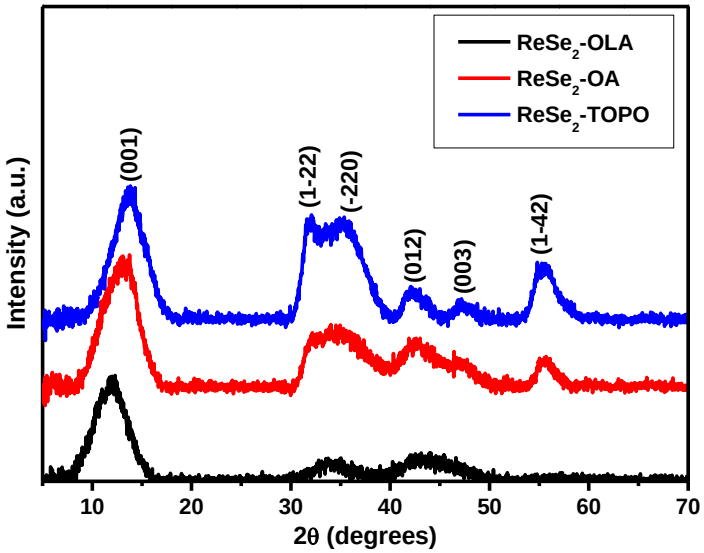


Figure 1: PXRD patterns for $ReSe_2$ nanostructures synthesized using the three specified surfactants. Oleylamine ($ReSe_2$-OLA), oleic acid ($ReSe_2$-OA), and trioctylphosphine oxide ($ReSe_2$-TOPO).

The high-intensity diffraction peak at 2θ = 13.87° is characteristic of $ReSe_2$ nanostructures. The appearance of the (001) peak is associated with the stacking of nanosheet layers along the c-axis, thus the PXRD confirms that the nanosheets are few-layer and not monolayer. The very broad peak at 2θ = 30-40° is also characteristic of $ReSe_2$ nanostructures, the broadness of this peak is due to an ensemble of smaller peaks that have overlapped to create a much broader peak.[23] In this case, the (1-22) and the (-220) at 31.9° and 35.2° respectively have overlapped to create a much broader peak in the $ReSe_2$-OLA and $ReSe_2$-OA. However, the $ReSe_2$-TOPO diffractogram shows a noticeable resolution of these two peaks, suggesting improved crystallinity compared to its counterparts. $ReSe_2$-OLA also shows the overlap of the (012) and (003) peaks at 42.6° And 47.1° respectively. The (-142) diffraction peak is also not observed in the $ReSe_2$-OLA sample. These observations suggest that the $ReSe_2$-OLA nanostructures exhibit less crystalline character as compared to that of the $ReSe_2$-TOPO nanostructures. This suggests that OLA has a somewhat inhibitory effect on the formation and growth of the $ReSe_2$ nanostructures. X-ray photoelectron spectroscopy (XPS) was used to evaluate the bonding configuration and elemental composition of the $ReSe_2$ nanostructures. The elemental composition of the nanostructures from the XPS analysis shown in **Table 1** shows that the Re and Se elemental ratio is 1:2 which further confirms the formation of $ReSe_2$ nanostructures in the expected configuration. The observed main XPS peaks of the $ReSe_2$ nanostructures are shown in **Fig.S2**. The Re 4f, Se 3d peaks were selected for further analysis. The High-resolution

XPS spectra of Re 4f and Se 3d are shown in **Fig.2**.

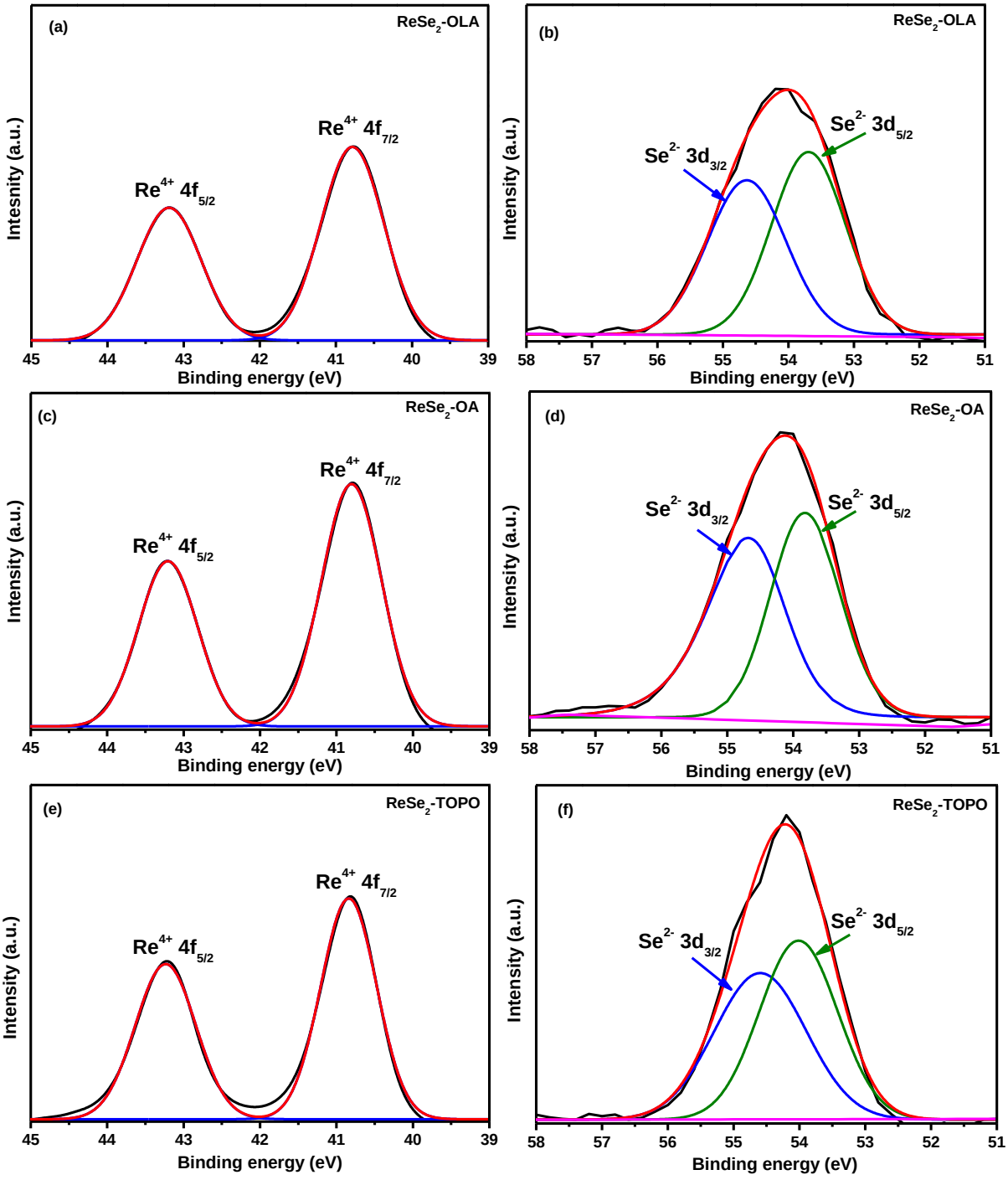


Figure 2: High-resolution XPS spectra of $ReSe_2$-OLA (a and b), $ReSe_2$-OA (c and d), and $ReSe_2$-TOPO (e and f).

.

The Re high-resolution XPS spectra of the $ReSe_2$ nanostructures are shown in **Fig.2(a, c and e)** for $ReSe_2$-OLA, $ReSe_2$-OA and $ReSe_2$-TOPO, respectively. These show the characteristic

core level $4f_{7/2}$ and $4f_{5/2}$ peaks of Re^{4+} at ~41 eV and ~43 eV, respectively.[24] The Se high-resolution XPS spectra of the $ReSe_2$ nanostructures are shown in **Fig.2(b, d, and f)** for $ReSe_2$-OLA, $ReSe_2$-OA, and $ReSe_2$-TOPO. The deconvoluted peak at ~54 eV shows the characteristic core level $3d_{5/2}$ and $3d_{3/2}$ peaks Se^{2-} at 53.7 eV and 54.7 eV, respectively.[24] Altering the surfactants used for the synthesis of the nanostructures does not change the bonding configuration of the nanostructures or their elemental composition as shown in the XPS spectra of the nanostructures synthesized using the three different surfactants. This confirms that regardless of the solvent/surfactant used in the synthesis, the synthetic protocol established will lead to the formation of the $ReSe_2$ nanostructures. **Table 1** summarizes of the bonding configuration and elemental composition data of the nanostructures.

Table 1: Summary of the bonding configuration and elemental composition data

Sample	Element	Assignment	Binding energy (eV)	Atomic (%)
	Re	Re^{4+} $4f_{5/2}$	41.2	4.9
		Re^{4+} $4f_{7/2}$	43.6	4.9
	Se	Se^{2-} $3d_{3/2}$	54.1	10.8
		Se^{2-} $3d_{5/2}$	55.0	10.8
$ReSe_2$-OLA	C	C-C	284.8	59.9
	N	Organic N	399.8	4.0
	O	(oxide)	530.6	0.9
	Re	Re^{4+} $4f_{5/2}$	41.2	3.6
		Re^{4+} $4f_{7/2}$	43.6	3.6
	Se	Se^{2-} $3d_{3/2}$	54.1	8.3
		Se^{2-} $3d_{5/2}$	55.0	8.3
$ReSe_2$-OA	C	C-C	284.8	58.0
		C-O	286.6	7.4
		O-C=C	288.9	5.7
	O	Organic C-O	532.1	6.1
		Organic C=O	533.5	5.6
		Organic O	535.2	0.3
		oxide	530.5	0.8
	Re	Re^{4+} $4f_{5/2}$	41.3	4.7
		Re^{4+} $4f_{7/2}$	43.6	4.7
$ReSe_2$-TOPO	Se	Se^{2-} $3d_{3/2}$	54.3	11.7
		Se^{2-} $3d_{5/2}$	55.1	11.7
	C	C-C	284.8	59.8

The XPS spectra can also lend some insight into the binding of the surfactants onto the surface of the nanostructures.[25] XPS is a surface-sensitive technique that can probe the outermost 5-10 nm of the sample. Thus, the surface composition of the capped $ReSe_2$ can be studied to investigate the nature of the surfactants that interact with the surface of the nanostructures. The

presence of the N 1s core level XPS spectra of $ReSe_2$-OLA in the binding energy region between 398 eV - 400 eV shown in **Fig.S3(a)** confirms the presence of an interaction between the surfactant and the surface of the nanostructures through the amine group.[17] The capping of the $ReSe_2$ nanostructures with oleic acid can also be investigated by XPS. The high-resolution XPS C 1s spectrum is shown in **Fig.S3(b)**, it can be used to identify the carbon-containing species on the surface of the nanostructures. The C 1s spectrum shows evidence of three carbon-containing species. The first and most intense peak at 284.8 eV is attributed to the alkyl chains of the oleic acid. The peak at 286.6 eV is due to the C-O and C=O bonds arising from the carboxylate functional group in oleic acid. The final peak at 288.9 eV corresponds to the O-C=O carboxylate functional group.[25] The appearance of these carbon-containing species confirms that there is an interaction between oleic acid and the surface of the nanostructures.[25] The appearance of these peaks suggests that the nature of the interaction between the $ReSe_2$ nanostructures and oleic acid may be mixed. The peak at 286.6 eV from the C-O and C=O suggest monodentate binding while the peak at 288.9 eV suggest bidentate binding through the carboxylate group. The O 1s spectrum was used to further investigate how the oleic acid interacts with the surface of the nanostructures. The deconvoluted signal in the O 1s spectrum has four peaks as shown in **Fig.S3(c)**. The first peak at 530.5 eV corresponds to the metal oxide which is due to the oxidation of the $ReSe_2$ surface. The peaks at 532.1 eV and 533.5 eV correspond to the C-O and C=O species, respectively.[25] The appearance of these peaks is attributed to the monodentate interaction of either the C-O and the C=O species to the surface of the nanostructures.[25] Studies have shown that a bidentate interaction is characterised by a single peak at ~ 531 eV, while the appearance of two peaks at 531 eV and 533 eV are associated with monodentate binding.[26] Since the two peaks are observed in the O 1s spectrum, this suggests monodentate binding.[26] The XPS analysis is therefore inconclusive in determining the nature of the interaction between the oleic acid and the $ReSe_2$ nanostructures, because the C 1s spectrum suggests bidentate binding, while the O 1s suggests monodentate binding. FTIR, NMR, and computational analysis were utilized to further investigate this interaction as well as the interaction of the $ReSe_2$ nanostructures with OLA and TOPO. The C 1s spectrum of $ReSe_2$-TOPO is shown in **Fig.S3(d)**, the spectrum only shows the C-C peak from the alkyl carbons of the TOPO at 284.8 eV.

Fourier transform infrared (FTIR) analysis was used to further investigate the interaction of the surfactants with the surface of the nanostructures. The surfactants are ideally supposed to bind to the surface of the nanostructures through their respective head groups; this is what allows

the surfactants to control the structure of the nanostructures during nucleation and growth of the nanoparticles. The FTIR analysis was conducted on both the free surfactant (uncapped surfactant) and the capped $ReSe_2$ nanostructures. The FTIR spectra is shown in **Fig.S4** and the results are summarized in **Table 2**.

Table 2: FTIR assignments for OLA, OA, and TOPO and the $ReSe_2$ nanostructures.

Assignment	OLA (cm^{-1})	$ReSe_2$-OLA (cm^{-1})	OA (cm^{-1})	$ReSe_2$-OA (cm^{-1})	TOPO (cm^{-1})	$ReSe_2$-TOPO (cm^{-1})
-C=H (stretching)	723	723	723	723	-	-
C=C (stretching)	964	934	934	934	-	-
C-H (stretching)	729	901	-	-	-	
	2849	2849	2854	2854	2854	2854
	2923	2913	2917	2923	2923	2917
N-H (Bending)	1622	1596	-	-	-	-
C=O (stretching)	-	-	1710	1704	-	-
C-O	-	-	1278	-	-	-
P=O (stretching)	-	-	-	-	1149	1173

To determine whether the surfactants have indeed capped the nanostructures, the vibrational energies of the bonds associated with the binding atoms are considered. In the OLA capped nanostructures the N-H bond is considered, the N-H bend vibrational energy is ~ 1622 cm^{-1}, and the vibrational energy experiences a small shift to 1596 cm^{-1} in the capped nanostructures and the peak is also broader which suggests that the surfactant has capped the nanostructures through the amine group.[27] In the OA capped nanostructures the intensity of the C=O stretching band becomes vastly diminished and has slightly shifted from 1710 cm^{-1} to 1704 cm^{-1} in the capped nanostructures compared to the free surfactant respectively which is expected for capped nanostructures.[28] This indicates monodentate binding through the carbonyl group. The C-O stretch which appear at 1289 cm^{-1} in the free OA is not observed in the FTIR spectrum of the OA capped $ReSe_2$ nanostructures.[26] This also suggests monodentate binding through the C-O. The analysis of the FTIR spectra does not indicate bidentate binding. Two bands for the asymmetric ν_{as} (COO^-) and symmetric ν_s (COO^-) stretch that are typically observed at 1556 cm^{-1} and 1410 cm^{-1}, respectively are associated with bidentate binding of the oleic acid on the surface of nanostructures.[26] These two prominent bands were not observed in the FTIR spectrum of the OA capped $ReSe_2$ nanostructures, which suggests no bidentate interaction had occured.[29] In the free TOPO, the vibrational stretching band of the P=O bond was observed at

1149 cm^{-1} but the band has slightly red-shifted to 1173 cm^{-1} in the capped nanostructures.[30] The shifting of the peak and the diminished intensity of the P=O band was ascribed to the complexation of the TOPO molecules to the nanostructures through the lone pairs of the oxygen.[30]

The interaction of the surfactants with the $ReSe_2$ nanostructures can be investigated using nuclear magnetic resonance (NMR). NMR can be useful in studying the organic layer around colloidally synthesized nanostructures. Specifically, NMR can be used to confirm the binding of the surfactants to the nanostructures through their head-groups. The NMR spectra of the capped $ReSe_2$ nanostructures are compared to that of free surfactant (unbound surfactant). The NMR spectra of capped nanostructures are normally accompanied by significant line broadening and chemical shifts compared to the spectra of free surfactants. The line broadening is due to the reduced rotational degrees of freedom of bound surfactants as compared to free surfactants.[31] The ^1H NMR assignments for the free surfactant and the capped nanostructures are shown in **Table 3**.

Table 3: NMR assignments for free surfactants and capped nanostructures

Sample	Type of H	Free Chemical shift (δ)	Capping Chemical shift (δ)
OLA	$-CH_3$	0.85-0.90	0.83-0.90
	$-CH_2-$	1.21-1.37	1.18-1.39
	R-CH=CH-R	1.92-2.05	1.92-2.04
	$-NH_2$	1.00-1.05	-
	$R-NH_2$	2.65-2.71	2.78-2.86
	CH=CH	5.31-5.40	5.32-5.42
	R_1-NH_2	1.38-1.46	1.51-1.73
OA	$-CH_3$	0.84-0.92	0.78-0.90
	$-CH_2-$	1.21-1.39	1.22-1.37
	$R_1-C=O$	1.59-1.67	1.60-1.68
	R-CH=CH-R	1.95-2.08	1.93-1.99
	R-C=O	2.30-2.38	2.31-2.39
	CH=CH	5.29-5.41	5.36-5.40
TOPO	O=P-R	1.51-1.69	1.49-1.67
	$-CH_2-$	1.35-1.43	-
	R_1-CH_3	1.22-1.34	1.19-1.36
	$-CH_3$	1.86-1.91	1.85-1.91

R = CH_2 and R_1 = CH_2-CH_2

The NMR spectra of the free surfactants and their capped counterparts are shown in **Fig.S5**. As expected for the reasons already mentioned, the peaks assignments for the surfactants are all observed in the NMR spectra of the capped nanostructures. However, they exhibit significant line broadening and shifts in the chemical signals of the various peaks. These effects are normally more pronounced on the resonance peaks closest to the coordinating atom of the surfactant. This is true for the signal from the hydrogen atoms on the amine (-NH_2, δ=1.04 ppm) which is also designated **(f)** in the NMR spectrum shown in **Fig.S5(a)**. This signal completely disappears in the NMR spectrum of the capped nanostructures, as expected considering the nitrogen in the amine is co-ordinating to the nanostructures.[31] Significant line broadening and downfield shifting is also observed for the hydrogen atoms on the carbon adjacent to the amine group (-H_2C-NH_2, δ=2.81 ppm) which was denoted as **(d)** in the NMR spectrum. The same trend can be observed for the hydrogen atoms adjacent to the carbonyl group in the NMR spectrum of the OA capped $ReSe_2$ nanostructures as shown in **Fig.S5(b)**. The signals for the hydrogen atoms (-CH_2-CH_2-) denoted as **(b)** and **(d)** on the NMR spectrum of the OA capped nanostructures are significantly downfield compared to their positions on the free surfactant. This has been shown to be due to the deprotonation of carboxylic acids and the absence of hydrogen bonding.[32] The NMR spectrum of the TOPO capped NMR also shows significant line broadening when the TOPO is bound to the nanostructures as shown in **Fig.S5(c)**. This broadening is clearly observed in the signal of the CH_2 adjacent to the phosphate group (O=P-CH_2, δ=1.56 ppm).[33] This also results in the disappearance of the **(b)** signal for the -CH_2 (δ=1.39 ppm) hydrogen atoms on the TOPO capped $ReSe_2$ nanostructures. It has not yet been understood why this phenomenon occurs. The analysis of the FTIR, XPS, and NMR data shows that there is a clear interaction between the surfactants and the $ReSe_2$ nanostructures.

Computational analysis of this interaction can give insights into the effect of the surfactants on the structural and catalytic properties of the nanostructures. This is especially true for the edge sites of the $ReSe_2$ nanostructures which are the catalytically active sites for the HER, while the basal plane has been shown to be catalytically inert.[10] The edges are oriented along the a and b axes, while c axis is perpendicular to the basal plane. The a and b axes with the associated crystal facets are shown in **Fig.3.**[34-35]

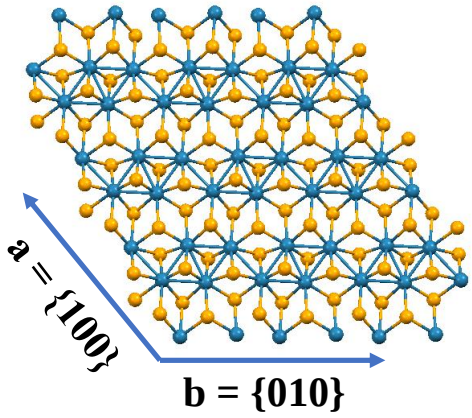


Figure 3: Crystal structure of $ReSe_2$, viewed perpendicular to the basal plane, with the a and b axes and their respective crystal planes.

To understand the adsorption of these surfactants on the surface of $ReSe_2$, different surfaces were created using molecular modelling. These surfaces were used to investigate the interaction of the surfactants with surfaces along the two crystal planes, namely {100} and {010} of the $ReSe_2$ nanostructures. The adsorption isotherms are shown in **Fig.4(a)**. The adsorption isotherms show that TOPO has the lowest number of adsorbed molecules on the {100} and {010} planes. This is not surprising, considering the bulky nature of the TOPO molecule. OA has the second largest number of adsorbed molecules. The maximum number of 9 OA molecules could be adsorbed on the surface of {100} $ReSe_2$ as shown in **Fig.4(a)**. OLA has the highest number of molecules adsorbed on the {100} and the second largest number of molecules adsorbed on the {010} plane, this shows that $ReSe_2$ is highly passivated by OLA. There is a larger number of OLA and OA molecules that can bind to the edge sites of the $ReSe_2$ nanostructures compared to the TOPO molecules. This suggests that the OLA molecules are more likely to block the active edge sites of the $ReSe_2$ nanostructures followed by the OA and then the TOPO molecules.

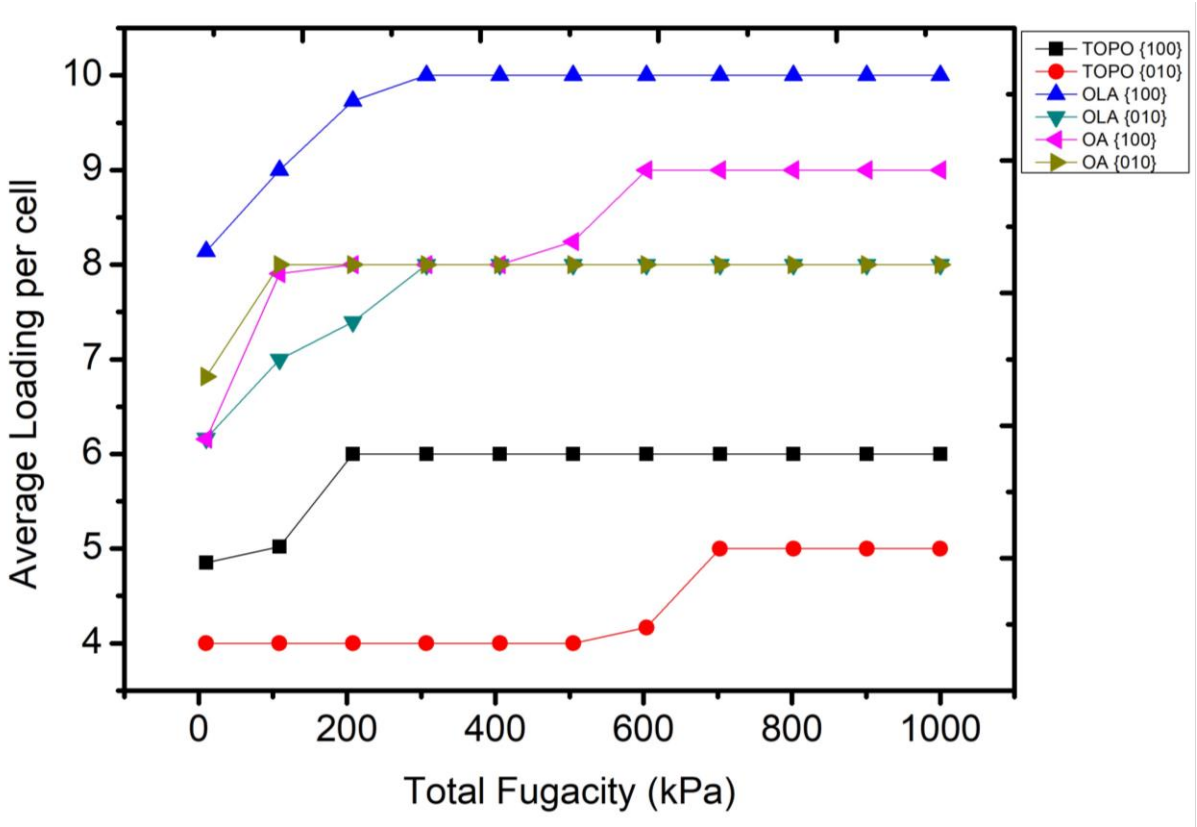


Figure 4: Adsorption isotherm of the surfactants on the $ReSe_2$ nanostructures indicating the average loading of the surfactant molecules per cell on the two crystal planes.

As shown by the PXRD analysis of the $ReSe_2$-OLA nanostructures, high passivation can result in growth restriction. Although the calculated adsorption isotherm in **Fig.4** above showed that 10 molecules of OLA could be adsorbed on the {100} crystal plane, this could indicate that {100} is the preferred and stable lattice plane. However, further calculations were done to optimize the two crystal planes as shown in **Fig.5(b and d)**. The results of the DFT optimization showed that the {010} crystal surface was more stable than the {100} crystal surface with the difference in relative energy of 4.79 eV. Thus, bearing that the {010} crystal surface was more stable, all calculations for adsorption of each passivating agent were performed on the {010} surface. The density of states was calculated to predict the change in the electronic band structures of the two crystal surfaces as shown in **Fig.5(a and c)**.

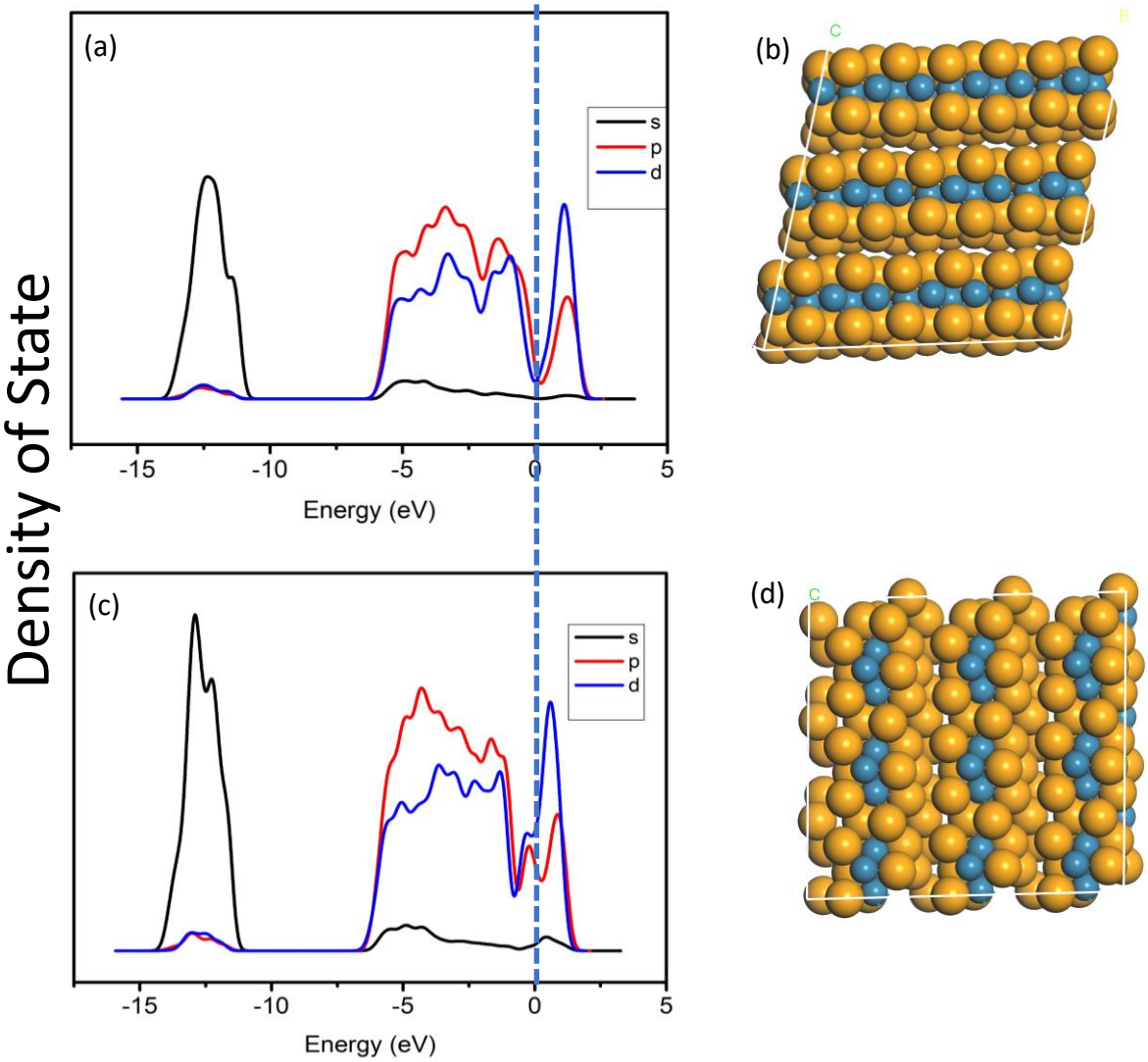


Figure 5: Density of state of (a) $ReSe_2$ cleaved along the {010} surface, (c) $ReSe_2$ cleaved along the {100}; supercell structures for (b) $ReSe_2$ cleaved along the {010} surface, (d) $ReSe_2$ cleaved along the {100}.

The electronic band structure of $ReSe_2$ has three main bands one from -15 to -10 eV, -5 to 0 eV, and lastly from 0 and 2.5 eV which were assigned to the lowest band associated with Se 4s, Se 4p hybridized with Re 5d, and last three Re 5d orbitals hybridized with Se 4p, respectively. This shows that the band structure is dominated by Re 5d states and the Se 4p states near the Fermi level. The bandgap of monolayer $ReSe_2$ was calculated to be 1.19 eV as shown in **Fig.S6(a)**, consistent with previously reported data.[36] However, the bandgap of the cleaved $ReSe_2$ monolayer along the {010} was calculated to be 0.739 eV as shown in **Fig.S6(b)**. The narrowing of the bandgap is also observed in the density of states of the cleaved surface in **Fig.5(a),** which shows a more semi-metallic character compared to the strictly semiconducting nature of $ReSe_2$ that is normally reported. This suggests that there may be

higher electrical conductivity of the $ReSe_2$ along the {010} plane which is attributed to the anisotropy of the $ReSe_2$ nanostructures.[37] The molecular models depicting the interaction between the surfactants and the $ReSe_2$ {010} surface are shown in **Fig.6**. The optimized models show that the amine group in OLA, the carbonyl group in OA, and the P=O group in TOPO anchor the surfactants to the $ReSe_2$ {010} surface as shown in **Fig.6(a, d, and g)**. This agrees with the XPS, FTIR, and NMR results, which suggested that the surfactants interact with the $ReSe_2$ nanostructures through their respective head groups. The density of states of the $ReSe_2$ cleaved along the {010} after passivation with the surfactants TOPO, OLA, and OA are shown in **Fig.6(a, d, and g)**, respectively. The interaction of the surfactants with the $ReSe_2$ {010} seems to have affected the Re 5d states and the Se 4p orbitals. There is a significant upshift in the Re d states and the Se p states near the Fermi level. The shift in the energy of the density of states shows that there is a strong interaction between the surfactants and the $ReSe_2$ {010} surface.[38]

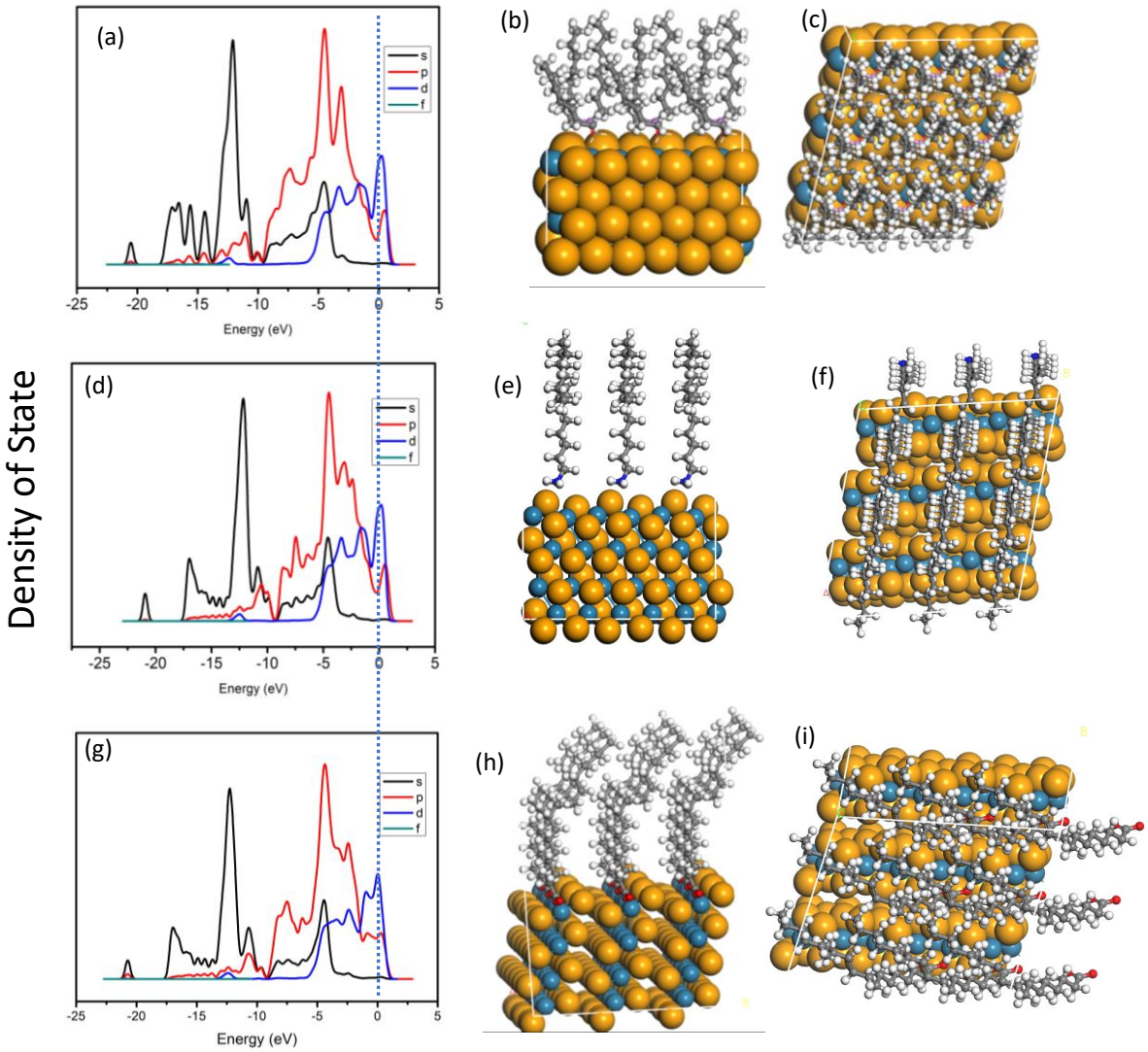


Figure 6: Supercell and density of state of the optimized cleaved crystal of $ReSe_2$, where Density of state of (a) $ReSe_2$-TOPO, (d) $ReSe_2$-OLA, (g) $ReSe_2$-OA; optimized structure of (b) $ReSe_2$-TOPO, (e) $ReSe_2$-OLA, (h) $ReSe_2$-OA; and (c) Top vi (c) $ReSe_2$-TOPO, (f) $ReSe_2$-OLA, (i) $ReSe_2$-OA.

Transmission electron microscopy (TEM) was used to investigate how the use of surfactants with different head groups affects the morphology of the synthesized nanostructures. TEM images of the $ReSe_2$ nanostructures synthesized using OLA, OA, and TOPO are shown in **Fig.7**.

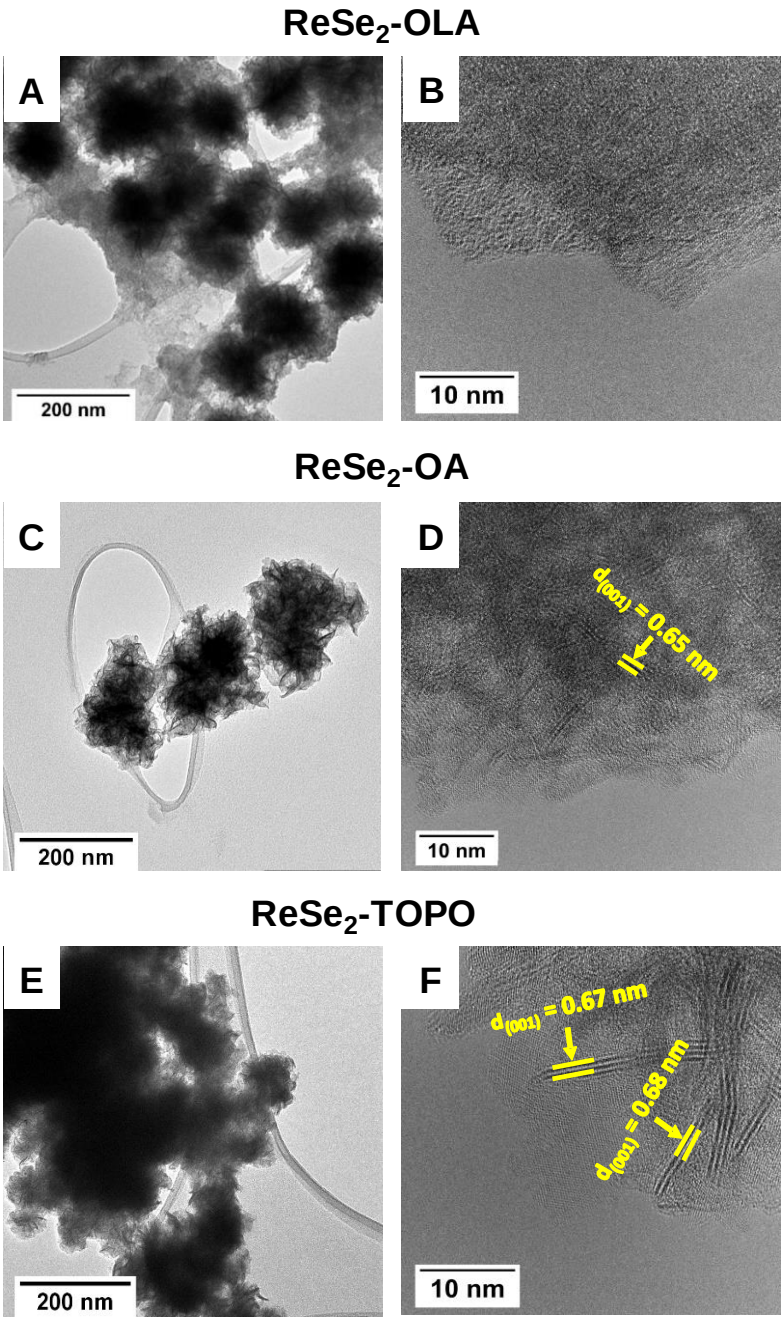


Figure 7: TEM images of the (a) $ReSe_2$-OLA (c) $ReSe_2$-OA and (e) $ReSe_2$-TOPO nanostructures. The HRTEM images of the images are shown in (b) $ReSe_2$-OLA, (d) $ReSe_2$-OA, and (f) $ReSe_2$-TOPO.

The $ReSe_2$-OLA TEM images show the formation of spherical-shaped nanostructures that resemble cotton balls growing from a flocculate as shown in **Fig.7(a)**. The flocculate explains the more amorphous nature of the $ReSe_2$-OLA nanostructures as compared to the $ReSe_2$-OA and $ReSe_2$-TOPO in the PXRD analysis. This may be due to the interaction of the OLA with

the $ReSe_2$ nanostructures. The high degree of passivation by the OLA as suggested by the computational analysis limits the growth of the $ReSe_2$ nanostructures, which in turn, affects the crystallinity and morphology of the nanostructures.[17] However, the $ReSe_2$-OA nanostructures show a very distinct flower-like morphology as shown in **Fig.7(c)**. A flower-like morphology is quite common in the colloidal synthesis of TMD nanostructures and normally arises when the nucleation process occurs rapidly in the reaction. This leads to the formation of a dense central core from which small lateral dimension nanosheets can grow, the nanosheets grow radially outward from the dense central core and this resembles a blooming flower.[39] The small lateral dimension nanosheets can also be observed in the HRTEM image of the nanoflowers shown in **Fig.7(d)**. The $ReSe_2$-TOPO nanostructures resembles an agglomerate of individual nanosheets as shown in **Fig.7(e)**. The HRTEM images of the $ReSe_2$-TOPO nanostructures in **Fig.7(f) and Fig.S7(a),** show that it is in fact a network or cluster of overlapping few-layer nanosheets. The interlayer spacing of the nanosheets was measured to be ~ 0.66 nm, which is in keeping with what has been reported in literature.[11] Moreover, these $ReSe_2$ nanoclusters are composed of nanosheets with a thickness of ~ 4-5 layers that are dominated by well-defined crystalline edges as shown in **Fig.S7(b)**, which results in an increase in the density of active sites.[40] This would suggest that this configuration of the $ReSe_2$-TOPO nanostructures would be ideal for increasing the number of active edge sites. This assertion is thoroughly explored in the electrochemical characterisation of the nanostructures.

Energy-dispersive X-ray spectroscopy (EDX) was used to investigate the elemental composition and distribution of the Se and Re elements in the $ReSe_2$ nanostructures. The EDX spectra of the $ReSe_2$ nanostructures are shown in **Fig.S8.** The spectra show the elemental composition of the nanostructures. The spectra show the presence of Re, Se, C, and Cu which is from the Cu grid used to mount the samples. The presence of O in the spectra of $ReSe_2$-OA and $ReSe_2$-TOPO is due to the oxygen in the head groups of the surfactants. The elemental mapping of the nanostructures is shown in **Fig.8**, the mapping shows that the Se atom distribution overlaps well with the Re mapping. This indicates that the Re and Se atoms are dispersed homogeneously throughout the nanostructures. This is also true for the nitrogen and oxygen atoms in the surfactants; this is to be expected as the surfactant would most likely also be homogeneously dispersed on the surface of the nanostructures.

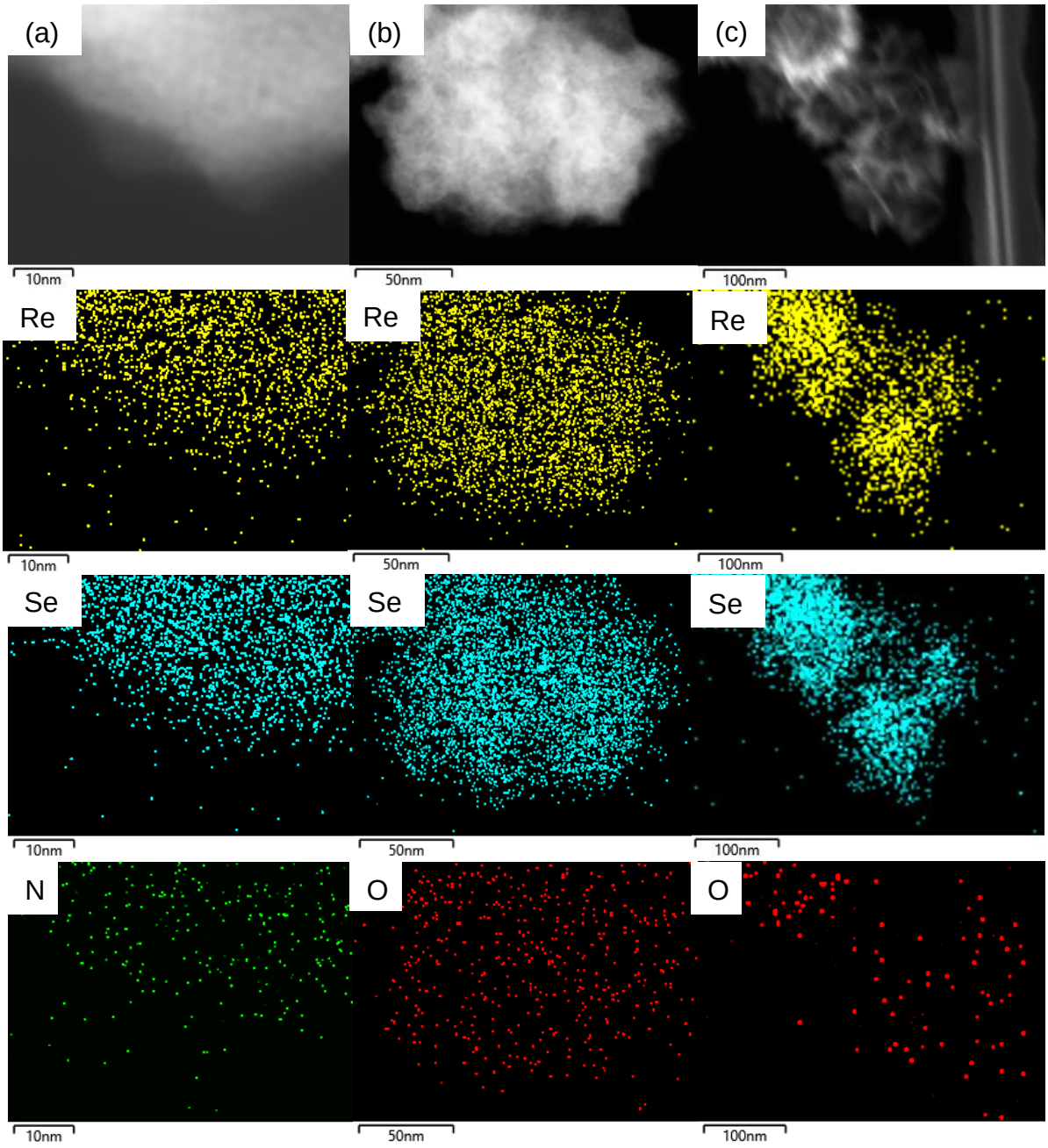


Figure 8: HAADF-STEM image and elemental mapping of the (a) $ReSe_2$-OLA, (b) $ReSe_2$-OA, and (c) $ReSe_2$-TOPO nanostructures.

Electrochemical studies of the $ReSe_2$ nanostructures were done to determine which surfactant produced the most ideal nanostructures for the HER. The polarization curves for the $ReSe_2$ nanostructures, 20% Pt/C and bare glassy carbon electrode are shown in **Fig.9(a)**. The 20% Pt/C polarization curve was included as the standard and to evaluate which of the nanostructures is ideal compared to Pt/C which is currently the best-performing catalyst.[41]

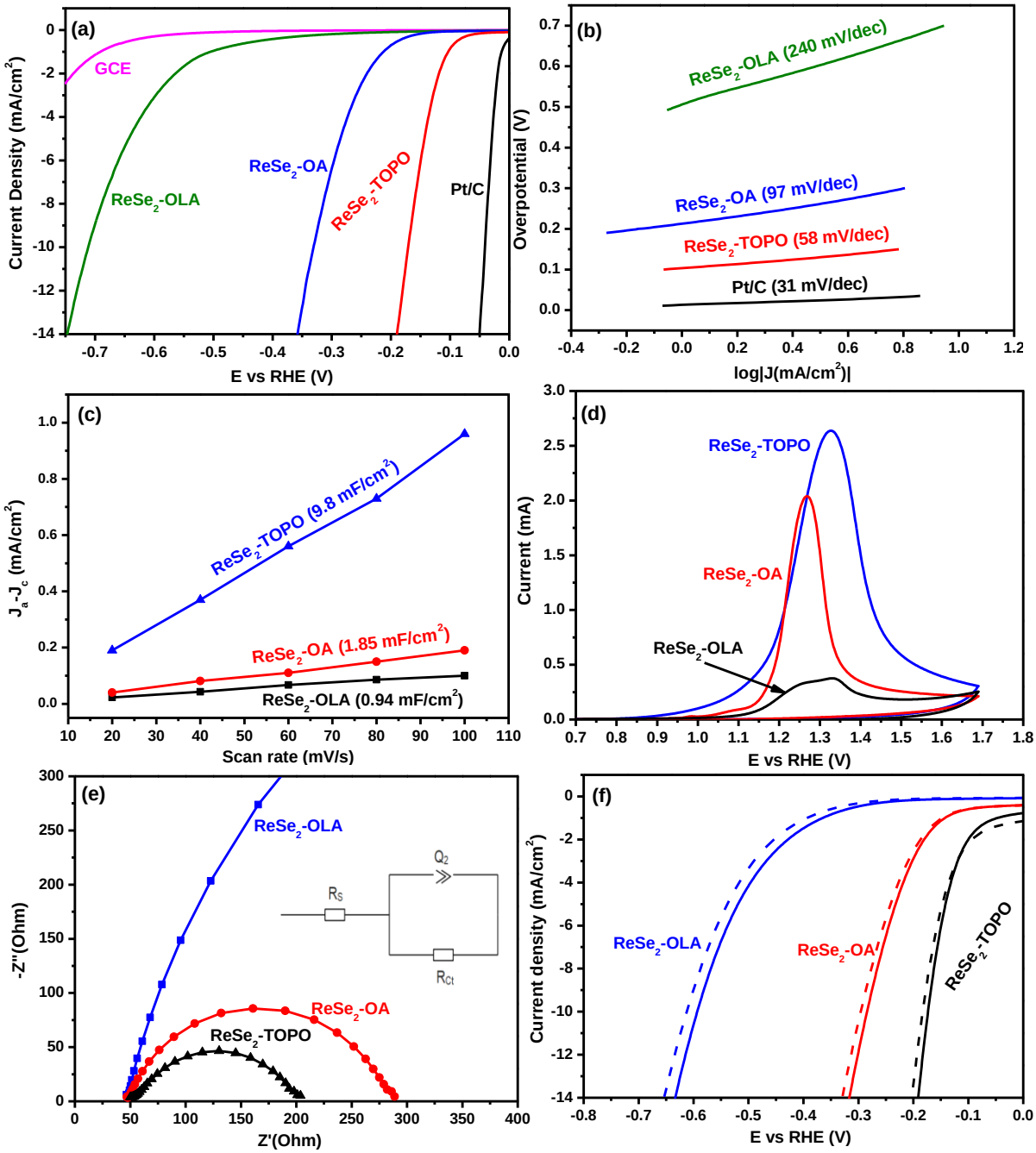


Figure 9: (a) Polarisation curves of $ReSe_2$ nanostructures, 20% Pt/C and glassy carbon (b) Tafel plots of the nanostructures synthesized with the various surfactants and that of 20% Pt/C. (c) Cdl plots of the $ReSe_2$ nanostructures (d) Anodic peaks due to the surface oxidation of the $ReSe_2$ nanostructures. (e) Nyquist plots of the $ReSe_2$ nanostructures. (f) Polarisation curves of the $ReSe_2$-TOPO nanostructures initially and after 1000 cycles.

The onset potential which is the overpotential at which the catalytic current is first observed for the $ReSe_2$ nanostructures were compared. Good performing catalysts are characterized by a low onset potential. The $ReSe_2$-TOPO nanostructures had the lowest on-set potential at 73

mV, followed by that of $ReSe_2$-OA at 168 mV and the highest on-set potential was for the $ReSe_2$-OLA nanostructures at 384 mV. Another useful parameter in evaluating the performance of electrocatalyst towards the HER, is the overpotential needed to reach a specified current density. The current density reported is typically 10 mA/cm^2 (η_{10}). This current density corresponds to the working current density of the most cost-competitive PEC (photoelectrochemical water splitting) system. Ultimately the lower the overpotential needed to reach this specified current density the better the catalyst performs. The $ReSe_2$-TOPO nanostructures had the lowest measured η_{10} at 171 mV. The overpotential was much higher for the $ReSe_2$-OA and $ReSe_2$-OLA at 331 mV and 712 mV respectively. As the $ReSe_2$-TOPO nanostructures have a lower overpotential needed to initiate the reaction and a lower overpotential to reach 10 mA/cm^2 this clearly suggests that the $ReSe_2$-TOPO nanostructures are more active for the HER. The Tafel slope is also a useful property to consider when evaluating nanostructures for the HER. The Tafel slope can be understood as the sensitivity of the electric current response to an applied potential. It can be used to provide insights into the mechanism and rate-determining step of the catalyst surface. The Tafel slope can thus be obtained from the Tafel plot (over-potential vs log |current density|) which is obtained by replotting the LSV curve. The Tafel slope is obtained by fitting a straight line to the Tafel plot and using the Tafel equation.

$$\eta = a + b\log(J) \qquad (2)$$

Where η is the overpotential, J is the current density, and b is the Tafel slope. As already mentioned, the Tafel slope can be used to give insights into the mechanism and rate-determining step of the catalyst surface. The HER in acidic media can be described in three steps:

(Volmer step) $H_3O^+ + e^- + M \rightleftharpoons M\text{-}H + H_2O$, (120 mV/dec) (3)

(Heyrovsky step) $M\text{-}H + H_3O^+ + e^- \rightleftharpoons H_2 + H_2O + M$, (40 mV/dec) (4)

(Tafel step) $2M\text{-}H \rightleftharpoons H_2 + 2M$, (30 mV/dec) (5)

The Volmer reaction is the primary discharge step in which protons are adsorbed to active sites on the surface of the catalysts and combine with electrons to form adsorbed hydrogen atoms. This step is followed by either an electrochemical desorption step (Heyrovsky reaction) or a

recombination step (Tafel reaction). The Tafel plots of the $ReSe_2$ nanostructures is shown in **Fig.9(b)**. The Tafel slope of the $ReSe_2$-TOPO nanostructures was lower than that of the other two nanostructures at 58 mV/dec, which suggests that the electrochemical desorption is the rate-determining step, and thus the reaction proceeds by the Volmer-Heyrovsky mechanism. While the Tafel slope of the $ReSe_2$-OA flower-like nanostructures and the $ReSe_2$-OLA nanostructures was measured at 97 mV/dec and 240 mV/dec respectively. This suggests that the Volmer step is the rate-determining step for the $ReSe_2$-OLA and $ReSe_2$-OA electrocatalysts. These results were unexpected as it has been reported that flower-like nanostructures are normally ideal for HER applications as they ensure maximal exposure of the active sites.[42-43] Indeed, the flower-like nanostructures had far better activity than the $ReSe_2$-OLA nanostructures with spherical morphology, but its activity paled in comparison to that of the $ReSe_2$-TOPO nanostructures which were composed of a network of numerous overlapping nanosheets. To further investigate the reason for this, the surface area of the nanostructures was determined. The geometric surface area was determined using BET surface area measurements and the electrochemically active surface area (ECSA) was determined using the double-layer capacitance (C_{dl}) of the nanostructures. Measuring the geometric catalyst surface area using BET may not give an accurate estimation of the active sites in TMD nanostructures as it cannot discriminate between the active edge sites and the inactive basal plane. However, doing so can still be useful because the number of active sites scales with catalyst surface area.[42] The $ReSe_2$-TOPO nanostructures had the highest measured specific surface area and pore volume at 43 m^2/g and 0.16 cm^3/g. The $ReSe_2$-OA nanostructures had the second highest with 17 m^2/g specific surface area and 0.13 cm^3/g pore volume. The $ReSe_2$-OLA had the lowest measured specific surface area and pore volume at 0.9 m^2/g and 0.06 cm^3/g respectively. This lines up perfectly with the electrochemical analysis of the nanostructures in terms of performance, this certainly suggests that the $ReSe_2$-TOPO has more exposed active edge sites compared to the other nanostructures. Cyclic voltammetry (CV) was employed to determine the C_{dl}, the current response from the CV curves in the potential range between 0.2V to 0.6V vs RHE shown in **Fig.S9** is due to the double-layer charging. The electrochemical double layer can be used to estimate the effective electrochemical surface area because it is expected that the double layer capacitance scales with the active surface area.[7] The estimation is done by plotting ΔJ (J_a-J_c) vs the scan rate at 0.41 V vs RHE which is shown in **Fig.9(c)**, in this linear plot, the slope is the C_{dl}. The double-layer capacitance of the TOPO synthesized nanostructures was far higher than that of the OA and OLA synthesized nanostructures at 9.8 mF/cm^2, 1.85 mF/cm^2, and 0.94 mF/cm^2, respectively. This is exactly what one would have expected when looking at the

activity of the nanostructures since the ECSA represents the electrode area that is accessible to the electrolyte and is available for charge transfer. It stands to reason that the TOPO synthesized nanostructures have more active edge-sites that are exposed for HER. This was also confirmed by looking at the anodic peaks due to the surface oxidation of the $ReSe_2$ nanostructures shown in **Fig.9(d)**.[19,44] The area of the peaks represents the amount of charge needed to fully oxidize the surface of the nanostructures. There is significantly more charge required for the oxidation of the $ReSe_2$-TOPO nanostructures, which suggests that there is far more available surface area to oxidize than for the $ReSe_2$-OA and $ReSe_2$-OLA nanostructures. This corroborates the results from the ECSA analysis which suggest that $ReSe_2$-TOPO has a higher number of exposed active sites, followed by $ReSe_2$-OA and lastly $ReSe_2$-OLA. The maximal exposure of the active sites in $ReSe_2$-TOPO coupled with the limited interaction of the TOPO molecules with the edge sites acts synergistically to enable the excellent catalytic activity of the nanostructures towards the HER. The use of OA and especially OLA as the surfactant results in a minimal exposure of the active sites which impedes the catalytic activity. Another important parameter to evaluate electrocatalysts for the HER is the stability of the electrocatalyst in acidic media. The stability was evaluated by performing a thousand repeated LSV scans at 100 mVs^{-1} on the $ReSe_2$-TOPO nanostructures. As shown in **Fig.9(f)**, the comparison of the polarisation curves measured initially and after 1000 cycles shows that there is only a slight decay in the current density which confirms the high stability of the nanostructures. Electrochemical impedance spectroscopy (EIS) was conducted to understand the electron transfer kinetics of the HER on the $ReSe_2$ nanostructures. The EIS results were represented in the form of Nyquist plots as shown in **Fig.9(e)**. The Nyquist plots were fitted to the equivalence circuit shown as an insert in **Fig.9(e)**. The equivalence circuit components labelled R_s, Q_2 and R_{ct} correspond to the solution resistance, constant phase element, and charge transfer resistance respectively. The Nyquist plots have a distinct semicircle shape, but the semicircles are slightly depressed which is why Q_2 is represented as a constant phase element instead of the ideal double capacitance.[45-46] The charge transfer resistance of the $ReSe_2$-TOPO nanostructures which gives information on the electrode kinetics was found to be 167.7 Ω which was smaller than that of the $ReSe_2$-OA and $ReSe_2$-OLA nanostructures. The charge transfer resistance of the $ReSe_2$-OA and $ReSe_2$-OLA was found to be 250.5 Ω and 175.2 Ω respectively. This shows that there is less resistance for the charge transfer processes of the HER on the $ReSe_2$-TOPO compared to the other catalysts. Overall, the R_{ct} and R_s are rather high compared to what is normally reported, this can be attributed to the passivation of the electrocatalysts which can impair the charge transfer and ion transport properties.[19,47] The performance of the electrocatalysts in this study

was compared to that of other $ReSe_2$ nanostructures synthesized using other methods. The comparison of the synthesized nanostructures and analogous nanostructures in literature is shown in **Table 4**. This shows that the performance of the $ReSe_2$-TOPO nanostructures towards HER is comparable to that of the best performing reported catalyst.

Table 4: Comparison of the catalytic performance of the synthesized nanostructures and other $ReSe_2$ nanostructures in literature

HER catalyst	Synthesis method	η_{10} (mV)	Tafel slope (mV/dec)	Onset potential (mV)	Ref
$ReSe_2$ Flower-shaped	CVD	270	76	-	8
$ReSe_2$ nanosheets	colloidal	143	62	-	49
$ReSe_2$ microspheres	Hydrothermal	-	68	80	7
$ReSe_2$	exfoliation	239	138		48
$ReSe_2$	Electrochemical treatment	430	130	-	50
$ReSe_2$-OLA	Colloidal	712	240	384	**This work**
$ReSe_2$-OA	Colloidal	331	97	168	**This work**
$ReSe_2$-TOPO	Colloidal	171	58	73	**This work**

4. Conclusions

In summary, the $ReSe_2$ nanostructures were successfully synthesized using three different solvents/surfactants. The FTIR, XPS, and NMR analysis of the synthesized nanostructures showed that the $ReSe_2$ nanostructures were capped with the surfactants through their respective head groups. The OLA capped the $ReSe_2$ through the amine, The OA capped the $ReSe_2$ in a monodentate fashion through either the C=O or the C-O, and the TOPO capped the $ReSe_2$ nanostructures through the P=O functional group. This result was corroborated by the computational analysis of the interaction between the nanostructures and the surfactants. The computational analysis showed that OLA had the largest number of molecules that could interact with the surface of the $ReSe_2$ nanostructures. This resulted in a high degree of

passivation that seemed to inhibit the growth of the $ReSe_2$ nanostructures. The limitation on the growth of the nanostructures and the OLA molecules blocking the active sites resulted in poor catalytic activity. However, the TOPO molecules had the least interaction with the $ReSe_2$ nanostructures which resulted in the formation of a network of few-layer nanosheets with well-defined crystalline edges. This resulted in maximal exposure of the active edge sites which was demonstrated in the electrochemical characterisation of the nanostructures. The bulky nature of the TOPO molecules also resulted in the lowest number of molecules that could interact with the surface of the $ReSe_2$ nanostructures. The exposure of the edge sites and the limited interaction with the surface of the $ReSe_2$ nanostructures worked synergistically to afford the TOPO capped nanostructures superior catalytic activity towards the HER. The OA capped nanostructures had the second largest number of molecules that could interact with the edge sites. This is reflected in the catalytic performance of the nanostructures as they exhibited improved catalytic performance compared to the OLA capped nanostructures. However, the catalytic performance of the OA capped nanostructures paled in comparison to the catalytic performance of the TOPO capped $ReSe_2$ nanostructures.

5. References

1. Carr, S.; Premier, G. C.; Guwy, A. J.; Dinsdale, R. M.; Maddy, J., Hydrogen storage and demand to increase wind power onto electricity distribution networks. *Int. J. Hydrog. Energy* **2014,** *39* (19), 10195-10207.

2. Wang, S.; Lu, A.; Zhong, C.-J., Hydrogen production from water electrolysis: role of catalysts. *Nano Converg.* **2021,** *8* (1), 1-23.

3. Wu, L.; Hofmann, J. P., Comparing the Intrinsic HER Activity of Transition Metal Dichalcogenides: Pitfalls and Suggestions. *ACS Energy Lett.* **2021,** *6* (7), 2619-2625.

4. Ruiz, K. H.; Liu, J.; Tu, R.; Li, M.; Zhang, S.; Garcia, J. R. V.; Mu, S.; Li, H.; Goto, T.; Zhang, L., Effect of microstructure on HER catalytic properties of MoS_2 vertically standing nanosheets. *J. Alloys Compd.* **2018,** *747*, 100-108.

5. Najafi, L.; Bellani, S.; Oropesa-Nuñez, R.; Ansaldo, A.; Prato, M.; Del Rio Castillo, A.E.; Bonaccorso, F. Engineered $MoSe_2$-based heterostructures for efficient electrochemical hydrogen evolution reaction. *Adv. Energy Mater.* **2018**, *8*, 1703212.

6. Najafi, L.; Bellani, S.; Oropesa-Nuñez, R.; Martín-García, B.; Prato, M.; Mazánek, V.; Debellis, D.; Lauciello, S.; Brescia, R.; Sofer, Z., Niobium disulphide (NbS_2)-based (heterogeneous) electrocatalysts for an efficient hydrogen evolution reaction. *J. Mater. Chem. A* **2019,** *7* (44), 25593-25608.

7. Qi, F.; Wang, X.; Zheng, B.; Chen, Y.; Yu, B.; Zhou, J.; He, J.; Li, P.; Zhang, W.; Li, Y.,Self-assembled chrysanthemum-like microspheres constructed by few-layer $ReSe_2$ nanosheets as a highly efficient and stable electrocatalyst for hydrogen evolution reaction. *Electrochim. Acta.* **2017,** *224*, 593-599.

8. Jiang, S.; Zhang, Z.; Zhang, N.; Huan, Y.; Gong, Y.; Sun, M.; Shi, J.; Xie, C.; Yang, P.; Fang, Q., Application of chemical vapor–deposited monolayer $ReSe_2$ in the electrocatalytic hydrogen evolution reaction. *Nano Res.* **2018,** *11* (4), 1787-1797.

9. Zhuang, M.; Xu, G.-L.; Gan, L.-Y.; Dou, Y.; Sun, C.-J.; Ou, X.; Xie, Y.; Liu, Z.; Cai, Y.; Ding, Y., Sub-5 nm edge-rich 1T′-$ReSe_2$ as bifunctional materials for hydrogen evolution and sodium-ion storage. *Nano Energy.* **2019,** *58*, 660-668.

10. Liu, Z.; Ou, X.; Zhuang, M.; Li, J.; Hossain, M. D.; Ding, Y.; Wong, H.; You, J.; Cai, Y.; Abidi, I. H., Confinement-Enhanced Rapid Interlayer Diffusion within Graphene-Supported Anisotropic $ReSe_2$ Electrodes. *ACS Appl. Mater. Interfaces.* **2019,** *11* (34), 31147-31154.

11. Li, J.; Zhou, Q.; Yuan, C.; Cheng, P.; Hu, X.; Huang, W.; Gao, X.; Wang, X.; Jin, M.; Nötzel, R., Direct growth of vertically aligned $ReSe_2$ nanosheets on conductive electrode for electro-catalytic hydrogen production. *J. Colloid Interface Sci.* **2019,** *553*, 699-704.

12. Coogan, Á.; Gun'ko, Y. K., Solution-based “bottom-up” synthesis of group VI transition metal dichalcogenides and their applications. *Mater. Adv.* **2021**, 2, 146-164.

13. Geisenhoff, J.Q.; Tamura, A.K.; Schimpf, A. Using ligands to control reactivity, size and phase in the colloidal synthesis of WSe_2 nanocrystals. *Chem. Commun.* **2019**, *55*, 8856–8859

14. Jeong, S.; Yoo, D.; Jang, J.-t.; Kim, M.; Cheon, J., Well-defined colloidal 2-D layered transition-metal chalcogenide nanocrystals via generalized synthetic protocols. *J. Am. Chem. Soc.* **2012,** *134* (44), 18233-18236.

15. Bakshi, M. S., How surfactants control crystal growth of nanomaterials. *Cryst. Growth & Des.* **2016,** *16* (2), 1104-1133.

16. Mansouri, A.; Semagina, N., Colloidal Synthesis Protocol of Shape-and Dimensionally-Controlled Transition-Metal Chalcogenides and Their Hydrodesulfurization Activities. *ACS Appl. Nano Mater.* **2018,** *1* (9), 4408-4412.

17. Machogo, L. F.; Sithole, R. K.; Phao, N.; Kolokoto, T.; Gqoba, S. S.; Mlambo, M.; Moloto, M. J.; Shumbula, P. M.; Mdluli, P. S.; Moloto, N., Probing the structure and functionalized surface of colloidal AuSe. *Mater. Sci. Eng., B* **2021,** *263*, 114878.

18. Jung, W.; Lee, S.; Yoo, D.; Jeong, S.; Miró, P.; Kuc, A.; Heine, T.; Cheon, J., Colloidal synthesis of single-layer MSe_2 (M= Mo, W) nanosheets via anisotropic solution-phase growth approach. *J. Am. Chem. Soc.* **2015,** *137* (23), 7266-7269.

19. Guo, W.; Chen, Y.; Wang, L.; Xu, J.; Zeng, D.; Peng, D.-L., Colloidal synthesis of $MoSe_2$ nanonetworks and nanoflowers with efficient electrocatalytic hydrogen-evolution activity. *Electrochim. Acta.* **2017,** *231*, 69-76.

20. Pandit, S.; Karunakaran, S.; Boda, S. K.; Basu, B.; De, M., High antibacterial activity of functionalized chemically exfoliated MoS_2. *ACS Appl. Mater. Interfaces.* **2016,** *8* (46), 31567-31573.

21. Cheng, L.; Liu, J.; Gu, X.; Gong, H.; Shi, X.; Liu, T.; Wang, C.; Wang, X.; Liu, G.; Xing, H., PEGylated WS_2 nanosheets as a multifunctional theranostic agent for in vivo dual-modal CT/photoacoustic imaging guided photothermal therapy. *Adv. Mater.* **2014,** *26* (12), 1886-1893.

22. Henckel, D. A.; Lenz, O. M.; Krishnan, K. M.; Cossairt, B. M., Improved HER catalysis through facile, aqueous electrochemical activation of nanoscale WSe_2. *Nano lett.* **2018,** *18* (4), 2329-2335.

23. Seley, D. B.; Nath, M.; Parkinson, B., $ReSe_2$ nanotubes synthesized from sacrificial templates. *J. Mater. Chem.* **2009,** *19* (11), 1532-1534.

24. Xing, L.; Yan, X.; Zheng, J.; Xu, G.; Lu, Z.; Liu, L.; Wang, J.; Wang, P.; Pan, X.; Jiao, L., Highly crystalline $ReSe_2$ atomic layers synthesized by chemical vapor transport. *InfoMat* **2019,** *1* (4), 552-558.

25. Wilson, D.; Langell, M., XPS analysis of oleylamine/oleic acid capped Fe_3O_4 nanoparticles as a function of temperature. *Appl. Surf. Sci.* **2014,** *303*, 6-13.

26. Mourdikoudis, S.; Liz-Marzán, L. M., Oleylamine in nanoparticle synthesis. *Chem. Mater.* **2013,** *25* (9), 1465-1476.

27. Wu, H.; Chen, W., Synthesis and reaction temperature-tailored self-assembly of copper sulfide nanoplates. *Nanoscale* **2011,** *3* (12), 5096-5102.

28. Caruntu, D.; Rostamzadeh, T.; Costanzo, T.; Parizi, S. S.; Caruntu, G., Solvothermal synthesis and controlled self-assembly of monodisperse titanium-based perovskite colloidal nanocrystals. *Nanoscale* **2015,** *7* (30), 12955-12969.

29. Zherebetskyy, D.; Scheele, M.; Zhang, Y.; Bronstein, N.; Thompson, C.; Britt, D.; Salmeron, M.; Alivisatos, P.; Wang, L.-W., Hydroxylation of the surface of PbS nanocrystals passivated with oleic acid. *Science* **2014,** *344* (6190), 1380-1384.

30. Onwudiwe, D. C.; Hrubaru, M.; Ebenso, E. E., Synthesis, structural and optical properties of TOPO and HDA capped cadmium sulphide nanocrystals, and the effect of capping ligand concentration. *J. Nanomater.* **2015,** *2015*.

31. Grisorio, R.; Quarta, D.; Fiore, A.; Carbone, L.; Suranna, G. P.; Giansante, C., The dynamic surface chemistry of colloidal metal chalcogenide quantum dots. *Nanoscale Adv.* **2019,** *1* (9), 3639-3646.

32. Zimdars, J.; Bredol, M., On the influence of coordinating solvents on the reduction of selenium for the phosphine-free synthesis of metal selenide nanoparticles. *New J. Chem.* **2016,** *40* (2), 1137-1142.

33. Hens, Z.; Moreels, I.; Martins, J. C., In situ 1H NMR study on the trioctylphosphine oxide capping of colloidal InP nanocrystals. *ChemPhysChem* **2005,** *6* (12), 2578-2584.

34. Kang, B.; Kim, Y.; Cho, J. H.; Lee, C., Ambipolar transport based on CVD-synthesized $ReSe_2$. *2D Mater.* **2017,** *4* (2), 025014.

35. Chen, X.; Lei, B.; Zhu, Y.; Zhou, J.; Liu, Z.; Ji, W.; Zhou, W., Pristine edge structures of T″-phase transition metal dichalcogenides ($ReSe_2$, ReS_2) atomic layers. *Nanoscale* **2020,** *12* (32), 17005-17012.

36. Ho, C.; Huang, Y.; Chen, J.; Dann, T.; Tiong, K.-K., Electronic structure of ReS_2 and $ReSe_2$ from first-principles calculations, photoelectron spectroscopy, and electrolyte electroreflectance. *Phys. Rev. B* **1999,** *60* (23), 15766.

37. Hu, S.; Liang, C.; Tiong, K.-K.; Huang, Y.; Lee, Y., Electrical anisotropy of W-doped $ReSe_2$ crystals. *J. Electrochem. Soc.* **2006,** *153* (8), J100.

38. Hou, W.; Mi, H.; Peng, R.; Peng, S.; Zeng, W.; Zhou, Q., First-principle insight into Ga-doped MoS_2 for sensing SO_2, SOF_2 and SO_2F_2. *Nanomaterials* **2021,** *11* (2), 314.

39. Sun, D.; Feng, S.; Terrones, M.; Schaak, R. E., Formation and interlayer decoupling of colloidal $MoSe_2$ nanoflowers. *Chem. Mater.* **2015,** *27* (8), 3167-3175.

40. He, Q.; Wang, L.; Yin, K.; Luo, S., Vertically aligned ultrathin 1T-WS_2 nanosheets enhanced the electrocatalytic hydrogen evolution. *Nanoscale Res. Lett.* **2018,** *13* (1), 1-9.

40. Vesborg, P. C.; Seger, B.; Chorkendorff, I., Recent development in hydrogen evolution reaction catalysts and their practical implementation. *J. Phys. Chem. Lett.* **2015,** *6* (6), 951-957.

41. Mahmood, N.; Yao, Y.; Zhang, J. W.; Pan, L.; Zhang, X.; Zou, J. J., Electrocatalysts for hydrogen evolution in alkaline electrolytes: mechanisms, challenges, and prospective solutions. *Adv. Sci.* **2018,** *5* (2), 1700464.

42. Qu, Y.; Shao, M.; Shao, Y.; Yang, M.; Xu, J.; Kwok, C. T.; Shi, X.; Lu, Z.; Pan, H., Ultra-high electrocatalytic activity of VS_2 nanoflowers for efficient hydrogen evolution reaction. *J. Mater. Chem. A.* **2017,** *5* (29), 15080-15086.

43. Liu, X.; Liu, L.; Wu, Y.; Wang, Y.; Yang, J.; Wang, Z., Rosette-like MoS_2 nanoflowers as highly active and stable electrodes for hydrogen evolution reactions and supercapacitors. *RSC Adv.* **2019,** *9* (24), 13820-13828.

44. Benck, J. D.; Hellstern, T. R.; Kibsgaard, J.; Chakthranont, P.; Jaramillo, T. F., Catalyzing the hydrogen evolution reaction (HER) with molybdenum sulfide nanomaterials. *ACS Catal.* **2014,** *4* (11), 3957-3971.

45. Bonde, J.; Moses, P. G.; Jaramillo, T. F.; Nørskov, J. K.; Chorkendorff, I., Hydrogen evolution on nano-particulate transition metal sulfides. *Faraday Discuss.* **2009,** *140*, 219-231.

46. Kumar, S.; Sahoo, P. K.; Satpati, A. K., Electrochemical and SECM investigation of MoS_2/GO and MoS_2/rGO nanocomposite materials for HER electrocatalysis. *ACS Omega.* **2017,** *2* (11), 7532-7545.

47. Zhao, W.; Dong, B.; Guo, Z.; Su, G.; Gao, R.; Wang, W.; Cao, L., Colloidal synthesis of VSe_2 single-layer nanosheets as novel electrocatalysts for the hydrogen evolution reaction. *Chem.Comm.* **2016,** *52* (59), 9228-9231.

48. Wang, R.; Han, J.; Xu, P.; Gao, T.; Zhong, J.; Wang, X.; Zhang, X.; Li, Z.; Xu, L.; Song, B., Dual-Enhanced Doping in $ReSe_2$ for Efficiently Photoenhanced Hydrogen Evolution Reaction. *Adv. Sci.* **2020,** *7* (9), 2000216.

49. Kwon, I. S.; Kwak, I. H.; Ju, S.; Kang, S.; Han, S.; Park, Y. C.; Park, J.; Park, J., Adatom Doping of Transition Metals in $ReSe_2$ Nanosheets for Enhanced Electrocatalytic Hydrogen Evolution Reaction. *ACS nano* **2020,** *14* (9), 12184-12194.

50. Luxa, J.; Marvan, P.; Lazar, P.; Sofer, Z., Chalcogenide vacancies drive the electrocatalytic performance of rhenium dichalcogenides. *Nanoscale* **2019,** *11* (31), 14684-14690.

6. Supplementary information

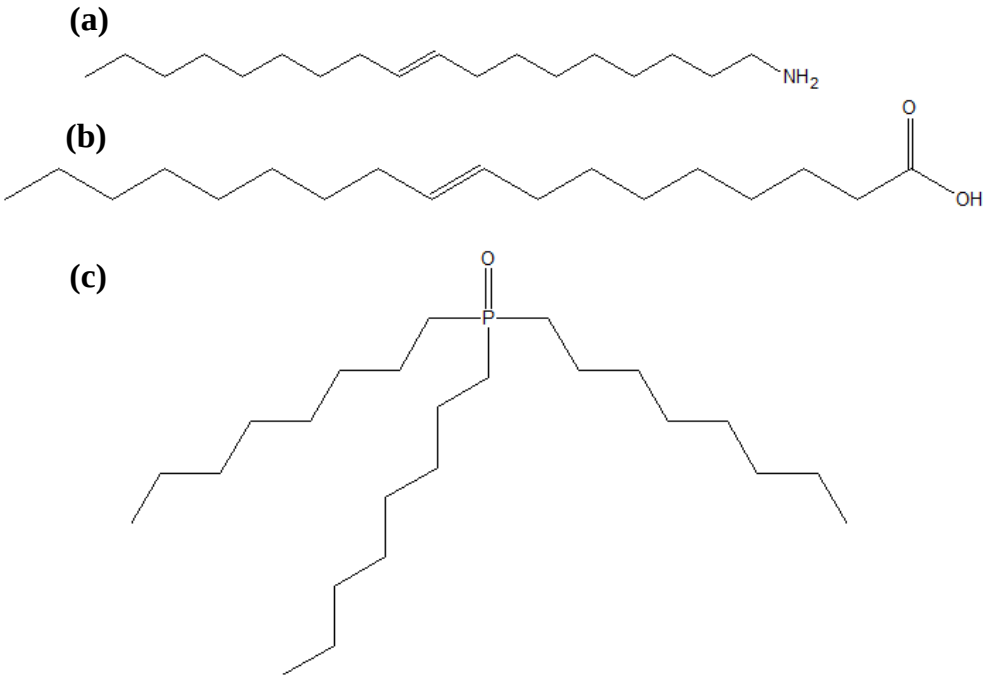


Figure S1: Structure of the surfactants and their respective head groups. (a) oleylamine, (b) oleic acid, and (c) trioctylphosphine oxide.

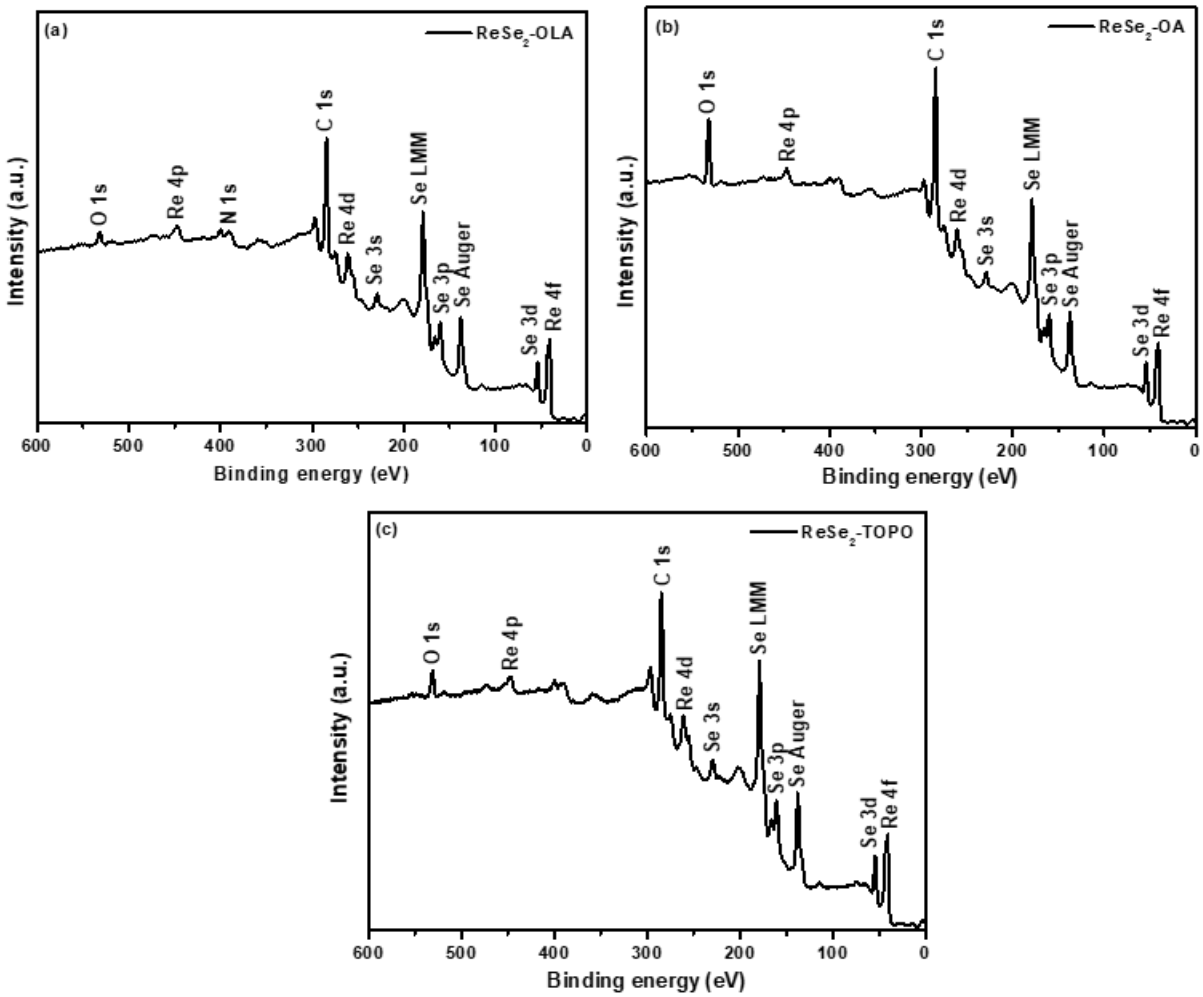


Figure S2: XPS survey spectra of (a) $ReSe_2$-OLA, (b) $ReSe_2$-OA, and $ReSe_2$-TOPO.

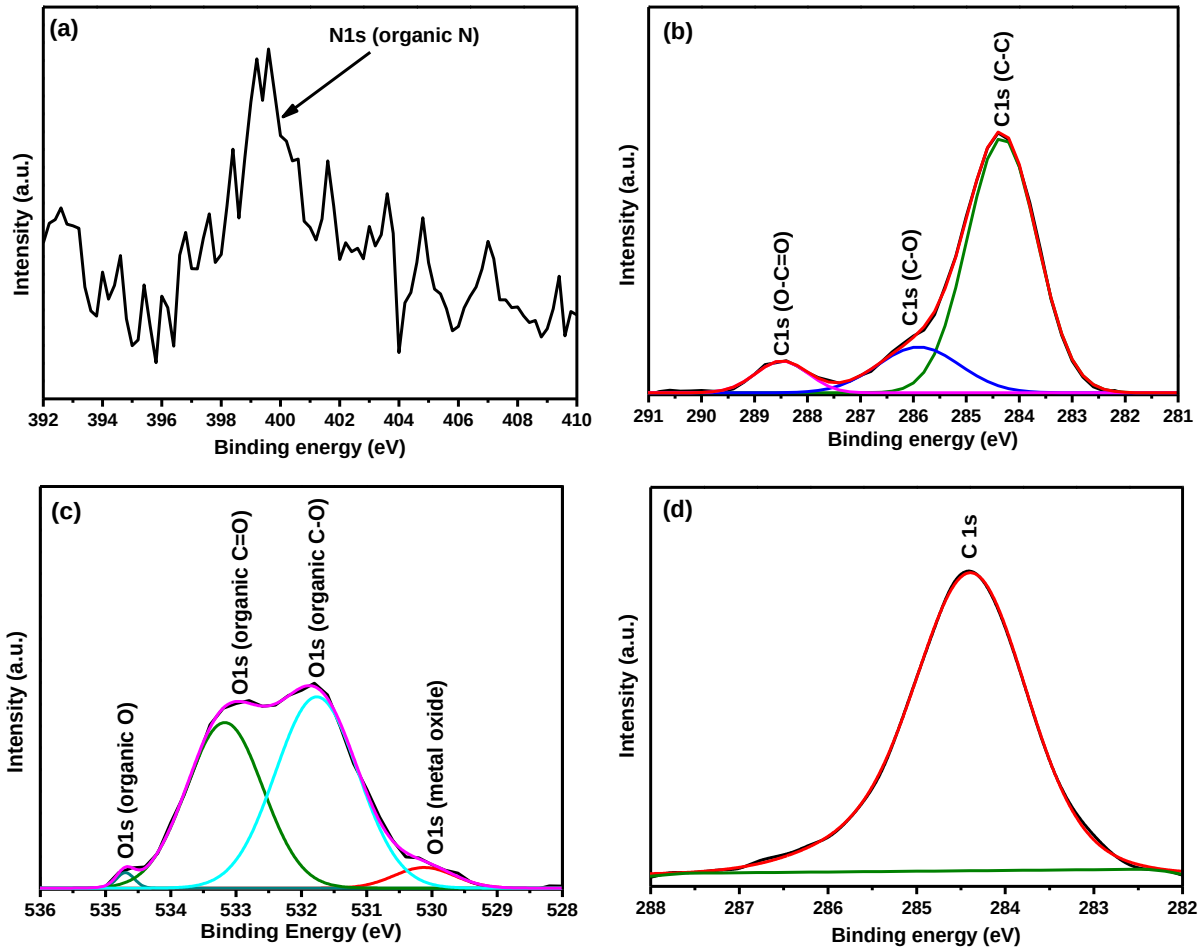


Figure S3: (a) N1s spectrum of $ReSe_2$-OLA, (b) C1s spectrum of $ReSe_2$-OA, and (c) O1s spectrum of $ReSe_2$-OA.

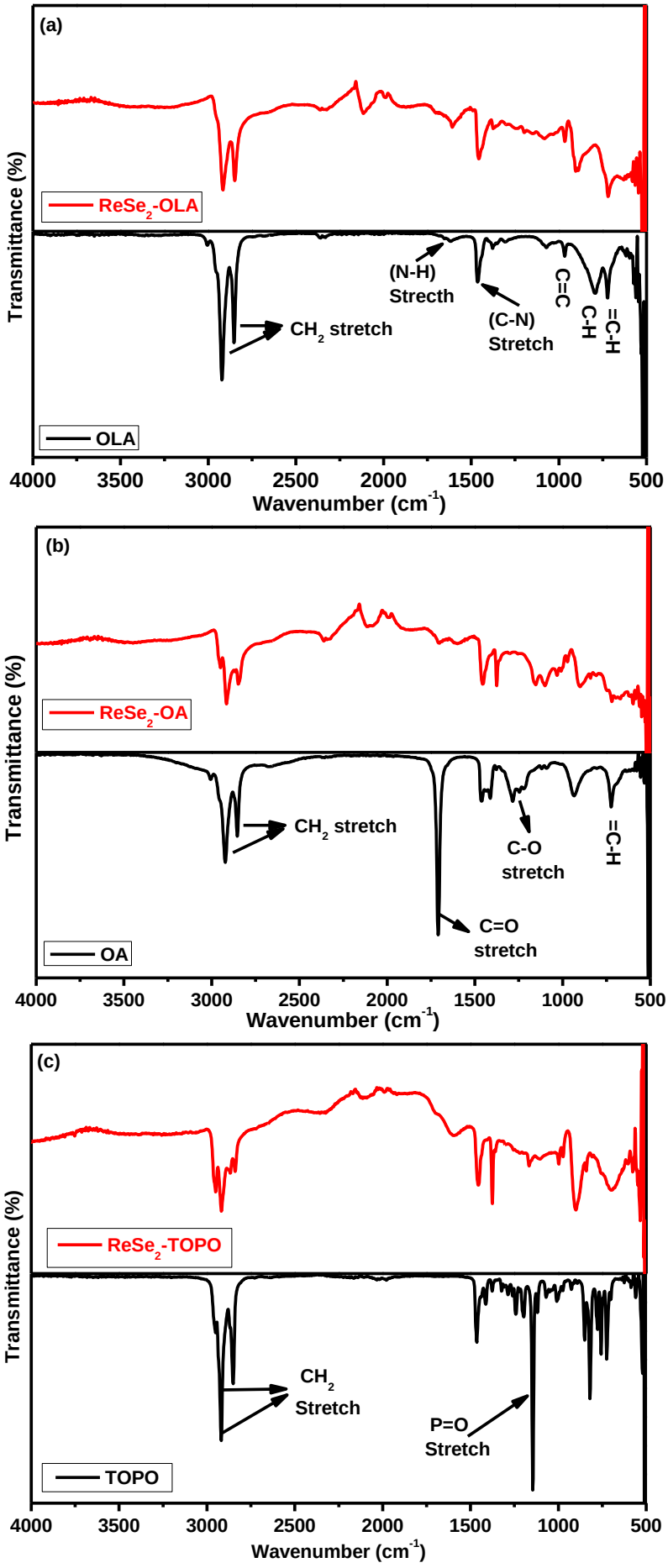

(a)
ReSe2-OLA
OLA
(N-H)
Strecth
(C-N)
Stretch
CH2 stretch
C=C
C-H
=C-H
Transmittance (%)
4000
3500
3000
2500
2000
1500
1000
500
Wavenumber (cm-1)
(b)
ReSe2-OA
OA
CH2 stretch
C-O
stretch
C=O
stretch
=C-H
Transmittance (%)
4000
3500
3000
2500
2000
1500
1000
500
Wavenumber (cm-1)
(c)
ReSe2-TOPO
TOPO
CH2
Stretch
P=O
Stretch
Transmittance (%)
4000
3500
3000
2500
2000
1500
1000
500
Wavenumber (cm-1)

Figure S4: FTIR spectra of free surfactant and capped nanomaterials for (a) $ReSe_2$-OLA, (b) $ReSe_2$-OA, and (c) $ReSe_2$-TOPO.

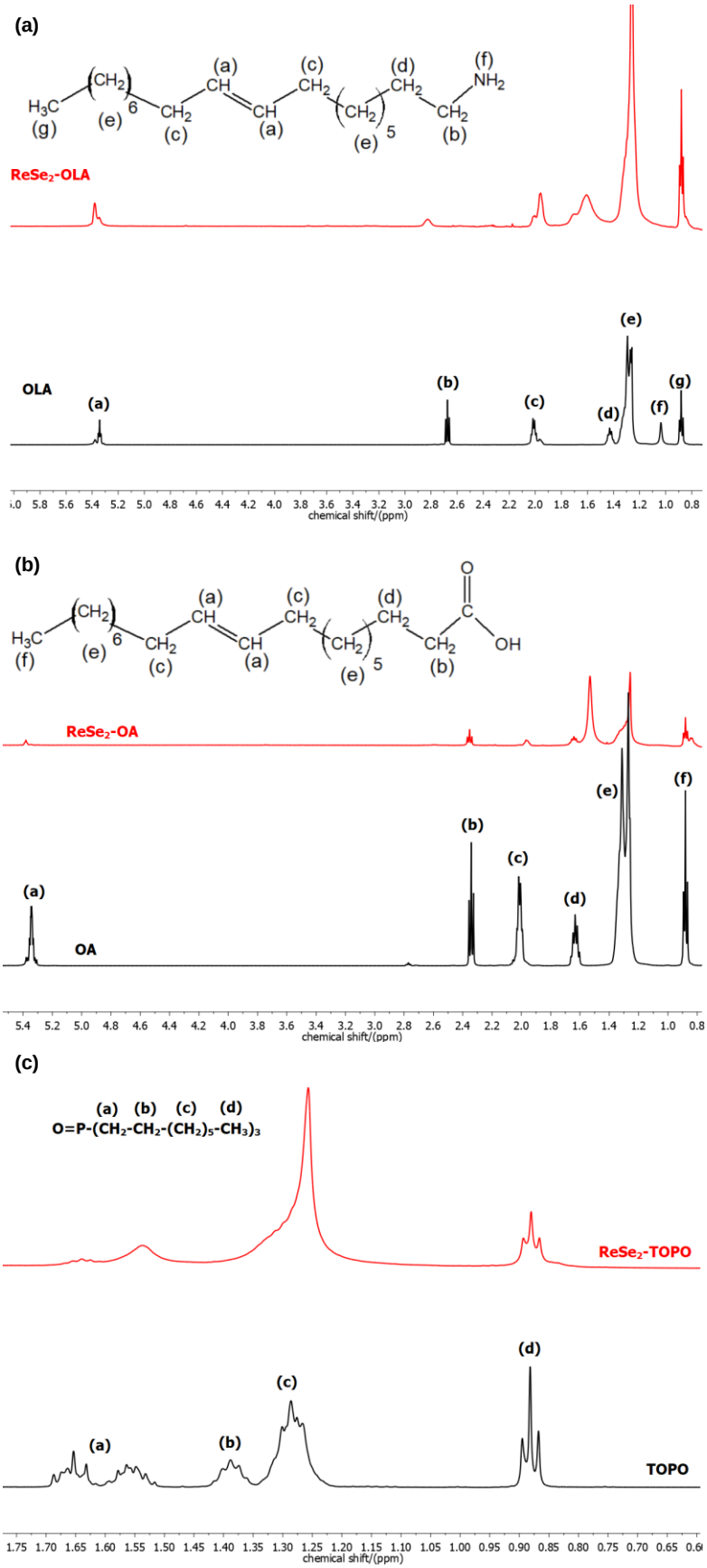


Figure S5: The ^{1}H NMR spectra of capped nanomaterials and their free surfactants for (a) $ReSe_2$-OLA, (b) $ReSe_2$-OA, and $ReSe_2$-TOPO.

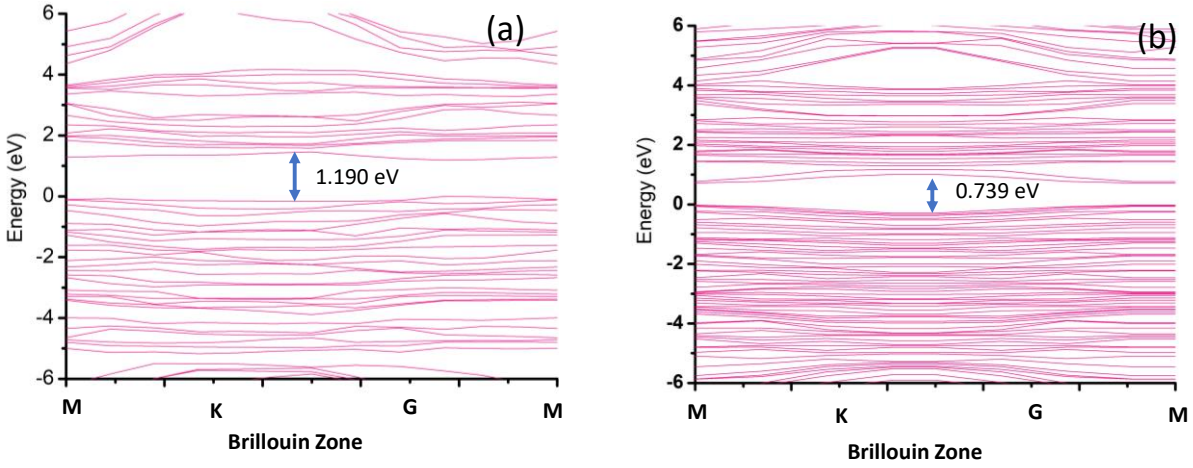


Figure S6: Band structures of $ReSe_2$ clusters where (a) un-cleaved layer and (b) cleaved layer along the {010} surface.

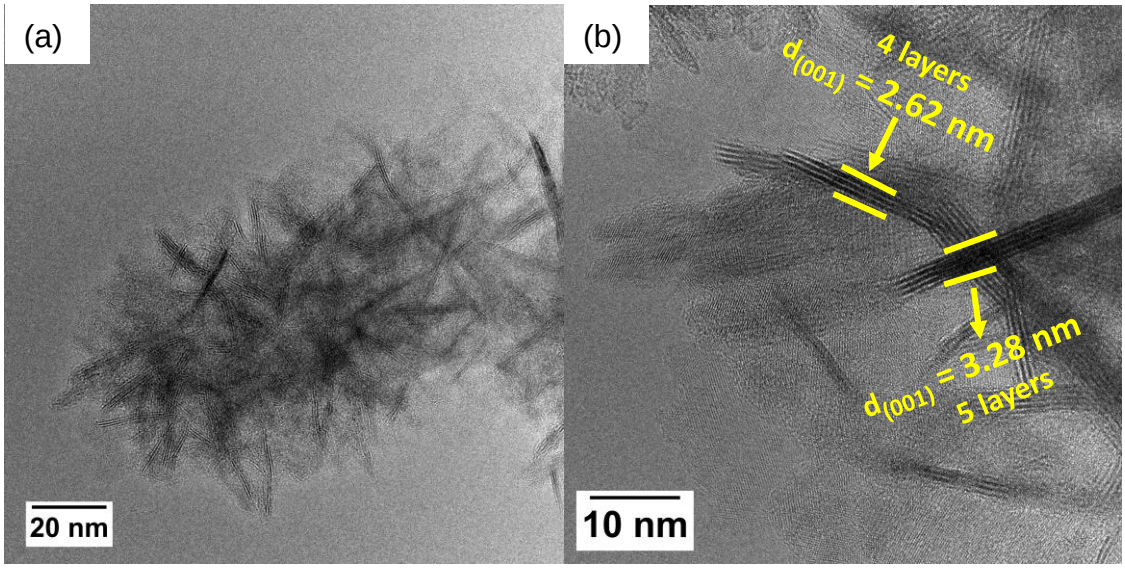
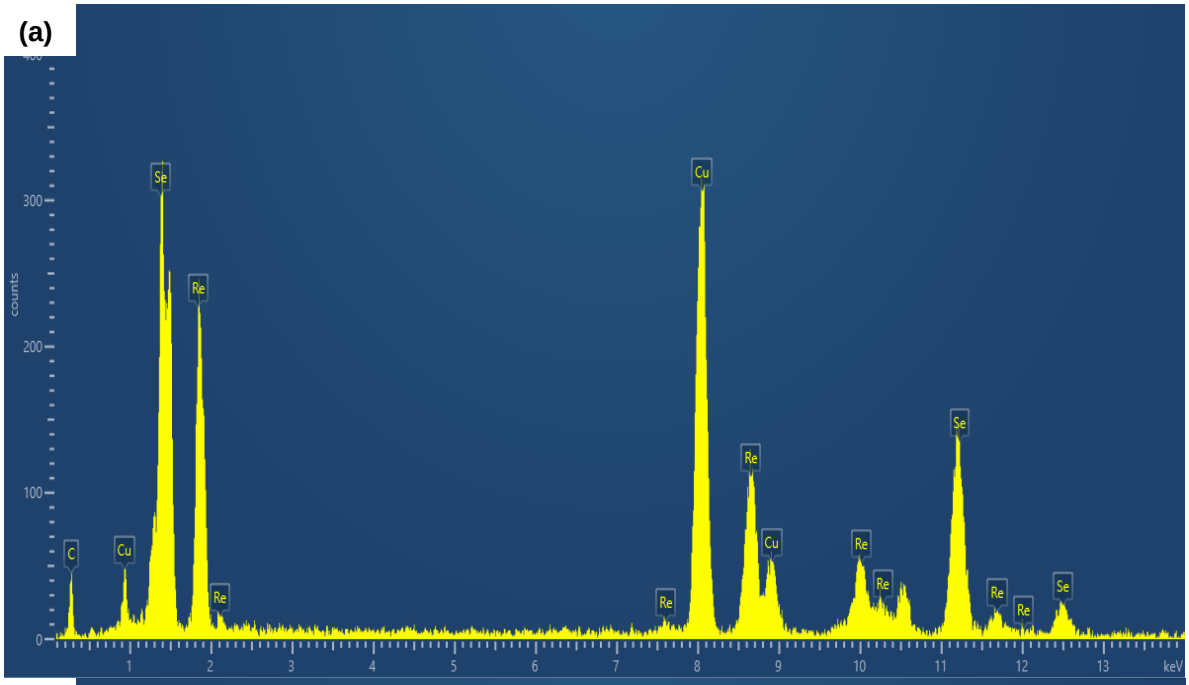
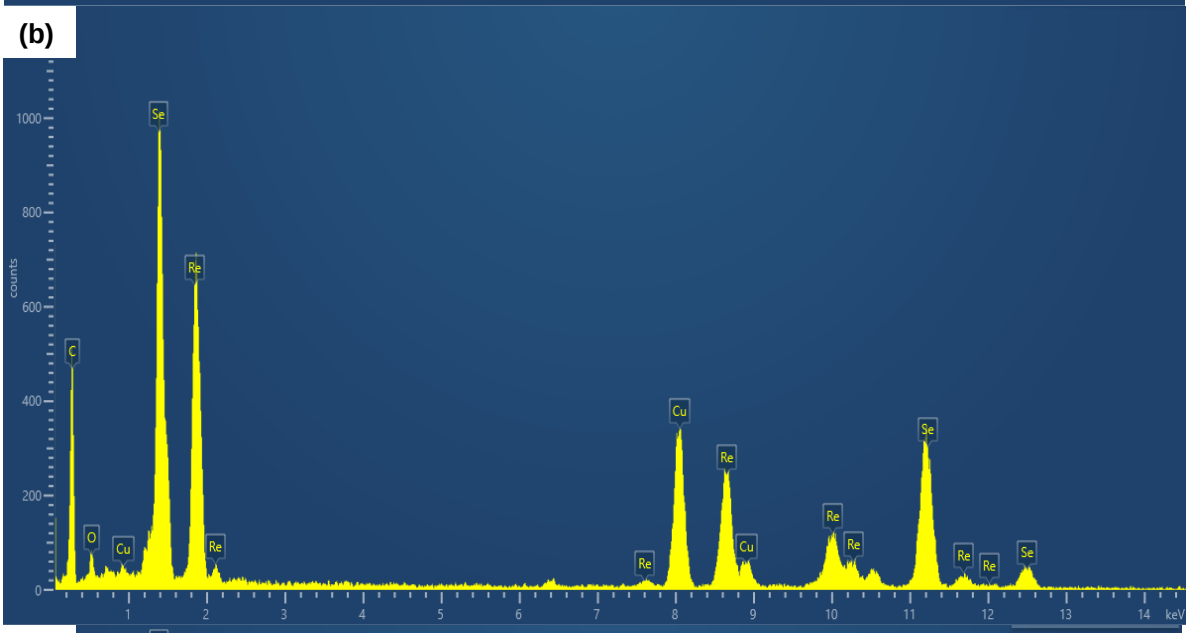


Figure S7: HRTEM images of the $ReSe_2$-TOPO nanomaterials. (a) the cluster of few-layer nanosheets, (b) thickness of the few-layered nanosheets.

(a)


counts
keV
C
Cu
Se
Re
O

(b)


counts
keV
C
O
Cu
Se
Re

(c)

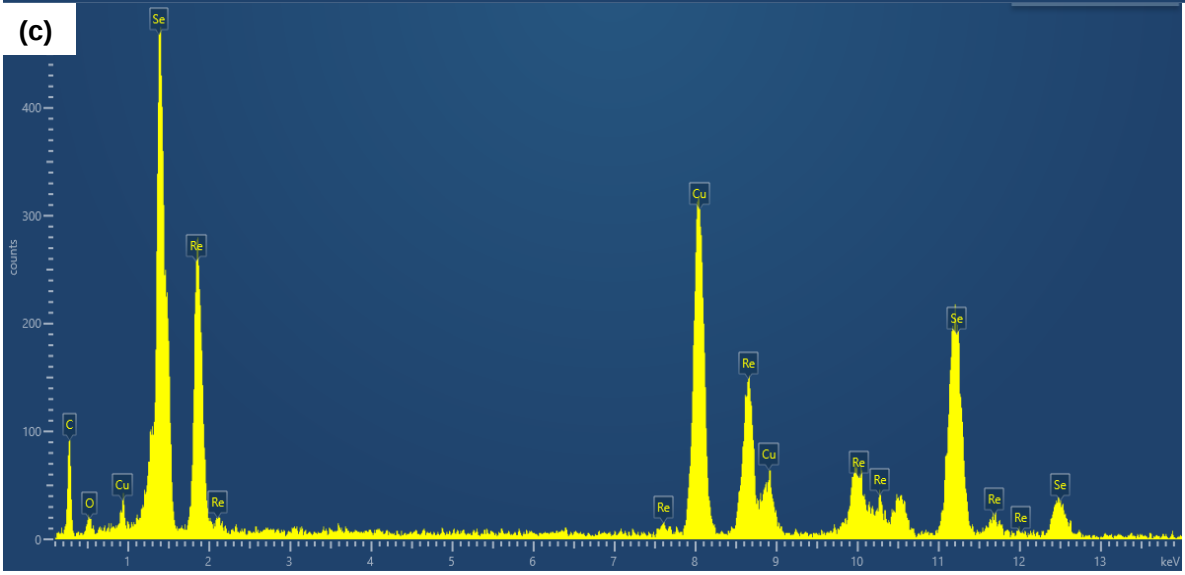

counts
keV
C
O
Cu
Se
Re

Figure S8: EDX spectra for the $ReSe_2$ nanomaterials (a) $ReSe_2$-OLA, (b) $ReSe_2$-OA, and $ReSe_2$-TOPO.

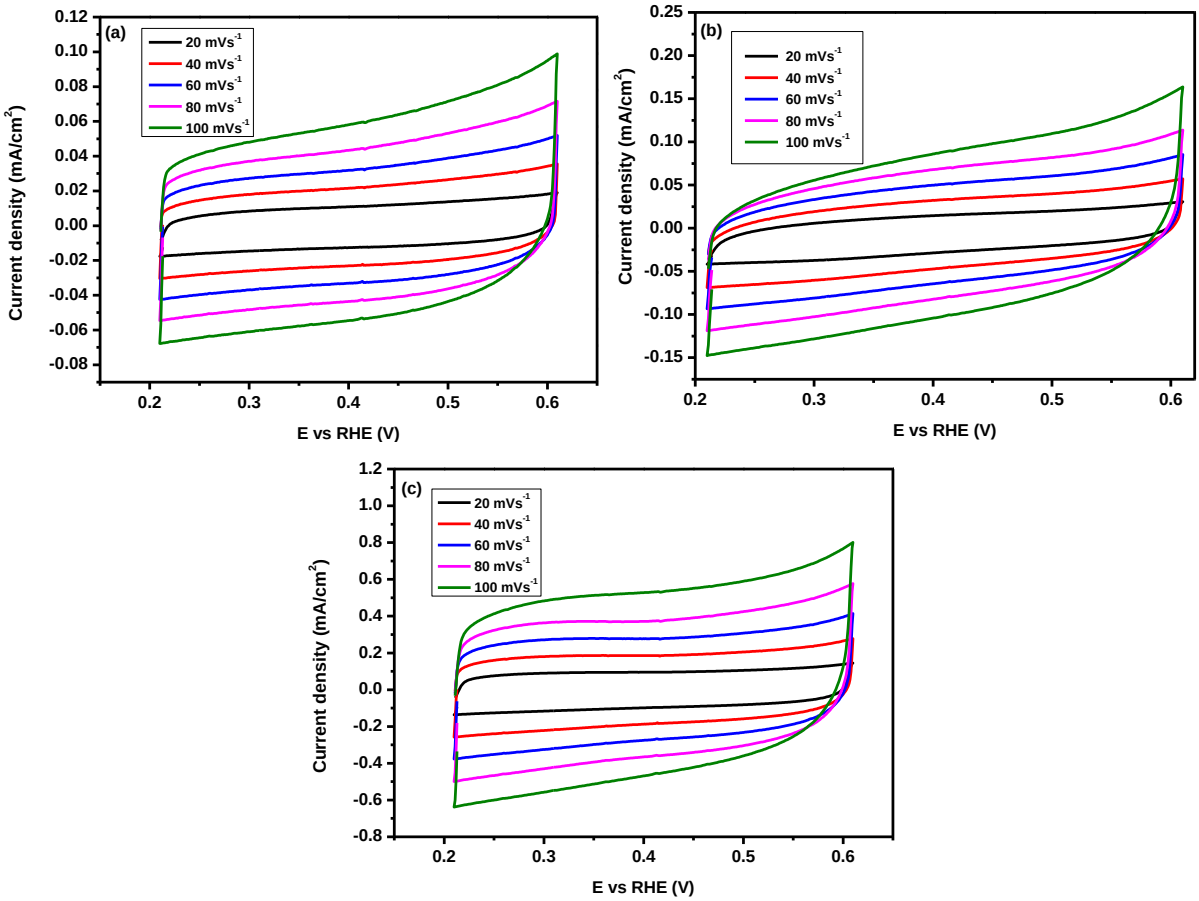


Figure S9: CV for the $ReSe_2$ nanomaterials (a) $ReSe_2$-OLA, (b) $ReSe_2$-OA and (c) $ReSe_2$-TOPO.

Chapter 5.2: Unravelling the effects of surface functionalization on the catalytic activity of $MoSe_2$ and $SnSe_2$ nanostructures towards the hydrogen evolution reaction

1. Introduction

The colloidal synthesis method is a solution-based technique that makes use of solvents that perform various functions. These solvents have been shown to perform three major functions during reactions. They act as a high boiling point solvent that can reach the required temperatures for the synthesis of nanomaterials, they are able to act as a reducing agent that reduces the chalcogens to the required reactive monomer, and they are able to bind to the surface of nanostructures in order to control their growth.[1-3] By binding to the surface of the nanostructures during synthesis, the surfactants are able to stabilize and functionalize the nanostructures.[4] The solvents are normally long-chained hydrocarbons that can preferentially bind to certain crystal facets on the surface of nanostructures through various functional groups (e.g. $-NH_2$, -OH, -COOH, and P=O) to produce a certain size, shape, and phase of the nanostructures.[5-6] The synthesis of nanostructures with favourable properties can be produced through an in-depth understanding of the interaction between the solvents and the surface of the nanostructures. Similar studies have already been conducted to produce monolayer TMD nanostructures.[7] Jung *et al.* discovered that monolayer $MoSe_2$ nanosheets could be synthesized using oleic acid as the solvent, while the use of oleyl alcohol and oleylamine produced multilayer $MoSe_2$ nanosheets.[7] They determined that the choice of surfactant can determine whether the TMDs can exclusively grow laterally to produce monolayer nanosheets or grow both laterally and vertically to produce multilayer nanosheets. In this work the effect of varying the solvents/surfactants in the colloidal synthesis of $MoSe_2$ and $SnSe_2$ nanostructures was explored. Three common solvents that are typically used in colloidal synthesis were explored for this study which are oleylamine (OLA), oleic acid (OA), and trioctylphosphine oxide (TOPO). These solvents were also chosen because they represent three different head groups. Oleylamine has an amine ($-NH_2$) head-group, oleic acid had a carboxyl head-group (-COOH), and TOPO has a phosphine oxide head group (-P=O). The structures of the solvents are shown in **Fig.S1** with their denoted head groups. The structural and electrocatalytic properties of the surface functionalized nanostructures were investigated. This was done to determine which solvent produced nanomaterials with favourable structural properties that would benefit the catalytic activity of the TMD nanostructures towards the hydrogen evolution reaction (HER).

The functionalization of nanostructures by these surfactants has been known to have advantageous properties in various applications.[8-9] Unfortunately, from an electrocatalysis standpoint these surfactants can also impede electrocatalytic reactions by blocking the active edge sites.[10-11] The surfactants can be removed using various methods, but this can sometimes have adverse effects on the catalytic activity of nanostructures.[12] It would be advantageous to select a solvent/surfactant that results in maximal exposure of the active edge sites without impeding the catalytic processes of the HER. To the best of our knowledge, extensive work that seeks to identify such solvents/surfactants for TMD nanostructures has not been undertaken.

2. Experimental section

2.1 Chemicals

Molybdic acid (H_2MoO_4, 85%), tin(IV) chloride ($SnCl_4$, 98%), selenium powder (Se, 99.99%), oleylamine (70%), oleic acid (90%), trioctylphosphine oxide (90%) were purchased from Sigma Aldrich and used as received without purification.

2.2 Synthesis of the $MoSe_2$ and $SnSe_2$ nanostructures

Synthesis of $MoSe_2$ nanostructures using OLA, OA, and TOPO

The selenium powder (Se, 0.559 mmol) was added into the three-neck round bottom flask containing the solvent/surfactant (20 ml) at room temperature. The temperature was increased to 220 ºC to thermally reduce the Se to Se^{2-} with the help of the solvent, which also acted as a reducing agent. Once all the Se was reduced, a mixture molybdic acid (H_2MoO_4, 0.15 mmol) and the solvent/surfactant was added into the reaction mixture. The temperature was then raised to 300 ºC and the reaction was run for 120 min. The nanoparticles formed were then washed with ethanol and toluene using a centrifuge and then left to dry

Synthesis of $SnSe_2$ nanostructures using OLA, OA, and TOPO

Selenium powder (Se, 0.051 mmol) was added into the three-neck round bottom flask containing the solvent/surfactant (20 ml) at room temperature. The temperature was increased to 220 ºC to thermally reduce the Se to Se^{2-} with the help of the solvent, which also acted as a reducing agent. Once all the Se was reduced, tin(IV) chloride ($SnCl_4$, 0.017 mmol) and the solvent/surfactant were added to the reaction mixture. The temperature was then raised to 300 ºC and the reaction was run for 120 min. The nanoparticles formed were then washed with ethanol and toluene using a centrifuge and then left to dry.

2.3 Characterization techniques

The phase purity, crystallinity, and preferred crystal orientation of the products were examined using powder X-ray diffraction (PXRD) on a Bruker MeasSrv D2-205530 diffractometer using secondary graphite monochromated CuKα radiation (λ 1.5406 Å) at 30 kV/10 mA. Measurements were taken using a glancing angle of incidence detector at an angle of 2°, for 2θ values over 10 - 90° in steps of 0.026° with a step time of 37 s and at a temperature of 25 °C. The Raman spectra were obtained using the MacroRAM (Horiba Jobin-Yvon, Ltd., Stanmore, UK) spectrophotometer which is fitted with a CCD detector that is cooled at -50 °C. All samples were measured after excitation with a laser wavelength of 785 nm. The sample morphologies were determined using the transmission electron microscopy (TEM) carried out on an FEI Tecnai T12 TEM microscope operated at an acceleration voltage of 120 kV. Analysis of organic solvents used was established using the Bruker TENSOR 27 Fourier Transform Infrared (FTIR) spectrophotometer, ATR mode was used for the analysis. The nuclear magnetic resonance (NMR) data was obtained using a 500 MHz Bruker AVANCE III, the samples were run using $CDCl_3$ as a solvent at 300 K.

2.4 Electrochemical characterization

The electrochemical measurements were carried out on a BASi epsilon E2. All measurements were carried out in 0.5 M H_2SO_4 using a three-electrode system. An Ag/AgCl electrode was used as the reference electrode, a platinum wire was used as the counter electrode. A modified glassy carbon electrode with a 3 mm diameter was used as the working electrode. The ink or fresh dispersion of the sample was prepared by dispersing 5.0 mg of the TMD powder with 0.5 mg carbon black and 40 µl of Nafion solution (5 wt%) in a 1 ml mixture of water and isopropanol at a 3:1 ratio. The solution was then sonicated for 30 min and ~ 5 µl of the ink was drop-casted onto the glassy carbon electrode. The electrode was allowed to dry at room temperature. The linear sweep voltammograms were obtained at a scan rate of 2 mVs^{-1} and the cyclic voltammograms were obtained at a potential range of 0.2 – 0.6 V vs RHE at 100 mVs^{-1} scan rate. The measured potentials vs Ag/AgCl were converted to the reversible hydrogen electrode (RHE) scale according to the Nernst equation:

$$E_{RHE} = E_{Ag/AgCl} + 00059\,pH + E^{0}_{Ag/AgCl} \quad (1)$$

Where E_{RHE} is the converted potential vs RHE, $E^{0}_{Ag/AgCl}$ = 0.210 V at 25 °C. The Impedance spectroscopy studies were conducted on a Biologic SP 300, the measurements were done at a potential of -200 mV vs RHE and a frequency range between 0.1 Hz and 100 kHz.

3. Results and discussion

Powder X-ray diffraction (PXRD) was used to confirm the synthesis of the $MoSe_2$ and $SnSe_2$ nanostructures and to determine their crystallinity, phase, and composition. The PXRD confirms that the $MoSe_2$ nanomaterials have crystallized in the 2H hexagonal phase (JCPDS card no: 01-089-0340). The broad nature of the diffraction peaks as shown in **Fig.1(a)** is indicative of nanosized materials, the peaks arise from an ensemble of small crystallite domains or small crystallites. The (002) peak is associated with the interlayer spacing of the nanosheets, the diffraction peak is due to the diffraction of x-rays along the c-axis of the nanosheets.[13] This shows that the $MoSe_2$ nanostructures synthesized using the three surfactants are composed of few-layer nanosheets.

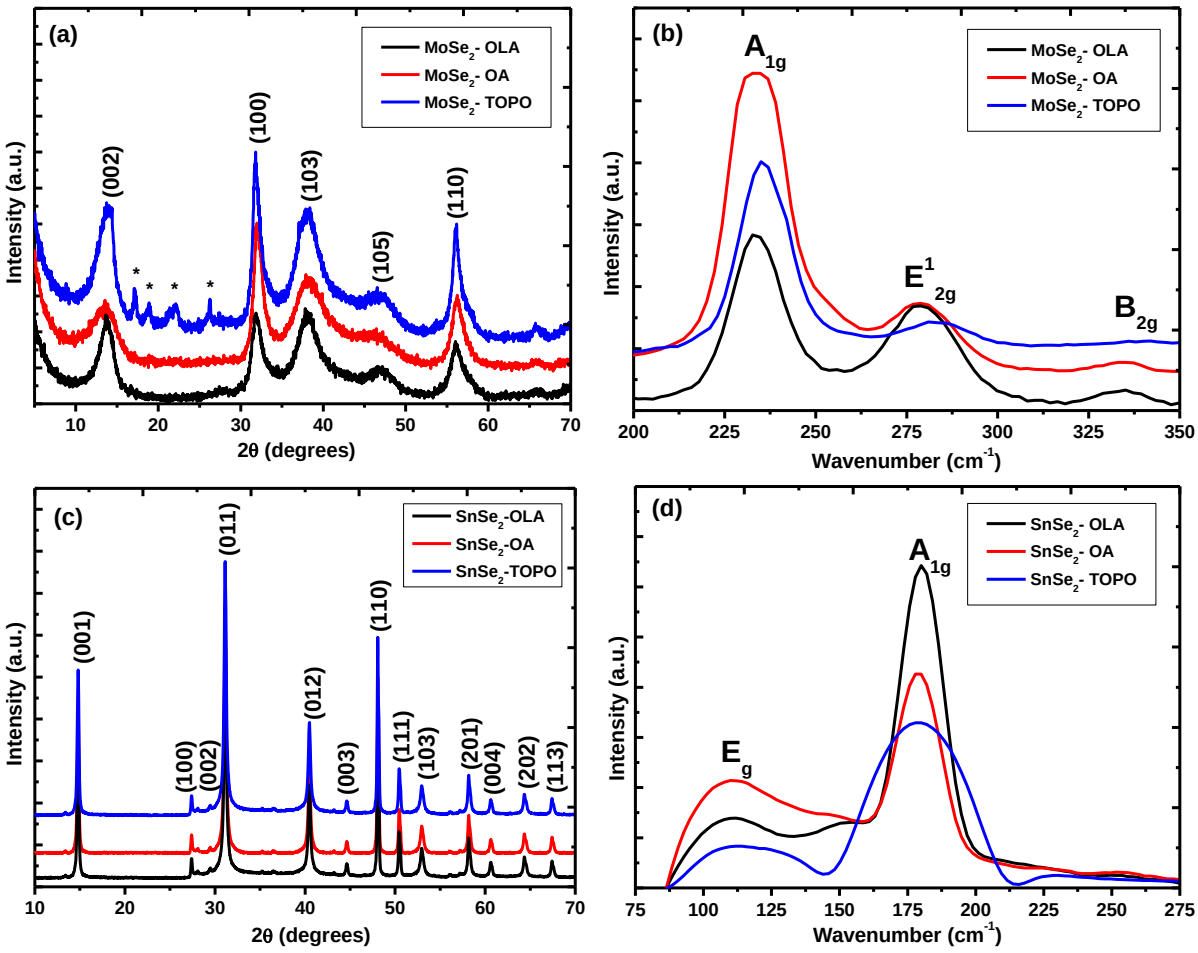


Figure 1: (a) PXRD patterns of $MoSe_2$, (b) Raman spectra of $MoSe_2$ nanostructures, (c) PXRD patterns of $SnSe_2$ nanostructures, and (d) Raman spectra of $SnSe_2$ nanostructures.

However, there are impurities that are observed in the diffractogram of $MoSe_2$-TOPO, which are denoted as (*). The peaks could not be matched to any of the precursor chemical reagents.

They could be due to the intermediate that is formed ($MoSe_4^{2-}$) before thermal conversion to $MoSe_2$.[14] The powder diffractograms of the $SnSe_2$ nanostructures are shown in Fig.1(c). The $SnSe_2$ crystallized in a hexagonal unit cell and a P-3m1 space group. The intense peak found at $2\Theta \approx 14°$, corresponds to the (001) lattice plane and is associated with the growth of the crystal along the c-axis.[15]

The Raman spectrum of $MoSe_2$ is known to have two characteristic peaks, the out-of-plane A_{1g}, and the in-plane E^1_{2g}. The positions of the A_{1g} and the E^1_{2g} are 242 cm^{-1} and 286 cm^{-1} respectively for the bulk sample.[16] The A_{1g} is known to red-shift from its bulk position for monolayer or few-layer $MoSe_2$ nanostructures. The E^1_{2g} has been known to blue shift from the bulk for mono or few-layer $MoSe_2$ nanostructures. The degree to which the peaks shift from their bulk positions can be used to estimate the number of layers on the nanosheets.[16] The Raman spectra of $MoSe_2$ nanostructures are shown in **Fig.1(b)**. The characteristic A_{1g} and E^1_{2g} peaks are observed in the spectra of the $MoSe_2$ nanostructures synthesized using the three solvents\surfactants. The A_{1g} for the $MoSe_2$-OLA and $MoSe_2$-OA was found to be 234 cm^{-1} which has red-shifted from the bulk, the same is true for the $MoSe_2$-TOPO nanostructures where the position of the A_{1g} was found to be 235 cm^{-1}.[17] The E^1_{2g} has also red-shifted for all the $MoSe_2$ nanostructures, the position of the peak was recorded at 279 cm^{-1} for $MoSe_2$-OLA and $MoSe_2$-OA. The position of the E^1_{2g} for the $MoSe_2$-TOPO was found to be 285 cm^{-1}. The appearance of the B^1_{2g} at 350 cm^{-1} which does not appear for monolayer or bulk layer nanosheets indicates that the nanosheets are few-layered with a layer number between 2 – 5 layers for the nanomaterials synthesized using the three surfactants.[17] The Raman spectra of the $SnSe_2$ are shown in **Fig.1(d)**. The typical Raman spectrum of $SnSe_2$ has two characteristic peaks, the in-plane E_g vibrational mode, and the out-of-plane A_{1g} vibrational mode.[18] The Raman spectra of the $SnSe_2$ synthesized using OLA, OA, and TOPO all show the E_g and A_{1g} peaks which confirms the formation of $SnSe_2$ nanomaterials. The position of the E_g can offer information about the polytype of the $SnSe_2$ (2H or 1T) as well the number of layers on the nanosheets. For 2H-$SnSe_2$ the position of the E_g is located at approximately 108 cm^{-1}. The position of the E_g peak is normally located at approximately 118 cm^{-1} for 1T-$SnSe_2$.[15] The E_g peak for the as-synthesized $SnSe_2$-OLA, $SnSe_2$-OA, and $SnSe_2$TOPO was located at 114 cm^{-1}, 113 cm^{-1}, and 114 cm^{-1} respectively which suggests that the nanomaterials crystallized in the 1T phase. The location of the E_g peak is also associated with $SnSe_2$ nanoflakes of layers between 1-3 layers.[15]

Fourier transform infrared (FTIR) analysis was used to confirm whether the surfactants had capped on the of the $MoSe_2$ and $SnSe_2$ nanostructures. The FTIR analysis was conducted on both the free surfactant (uncapped surfactant) and the capped $MoSe_2$ nanomaterials. The FTIR spectra are shown in **Fig.S2**. **Table 1** shows a summary of the FTIR results.

Table 1: Assignments of the FTIR peaks in the free surfactants and capped nanostructures

Sample	Assignments	Free Assignment (cm^{-1})	Capped $MoSe_2$ Assignment (cm^{-1})	Capped $SnSe_2$ Assignment (cm^{-1})
OLA	-C=H (stretching)	723	723	723
	C=C (stretching)	968	963	964
	C-H (stretching)	729	-	-
		2848	2844	2544
		2917	2912	2917
	C-N (stretching)	1465	1460	1455
	N-H (bending)	1623	1627	1608
OA	-C=H	723	723	726
	C=C (stretching)	934	-	-
	C-H (stretching)	2854	2854	2848
		2917	2917	2932
	C=O (stretching)	1711	-	-
TOPO	C-H (stretching)	2854	2834	2853
		2917	2917	2932
	O=P	1149	-	-

The binding of the OLA on the surface of the TMD nanostructures was investigated by considering the N-H functional group. The vibration energy of the N-H bending was measured to be 1623 cm^{-1} as shown in **Fig.S2(a)**. The N-H bending vibrational energy shifts to 1627 cm^{-1} for $MoSe_2$-OLA and to 1608 cm^{-1} for $SnSe_2$-OLA.[19] The shift of the vibrational bands shows that the OLA binds to the TMD nanostructures through the amine functional group.[19] The vibrational energy of the C=O stretching band was measured at 1711 cm^{-1}.[20] The C=O stretching band in the OA capped $MoSe_2$ and $SnSe_2$ is severely suppressed as shown in **Fig.S2(b)**. This is consistent with previously reported work which suggests that this corresponds with the binding of the OA molecule to the surface of the nanostructures through

the C=O group.[20] A similar trend is shown in FTIR spectrum of the TOPO capped nanomaterials shown in **Fig.S2(c)**. In the free TOPO the vibrational stretching band of the P=O bond was observed at 1145 cm^{-1}.[21] The diminished intensity of the P=O band in the TOPO capped nanostructures was ascribed to the binding of the TOPO molecules to the nanostructures through the lone pairs of the oxygen.[21]

Further investigation into the interaction of the surfactants with the $MoSe_2$ and $SnSe_2$ nanostructures was done using nuclear magnetic resonance (NMR). An interaction between the surfactant and nanostructured materials can be identified by the broadening and shifting of the peaks in the NMR spectrum of the capped nanostructures. The NMR spectra of the free surfactants and capped nanostructures are shown in **Fig.S3**. **Table 2** shows a summary of the peak assignments for the free surfactants and capped nanostructures.

Table 2: Assignments of the ^1H NMR peaks in the free surfactants and capped nanostructures

Sample	Type of H	Free Chemical shift (ppm)	$MoSe_2$ capping Chemical shift (ppm)	$SnSe_2$ capping Chemical shift (ppm)
OLA	$-CH_3$	0.82-0.92	0.79-0.92	0.80-0.92
	$-CH_2-$	1.19-1.38	1.16-1.39	1.09-1.42
	R-CH=CH-R	1.92-2.07	1.92-2.09	1.86-2.07
	$-NH_2$	1.10-1.19	-	-
	$R-NH_2$	2.61-2.71	-	2.76-2.90
	CH=CH	5.31-5.43	5.31–5.41	5.31-5.41
	R_1-NH_2	1.3-1.47	1.50-1.63	1.43-1.75
OA	$-CH_3$	0.83-0.93	0.84-0.92	0.84-0.92
	$-CH_2-$	1.19-2.09	1.18-1.40	1.17-1.52
	$R_1-C=O$	1.57-1.69	1.45-1.74	1.47-1.71
	R-CH=CH-R	1.93-2.10	1.91-2.06	1.91-2.07
	R-C=O	2.30-2.40	2.32-2.37	2.31-2.42
	CH=CH	5.29-5.41	5.36-5.40	5.30-5.41
TOPO	O=P-R	1.51-1.69	1.49-1.67	1.49-1.70
	$-CH_2-$	1.35-1.43	-	-
	R_1-CH_3	1.22-1.34	1.19-1.36	1.21-1.35
	$-CH_3$	1.86-1.91	1.85-1.91	1.83-1.92

The broadening and shifting of the peaks are typically prominent in peaks of hydrogens near the binding atom. The peak for the hydrogens on the amine (NH_2, δ = 1.10-119 ppm), is not observed on the spectrum of the capped $MoSe_2$ and $SnSe_2$ nanostructures as shown in **Fig.S3(a) and (d)**. This phenomenon occurs when the nitrogen binds to the surface of the nanostructures. This is further confirmed by the disappearance of the R-NH_2 (δ = 2.61-2.71 ppm) peak which represents the hydrogens on the carbon adjacent to the amine functional group.[22] A similar trend can be observed for the hydrogen atoms on the carbons adjacent to the carbonyl group (R-C=O, 2.30-2.40 ppm and R_1-C=O, 1.57-1.69 ppm), the NMR spectrum of $MoSe_2$-OA and $SnSe_2$-OA are shown in **Fig.S3(b) and (e)**.[23] The peaks are significantly shifted in the OA capped nanostructures which signifies the binding of the OA through the carbonyl. The NMR spectrum of the TOPO capped nanostructures shows significant line broadening compared to the free TOPO. This is clearly observed in the signal for the -CH_2- hydrogens adjacent to the phosphate group (O=P-R, δ = 1.51-1.69) shown in **Fig.S3(c) and (f)**.[24] This clearly indicates the binding of the TOPO to the nanostructures through the phosphine oxide group.

Transmission electron microscopy (TEM) was used to investigate how the use of surfactants with different head groups affects the morphology of the synthesized nanomaterials. TEM images of the $MoSe_2$ and $SnSe_2$ nanostructures synthesized using OLA, OA and TOPO are shown in **Fig.2**.

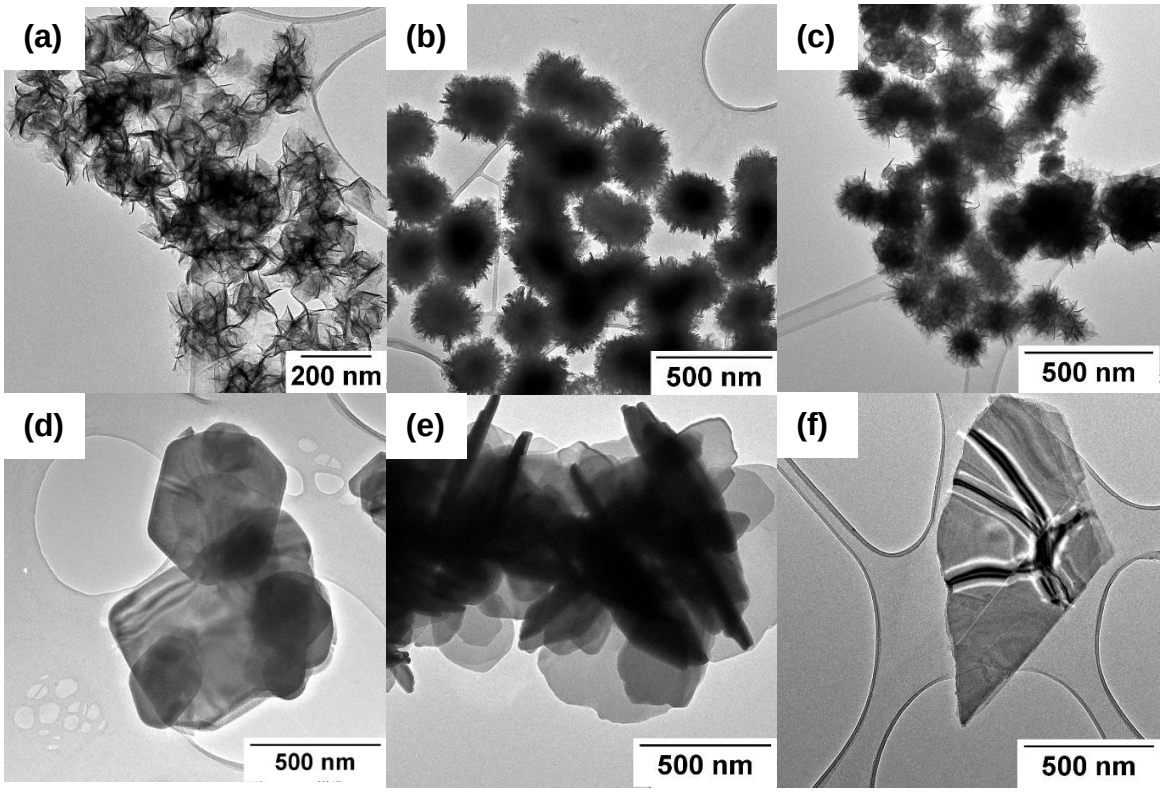


Figure 2: TEM images of (a) $MoSe_2$-OLA, (b) $MoSe_2$-OA, (c) $MoSe_2$-TOPO, (d) $SnSe_2$-OLA, (e) $SnSe_2$-OA, and (f) $SnSe_2$-TOPO.

The $MoSe_2$ synthesized using OA has already been shown to form a cotton ball-like microspheres with nanosheets growing out from a central core which gives them an almost flower-like configuration. The $MoSe_2$ nanostructures synthesized using TOPO show the same morphology as $MoSe_2$-OA shown in **Fig.2(b) and (c)** which is to be expected as OA and TOPO both bind to the nanomaterials through the oxygen-containing head groups, which are C=O or C-O for oleic acid and P=O for trioctylphosphine oxide. The OLA synthesized $MoSe_2$ nanomaterials take up a different morphology as they resemble wrinkled sheets of paper that are overlapping as shown in **Fig.2(a)**. The slight change in morphology shows that the binding of the OLA to the surface of the $MoSe_2$ is distinctly different as compared to that of the surfactants with oxygen-containing functional groups. The TEM image of $SnSe_2$-OLA is shown in **Fig.2(d)**, show that the OLA capped $SnSe_2$ nanostructures form into nanoplates with a mixed morphology of hexagonal nanoplates and semi-spherical nanoparticles. The TEM images of $SnSe_2$-OA also show a mixed morphology with nanoplates and rod-like structures in **Fig.2(e)**. The rod-like structures can be seen more clearly in **Fig.S4(a)**, the rod-like structures seem to form from the nanoplates. The 2D structures become unstable and begin to roll in on themselves to form the rod-like structures, a schematic representation of this is shown in **Fig.3**.

The ridges on the sides of the rods as shown in **Fig.S4(a)** indicate that they are formed from the nanoplates. The TEM image of $SnSe_2$-TOPO is shown in **Fig.2(f)**. The $SnSe_2$-TOPO nanomaterials form into large lateral dimension nanoplates. The rolling of the nanoplates observed in the OA capped $SnSe_2$ nanostructures is also observed in $SnSe_2$-TOPO as shown in **Fig.S4(b)**. The phenomenon is not as significant as in $SnSe_2$-OA.

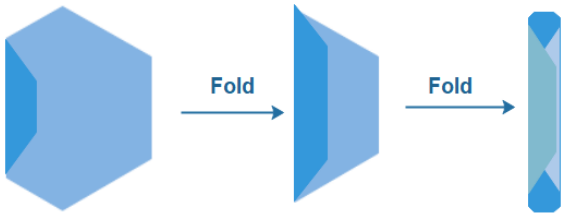


Figure 3: Schematic representation of the rod formation.

Electrochemical characterisation of the TMD nanostructures was conducted to determine the catalytic activity of the nanostructures towards the HER. The polarisation curves for the TMD nanostructures and 20% Pt/C are shown in **Fig.4**. The polarisation curves for the $MoSe_2$ nanostructures are shown in **Fig.4(a)**. The onset potential of the $MoSe_2$ nanostructures was found to be 167 mV, 193 mV, and 205 mV for $MoSe_2$-OLA, $MoSe_2$-TOPO, and $MoSe_2$-OA respectively. The onset potential is the overpotential at which catalytic current is first observed which indicates that the $MoSe_2$-OLA requires the lowest overpotential to initiate the HER. The polarisation curves for the $SnSe_2$ nanostructures are shown in **Fig.4(b)**. The $SnSe_2$-TOPO nanostructures had the lowest onset potential at 229 mV for the $SnSe_2$ nanostructures. This was followed by the $SnSe_2$-OLA and $SnSe_2$-OA nanostructures at 319 mV and 390 mV respectively. A similar trend was observed for the overpotential at 10 mA/cm^2. This is the overpotential needed to reach 10 mA/cm^2, which is the operating current density for a cost-competitive photoelectrochemical cell (PEC). The $MoSe_2$-OLA and $SnSe_2$-TOPO had the lowest overpotential which along with the onset potentials show that these nanostructures are the best performing catalysts among the $MoSe_2$ and $SnSe_2$ nanostructures. The η_{10} was measured at 285 mV and 569 mV for $MoSe_2$-OLA and $SnSe_2$-TOPO respectively.

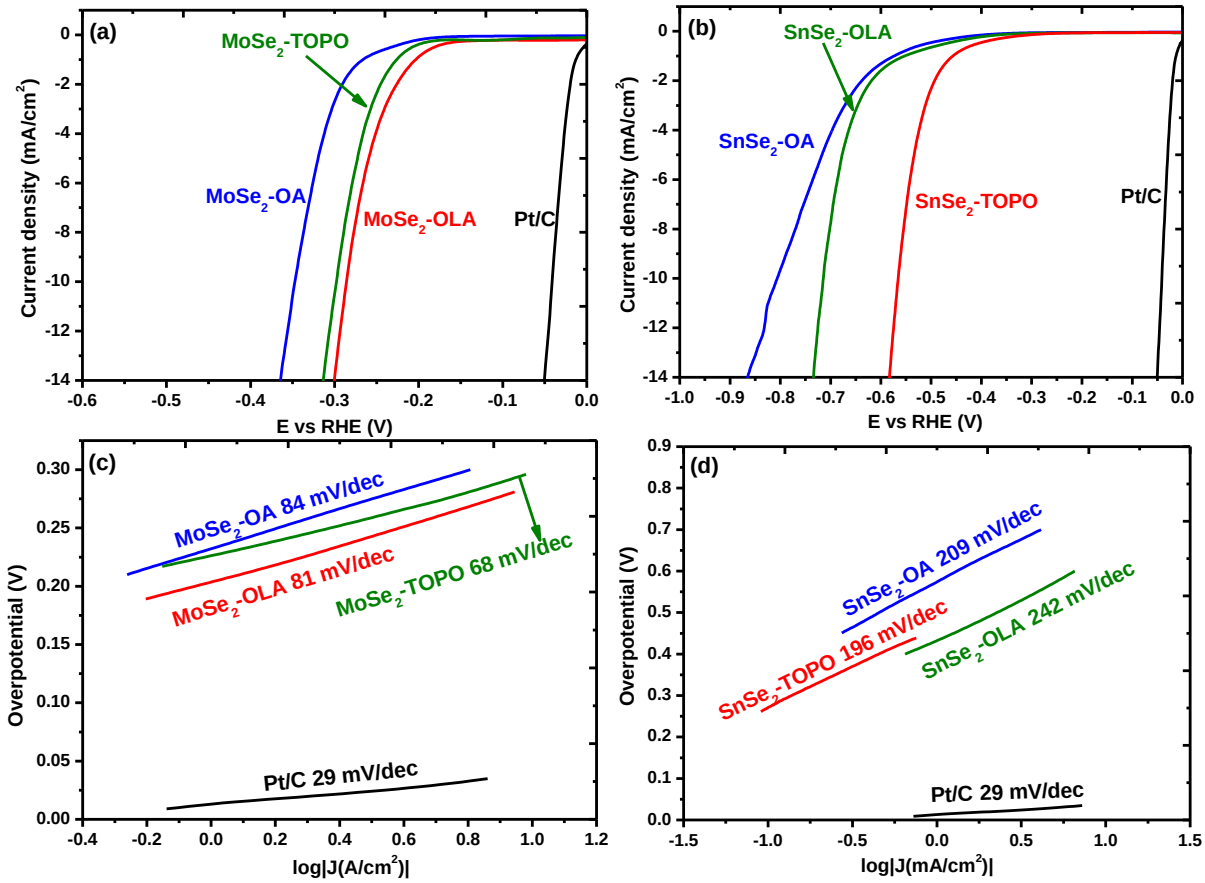


Figure 4: (a) Polarisation curves of $MoSe_2$ nanostructures. (b) Polarisation curves of the $SnSe_2$ nanostructures. (c) Tafel plots of $MoSe_2$ nanostructures. (d) Tafel plots of $SnSe_2$ nanostructures.

The overpotential of the $MoSe_2$-TOPO and $MoSe_2$-OA was measured at 297 mV and 319 mV respectively. The overpotential of the $SnSe_2$-OLA and $SnSe_2$-OA was measured at 618 mV and 804 mV respectively. The Tafel slope is also a useful property to consider when evaluating nanostructures for the HER. The Tafel plots for the $MoSe_2$ and $SnSe_2$ nanostructures are shown in **Fig.4(c) and (d)** respectively. The Tafel slope can be understood as the sensitivity of the electric current response to an applied potential. It can be used to provide insights into the mechanism and rate-determining step of the catalyst surface.[25] The Tafel slope can thus be obtained from the Tafel plot (over-potential vs log |current density|) which is obtained by replotting the LSV curve. The Tafel slope is obtained by fitting a straight line to the Tafel plot and using the Tafel equation;

$$\eta = a + b\log(J) \qquad (2)$$

Where ɳ is the overpotential, J is the current density, and b is the Tafel slope. As already mentioned, the Tafel slope can be used to give insights into the mechanism and rate-determining step of the catalyst surface. The HER in acidic media can be described in three steps:

(Volmer step) $H_3O^+ + e^- + M \rightleftharpoons M\text{-}H + H_2O$, (120 mV/dec) (3)

(Heyrovsky step) $M\text{-}H + H_3O^+ + e^- \rightleftharpoons H_2 + H_2O + M$, (40 mV/dec) (4)

(Tafel step) $2M\text{-}H \rightleftharpoons H_2 + 2M$, (30 mV/dec) (5)

The Volmer reaction is the primary discharge step in which protons are adsorbed to active sites on the surface of the catalysts and combine with electrons to form adsorbed hydrogen atoms. This step is followed by either an electrochemical desorption step (Heyrovsky reaction) or a recombination step (Tafel reaction).[25] The Tafel slopes of the $MoSe_2$ nanostructures were measured to be 81 mV, 68 mV, and 85 mV for $MoSe_2$-OLA, $MoSe_2$-TOPO, and $MoSe_2$-OA respectively. This indicates that the rate-limiting step is the Heyrovsky step, this shows that the HER goes through the Volmer-Heyrovsky pathway when using the $MoSe_2$ nanostructures. The Tafel slopes of the $SnSe_2$-OLA, $SnSe_2$-OA, and $SnSe_2$-TOPO nanomaterials were measured at 242 mV/dec, 209 mV/dec, and 193 mV/dec respectively. This suggests the Volmer step is the rate-determining step for the HER on the $SnSe_2$ nanostructures. The kinetics of the reaction was evaluated using the exchange current density. The exchange current density can be described as the rate of oxidation and reduction at an equilibrium reaction expressed in terms of current density.[26] The exchange current density of the nanostructures was determined using the Tafel plots. Therefore, an excellent catalyst is characterized by a high exchange current density. The highest exchange current density was that of the $MoSe_2$-OLA at 0.63 mA/cm^2 as expected. Followed by that of the $MoSe_2$-OA at 0.58 mA/cm^2 and lastly that of $MoSe_2$-TOPO at 0.56 mA/cm^2. Among the $SnSe_2$ nanostructures, the $SnSe_2$ had the highest exchange current density which was 0.34 mA/cm^2. The exchange current density of the $SnSe_2$-OLA and $SnSe_2$-OA was determined to be 0.29 mA/cm^2 and 0.26 mA/cm^2 respectively. The electrochemically active surface area (ECSA) was estimated using the electrochemical double layer (C_{dl}). The C_{dl} provides a good estimation of the ECSA as it has been shown to scale with the C_{dl}.[27] The Cdl plots of the $MoSe_2$ and $SnSe_2$ nanostructures are shown in **Fig.5(a) and (b)** respectively.

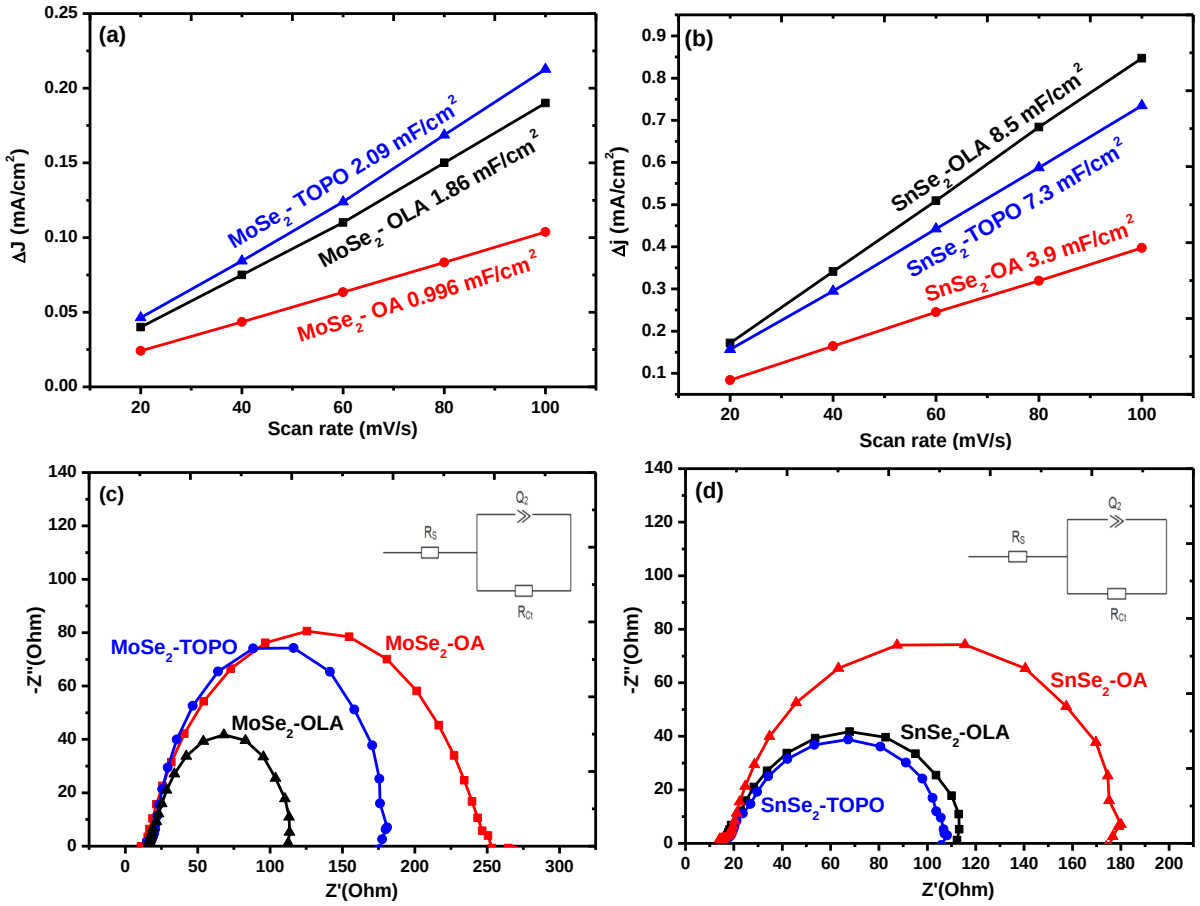


Figure 5: (a) C_{dl} plots of the $MoSe_2$ nanostructures. (b) C_{dl} plots of the $SnSe_2$ nanostructures. (c) Nyquist plots of the $MoSe_2$ nanomaterials. (d) Nyquist plots of the $SnSe_2$ nanostructures.

The C_{dl} of the nanostructures was determined using cyclic voltammetry curves which are shown in **Fig.S5**. The C_{dl} of the $MoSe_2$ nanostructures was determined to be 2.09 mF/cm^2, 1.86 mF/cm^2 and 0.99 mF/cm^2 for $MoSe_2$-TOPO, $MoSe_2$-OLA, and $MoSe_2$-OA respectively. The C_{dl} of the $SnSe_2$ nanostructures was determined to be 8.5 mF/cm^2, 7.3 mF/cm^2, and 3.9 mF/cm^2 for $SnSe_2$-OLA, $SnSe_2$-TOPO, and $SnSe_2$-OA respectively. This shows that the TOPO and OLA synthesized TMD nanostructures have the highest ECSA compared to the OA synthesized nanostructures. The ECSA represents the electrode area that is accessible to the electrolyte and is available for charge transfer, thus the catalyst with the largest ECSA would most likely have the best catalytic performance. Since the TOPO and OLA synthesized nanostructures have the highest onset potential, η_{10}, and exchange current density, the ECSA is in agreement with the results obtained from the polarisation curves and Tafel plots. The kinetics of the charge transfer processes was evaluated using electrochemical impedance spectroscopy (EIS). The results of the EIS results were represented in the form of Nyquist plots

which are shown in **Fig.5(c)**, and the equivalence circuit used to fit the data is shown as an insert in the same figure. The charge transfer resistance (R_{ct}) of the nanostructures was shown to be 96 Ω, 162 Ω, and 247 Ω for the $MoSe_2$-OLA, $MoSe_2$-TOPO, and $MoSe_2$-OA respectively. The OLA capped nanostructures had the lowest measured R_{ct}. This also shows that the OLA capped nanostructures are the best catalysts for HER compared to the nanostructures synthesized with the other two surfactants. The Nyquist plots of the $SnSe_2$ nanostructures is shown in **Fig.5(d)**. The charge transfer resistance (R_{ct}) of the $SnSe_2$-TOPO nanostructures was the lowest at 86 Ω which was comparable to that of the $SnSe_2$-OLA nanostructures at 90 Ω. As expected the $SnSe_2$-OA nanostructures had the highest R_{ct} at 160 Ω. The OLA and TOPO capped $MoSe_2$ and $SnSe_2$ nanostructures showed excellent catalytic activity compared to the OA capped nanostructures. The $MoSe_2$-TOPO nanostructures showed excellent catalytic activity which was comparable to that of the $MoSe_2$-OLA nanostructures. The $SnSe_2$-TOPO nanostructures are the most catalytically active among the $SnSe_2$ nanostructures as well. This suggests that the use of TOPO as a surfactant can consistently result in excellent catalytic activity in both TMDs. This was attributed to the bulky nature of the surfactant that resulted in limited blocking of the catalytically active sites of TMDs as compared to the two other surfactants. This result is further confirmed in the study of the catalytic activity of OLA, OA, and TOPO functionalized $ReSe_2$ nanostructures, where the TOPO functionalized nanostructures resulted in the best performing $ReSe_2$ catalyst as already discussed in **Chapter 5.1**. The stability studies of the nanostructures are shown in **Fig.S6**. The LSV scan of the OLA capped and TOPO capped nanomaterials shows very negligible reduction in catalytic activity towards the HER which shows that the nanomaterials are stable in acidic media after 1000 cycles. The $MoSe_2$ undergoes electrochemical activation as shown in **Chapter 4**. The electrochemical activation has also been observed in the $SnSe_2$-OLA nanostructures, the electrochemical activation has been shown to occur through the intercalation of H^+ ions in the internal structure of the nanomaterials as demonstrated in **Chapter 4**. This phenomenon results in an increase in electrocatalytic activity of the nanomaterials towards the HER. This phenomenon is also observed in the $SnSe_2$-TOPO nanomaterials, which also saw an increase in the catalytic activity. The decrease in the η_{10}, onset potential, and Tafel slope is clear indication of electrochemical activation. Surprisingly the $SnSe_2$-OA did not show any electrochemical activation as the catalytic activity seems to decrease after a 1000 LSV scans. This suggests that the activation is dependent on the morphology of the nanomaterials, the formation of the rod-like structure seems to hinder the intercalation of H^+ ions which inhibits the activation process. A comparison of the catalytic activity of the as synthesized $MoSe_2$ and

$SnSe_2$ nanostructures and their counterparts synthesized with other methods is shown in **Table 3**. The electrochemical characterisation of the nanostructures compared were conducted in 0.5 M H_2SO_4.

Table 3: Comparison of the catalytic activity of the as synthesized $MoSe_2$ and $SnSe_2$ and their literature counterparts

HER catalyst	Synthesis method	η_{10} (mV)	Tafel slope (mV/dec)	Onset potential (mV)	Ref
$MoSe_2$ nanosheets	Hydrothermal	305	69	171	28
$MoSe_2$ nanoflowers	CVD	220	61	170	29
$MoSe_2$ nanosheets	Colloidal	340	80	182	14
$MoSe_2$ nanoflowers	Colloidal	301	73	156	14
$MoSe_2$	Colloidal	319	85	108	**This work**
$MoSe_2$-OLA	Colloidal	285	68	167	**This Work**
$MoSe_2$-TOPO	Colloidal	297	81	193	**This work**
$SnSe_2$	CVD	439	131	-	30
$SnSe_2$	colloidal	618	242	319	**This work**
$SnSe_2$-OA	Colloidal	804	209	390	**This work**
$SnSe_2$-TOPO	Colloidal	569	193	229	**This work**

Table 3 Shows that the choice of surfactant can drastically affect the catalytic activity of the TMD nanostructures. The use of TOPO and OLA as the solvent for the synthesis of $MoSe_2$ resulted in the best performing $MoSe_2$ which is comparable to the performance of catalyst synthesized using other methods. The OLA synthesized nanostructures performed better than the performance of OLA synthesized $ReSe_2$ nanostructures. This what attributed to the difference in interaction between the surfactants and the different metals.[1,4] The TOPO synthesized $SnSe_2$ nanostructures were the best performing among the $SnSe_2$ nanostructures.

This reinforces the conclusions found in **chapter 5.1**. The interaction of TOPO with the surface of the TMD nanostructure may be ideal for HER.

4. Conclusions

In summary, $MoSe_2$ and $SnSe_2$ nanostructures were synthesized using three different solvents. The FTIR and NMR analysis showed that the solvents are able to interact with the surface of the nanostructures through their respective head groups. The TEM images show that there are no major differences in the morphology of the $MoSe_2$ nanostructures when altering the solvent used. However, the TEM images of the $SnSe_2$ show that the nanoplates tend to curl and form nanorods when OA is used as the solvent. This also occurs to a lesser extent in TOPO functionalised $SnSe_2$ nanostructure, which shows that this occurs when solvents with oxygen containing functional groups are used. The electrocatalytic activity of the nanostructures was found to be dependent on the solvents used. The different solvents interact differently with various metal precursors which makes it difficult to find trends in how the different solvents affect the catalytic activity of different TMDs. However, this work has shown that TOPO functionalized nanostructures tend to have excellent catalytic activity. This is due to the limited interaction of the bulky TOPO molecules with the surface of the nanostructures; this ensures that the TOPO surfactant is less likely to block active sites for the HER.

5. References

1. Ananthakumar, S.; Kumar, J. R.; Babu, S. M., Evolution of non-phosphine solvents in colloidal synthesis of I-III-VI2 and I2-II-IV-VI4 group semiconductor nanomaterials–Current status. *Materials Science in Semiconductor Processing* **2017,** *67*, 152-174.

2. Kadim, A. M. In *Colloidal Synthesis of CdSe Nanocrystals: Preparation, Characterization in Different Organic Solvent*, Nano Hybrids and Composites, Trans Tech Publ: 2020; pp 1-7.

3. Mourdikoudis, S.; Liz-Marzán, L. M., Oleylamine in nanoparticle synthesis. *Chemistry of Materials* **2013,** *25* (9), 1465-1476.

4. Bakshi, M. S., How surfactants control crystal growth of nanomaterials. *Cryst. Growth & Des.* **2016,** *16* (2), 1104-1133.

5. Machogo, L. F.; Sithole, R. K.; Phao, N.; Kolokoto, T.; Gqoba, S. S.; Mlambo, M.; Moloto, M. J.; Shumbula, P. M.; Mdluli, P. S.; Moloto, N., Probing the structure and functionalized surface of colloidal AuSe. *Mater. Sci. Eng., B* **2021,** *263*, 114878.

6. Chang, J.; Waclawik, E. R., Colloidal semiconductor nanocrystals: controlled synthesis and surface chemistry in organic media. *RSC Advances* **2014,** *4* (45), 23505-23527.

7. Jung, W.; Lee, S.; Yoo, D.; Jeong, S.; Miró, P.; Kuc, A.; Heine, T.; Cheon, J., Colloidal synthesis of single-layer MSe_2 (M= Mo, W) nanosheets via anisotropic solution-phase growth approach. *J. Am. Chem. Soc.* **2015,** *137* (23), 7266-7269.

8. Pandit, S.; Karunakaran, S.; Boda, S. K.; Basu, B.; De, M., High antibacterial activity of functionalized chemically exfoliated MoS_2. *ACS Appl. Mater. Interfaces.* **2016,** *8* (46), 31567-31573.

9. Cheng, L.; Liu, J.; Gu, X.; Gong, H.; Shi, X.; Liu, T.; Wang, C.; Wang, X.; Liu, G.; Xing, H., PEGylated WS_2 nanosheets as a multifunctional theranostic agent for in vivo dual-modal CT/photoacoustic imaging guided photothermal therapy. *Adv. Mater.* **2014,** *26* (12), 1886-1893.

10. Henckel, D. A.; Lenz, O. M.; Krishnan, K. M.; Cossairt, B. M., Improved HER catalysis through facile, aqueous electrochemical activation of nanoscale WSe_2. *Nano lett.* **2018,** *18* (4), 2329-2335.

11. Guo, W.; Chen, Y.; Wang, L.; Xu, J.; Zeng, D.; Peng, D.-L., Colloidal synthesis of $MoSe_2$ nanonetworks and nanoflowers with efficient electrocatalytic hydrogen-evolution activity. *Electrochim. Acta.* **2017,** *231*, 69-76.

12. Niu, Z.; Li, Y., Removal and utilization of capping agents in nanocatalysis. *Chemistry of Materials* **2014,** *26* (1), 72-83.

13. Liu, H.; Guo, H.; Liu, B.; Liang, M.; Lv, Z.; Adair, K. R.; Sun, X., Few-Layer $MoSe_2$ Nanosheets with Expanded (002) Planes Confined in Hollow Carbon Nanospheres for Ultrahigh-Performance Na-Ion Batteries. *Advanced Functional Materials* **2018,** *28* (19), 1707480.

14. Ndala, Z.; Shumbula, N.; Nkabinde, S.; Kolokoto, T.; Nchoe, O.; Shumbula, P.; Tetana, Z. N.; Linganiso, E. C.; Gqoba, S. S.; Moloto, N., Evaluating the Effect of Varying the Metal Precursor in the Colloidal Synthesis of $MoSe_2$ Nanomaterials and Their Application as Electrodes in the Hydrogen Evolution Reaction. *Nanomaterials* **2020,** *10* (9), 1786.

15. Zhang, Y.; Shi, Y.; Wu, M.; Zhang, K.; Man, B.; Liu, M., Synthesis and surface-enhanced Raman scattering of ultrathin $SnSe_2$ nanoflakes by chemical vapor deposition. *Nanomaterials* **2018,** *8* (7), 515.

16. Niu, L.; Li, K.; Zhen, H.; Chui, Y. S.; Zhang, W.; Yan, F.; Zheng, Z., Salt-Assisted High-Throughput Synthesis of Single-and Few-Layer Transition Metal Dichalcogenides and Their Application in Organic Solar Cells. Small 2014, 10 (22), 4651-4657.

17. Tonndorf, P.; Schmidt, R.; Böttger, P.; Zhang, X.; Börner, J.; Liebig, A.; Albrecht, M.; Kloc, C.; Gordan, O.; Zahn, D. R., Photoluminescence emission and Raman response of monolayer MoS_2, $MoSe_2$, and WSe_2. Optics express 2013, 21 (4), 4908-4916.

18. Kang, M.; Rathi, S.; Lee, I.; Li, L.; Khan, M. A.; Lim, D.; Lee, Y.; Park, J.; Pham, A. T.; Duong, A. T., Photodetector Based on Multilayer SnSe2 Field Effect Transistor. *Journal of nanoscience and nanotechnology* **2018,** *18* (6), 4243-4247.

19. Wu, H.; Chen, W., Synthesis and reaction temperature-tailored self-assembly of copper sulfide nanoplates. Nanoscale 2011, 3 (12), 5096-5102.

20. Zherebetskyy, D.; Scheele, M.; Zhang, Y.; Bronstein, N.; Thompson, C.; Britt, D.; Salmeron, M.; Alivisatos, P.; Wang, L.-W., Hydroxylation of the surface of PbS nanocrystals passivated with oleic acid. Science 2014, 344 (6190), 1380-1384.

21. Onwudiwe, D. C.; Hrubaru, M.; Ebenso, E. E., Synthesis, structural and optical properties of TOPO and HDA capped cadmium sulphide nanocrystals, and the effect of capping ligand concentration. *J. Nanomater.* **2015,** *2015*.

22. Grisorio, R.; Quarta, D.; Fiore, A.; Carbone, L.; Suranna, G. P.; Giansante, C., The dynamic surface chemistry of colloidal metal chalcogenide quantum dots. *Nanoscale Adv.* **2019,** *1* (9), 3639-3646.

23. Zimdars, J.; Bredol, M., On the influence of coordinating solvents on the reduction of selenium for the phosphine-free synthesis of metal selenide nanoparticles. *New J. Chem.* **2016,** *40* (2), 1137-1142.

24. Hens, Z.; Moreels, I.; Martins, J. C., In situ 1H NMR study on the trioctylphosphine oxide capping of colloidal InP nanocrystals. *ChemPhysChem.* **2005,** *6* (12), 2578-2584.

25. Murthy, A. P.; Theerthagiri, J.; Madhavan, J., Insights on Tafel constant in the analysis of hydrogen evolution reaction. *The Journal of Physical Chemistry C* **2018,** *122* (42), 23943-23949.

26. Zeng, M.; Li, Y., Recent advances in heterogeneous electrocatalysts for the hydrogen evolution reaction. *Journal of Materials Chemistry A* **2015,** *3* (29), 14942-14962.

27. Qi, F.; Wang, X.; Zheng, B.; Chen, Y.; Yu, B.; Zhou, J.; He, J.; Li, P.; Zhang, W.; Li, Y., Self-assembled chrysanthemum-like microspheres constructed by few-layer $ReSe_2$ nanosheets as a highly efficient and stable electrocatalyst for hydrogen evolution reaction. *Electrochimica Acta.* **2017,** *224*, 593-599.

28. Zhang, L.; Wang, T.; Sun, L.; Sun, Y.; Hu, T.; Xu, K.; Ma, F., Hydrothermal synthesis of 3D hierarchical $MoSe_2$/$NiSe_2$ composite nanowires on carbon fiber paper and their enhanced

electrocatalytic activity for the hydrogen evolution reaction. *J. Mater. Chem A.* **2017,** *5* (37), 19752-19759.

29. Kwon, I. S.; Kwak, I. H.; Ju, S.; Kang, S.; Han, S.; Park, Y. C.; Park, J.; Park, J., Adatom Doping of Transition Metals in $ReSe_2$ Nanosheets for Enhanced Electrocatalytic Hydrogen Evolution Reaction. *ACS nano* **2020,** *14* (9), 12184-12194.

30. Liu, Y.; Xu, Y.; Han, Y.; Zhang, Z.; Xu, J.; Du, Y.; Bao, J.; Zhou, X., Facile synthesis of $SnSe_2$ nanoparticles supported on graphite nanosheets for improved sodium storage and hydrogen evolution. *Journal of Power Sources* **2019,** *436*, 226860.

6. Supplementary information

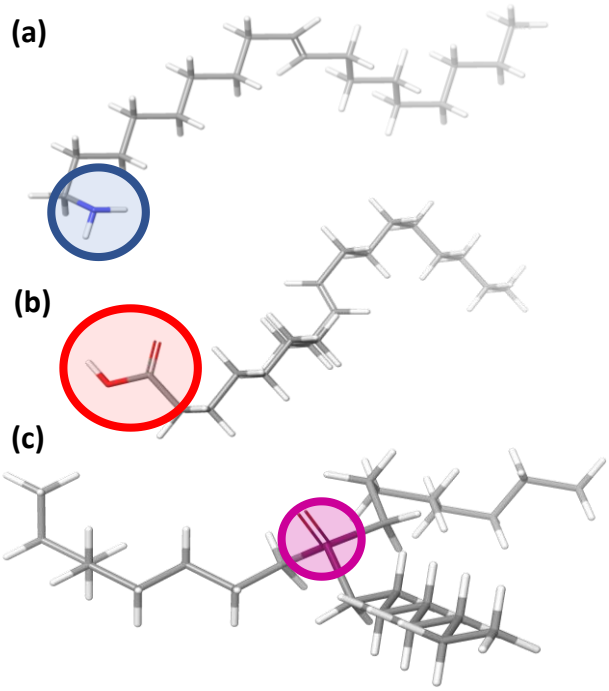


Figure S1: Structure of the solvents (a) oleylamine, (b) oleic acid, and (c) trioctylposphine oxide.

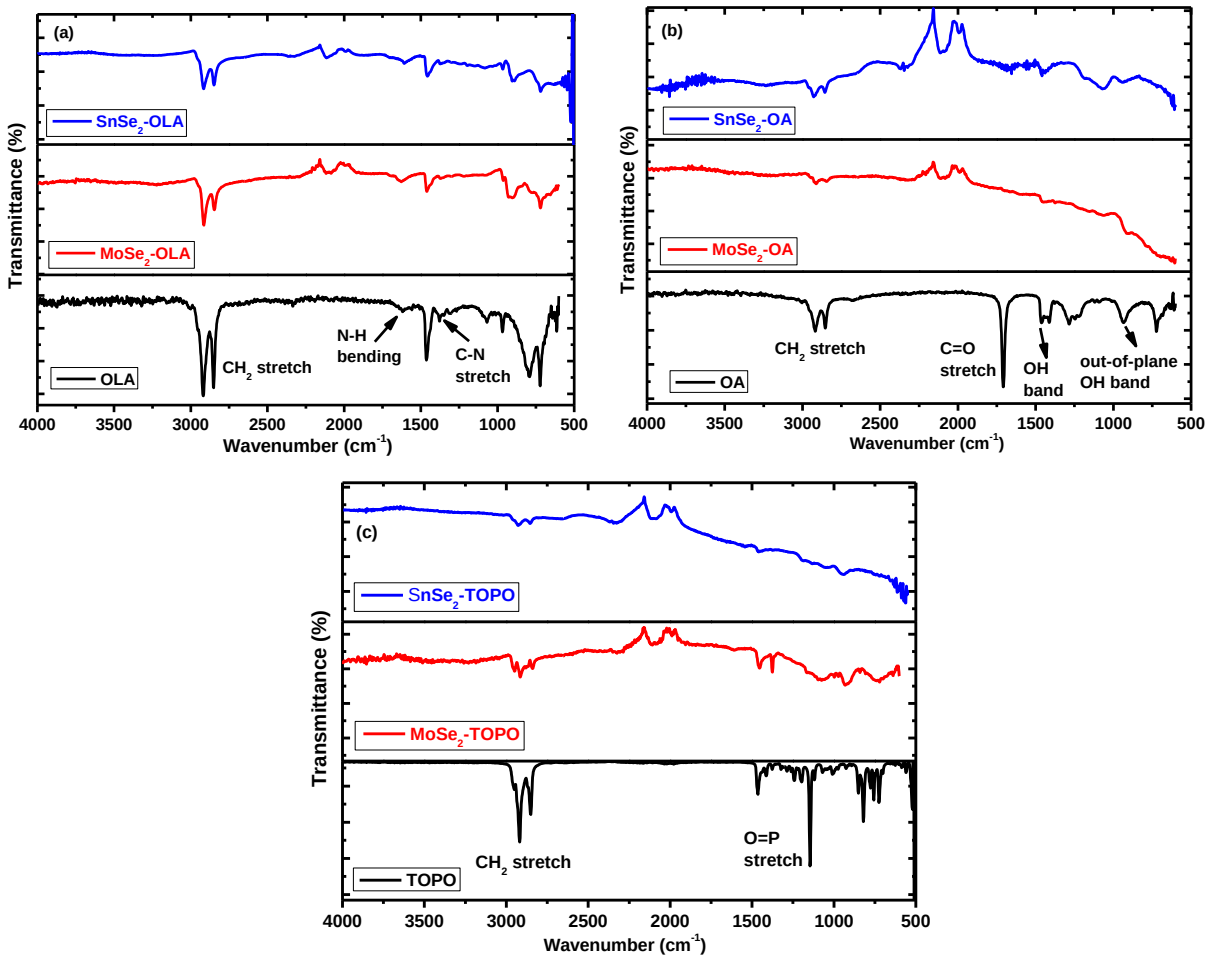


Figure S2: FTIR spectra of (a) OLA, $MoSe_2$-OLA, and $SnSe_2$-OLA. (b) OA, $MoSe_2$-OA, and $SnSe_2$-OA. (c) TOPO, $MoSe_2$-TOPO, and $SnSe_2$-TOPO.

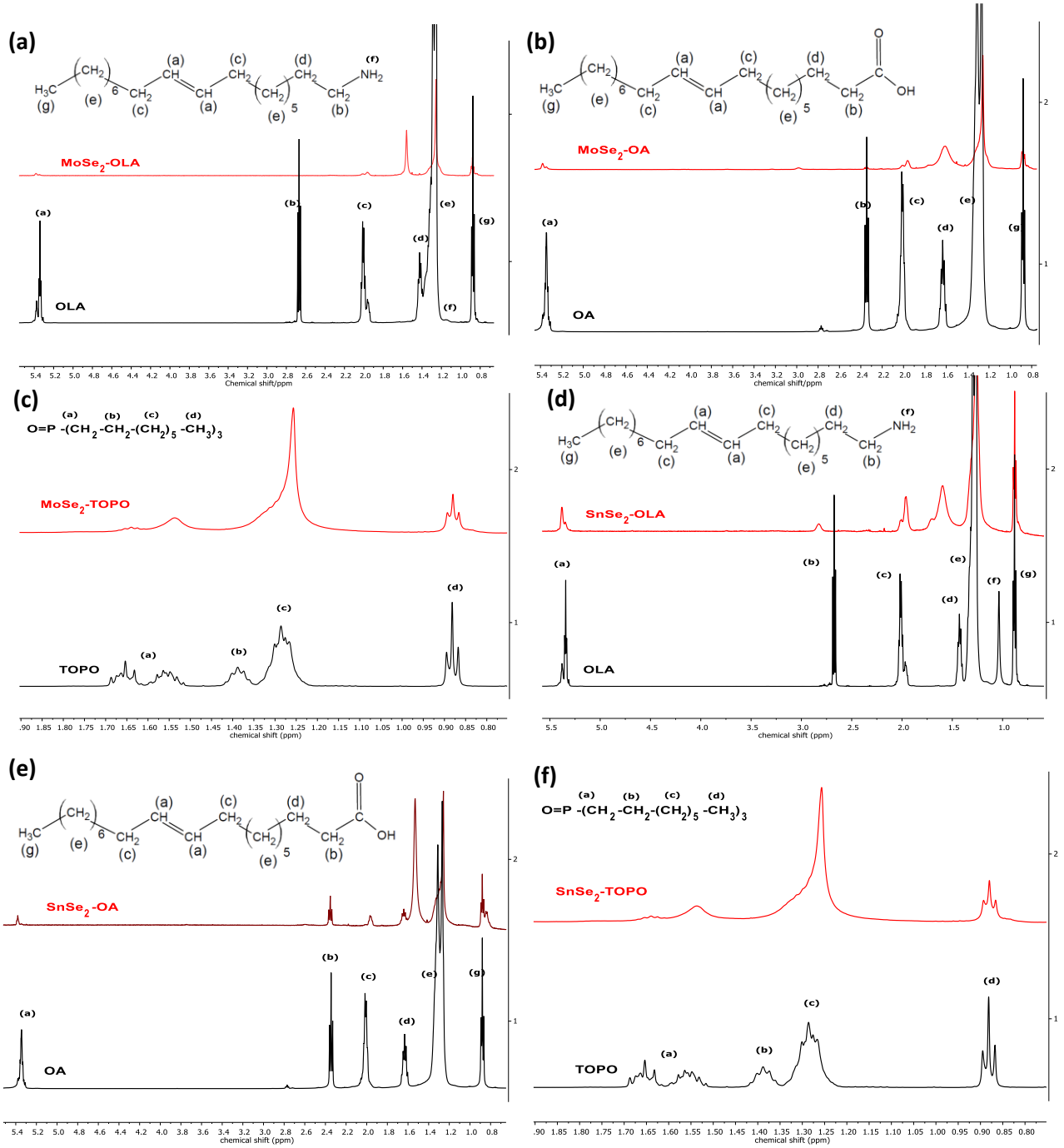


Figure S3: NMR spectra of (a) OLA and $MoSe_2$-OLA, (b) OA and $MoSe_2$-OA, (c) TOPO and $MoSe_2$-TOPO, (d) OLA and $SnSe_2$-OLA, (e) OA and $SnSe_2$-OA, (f) TOPO and $SnSe_2$-TOPO.

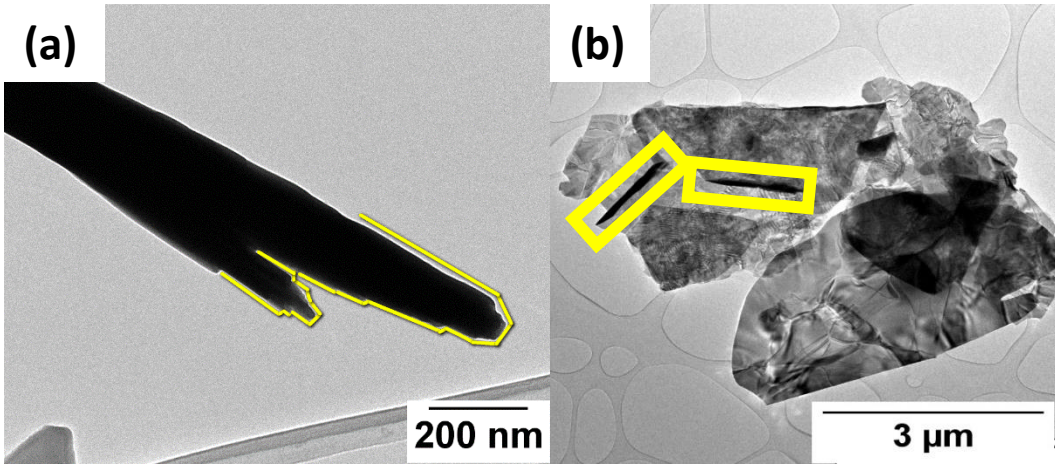


Figure S4: TEM images of the (a) $SnSe_2$-OA rod-like nanostructures and (b) curling in the $SnSe_2$-TOPO nanoplates.

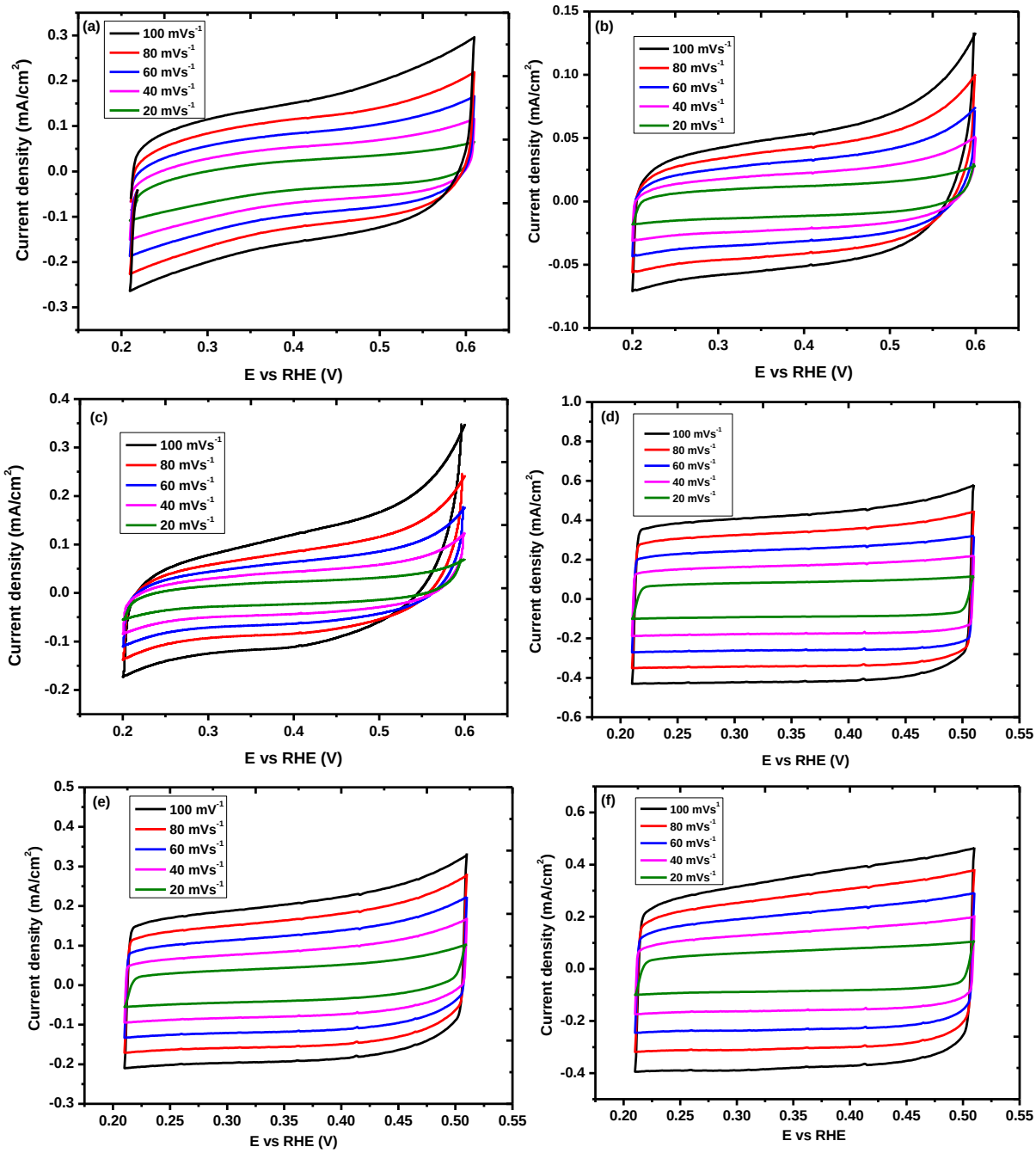


Figure S5: CV curves for the stability studies of (a) $MoSe_2$-OLA, (b) $MoSe_2$-OA and (c) $MoSe_2$-TOPO. CV curves for the stability of studies of (a) $SnSe_2$-OLA, $SnSe_2$-OA, and $SnSe_2$-TOPO.

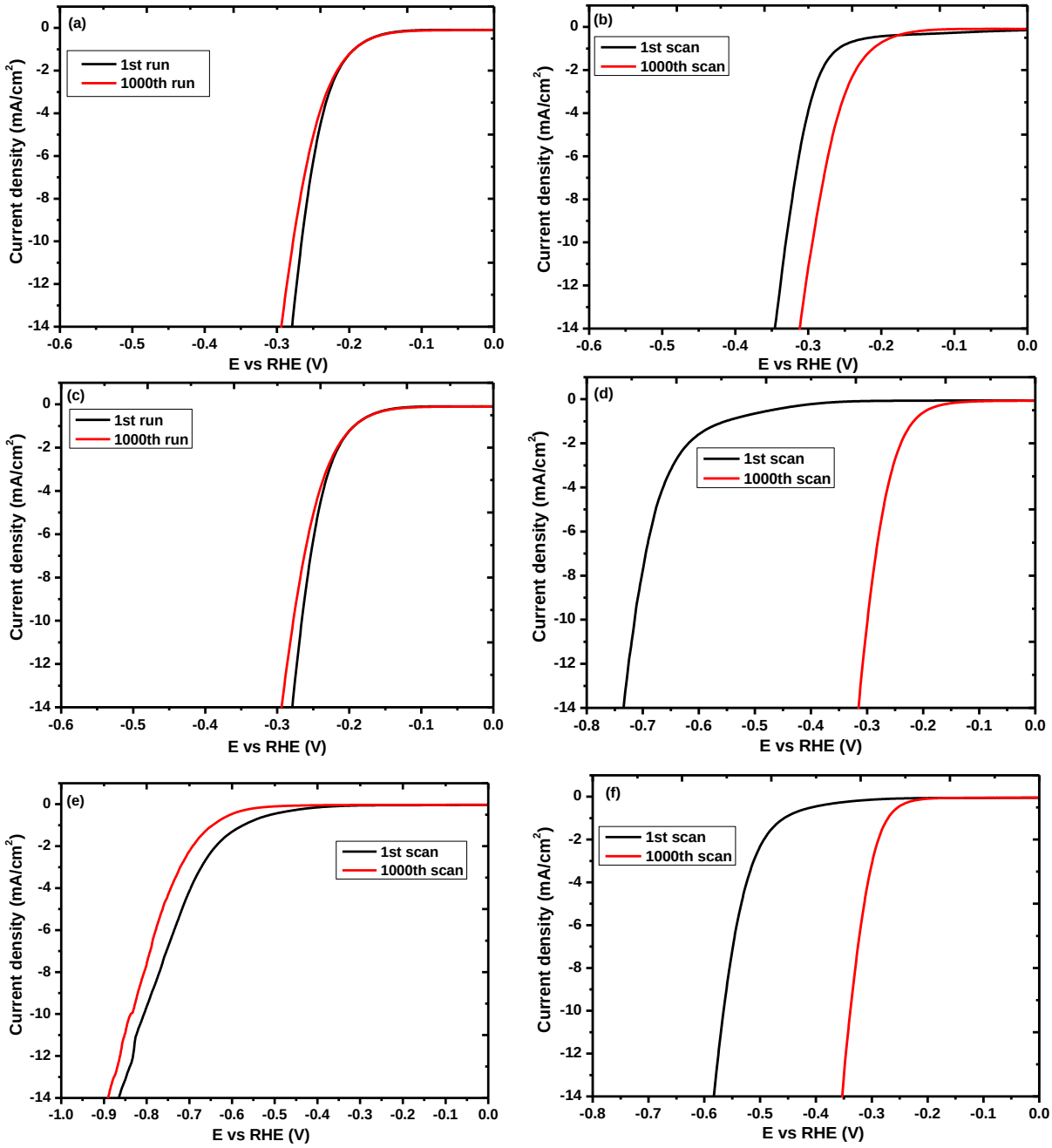


Figure S6: Polarisation curves for the stability studies of (a) $MoSe_2$-OLA, (b) $MoSe_2$-OA and (c) $MoSe_2$-TOPO. Polarisation curves for the stability of studies of (a) $SnSe_2$-OLA, $SnSe_2$-OA, and $SnSe_2$-TOPO.

Chapter 6: Colloidal synthesis of TMD nanostructures on pristine and nitrogen-doped reduced graphene oxide for use as electrocatalysts in the hydrogen evolution reaction

Chapter 6.1: The colloidal synthesis of $ReSe_2$ nanostructures on pristine and nitrogen-doped reduced graphene oxide for use as electrocatalysts in the hydrogen evolution reaction

1. Introduction

Transition metal dichalcogenides (TMDs) have been readily explored as potential electrocatalysts in the hydrogen evolution reaction (HER).[1-2] There has particularly been increased effort into improving the catalytic activity of TMDs towards HER to rival that of platinum (Pt). This includes efforts to ensure maximal exposure of the active edge sites of TMDs, directing phase changes of the normally 2H phase TMDs to the more catalytically active 1T phase, and making composites of the TMDs with carbon nanomaterials to improve the electron transfer processes and thus improve the catalytic activity.[3-5] Incorporating TMDs onto various carbon nanomaterials has proven to be incredibly effective in improving the catalytic activity of TMDs towards the HER.[5-6] This has been especially true when graphene oxide (GO) nanomaterials have been used to augment the TMDs.[7-8] This has been possible through the use of the functional groups on the GO acting as anchor sites for the growth of the TMD nanomaterials which ensures optimal interaction between the two components.[8] The conversion of the GO to rGO, while the TMDs are already situated on the GO, has been able to ensure improvements in the electron transfer processes of the TMDs in the HER. This has also had the added benefit of ensuring maximal exposure of the edge sites of the TMDs owing to the orientation of the TMDs as they grow on the GO.[8-9] There has recently been an effort to improve the performance of these hybrid nanomaterials even further by using doped carbon nanostructures. This owing to the well-documented superior electron transfer capabilities of the doped carbon nanostructures compared to the pristine carbon nanostructures.[10-11] Due to this push to synthesize hybrid nanostructures of TMDs and doped carbon nanostructures, an understanding of the interaction between the defects created through doping and the TMDs is essential. $ReSe_2$ has already been shown to be a rather promising electrocatalyst for HER.[12-13]

However, $ReSe_2$ like many other TMDs has been known to have relatively poor electron conductivity which compromises its catalytic activity towards the HER.[9,13] In this work, $ReSe_2$ nanostructures were grown on rGO and nitrogen-doped rGO to form hybrid nanostructures and the catalytic activity of the hybrid nanostructures towards the HER was investigated.

2. Experimental section

2.1 Chemicals

Ammonium perrhenate (NH_4ReO_4, 99.98%), selenium powder (Se, 99.99%), oleic acid (90%), graphene oxide (90%) all reagents were purchased from Sigma-Aldrich and used as received without purification.

2.2 Synthesis of nanostructures

2.2.1 Synthesis of $ReSe_2$ nanostructures

The selenium powder (Se, 0.559 mmol) was added into the three-neck round bottom flask containing 20 ml of oleic acid at room temperature. The temperature was increased to 220 ºC to thermally reduce the Se to Se^{2-} with the help of the solvent, which also acted as a reducing agent. Once all the Se was reduced, a mixture of ammonium perrhenate (NH_4ReO_4, 0.186 mmol) and the solvent/surfactant was added into the reaction mixture. The temperature was then raised to 330 ºC and the reaction was run for 120 min. The nanoparticles formed were then washed with ethanol and toluene using a centrifuge and then left to dry.

2.2.2 Doping of rGO

A quartz tube was purged with Ar for 60 min while the temperature was increased to 800 °C at a rate of 10 °C/min. The rGO was doped using ammonia gas as the nitrogen source, with Ar as the carrier gas at a flow-rate of 50 ml/min. The temperature was held at 800 °C for 3 hrs then cooled to room temperature.

2.2.3 Synthesis of $ReSe_2$-rGO and $ReSe_2$-N-rGO nanocomposites

The selenium powder (Se, 0.559 mmol) was added into the three-neck round bottom flask containing 20 ml of oleic acid at room temperature. The temperature was increased to 220 ºC to thermally reduce the Se to Se^{2-} with the help of the solvent, which also acted as a reducing agent. A sample vial containing 30 mg of rGO/N-rGO, ammonium perrhenate (NH_4ReO_4, 0.186 mmol), and 5 ml of oleic acid was sonicated for 30 minutes. The vial was then heated to dissolve the ammonium perrhenate and injected into the Se-oleic acid mixture at 220 °C. The

temperature was then raised to 330 ºC and the reaction was run for 120 min. The nanoparticles formed were then washed with ethanol and toluene using a centrifuge and then left to dry.

2.3 Characterization techniques

The phase purity, crystallinity, and preferred crystal orientation of the products were examined using powder X-ray diffraction (PXRD) on a Bruker MeasSrv D2-205530 diffractometer using secondary graphite monochromated CuKα radiation (λ 1.5406 Å) at 30 kV/10 mA. Measurements were taken using a glancing angle of incidence detector at an angle of 2°, for 2θ values over 10 - 80° in steps of 0.026° with a step time of 37 s and at a temperature of 25 °C. The XPS measurements of the powder samples were obtained using a Thermo ESCAlab 250Xi with Al kα photon source (1486.7 eV), X-ray power of 300W, X-ray spot size of 900 µm, pass energy (survey) of 100 eV, pass energy (20 eV), and pressure of $<10^{-8}$ mBar. The sample morphologies were determined using the transmission electron microscopy (TEM) carried out on an FEI Tecnai T12 TEM microscope operated at an acceleration voltage of 120 kV The TEM samples were prepared by sonicating a spatula tip of the sample in ethanol and drop-casting that dispersion on a lacey carbon Cu grid. The total surface area and pore volume of the nanostructures were ascertained using a Micromeritics TriStar 3000 Surface Area and Porosity Analyzer. Thermal analysis was done using a Perkin Elmer TGA 6000 thermogravimetric analyzer using high purity nitrogen and air at a heating rate of 10 °C/min and gas flow rate of 20 mL/min.

2.4. Electrochemical characterization

The electrochemical measurements were carried out on a BASi epsilon E2. All measurements were carried out in 0.5 M H_2SO_4 using a three-electrode system. An Ag/AgCl electrode was used as the reference electrode, a platinum wire was used as the counter electrode. A modified glassy carbon electrode with a 3 mm diameter was used as the working electrode. The ink or fresh dispersion of the sample was prepared by dispersing 5.0 mg of the $ReSe_2$ or the $ReSe_2$ and rGO/N-rGO nanocomposites with 0.5 mg carbon black and 40 µl of Nafion solution (5 wt%) in a 1 ml mixture of water and isopropanol at a 3:1 ratio. The solution was then sonicated for 30 min and ~ 5 µl of the ink was drop-casted onto the glassy carbon electrode. The electrode was allowed to dry at room temperature. The linear sweep voltammograms were obtained at a scan rate of 2 mVs^{-1} and the cyclic voltammograms were obtained at a potential range of 0.2 – 0.6 V vs RHE at 100 mVs^{-1} scan rate. The measured potentials vs Ag/AgCl were converted to the reversible hydrogen electrode (RHE) scale according to the Nernst equation:

$E_{RHE} = E_{Ag/AgCl} + 00059\,pH + E^{0}_{Ag/AgCl}$ (1)

Where E_{RHE} is the converted potential vs RHE, $E^{0}_{Ag/AgCl}$ = 0.210 V at 25 °C. The Impedance spectroscopy studies were conducted on a Biologic SP 300, the measurements were done at a potential of -200 mV vs RHE and a frequency range between 0.1 Hz and 100 kHz.

3. Results and discussion

Powder X-ray diffraction (PXRD) was used to characterize the phase, composition, and crystallinity of the nanostructures. The PXRD patterns of reduced graphene oxide (rGO) and nitrogen-doped reduced graphene oxide (N-rGO) are shown in **Fig.1(a).**

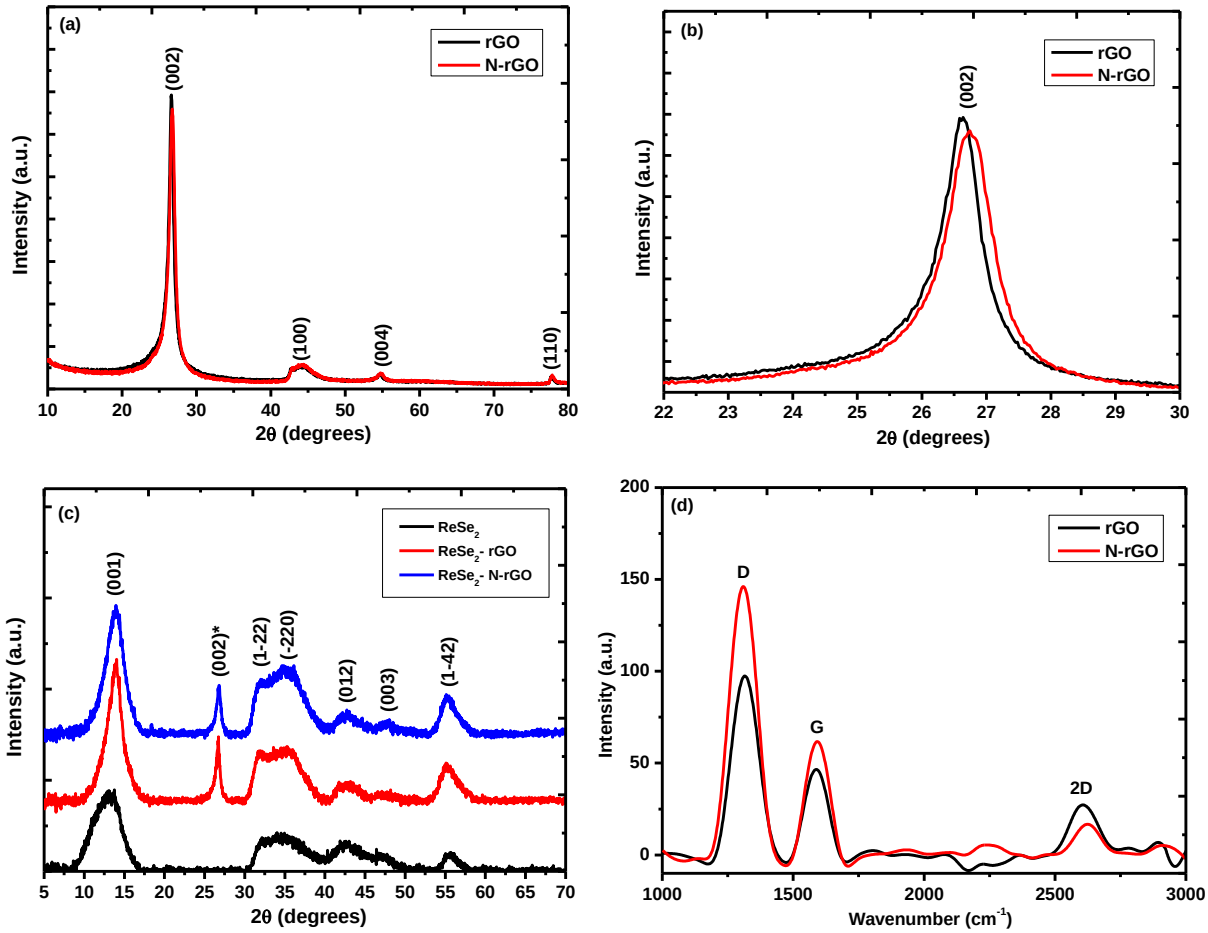


Figure 1: PXRD patterns of (a) rGO and N-rGO. (b) PXRD shows the shift of the (002) in rGO and N-rGO. (c) the PXRD pattern of the $ReSe_2$ and the nanocomposites (d) Raman spectra of the rGO and N-rGO.

The (002) peak is observed for both the rGO and N-rGO at 26.6° and 26.8° respectively. This peak is indicative of the crystalline nature of the graphene layers, the crystalline nature of the rGO is conserved after nitrogen doping as expected.[14] The appearance of the (100), (004), and

(110) peaks at 43.8°, 54.7°, and 77.8° degrees respectively indicates that the rGO nanosheets are not monolayer.[14] The appearance of the (004) peaks specifically indicates that the nanostructures are highly crystalline and that there is a high average number of stacked graphene sheets.[15] There is an observable shift to the right in the (002) peak in the N-rGO sample as shown in **Fig.1(b)**, this has been attributed to the doping of nitrogen in the graphene oxide lattice structure.[14] The diffraction peaks as shown in **Fig.1(c)** are observed at 13.7°, 31.9°, 35.2°, 42.6°, 47.1, and 55.2°. These diffraction peaks correspond to the lattice planes (001), (1-22), (-220), (012), (003) and (1-42) of $ReSe_2$. The PXRD confirms that the $ReSe_2$ nanostructures have crystallized in the distorted 1T phase triclinic system with the P-1 space group (JCPDS card no: 01-065-4275). The (002) peak of the rGO and N-rGO can still be observed in the powder patterns of the hybrid nanostructures which confirms the incorporation of the $ReSe_2$ nanostructures on the rGO and N-rGO. Raman spectroscopy was also used to characterize the rGO and N-rGO. This was done by analyzing the characteristics of the D, G, and 2D bands of the nanostructures. The Raman spectra of the rGO and N-rGO are shown in **Fig.1(d)**. The position of the G-band in rGO and N-rGO was observed at ~1588 cm^{-1} and 1591 cm^{-1} respectively, this is in accordance with what has been previously reported in the literature.[16-17] The G-band is attributed to the in-plane stretching vibrations of the sp^2 hybridized carbon-carbon bonds. The D band is associated with the defects that exist in the structure of the materials. The D-bands of the rGO and N-rGO were observed at 1316 cm^{-1} and 1307 cm^{-1} respectively. The broad and high-intensity D band observed in both the undoped rGO and N doped rGO signifies a high level of lattice distortion and sp^3 like defects which show that there are still functional groups that exist at the surface of the rGO.[17] The rGO was further reduced in the doping process which occurred at 800 °C. The I_D/I_G ratio of the N-rGO was found to be 2.09 which was higher than that of the rGO at 1.86, this indicates that there is an increase in the number of defects in the structure of the N-rGO which is due to the nitrogen-doping.[18] The 2D peak occurs due to two lattice vibrational processes, this peak can be used to assess the quality of graphene because it is very sensitive to disorder. It is normally very prominent in highly crystalline high-quality graphene. The peak experiences a decrease in intensity when there are defects in the structure of the materials.[17] The notable decrease in the intensity of the 2D peak of the N-rGO compared to the rGO is indicative of the introduction of more disorder in the structure through the introduction of nitrogen defects.

X-ray photoelectron spectroscopy (XPS) was used to evaluate the bonding configuration and the elemental composition of the nanomaterials. The XPS spectra of rGO and N-rGO are shown in **Fig.S1(a) and (b)**. The C1s and O1s peaks were detected in the survey scan of the rGO

nanostructures. The survey scan of the N-rGO nanomaterials also shows the N1s peak which confirms the doping of the rGO with nitrogen.[19] The elemental composition of rGO and N-rGO is shown in **Table 1**.

Table1: Summary of the elemental composition of rGO and N-rGO

Sample	Element	Binding energy (eV)	Atomic (%)
rGO	C	284.9	86.4
	O	532.8	13.6
	N	-	-
N-rGO	C	284.4	97.5
	O	532.7	1.6
	N	399.1	0.9

The elemental composition shows that the percentage of oxygen is much larger in rGO compared to the N-rGO. This shows that the rGO contains more of oxygen-containing functional groups and that these functional groups are effectively removed in the doping process. The elemental composition of the N-rGO only shows a doping concentration of 0.9 % which is relatively small. The C 1s spectra of the rGO and N-rGO are shown in **Fig.S2(a) and (b)** and a summary of the atomic composition is shown in **Table 2**.

Table 2: Summary of the C 1s assignments and composition

Sample	Assignment	Binding energy (eV)	Atomic (%)
rGO	C-C sp^2	284.2	35.5
	C-C sp^3	284.9	23.0
	C-O	285.8	20.3
	C=O	533.5	7.1
	O-C=O	288.7	6.8
N-rGO	C-C sp^2	284.4	69.7
	C-C sp^3	532.7	15.6
	C-O	-	-
	C=O	-	-
	O-C=O	399.1	0.9

The peak binding energies were found to be 284.9 eV, 285.8 eV, and 288.7 for C-C, C-O, and O-C=O functional groups respectively for rGO.[20] The peak binding energies were found to be

284.4 eV and 285.7 for C-C and C-O functional groups respectively for N-rGO.[20] **Table 2** shows there is a notable decrease in the amount of oxygen-containing functional groups in N-rGO, this is due to the removal of the functional groups during doping. The N 1s spectrum of N-rGO is shown in **Fig.2(a)**, the N1s peak can be deconvoluted into several individual peaks, namely the pyridinic-N (398.1–399.3 eV), pyrrolic-N (399.8–401.2 eV), and graphitic-N (401.1–402.7 eV).[20,21] These characteristic peaks are observed in the N1s XPS spectrum and are shown in **Fig.2(a)**, the nitrogen-doped graphene oxide seems to be dominated by pyridinic-N sites followed by pyrrolic-N sites. The graphitic-N sites are the least prevalent, while the peak at 405 eV is attributed to chemisorbed nitrogen oxide. The types of nitrogen defects introduced are shown graphically in **Fig.2(b)**. The XPS spectra of the hybrid nanostructures shown in **Fig.S3(a) and (b)** show the characteristic peaks of $ReSe_2$, the Re 4f, and Se 3d peaks. The peaks were observed in both the $ReSe_2$-rGO and $ReSe_2$-N-rGO. The XPS spectra of the Re 4f and Se 3d are shown in **Fig.2(c) and (d)** respectively.

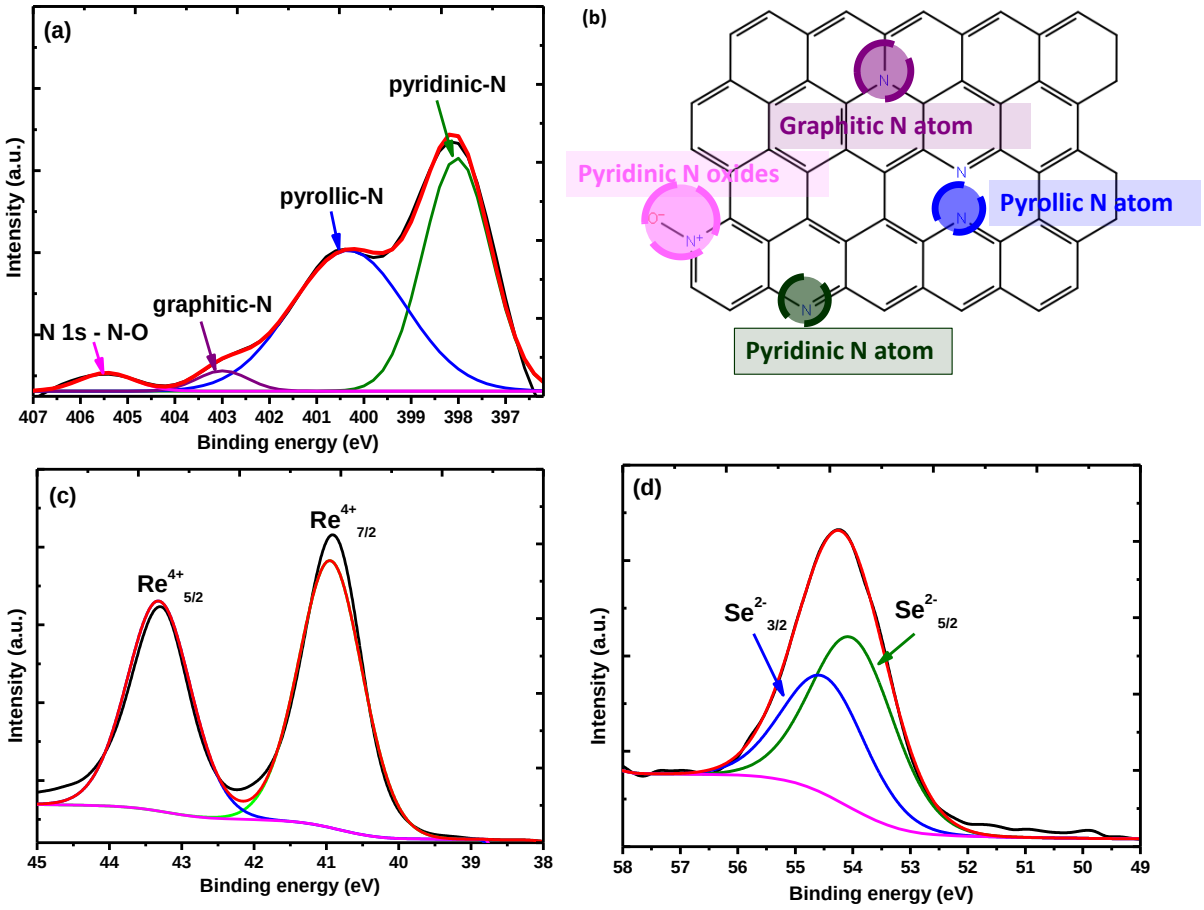


Figure 2: (a) Deconvoluted XPS spectrum of the N 1s peak. (b) Graphical representation of the types of nitrogen defects introduced. (c) High-resolution XPS spectrum of Re. (d) High-resolution XPS spectrum of Se.

The high-resolution XPS spectrum of Re^{4+} is shown in **Fig.2(c)**, the core level peaks $4f_{7/2}$ and $4f_{5/2}$ were measured at ~41 eV and ~43 eV respectively.[22] The Se high-resolution XPS spectrum of the $ReSe_2$ nanomaterials is shown in **Fig.2(d)**. The deconvoluted peak at ~54 eV shows the characteristic core level $3d_{5/2}$ and $3d_{3/2}$ peaks Se^{2-} at 53.7 eV and 54.7 eV respectively.[22]

The TEM images of the rGO, N-rGO, and the $ReSe_2$ nanocomposites are shown in **Fig.3**.

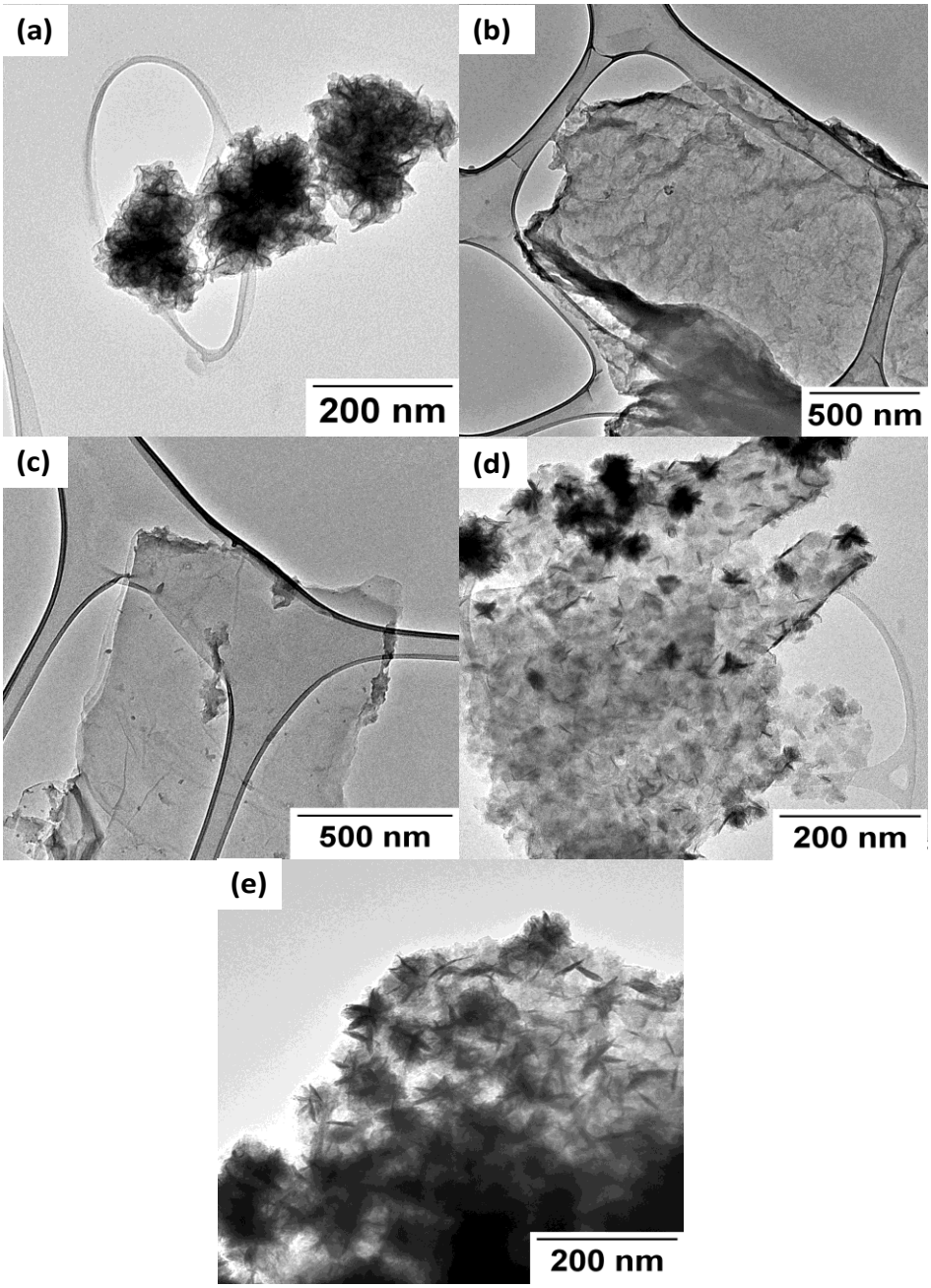
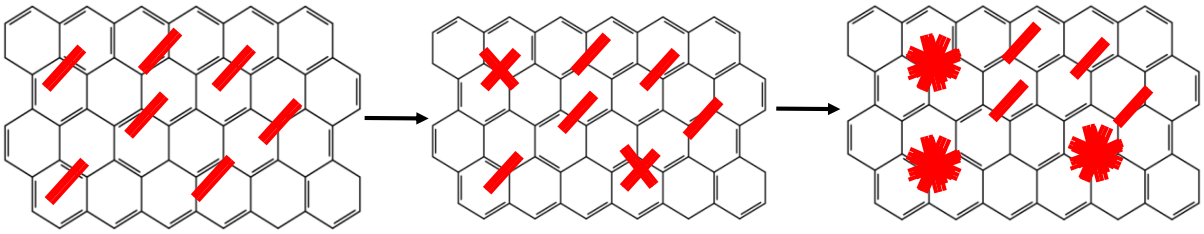


Figure 3: TEM images of (a) $ReSe_2$ nanoflowers, (b) rGO, (c) N-rGO, (d) $ReSe_2$-rGO, and (e) $ReSe_2$-N-rGO.

The TEM image of the $ReSe_2$ nanostructures is shown in **Fig.3(a)**, the image shows that the $ReSe_2$ form in a flower-like morphology. The TEM images of rGO and N-rGO are shown in **Fig.3(b) and (c)** show that they are both composed of nanosheets that are wrinkled and folded in some regions. The nanosheets are not single sheets, as was already confirmed by the PXRD analysis. There are no significant and notable changes in the morphology of the rGO before and after nitrogen doping. The images of the hybrid nanostructures of the $ReSe_2$-rGO and $ReSe_2$-N-rGO are shown in **Fig.3(e)**. The images show that few-layered $ReSe_2$ nanoflakes have grown on the surface of the rGO and N-rGO. The images also show how $ReSe_2$ nanoflowers are able to fully grow on the rGO and N-rGO, this occurs through the overlap of individual nanoflakes that grow on top of each other. A schematic representation of this process is shown in **Scheme 1**.



Scheme 1: Growth of $ReSe_2$ few-layer nanosheets and formation of flower-like nanostructures from the few-layer nanosheets.

Thermogravimetric analysis (TGA) was used to investigate the decomposition of the rGO, N-rGO, and the hybrid nanostructures under an airflow of 20ml/min. The decomposition profiles are shown in **Fig.4**.

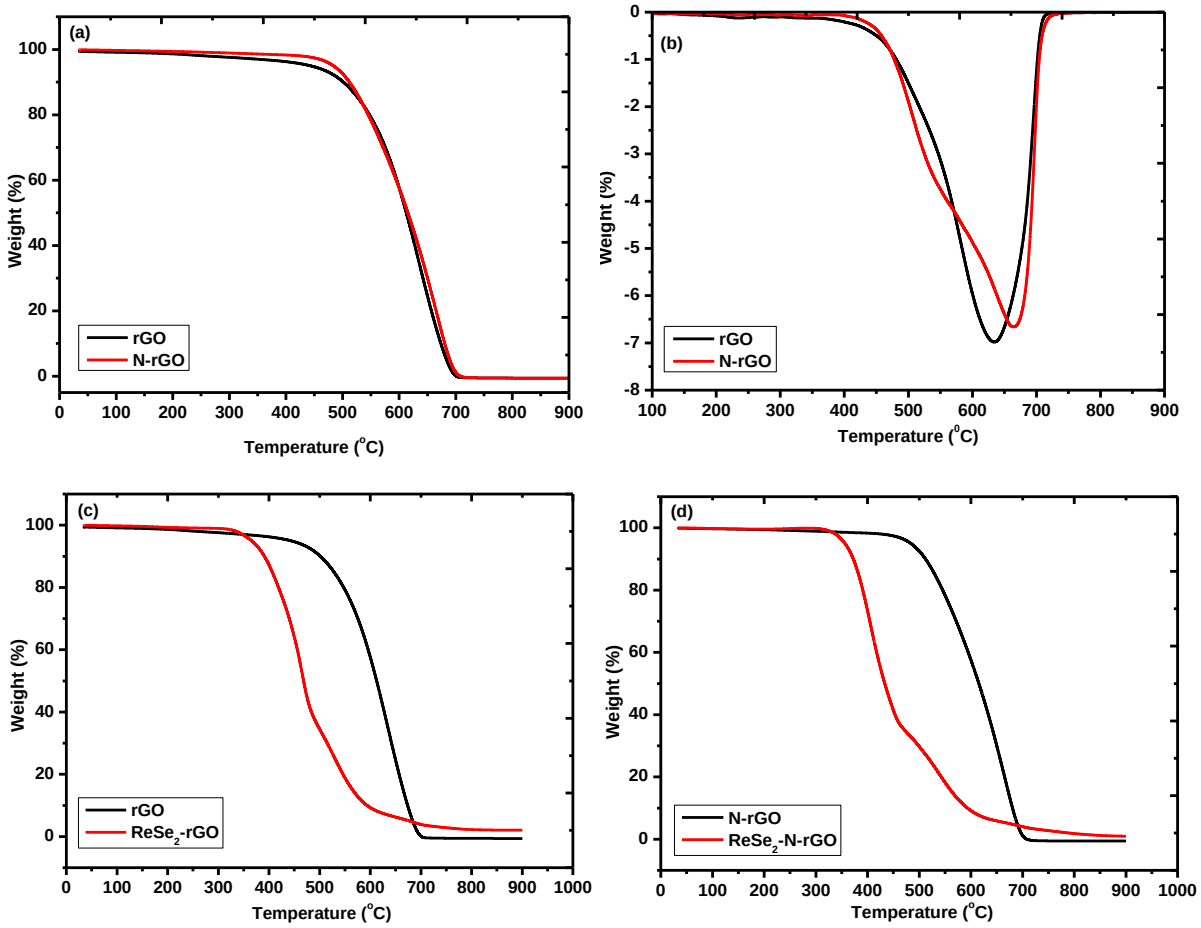


Figure 4: Decomposition profiles of (a) rGO and N-rGO, (c) rGO and $ReSe_2$-rGO, (d) N-rGO and $ReSe_2$-N-rGO. (b) derivative decomposition profile of rGO and N-rGO.

The TGA profiles of the rGO and N-rGO are shown in **Fig.4(a)**. The initial weight losses on both profiles at ~ 150 °C are attributed to the evaporation of water molecules adsorbed on the rGO and N-rGO.[22] The second largest mass loss was measured at 6% for rGO and 3% for N-rGO which was attributed to the oxygen-containing functional groups.[23] There is twice the loss of these functional groups in rGO which suggests that the doping process was able to remove most of these functional groups in the N-rGO beforehand. The largest weight loss between 400 °C-700 °C which accounted for 94% in rGO and 97% in N-rGO was attributed to the decomposition of the carbon skeleton of graphene.[22] The decomposition temperature for this weight loss on N-rGO was slightly higher than that of rGO which was expected as doped carbon structures have been known to be more stable than undoped rGO structures.[24] The difference in decomposition temperatures can be clearly seen in the derivative decomposition profile in **Fig.3(b)**. The TGA curves of the hybrid nanostructures are shown in **Fig.4(c) and (d)**. The

nanocomposites show two mass losses, one between 400-500 °C and another between 500 to 600 °C. The first mass loss was measured at 60% for rGO and 63% for N-rGO. The mass loss was attributed to the decomposition of the graphene backbone. The second mass loss was attributed to the decomposition of the oleic acid that is bound to the $ReSe_2$ nanostructures which accounted for 37% and 36% of the $ReSe_2$-rGO and $ReSe_2$-N-rGO respectively.[23] The increase in the temperature of the decomposition compared to literature was attributed to the bound oleic acid (oleic acid interacting with the $ReSe_2$ nanostructures) as opposed to unbound oleic acid.[23] The residues that remained after decomposition were accounted for 2.7 % and 1.7% for $ReSe_2$-rGO and $ReSe_2$-N-rGO respectively. This suggests that the rGO had a larger mass loading of the $ReSe_2$ compared to the N-rGO, which suggests that the oxygen functional groups may be a better anchor for the $ReSe_2$ nanoflowers than the nitrogen defects on the N-rGO.

The adsorption-desorption curves of all the nanostructures show a type-IV isotherm with a distinct hysteresis loop (IUPAC classification) as shown in **Fig.S4 and Fig.4**, this suggests that the nanostructures assume a mesoporous structure.[24]

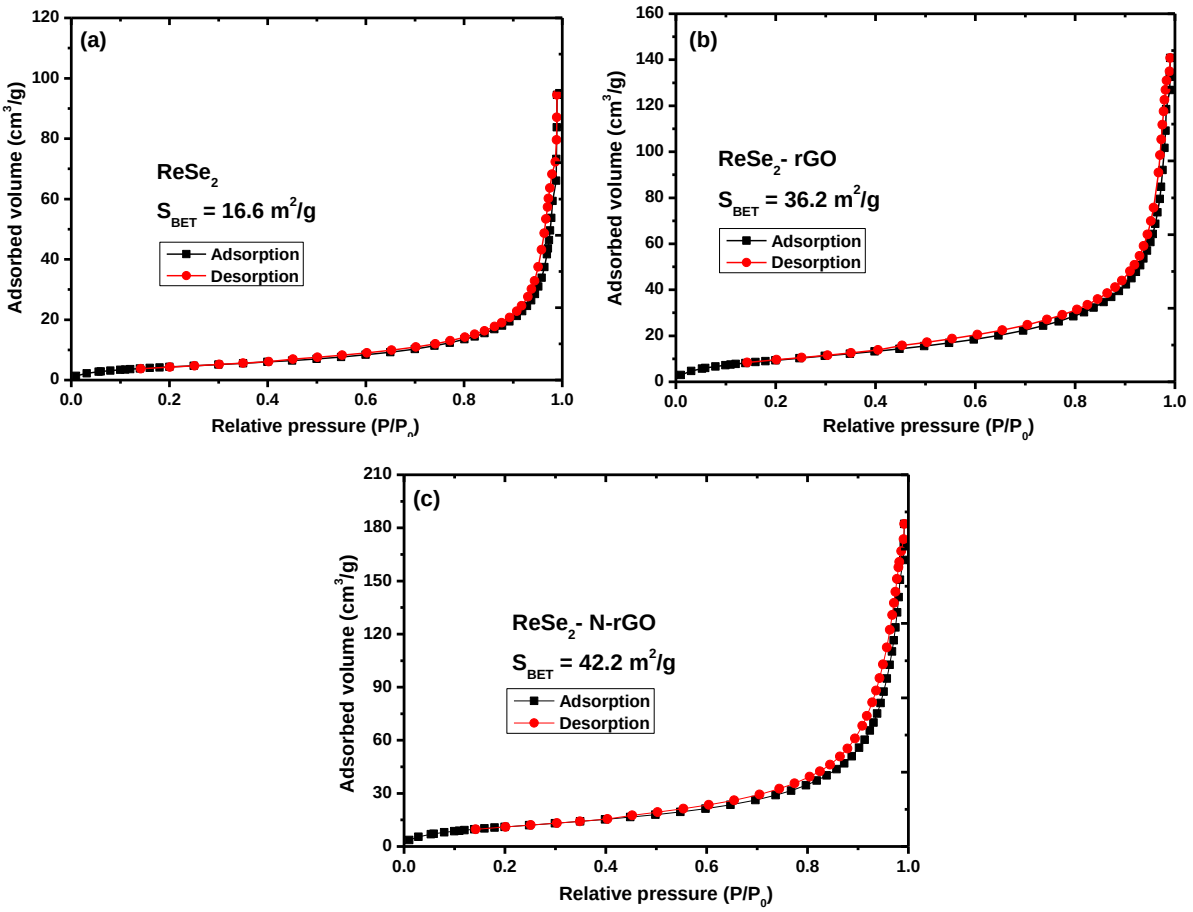


Figure 5: Adsorption- desorption isotherms of (a) $ReSe_2$, (b) $ReSe_2$-rGO, and (c) $ReSe_2$-N-rGO.

The BET surface area of the rGO and N-rGO was calculated to be 231.3 m^2/g and 236.3 m^2/g as shown in Fig.S3(a) and (b). The surface area of the doped and undoped area is virtually identical which suggests that there was no significant folding or wrinkling of the nanosheets during the doping process which would have reduced the surface area**.** The BET surface area of the pristine $ReSe_2$ nanoflowers was measured to be 16.6 m^2/g as shown in **Fig.5(a)**. The surface area of the $ReSe_2$-rGO and $ReSe_2$-N-rGO was calculated to be 36.2 m^2/g and 42.2 m^2/g respectively as shown in **Fig.5(b) and (c)**, the boosted surface area of the pristine $ReSe_2$ nanoflowers is due to the confined growth of vertically aligned nanosheets.[25]

Several parameters are used to evaluate the catalytic activity of nanomaterials towards the HER. The polarization curves can be used to determine two useful parameters, which are the onset potential and the overpotential at 10 mA/cm^2 (η_{10}). The onset potential is the lowest potential at which the HER can be produced. A good HER catalyst is characterized by a low onset potential. The onset potential of the $ReSe_2$ nanoflowers was determined to be 159 mV. The incorporation of the $ReSe_2$ nanoflowers on the carbon nanostructures significantly reduces the onset potential. The onset potential of the $ReSe_2$-rGO and $ReSe_2$-N-rGO was measured to be 128 and 115 mV respectively. The use of nitrogen-doped rGO has a positive effect on the catalytic activity of the $ReSe_2$ nanoflowers as it results in the lowest onset potential. The overpotential at 10 mA/cm^2 (η_{10}) is a measure of the overpotential at a specified current density, 10 mA/cm^2 is chosen because it represents the operating current density of a commercial cost-competitive photoelectrochemical cell (PEC). This parameter is useful when comparing the catalytic activity of nanomaterials, an ideal HER catalyst has the lowest possible η_{10}. The η_{10} of the $ReSe_2$ nanoflowers was recorded at 331 mV. The η_{10} of the $ReSe_2$ nanocomposites were recorded at 259 mV and 218 mV for the $ReSe_2$-rGO and $ReSe_2$-N-rGO respectively. Incorporating the $ReSe_2$ nanoflowers on rGO improves the overpotential which is attributed to the improved electron conductivity of the nanocomposites. The doping of the rGO with nitrogen further improves the overpotential as expected. The Tafel plot analysis is crucial in evaluating the catalytic activity of nanomaterials towards the HER. The Tafel equation ($\eta = b\log J + a$, where η is the overpotential, J is the current density and b is the Tafel slope) fitted to the Tafel plots to determine the Tafel slope.[26] The Tafel slope can be used to gain insights into the mechanistic details of the HER on the specified catalyst. The Tafel slope can be used to determine the rate-limiting step of the reaction and the reaction pathway of the HER on the surface of the nanostructures. The Tafel slopes of the $ReSe_2$ nanoflowers and the

nanocomposites were determined to be 97 mV/dec, 84 mV/dec, and 72 mV/dec for the $ReSe_2$ nanoflowers, $ReSe_2$-rGO, and $ReSe_2$-N-rGO respectively. This shows that the HER on the nanostructures proceeds under the Volmer-Heyrovsky pathway. This pathway involves the adsorption of protons on the surface of the catalyst which then combines with electrons to form adsorbed hydrogen atoms (Volmer step), this is followed by the electrochemical desorption of the hydrogen from the surface of the electrode (Heyrovsky step). The electrochemical desorption is the rate-limiting step in this case.

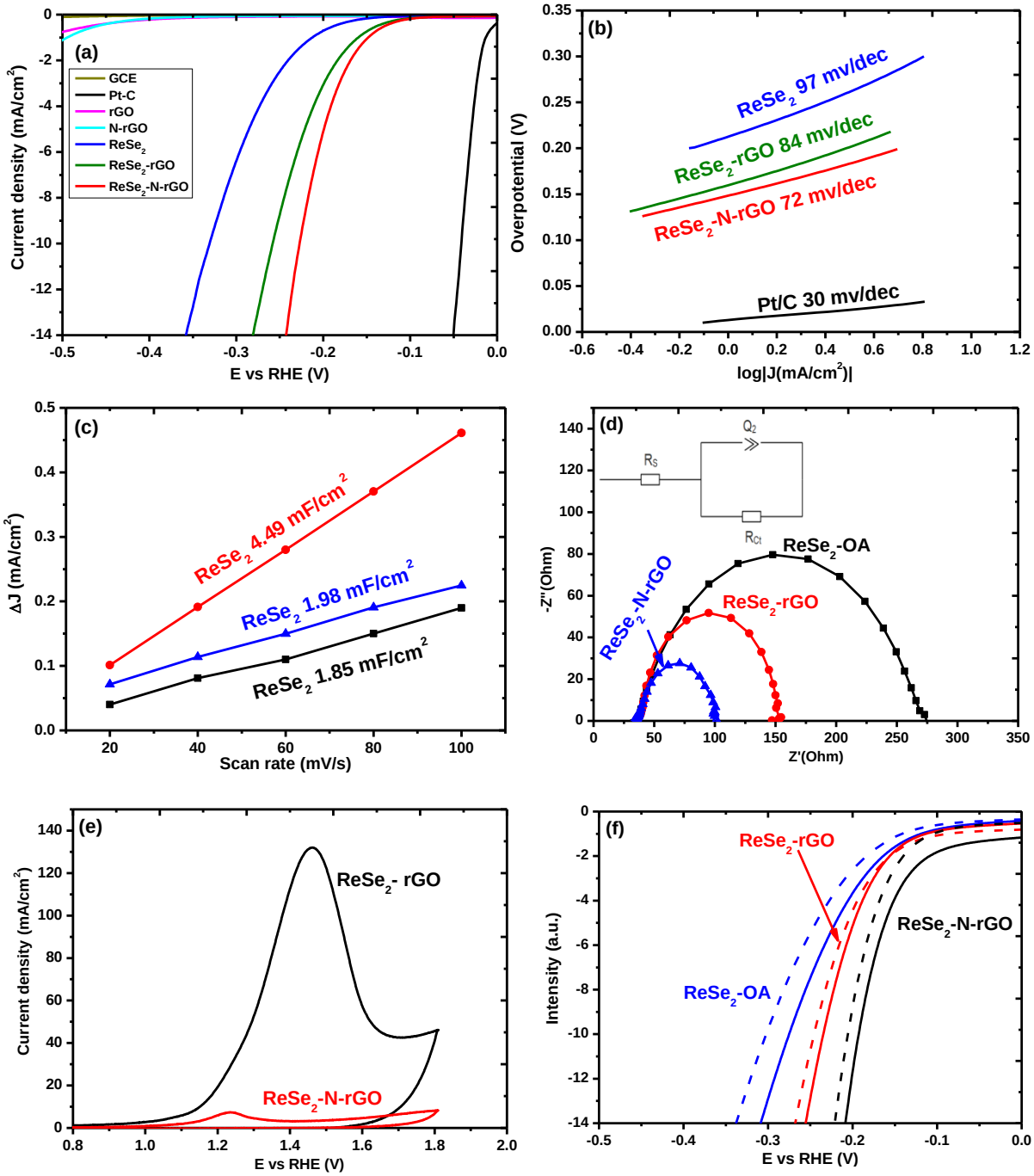


Figure 6: (a) Polarisation curves of the $ReSe_2$ nanostructures and their nanocomposites. (b) Tafel plots of the $ReSe_2$ nanostructures and nanocomposites. (c) C_{dl} plots of the $ReSe_2$

nanostructures and nanocomposites. (d) Nyquist plots of the $ReSe_2$ nanostructures and nanocomposites. (e) Irreversible surface oxidation profile of $ReSe_2$-rGO and $ReSe_2$-N-rGO. (f) Stability studies of the $ReSe_2$ nanostructures and nanocomposites.

The electrochemically active surface area (ECSA) was determined using the C_{dl} (double layer capacitance). The C_{dl} has been shown to be proportional to the ECSA, the C_{dl} was determined using cyclic voltammetry (CV) as shown in **Fig.S5**.[27] The estimation is done by plotting ΔJ (J_a-J_c) vs the scan rate at 0.41 V vs RHE which is shown in **Fig.6(c)**, in this linear plot, the slope is the C_{dl}. The C_{dl} of the nanostructures was determined to be 1.85 mF/cm^2, 1.98 mF/cm^2, and 4.45 mF/cm^2 for $ReSe_2$, $ReSe_2$-rGO, and $ReSe_2$-N-rGO respectively. The nanocomposites have a higher ECSA which indicates that the exposure of the active sites was enhanced when the rGO and N-rGO were introduced. The $ReSe_2$ with the nitrogen-doped rGO had a lower ECSA than that of the undoped rGO. This is expected considering the TGA analysis showed that the was much less loading of the $ReSe_2$ catalyst on the nitrogen-doped rGO. However, by every other metric, the $ReSe_2$ catalyst with the nitrogen-doped rGO has better electrocatalytic activity than the $ReSe_2$ with the undoped rGO. This suggests that the improved catalytic activity of the $ReSe_2$ with the nitrogen-doped rGO is not just due to the improved exposure of the active sites. It may also be due to the superior electron conductivity of the N-rGO compared to the rGO. This was investigated using the electrochemical impedance spectroscopy (EIS) analysis of the nanostructures. The EIS can be used to study the electron transfer properties of the nanostructures during the HER. The EIS results are represented as Nyquist plots as shown in Fig.6(d). The equivalence circuit fitted to the data is shown as an insert in **Fig.6(d)**, the circuit components are shown as R_s (solution resistance), Q_2 (constant phase element), and the R_{ct} which is the charge transfer resistance. The charge transfer resistance represents the ease or difficulty of charge transfer at the interface between the electrode and the electrolyte. The lower the R_{ct} the better the rate of electron transfer and thus the better the performance of the catalyst. The $ReSe_2$ nanostructures had the highest R_{ct} at 251 Ω. The electron transfer processes improve when the $ReSe_2$ is incorporated into the doped and undoped rGO. The R_{ct} of the $ReSe_2$-rGO and $ReSe_2$-N-rGO was determined to be 117 Ω and 65 Ω respectively. The electron transfer of the HER processes is more effective in the $ReSe_2$-N-rGO as compared to the $ReSe_2$-rGO. This is due to the improved electron conductivity of the rGO after nitrogen doping. The irreversible surface oxidation of the $ReSe_2$ nanostructures can be used to investigate the electrochemically available surface area. The anodic peaks shown in **Fig.6(e)** show represent the surface oxidation process, the area under the peaks represents the amount of charge needed to fully

oxidize the surface of the nanostructures.[28] There is significantly more charge required for the oxidation of the $ReSe_2$-rGO nanostructures, which suggests that there is far more available surface area to oxidize than for the $ReSe_2$-N-rGO. This indicates that the higher catalyst loading on the rGO leads to more available active sites compared to the $ReSe_2$-N-rGO, this is corroborated by the ECSA. The stability of the electrocatalysts was evaluated by conducting a 1000 LSV scans and observing how the performance of the catalysts changes after continuous voltage sweeps as shown in **Fig.6(f)**. The LSV scans of the $ReSe_2$ nanostructures and that of the nanocomposites after 1000 scans did not show significant changes compared to the initial scans. This shows the relatively good stability of the nanomaterials in acidic media. A comparison of the catalytic activity of the as synthesized and $ReSe_2$, the hybrid nanostructures, and their counterparts found in literature that are synthesized with other methods is shown in **Table 3**. The electrochemical characterisation of the nanostructures compared were conducted in 0.5 M H_2SO_4.

Table 3: Comparison of the catalytic activity of the as synthesized $ReSe_2$, the hybrid nanostructures and their literature counterparts

HER catalyst	Synthesis method	η_{10} (mV)	Tafel slope (mV/dec)	Onset potential (mV)	Ref
$ReSe_2$@rGO	Hydrothermal	145	40.7	-	**9**
$ReSe_2$	Colloidal	331	91	168	**This work**
$ReSe_2$-rGO	Colloidal	259	84	128	**This work**
$ReSe_2$-N-rGO	Colloidal	218	72	115	**This work**

Table 3 clearly shows how the catalytic activity of the $ReSe_2$ has improved after the nanostructures were grown on the rGO and N-rGO. This work could only be compared to the work by Yan *et al.* This was the only recorded work that could be found in literature to the best of our knowledge. Moreover, this work only included the hybrid nanostructure of $ReSe_2$ and rGO. There is currently no work that studies the use of nitrogen doped reduced graphene oxide. The $ReSe_2$@rGO synthesized by Yan *et al.* had higher catalytic activity than the hybrid nanostructures synthesized in this work. This was attributed to the catalyst loading; the loading was recorded as 9.5 wt%. This was much higher than the catalyst loading recorded in this work,

the catalyst loading was recorded at 2.7% and 1.7% for $ReSe_2$-rGO and $ReSe_2$-N-rGO respectively. This indicates that there is still a lot of work to be done in optimizing the reaction conditions in order to ensure higher catalyst loading.

4. Conclusions

In summary, $ReSe_2$ nanostructures were grown on both pristine and nitrogen-doped reduced graphene oxide. Anchored few-layered nanosheets of $ReSe_2$ were shown to grow directly on the rGO and nitrogen-doped rGO, the few-layered nanosheets tend to overlap and form flower-like $ReSe_2$ nanostructures on the surface of the carbon nanostructures. TGA and ECSA analysis showed that the undoped rGO was more effective at anchoring the $ReSe_2$ and thus had nearly double the loading of $ReSe_2$ than the nitrogen-doped rGO. This was attributed to the higher availability of the oxygen functional groups on the surface of the rGO as opposed to the N-rGO. The evaluation of the electrocatalytic activity of the hybrid nanostructures showed that anchoring the $ReSe_2$ on the carbon nanostructures significantly increases the catalytic activity of the $Rese_2$ nanostructures. This was true for the $ReSe_2$ grown on both the nitrogen-doped and undoped rGO nanostructures. However, the $ReSe_2$-N-rGO had better catalytic activity toward the HER as opposed to the $ReSe_2$-rGO. This work demonstrated that even though the $ReSe_2$-rGO had a higher loading of $ReSe_2$ which resulted in a higher ECSA, the influence of the superior electric conductivity offered by the nitrogen-doped rGO on the $ReSe_2$-N-rGO resulted in higher catalytic activity towards the HER. The EIS analysis showed that the R_{ct} of the $ReSe_2$-N-rGO was much lower than that of the $ReSe_2$-rGO hybrid nanostructures which is due to the superior electrical conductivity of the nitrogen-doped rGO. The XPS analysis indicated that the nitrogen doping of the rGO only resulted in the introduction of 0.9% nitrogen dopant on the rGO which is relatively small. Increasing the amount of dopant could further increase the catalytic activity of the hybrid nanostructures.

5. References

1. Lin, L.; Sherrell, P.; Liu, Y.; Lei, W.; Zhang, S.; Zhang, H.; Wallace, G. G.; Chen, J., Engineered 2D transition metal dichalcogenides—A vision of viable hydrogen evolution reaction catalysis. *Adv. Energy Mater.* **2020,** *10* (16), 1903870.

2. Chia, X.; Ambrosi, A.; Lazar, P.; Sofer, Z.; Pumera, M., Electrocatalysis of layered Group 5 metallic transition metal dichalcogenides (MX_2, M= V, Nb, and Ta; X= S, Se, and Te). *J. Mater. Chem. A* **2016,** *4* (37), 14241-14253.

3. Kibsgaard, J.; Chen, Z.; Reinecke, B. N.; Jaramillo, T. F., Engineering the surface structure of MoS_2 to preferentially expose active edge sites for electrocatalysis. *Nat. Mater.* **2012,** *11* (11), 963-969.
4. Ambrosi, A.; Sofer, Z.; Pumera, M., 2H→ 1T phase transition and hydrogen evolution activity of MoS_2, $MoSe_2$, WS_2 and WSe_2 strongly depends on the MX_2 composition. *Chem. Commun.* **2015,** *51* (40), 8450-8453.
5. Park, G. D.; Kim, J. H.; Park, S.-K.; Kang, Y. C., MoSe2 embedded CNT-reduced graphene oxide composite microsphere with superior sodium ion storage and electrocatalytic hydrogen evolution performances. *ACS Appl. Mater. Interfaces* **2017,** *9* (12), 10673-10683.
6. Cao, J.; Zhou, J.; Zhang, Y.; Liu, X., A clean and facile synthesis strategy of MoS_2 nanosheets grown on multi-wall CNTs for enhanced hydrogen evolution reaction performance. *Sci. Rep,* **2017,** *7* (1), 1-8.
7. Lee, H. J.; Lee, S. W.; Hwang, H.; Yoon, S. I.; Lee, Z.; Shin, H. S., Vertically oriented MoS_2/WS_2 heterostructures on reduced graphene oxide sheets as electrocatalysts for hydrogen evolution reaction. *Mater. Chem. Front.* **2021,** *5* (8), 3396-3403.
8. Guo, W.; Le, Q. V.; Hasani, A.; Lee, T. H.; Jang, H. W.; Luo, Z.; Kim, S. Y., $MoSe_2$-GO/rGO composite catalyst for hydrogen evolution reaction. *Polymers* **2018,** *10* (12), 1309.
9. Yan, Y.; Xu, S.; Li, H.; Selvam, N. C. S.; Lee, J. Y.; Lee, H.; Yoo, P. J., Perpendicularly anchored $ReSe_2$ nanoflakes on reduced graphene oxide support for highly efficient hydrogen evolution reactions. *Chem. Eng. Sci.* **2021,** *405*, 126728.
10. Park, B. J.; Park, H. S., Enhanced electrical conductivity of doped graphene fiber via vacuum deposition. *Carbon Lett.* **2021,** *31* (4), 613-618.
11. Ngidi, N. P.; Ollengo, M. A.; Nyamori, V. O., Effect of doping temperatures and nitrogen precursors on the physicochemical, optical, and electrical conductivity properties of nitrogen-doped reduced graphene oxide. *Materials* **2019,** *12* (20), 3376.
12. Luxa, J.; Marvan, P.; Lazar, P.; Sofer, Z., Chalcogenide vacancies drive the electrocatalytic performance of rhenium dichalcogenides. *Nanoscale* **2019,** *11* (31), 14684-14690.
13. Crane, M. J.; Lim, M. B.; Zhou, X.; Pauzauskie, P. J., Rapid synthesis of transition metal dichalcogenide–carbon aerogel composites for supercapacitor electrodes. *Microsyst. Nanoeng.* **2017,** *3* (1), 1-9.
14. Ouyang, W.; Zeng, D.; Yu, X.; Xie, F.; Zhang, W.; Chen, J.; Yan, J.; Xie, F.; Wang, L.; Meng, H., Exploring the active sites of nitrogen-doped graphene as catalysts for the oxygen reduction reaction. *Int. J. hydrog. Energy* **2014,** *39* (28), 15996-16005.

15. Mu, X.; Yuan, B.; Feng, X.; Qiu, S.; Song, L.; Hu, Y., The effect of doped heteroatoms (nitrogen, boron, phosphorus) on inhibition thermal oxidation of reduced graphene oxide. *RSC adv.* **2016,** *6* (107), 105021-105029.
16. Hidayah, N.; Liu, W.-W.; Lai, C.-W.; Noriman, N.; Khe, C.-S.; Hashim, U.; Lee, H. C. In Comparison on graphite, graphene oxide and reduced graphene oxide: Synthesis and characterization, *AIP. Conf. Proc.* AIP Publishing LLC: 2017; p 150002.
17. Wei, L.; Wang, P.; Yang, Y.; Luo, R.; Li, J.; Gu, X.; Zhan, Z.; Dong, Y.; Song, W.; Fan, R., Facile synthesis of nitrogen-doped reduced graphene oxide as an efficient counter electrode for dye-sensitized solar cells. *J. Nanopart. Res.* **2018,** *20* (4), 1-12.
18. Witjaksono, G.; Junaid, M.; Khir, M. H.; Ullah, Z.; Tansu, N.; Saheed, M. S. B. M.; Siddiqui, M. A.; Ba-Hashwan, S. S.; Algamili, A. S.; Magsi, S. A., Effect of Nitrogen Doping on the Optical Bandgap and Electrical Conductivity of Nitrogen-Doped Reduced Graphene Oxide. *Molecules* **2021,** *26* (21), 6424.
19. Xing, Z.; Ju, Z.; Zhao, Y.; Wan, J.; Zhu, Y.; Qiang, Y.; Qian, Y., One-pot hydrothermal synthesis of Nitrogen-doped graphene as high-performance anode materials for lithium ion batteries. *Sci. Rep.* **2016,** *6* (1), 1-10.
20. Tian, Y.; Cao, Y.-y.; Pang, F.; Chen, G.-q.; Zhang, X., Ag nanoparticles supported on N-doped graphene hybrids for catalytic reduction of 4-nitrophenol. *RSC Adv.* **2014,** *4* (81), 43204-43211.
21. Lu, S.; Sui, L.; Wu, M.; Zhu, S.; Yong, X.; Yang, B., Graphitic nitrogen and high-crystalline triggered strong photoluminescence and room-temperature ferromagnetism in carbonized polymer dots. *Adv. Sci.* **2019,** *6* (2), 1801192.
22. Huang, L.; Zhu, P.; Li, G.; Lu, D. D.; Sun, R.; Wong, C., Core–shell SiO_2@ RGO hybrids for epoxy composites with low percolation threshold and enhanced thermo-mechanical properties. *J. Mater. Chem. A.* **2014,** *2* (43), 18246-18255.
23. Kukreja, A.; Kang, B.; Han, S.; Shin, M.-K.; Son, H. Y.; Choi, Y.; Lim, E.-K.; Huh, Y.-M.; Haam, S., Inner structure-and surface-controlled hollow MnO nanocubes for high sensitive MR imaging contrast effect. *Nano. Converg.* **2020,** *7* (1), 1-11.
24. Tian, C.; Wu, J.; Ma, Z.; Li, B.; Li, P.; Zu, X.; Xiang, X., Design and facile synthesis of defect-rich C-MoS_2/rGO nanosheets for enhanced lithium–sulfur battery performance. *Beilstein. J. Nanotechnol.* **2019,** *10* (1), 2251-2260.
25. Baig, M. M.; Pervaiz, E.; Yang, M.; Gul, I. H., High-performance supercapacitor electrode obtained by directly bonding 2D materials: hierarchal MoS_2 on reduced graphene oxide. *Front. Mater.* **2020**, 323.

26. Murthy, A. P.; Theerthagiri, J.; Madhavan, J., Insights on Tafel constant in the analysis of hydrogen evolution reaction. *J. Phys. Chem. C.* **2018,** *122* (42), 23943-23949.
27. Qi, F.; Wang, X.; Zheng, B.; Chen, Y.; Yu, B.; Zhou, J.; He, J.; Li, P.; Zhang, W.; Li, Y., Self-assembled chrysanthemum-like microspheres constructed by few-layer $ReSe_2$ nanosheets as a highly efficient and stable electrocatalyst for hydrogen evolution reaction. *Electrochim. Acta.* **2017,** *224*, 593-599.
28. Benck, J. D.; Hellstern, T. R.; Kibsgaard, J.; Chakthranont, P.; Jaramillo, T. F., Catalyzing the hydrogen evolution reaction (HER) with molybdenum sulfide nanomaterials. *ACS Catal.* **2014,** *4* (11), 3957-3971.

6. Supplementary information

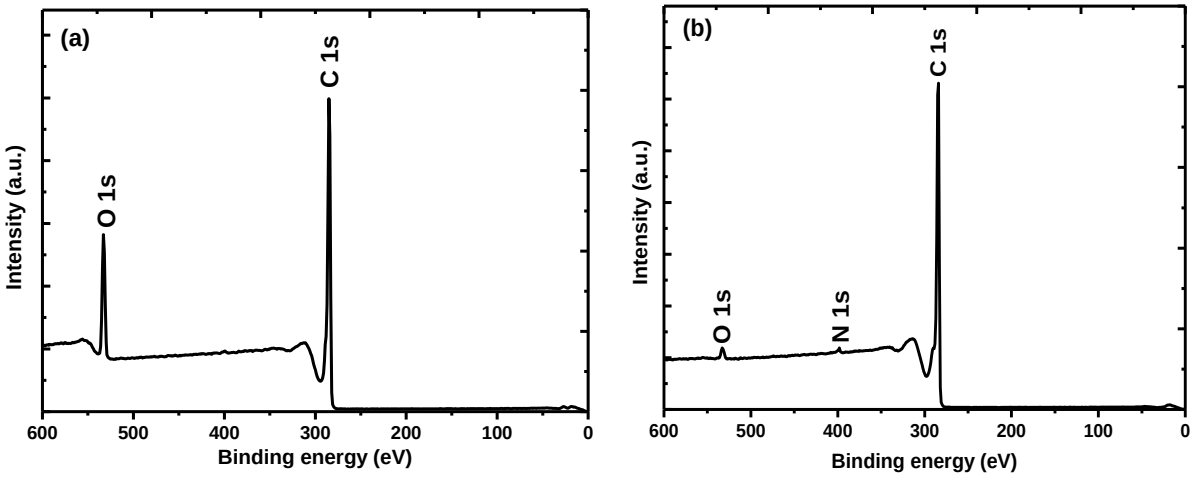


Figure S1: XPS survey scan of (a) rGO and (b) N-rGO.

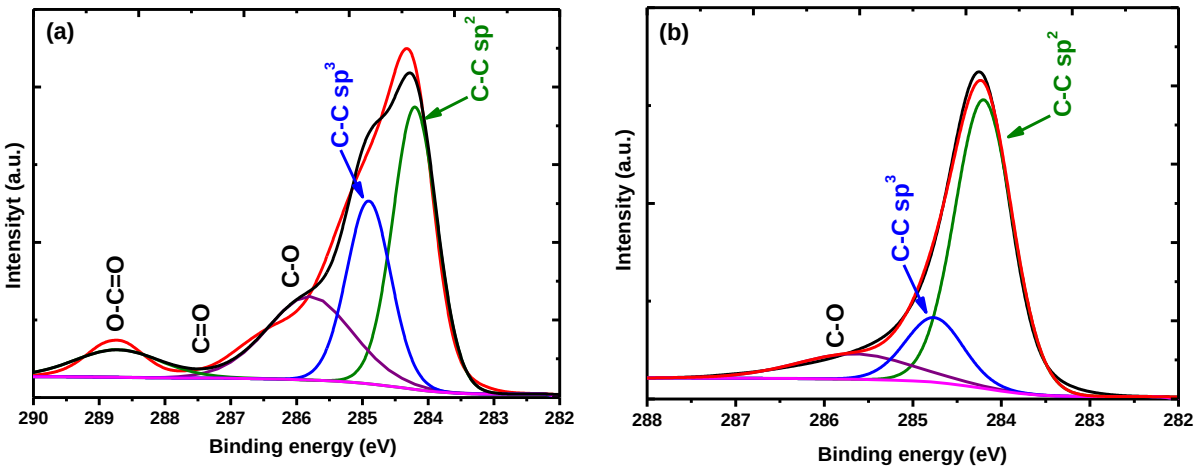


Figure S2: C1s XPS spectrum of (a) rGO and (b) N-rGO.

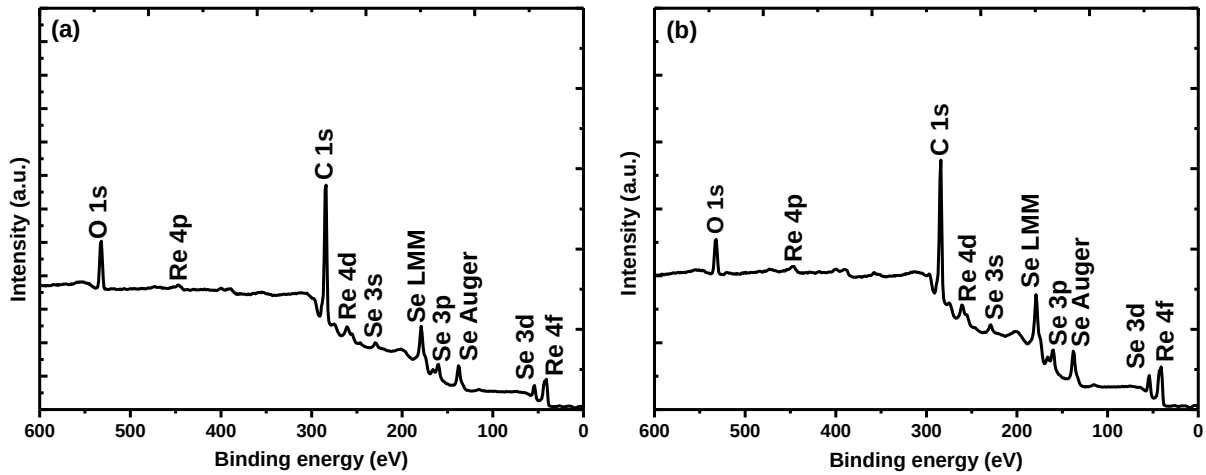


Figure S3: XPS survey spectra of (a) $ReSe_2$-rGO and (b) $ReSe_2$-N-rGO.

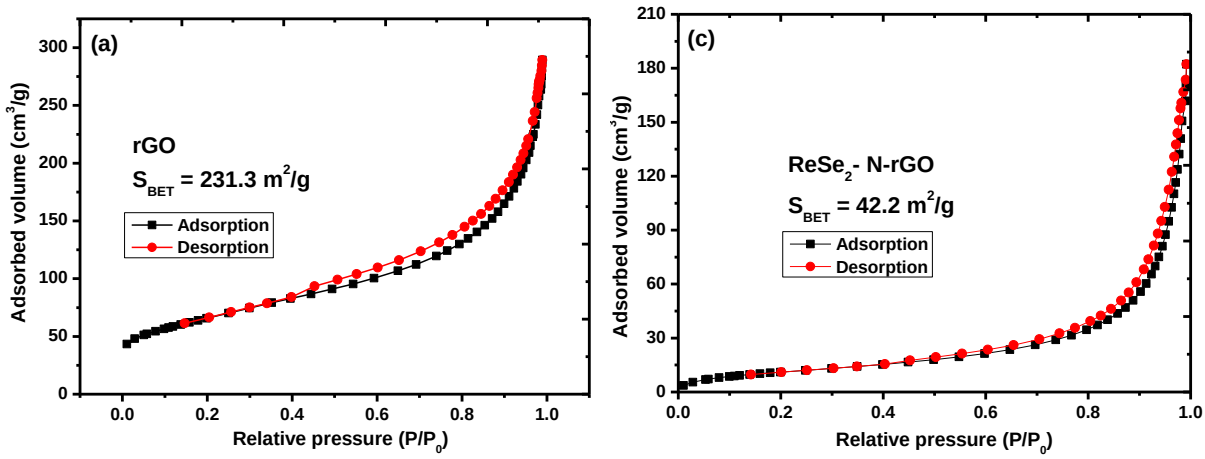


Figure S4: Adsorption-desorption isotherm of (a) rGO and (b) N-rGO.

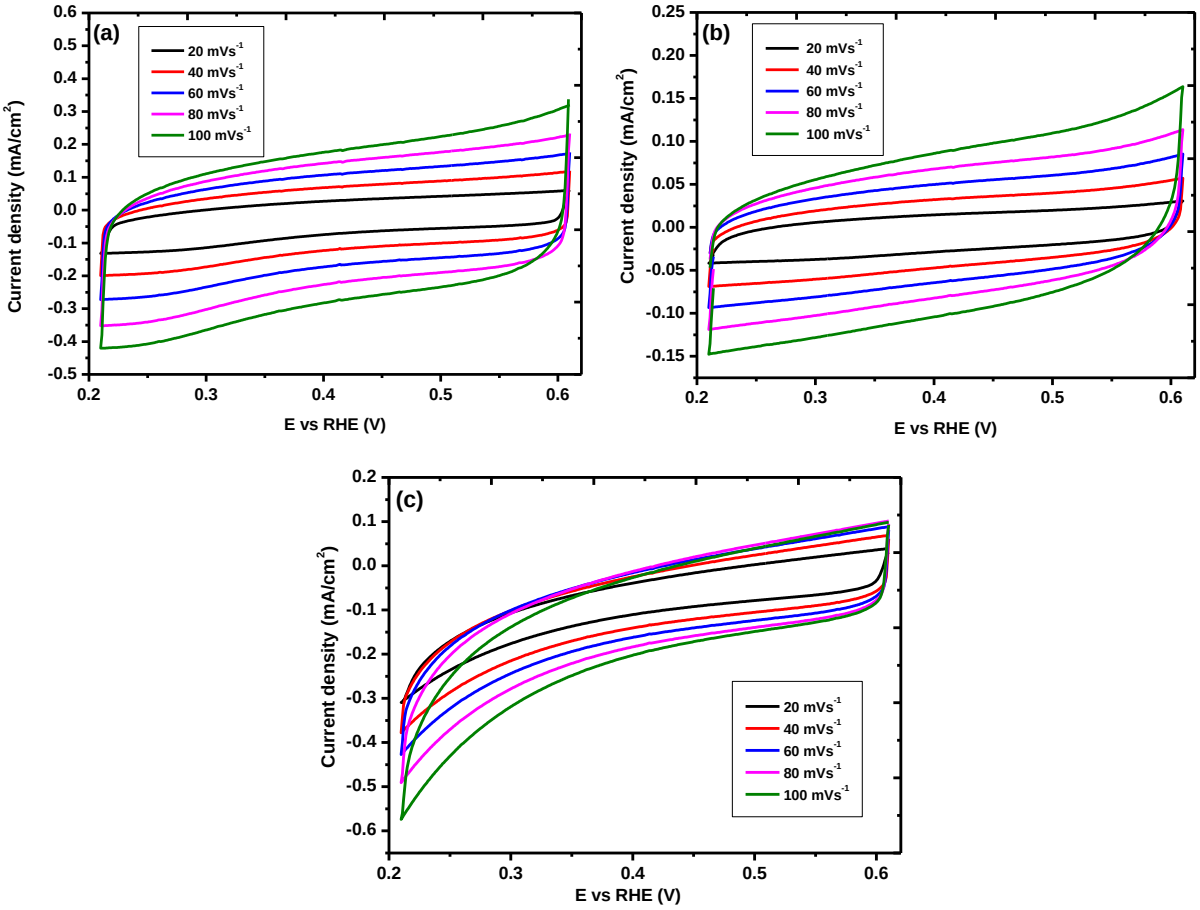


Figure S5: Cdl plots of (a) $ReSe_2$, (b) $ReSe_2$-rGO, and (b) $ReSe_2$-N-rGO.

Chapter 6.2: Colloidal synthesis of $MoSe_2$ and $SnSe_2$ nanostructures on nitrogen-doped reduced graphene oxide for use as electrocatalysts in the hydrogen evolution reaction

1. Introduction

This work follows from the insights of **Chapter 6.1**. The nitrogen-doped reduced graphene oxide (N-rGO) was shown to be more effective in improving the catalytic activities of $ReSe_2$ towards the HER. Thus, the $MoSe_2$ and $SnSe_2$ nanostructures were grown on N-rGO nanostructures. $MoSe_2$ is one of the most extensively studied TMDs in literature, while $SnSe_2$ has not been extensively explored for HER applications.[1-3] There have been many reports on the synthesis of $MoSe_2$ hybrid nanostructures with rGO using various synthesis techniques including colloidal synthesis.[4-5] However, there have not been many reports that investigate the synthesis of $MoSe_2$ and $SnSe_2$ hybrid nanostructures with nitrogen-doped rGO using colloidal synthesis.[6-7] In this work, colloidal synthesis was used to produce $MoSe_2$ and $SnSe_2$ hybrid nanostructures with N-rGO. The $MoSe_2$-N-rGO and $SnSe_2$-N-rGO nanostructures were successfully synthesized using colloidal synthesis. A study of the catalytic activity of the nanostructures towards the HER gave interesting results. The catalytic activity of the $SnSe_2$ nanostructures was improved after they were grown on the N-rGO, this was in keeping with the results obtained in **Chapter 6.1**. However, the catalytic activity of the $MoSe_2$ was not improved after the nanostructures were grown on the N-rGO. This was attributed to the limited interaction between the $MoSe_2$ nanostructures and the N-rGO. The $SnSe_2$ nanoplates were able to grow directly onto the N-rGO similar to how the $ReSe_2$ nanostructures were able to grow onto the N-rGO nanosheets. The $MoSe_2$ nanostructures were not shown to grow on the N-rGO nanosheets but were growing separately from the nanosheets which limited the interaction. This demonstrated the importance of the interaction between the TMDs and the carbon nanostructures in improving the catalytic activity towards HER.

2. Experimental section

2.1 Chemicals

Molybdic acid (H_2MoO_4, 85%), Tin(IV) chloride ($SnCl_4$, 98%), selenium powder (Se, 99.99%), oleylamine (70%), oleic acid (90%) were purchased from Sigma Aldrich and used as received without purification. nitrogen-doped reduced graphene oxide (N-rGO, synthesized in **Chapter 6.1**).

2.2 Synthesis of nanostructures

2.2.1 Synthesis of $MoSe_2$-N-rGO nanocomposite

The selenium powder (Se, 0.559 mmol) was added into the three-neck round bottom flask containing 20 ml of oleic acid at room temperature. The temperature was increased to 220 ºC to thermally reduce the Se to Se^{2-} with the help of the solvent, which also acted as a reducing agent. A sample vial containing 30 mg of N-rGO, molybdic acid (H_2MoO_4, 0.15 mmol), and 5 ml of oleic acid was sonicated for 30 minutes. The vial was then heated to dissolve the molybdic acid and injected into the Se-oleic acid mixture at 220 °C. The temperature was then raised to 330 ºC and the reaction was run for 120 min. The nanoparticles formed were then washed with ethanol and toluene using a centrifuge and then left to dry.

2.2.2 Synthesis $SnSe_2$-N-rGO nanocomposite

The selenium powder (Se, 0.051 mmol) was added into the three-neck round bottom flask containing 20 ml of oleylamine at room temperature. The temperature was increased to 220 ºC to thermally reduce the Se to Se^{2-} with the help of the solvent, which also acted as a reducing agent. A sample vial containing 30 mg of N-rGO, tin chloride ($SnCl_4$, 0.017 mmol), and 5 ml of oleic acid was sonicated for 30 minutes. The vial was then heated to dissolve the ammonium perrhenate and injected into the Se-oleic acid mixture at 220 °C. The temperature was then raised to 330 ºC and the reaction was run for 120 min. The nanoparticles formed were then washed with ethanol and toluene using a centrifuge and then left to dry.

2.3 Characterization techniques

The phase purity, crystallinity, and preferred crystal orientation of the products were examined using powder X-ray diffraction (PXRD) on a Bruker MeasSrv D2-205530 diffractometer using secondary graphite monochromated CuKα radiation (λ 1.5406 Å) at 30 kV/10 mA. Measurements were taken using a glancing angle of incidence detector at an angle of 2°, for 2θ values over 10 - 80° in steps of 0.026° with a step time of 37 s and at a temperature of 25 °C. The XPS measurements of the powder samples were obtained using a Thermo ESCAlab 250Xi with Al kα photon source (1486.7 eV), X-ray power of 300W, X-ray spot size of 900 µm, pass energy (survey) of 100 eV, pass energy (20 eV), and pressure of $<10^{-8}$ mBar. The sample morphologies were determined using the transmission electron microscopy (TEM) carried out on an FEI Tecnai T12 TEM microscope operated at an acceleration voltage of 120 kV The TEM samples were prepared by sonicating a spatula tip of the sample in ethanol and drop-casting that dispersion on a lacey carbon Cu grid. The total surface area and pore volume of

the nanostructures were ascertained using a Micromeritics TriStar 3000 Surface Area and Porosity Analyzer. Thermal analysis was done using a Perkin Elmer TGA 6000 thermogravimetric analyzer using high purity nitrogen and air at a heating rate of 10 °C/min and gas flow rate of 20 mL/min.

2.4 Electrochemical characterization

The electrochemical measurements were carried out on a BASi epsilon E2. All measurements were carried out in 0.5 M H_2SO_4 using a three-electrode system. An Ag/AgCl electrode was used as the reference electrode, a platinum wire was used as the counter electrode. A modified glassy carbon electrode with a 3 mm diameter was used as the working electrode. The ink or fresh dispersion of the sample was prepared by dispersing 5.0 mg of the $ReSe_2$ or the $ReSe_2$ and rGO/N-rGO nanocomposites with 0.5 mg carbon black and 40 µl of Nafion solution (5 wt%) in a 1 ml mixture of water and isopropanol at a 3:1 ratio. The solution was then sonicated for 30 min and ~ 5 µl of the ink was drop-casted onto the glassy carbon electrode. The electrode was allowed to dry at room temperature. The linear sweep voltammograms were obtained at a scan rate of 2 mVs^{-1} and the cyclic voltammograms were obtained at a potential range of 0.2 – 0.6 V vs RHE at 100 mVs^{-1} scan rate. The measured potentials vs Ag/AgCl were converted to the reversible hydrogen electrode (RHE) scale according to the Nernst equation:

$$E_{RHE} = E_{Ag/AgCl} + 00059\,pH + E^{0}_{Ag/AgCl} \quad (1)$$

Where E_{RHE} is the converted potential vs RHE, $E^{0}_{Ag/AgCl}$ = 0.210 V at 25 °C. The Impedance spectroscopy studies were conducted on a Biologic SP 300, the measurements were done at a potential of -200 mV vs RHE and a frequency range between 0.1 Hz and 100 kHz.

3. Results and discussion

Powder X-ray diffraction (PXRD) was used to determine the phase, crystallinity, and composition of the nanostructures. The powder patterns of the $SnSe_2$-N-rGO and $MoSe_2$-N-rGO are shown **in Fig.1(a) and (b)**. The powder patterns show that the $MoSe_2$-N-rGO and $SnSe_2$-N-rGO were successfully synthesized. The powder patterns show the characteristic diffraction peaks of the $MoSe_2$ and $SnSe_2$ nanostructures as well as the (002) peak of the N-rGO. The (002) peak of the $MoSe_2$ and the (001) peak of the $SnSe_2$ indicate that the TMD nanostructures are in multi-layer form as opposed to monolayer.[8-9] The PXRD pattern of $SnSe_2$-N-rGO does show some unidentified impurities which were denoted as #. This may indicate that the N-rGO interferes with the formation of the $SnSe_2$ nanostructures.

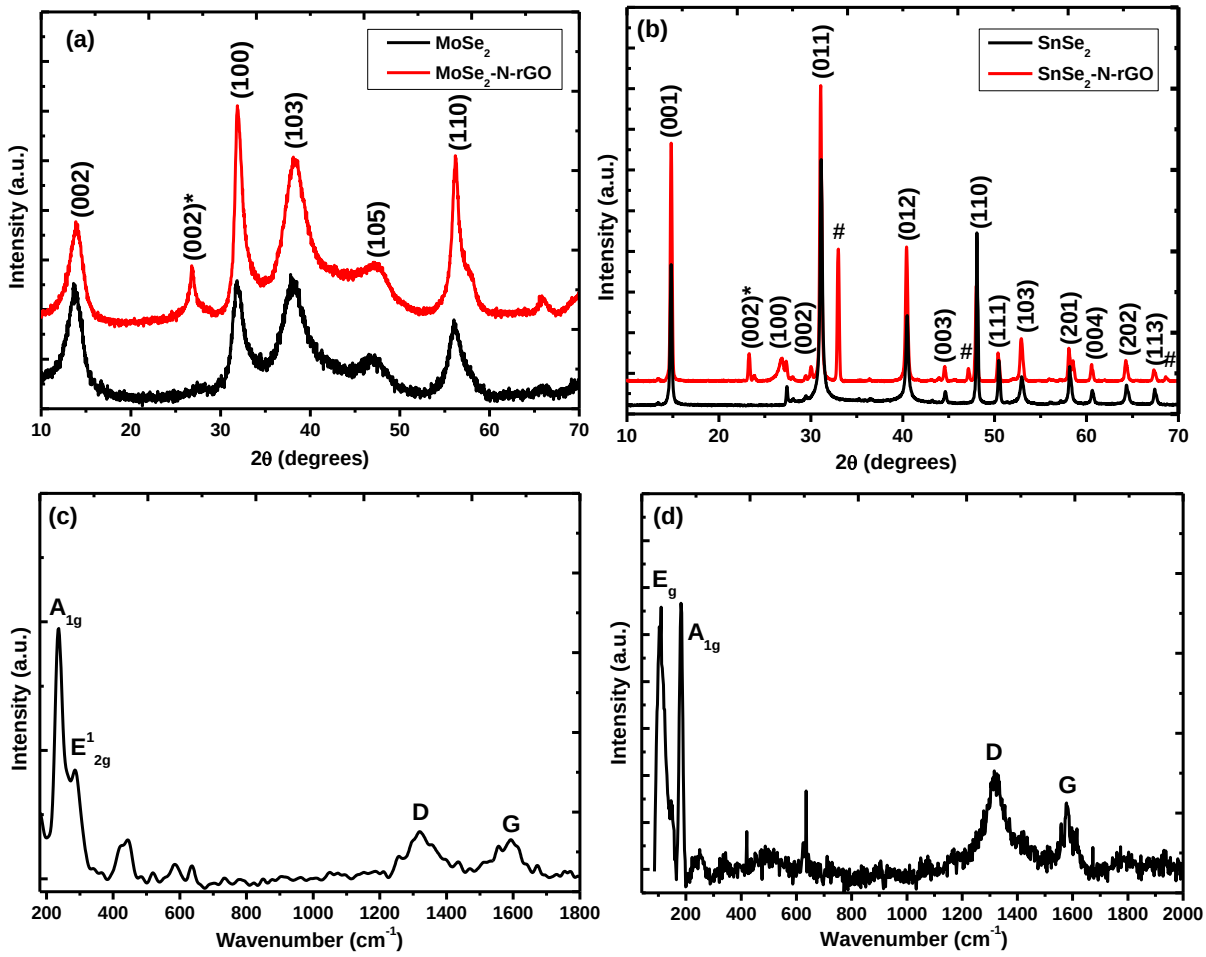


Figure 1: PXRD patterns of (a) $MoSe_2$-N-rGO and (b) $SnSe_2$-N-rGO. Raman spectra of (c) $MoSe_2$-N-rGO and (d) $SnSe_2$-N-rGO.

The Raman spectrum of $MoSe_2$-N-rGO is shown in **Fig.1(c)**. The position of the A_{1g} was determined to be 237 cm^{-1} and the E^1_{2g} was determined to be 283 cm^{-1}, which were both red-shifted from their bulk positions.[10] This indicates that the nanostructures are few-layered and not classified as bulk structures. The typical Raman spectrum of $SnSe_2$ has two characteristic peaks, the in-plane E_g vibrational mode, and the out-of-plane A_{1g} vibrational mode. The Raman spectrum of the $SnSe_2$-N-rGO shows the E_g and A_{1g} peaks which confirms the formation of $SnSe_2$ nanostructures.[9] The D and G peaks of the N-rGO can also be observed in the Raman spectra. The position of the D peak was measured at 1318 cm^{-1} and 1320 cm^{-1} for the $MoSe_2$-N-rGO and $SnSe_2$-N-rGO respectively. The position of the G peaks was measured at 1591 cm^{-1} and 1577 cm^{-1} for the $MoSe_2$-N-rGO and $SnSe_2$-N-rGO respectively. These values are in agreement with values observed in literature for the D and G peaks.[11]

Thermogravimetric analysis (TGA) was used to study the decomposition of the hybrid nanostructures. The TGA profile of the $MoSe_2$-N-rGO and $SnSe_2$-N-rGO nanostructures is shown in **Fig.2(a) and (b)**.

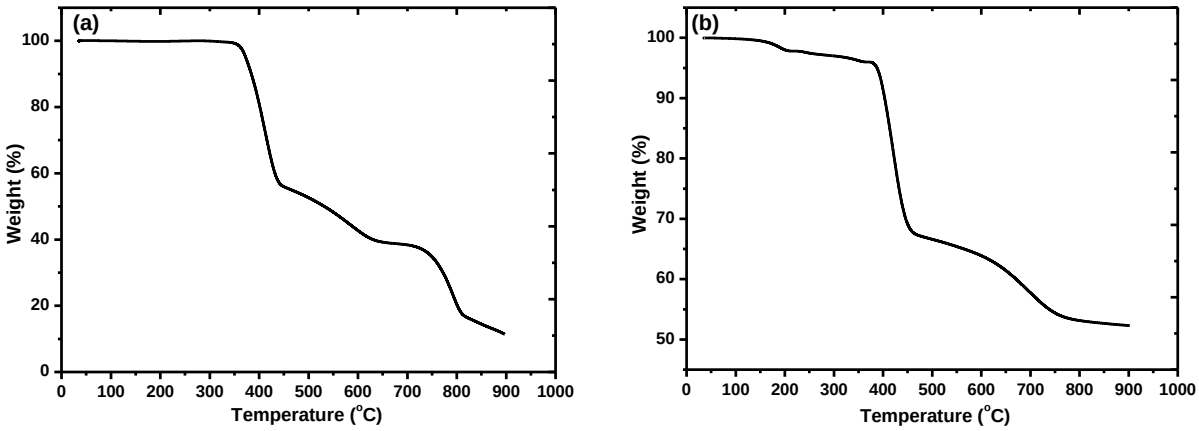


Figure 2: TGA profiles of (a) $MoSe_2$-N-rGO and (b) $SnSe_2$-N-rGO.

The initial mass loss at 150 °C was attributed to the evaporation of water molecules. The second mass beginning at 400 °C amounting to 44% mass loss for $MoSe_2$-N-rGO and 32% for $SnSe_2$-N-rGO was attributed to the decomposition of the carbon skeleton.[12] The mass loss of 17% and 22% in the temperature range of 420-800 °C for the $MoSe_2$-N-rGO TGA profile was attributed to the decomposition of labile and bound oleic acid respectively.[13] The mass loss of 15% at the temperature range of 500-700 °C was attributed to the decomposition of the bound oleylamine on the surface of the $SnSe_2$-N-rGO nanostructures.[14] The residue of the TGA studies gives an indication of the catalyst loading on the N-rGO. The residue of the TGA analysis of $MoSe_2$-N-rGO showed that 11% of the $MoSe_2$ was loaded onto the N-rGO. The residue of the TGA analysis of $SnSe_2$-N-rGO indicated that 47% of the sample was composed of the $SnSe_2$ nanostructures.

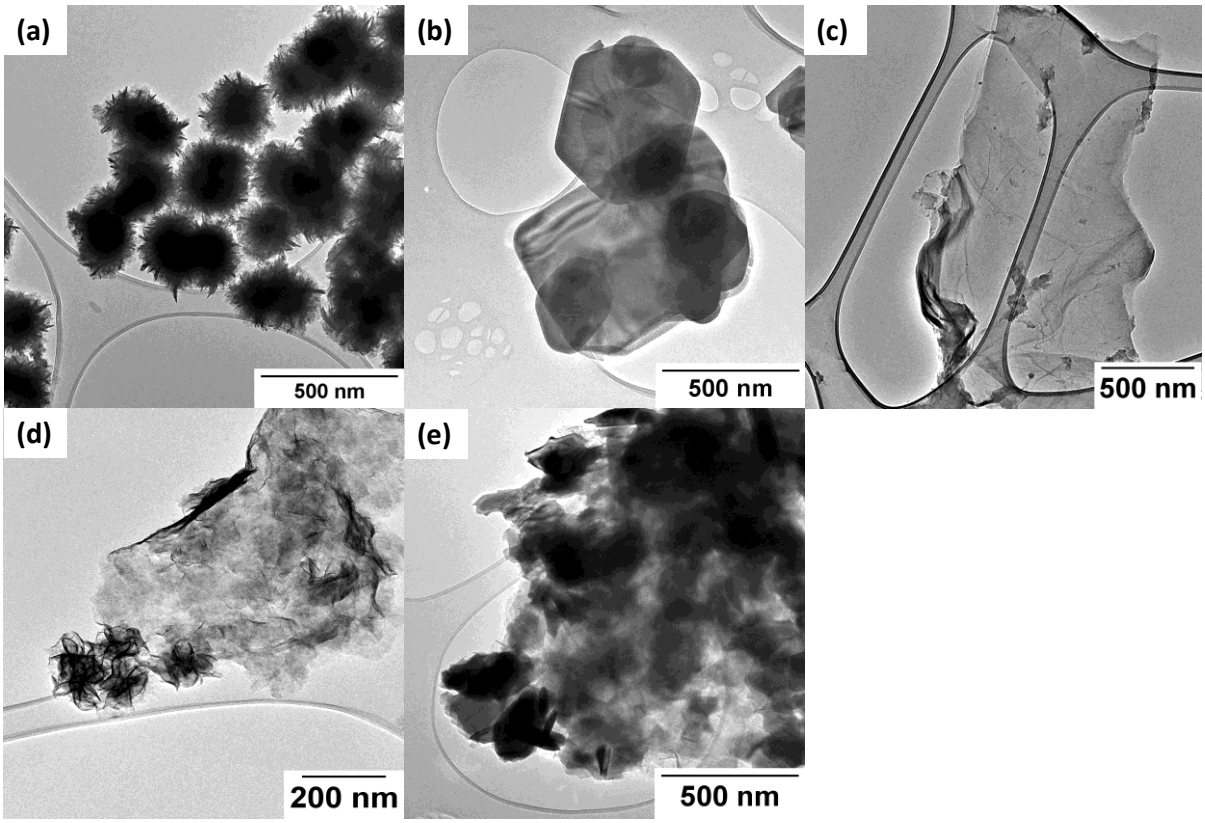


Figure 3: TEM images of (a) $MoSe_2$, (b) $SnSe_2$, (c) N-rGO, (d) $MoSe_2$-rGO, and (e) $SnSe_2$-N-rGO.

The TEM image of the $MoSe_2$ nanostructures is shown in **Fig.3(a)**, the image shows that the $MoSe_2$ form into cotton ball-like microspheres. The TEM image of the $SnSe_2$ shown in **Fig.3(b)** shows that they form into 2D nanoplates. The TEM images of N-rGO shown in **Fig.3(c)** shows nanosheets that are wrinkled and folded in some regions. The TEM image of the $MoSe_2$-N-rGO shown in **Fig.3(d)** shows the growth of $MoSe_2$ nanoflowers at the edge of the N-rGO nanosheets. This shows that the $MoSe_2$ nanoflowers grow independently of the nanosheets, showing very limited interaction. This is in stark difference to the growth of $ReSe_2$ nanostructures which grew as few-layered nanosheets directly on the N-rGO nanosheets as shown in **chapter 5.1**. The TEM image of the $SnSe_2$-N-rGO nanocomposite is shown in **Fig.3(e)**, the image shows the $SnSe_2$ nanoplate growing on the surface of the N-rGO nanosheets. A close-up image of the $SnSe_2$-N-rGO is shown in **Fig.S1.** The $SnSe_2$ nanoplates may have a better interaction with the N-rGO nanosheets due to the interaction of the Sn(IV) monomer and the nitrogen defects in the structure of the N-rGO.

The adsorption-desorption curves of all the nanostructures show a type-IV isotherm with a distinct hysteresis loop (IUPAC classification) as shown in **Fig.S2 and Fig.4**, this suggests that the nanostructures assume a mesoporous structure.[15] The BET surface area of N-rGO was calculated to be 236.3 m^2/g as shown in **Fig.S2**.

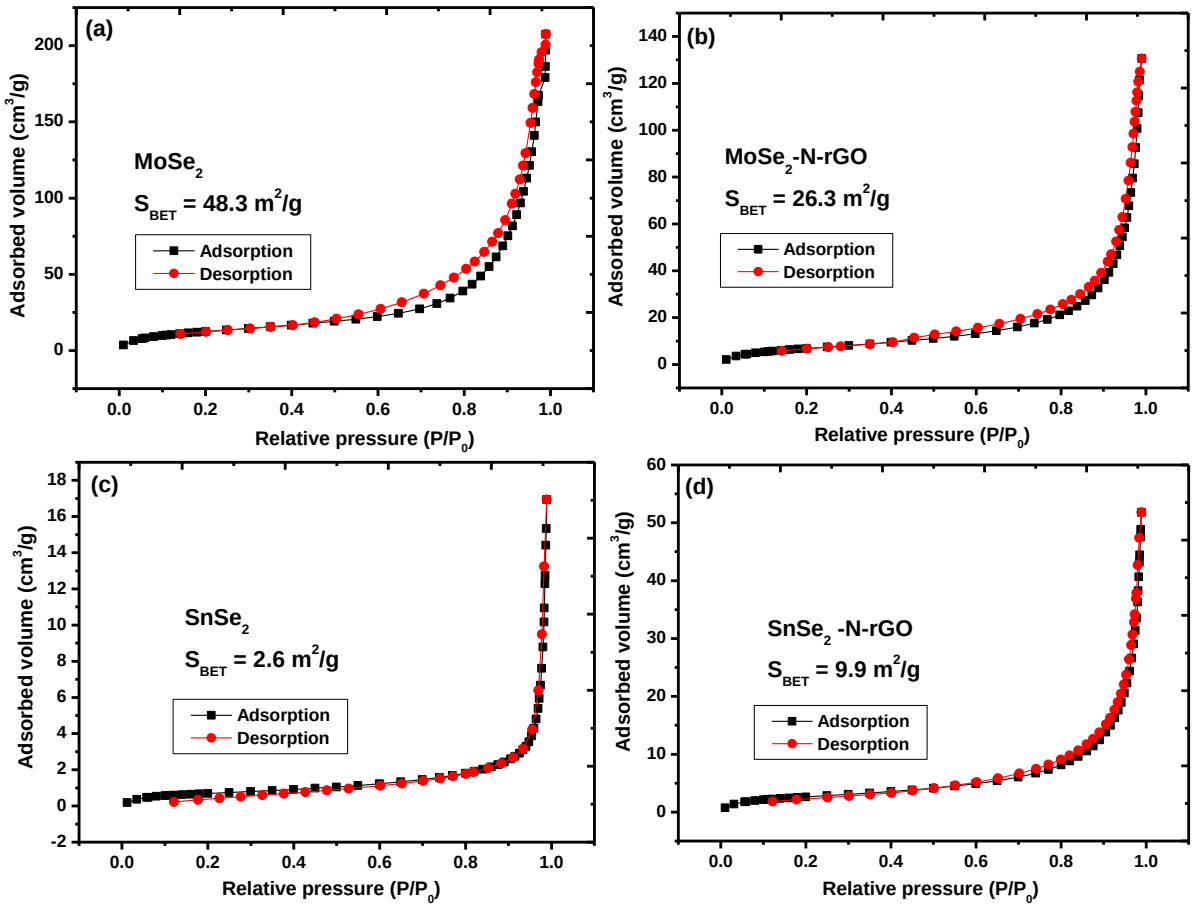


Figure 4: Adsorption- desorption isotherms of (a) $MoSe_2$, (b) $MoSe_2$-rGO, (c) $SnSe_2$, and (d) $SnSe_2$-N-rGO.

The BET surface area of the $MoSe_2$ and $SnSe_2$ nanostructures was measured to be 48.3 m^2/g and 2.6 m^2/g as shown in **Fig.4(a) and (c)**. The surface area of the $MoSe_2$-N-rGO and $SnSe_2$-N-rGO was calculated to be 26.3 m^2/g and 9.9 m^2/g respectively as shown in **Fig.4(b) and (d)**. The surface area of the $SnSe_2$ was boosted while the surface area of the $MoSe_2$ was reduced. The incorporation of the $MoSe_2$ nanostructures on the N-rGO seems to have an unfavorable effect on the surface area of the hybrid nanostructures which may affect their catalytic activity towards the HER. The catalytic activity of the TMD nanostructures and their hybrid nanostructures with N-rGO was determined using electrochemical characterization. The polarization curves of the nanostructures are shown in **Fig.5(a)**. The onset potential of the

$MoSe_2$ and $SnSe_2$ nanostructures was determined to be 205 mV and 390 mV respectively. The onset potential of the hybrid nanostructures was determined to 235 mV and 322 mV for $MoSe_2$-N-rGO and $SnSe_2$-N-rGO respectively. The η_{10} of the $MoSe_2$ and $SnSe_2$ was determined to be 319 mV and 681 mV respectively. The η_{10} of the $MoSe_2$-N-rGO and $SnSe_2$-N-rGO hybrid nanostructures were recorded at 407 mV and 600 mV respectively. Growth of the $SnSe_2$ nanostructures on the N-rGO resulted in improved catalytic activity while the incorporation of the $MoSe_2$ on N-rGO impairs the catalytic activity of the $MoSe_2$. These observations were attributed to the interaction between the TMD nanostructures and the N-rGO. The limited interaction of the $MoSe_2$ nanostructures and the N-rGO results in the reduction of the catalytic activity of the $MoSe_2$.[16] The Tafel plots of the nanostructures are shown **Fig.5(b)**. The Tafel slopes of the $MoSe_2$ and $SnSe_2$ nanostructures and the hybrid nanostructures were determined to be 84 mV/dec, 242 mV/dec, 85 mV/dec, and 168 mV/dec for the $MoSe_2$, $SnSe_2$, $MoSe_2$-N-rGO, and $SnSe_2$-N-rGO respectively. This shows that the rate-determining step for the $SnSe_2$ and $SnSe_2$-N-rGO is the Volmer step. The Tafel slopes of the $MoSe_2$ and $MoSe_2$-N-rGO indicate that the HER proceeds under the Volmer-Heyrovsky pathway on the surface of these catalysts.

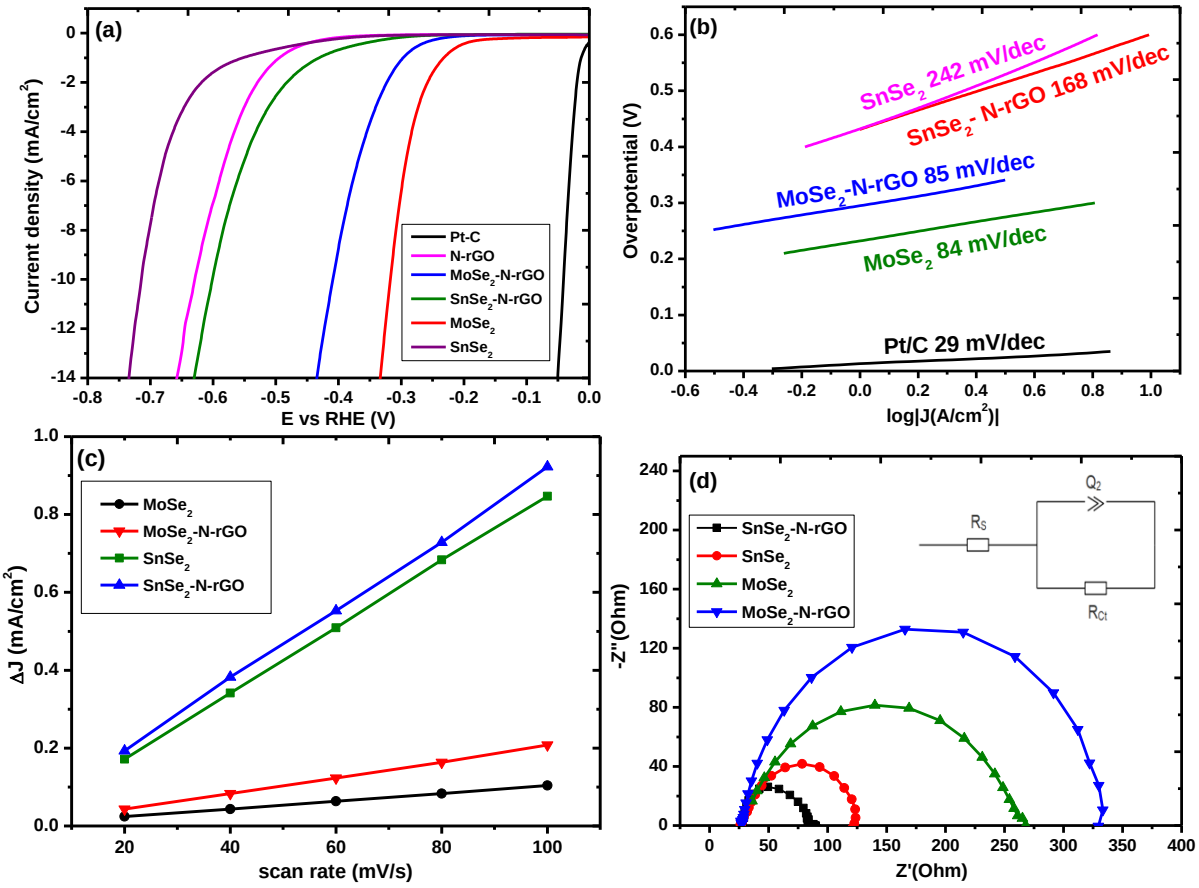


Figure 5: (a) Polarisation curves of the $MoSe_2$, $SnSe_2$ nanostructures and their N-rGO nanocomposites. (b) Tafel plots of the $MoSe_2$, $SnSe_2$ nanostructures and N-rGO nanocomposites. (c) C_{dl} plots of $MoSe_2$, $SnSe_2$, $MoSe_2$-N-rGO, and $SnSe_2$-N-rGO. (d) Nyquist plots of $MoSe_2$, $SnSe_2$, $MoSe_2$-N-rGO, and $SnSe_2$-N-rGO.

The electrochemically active surface area (ECSA) was determined using the C_{dl} (double layer capacitance). The ECSA of the nanostructures was determined to be 0.996 mF/cm^2, 8.52 mF/cm^2, 2.04 mF/cm^2, and 9.02 mF/cm^2 for $MoSe_2$, $SnSe_2$, $MoSe_2$-N-rGO, and $SnSe_2$-N-rGO respectively. The $SnSe_2$-N-rGO has a higher ECSA than the pristine $SnSe_2$, this is expected considering the increased geometrical surface area of the nanocomposite and the improved catalytic activity. Even though the hybrid nanostructures of the $MoSe_2$ had a higher ECSA than the $MoSe_2$ alone, all other parameters suggest that the hybrid nanostructures have lower catalytic activity. The increased double-layer capacitance may be due to the contribution of the N-rGO and not necessarily due to the nanocomposite. The electron transfer properties of the nanostructures during HER were investigated using electrochemical impedance spectroscopy (EIS). The EIS results are represented as Nyquist plots as shown in **Fig.5(d)**. The equivalence circuit fitted to the data is shown as an insert in **Fig.5(d)**, the circuit components are shown as

R_s (solution resistance), Q_2 (constant phase element), and the R_{ct} which is the charge transfer resistance. The charge transfer resistance represents the ease or difficulty of charge transfer at the interface between the electrode and the electrolyte. The lower the R_{ct} the better the rate of electron transfer and thus the better the performance of the catalyst. The R_{ct} of $MoSe_2$ and $SnSe_2$ was found to be 247 Ω and 90 Ω respectively. The R_{ct} of $MoSe_2$-N-rGO and $SnSe_2$-N-rGO was found to be 299 Ω and 57 Ω respectively. The R_{ct} of the $MoSe_2$-N-rGO was higher than that of the pristine $MoSe_2$ which indicates less effective electron transfer, this was to be expected due to the lack of significant interaction between the $MoSe_2$ and the N-rGO as evidenced by the TEM images. The $SnSe_2$-N-rGO had a higher R_{ct} than the pristine $SnSe_2$ which shows improve electron transfer kinetics. A comparison of the catalytic activity of the as-synthesized $MoSe_2$, $SnSe_2$, the hybrid nanostructures, and their counterparts found in the literature that were synthesized with other methods is shown in **Table 1**. The electrochemical characterization of the nanostructures compared was conducted in 0.5 M H_2SO_4.

Table 1: Comparison of the catalytic activity of the as-synthesized $MoSe_2$, $SnSe_2$, the hybrid nanostructures, and their literature counterparts

HER catalyst	Synthesis method	η_{10} (mV)	Tafel slope (mV/dec)	Onset potential (mV)	Ref
N-doped rGO/$MoSe_2$ composite	Hydrothermal	120	69	-	6
Aerogel hybrid $MoSe_2$/NG-2	Hydrothermal	229	78	-	7
$MoSe_2$	Colloidal	319	85	108	**This work**
$MoSe_2$-N-rGO	Colloidal	407	85	235	**This work**
$SnSe_2$-graphite nanosheets	High energy ball milling	382	109	-	17
$SnSe_2$	Colloidal	618	242	319	**This work**
$SnSe_2$-N-rGO	Colloidal	600	168	322	**This work**

Table 1 shows that the catalytic activity of $MoSe_2$ and $MoSe_2$-N-rGO was lower than the catalytic activity of similar materials found in the literature. Moreover, the catalytic activity of $MoSe_2$ did not improve after the nanostructure was introduced on the N-rGO. This further shows the importance of the interaction of the $MoSe_2$ with the N-rGO to the catalytic activity.[1] Zheng et al. were able to show how the $MoSe_2$ nanostructures were able to form on the surface of the N-rGO nanosheets. This was necessary in order to improve the catalytic activity of the $MoSe_2$. The $SnSe_2$ on the other hand did improve after being introduced to the N-rGO but the catalytic activity paled in comparison to what Liu et al were able to accomplish. This shows that there is still plenty of work o be done in order to optimize the process of making the hybrid nanostructure. Parameters such as the ratio of TMD to N-rGO can be optimized to get a better result.

4. Conclusions

In summary, the $MoSe_2$ and $SnSe_2$ hybrid nanostructures with N-rGO were synthesized. The catalytic activity of the $SnSe_2$ nanostructures was improved by incorporating the nanostructures on N-rGO nanosheets. However, the catalytic activity of the $MoSe_2$ did not improve upon incorporation on N-rGO nanosheets. The TEM image shows that the $SnSe_2$ nanoplates are able to grow directly on the surface of the N-rGO nanosheets while the $MoSe_2$ nanoflowers were able to grow on the edges of N-rGO. In **Chapter 6.1**, it was shown that the oxygen-containing groups of rGO are effective in anchoring TMD nanostructures on rGO. Since these functional groups are removed during the doping process of rGO to form N-rGO, the nitrogen-doped rGO is not as effective at anchoring the TMD nanostructures. This phenomenon is what results in the limited interaction of the $MoSe_2$ nanoflowers to the N-rGO. However, the large area $SnSe_2$ nanoplates are still able to do not seem to be as affected, This may be due to the interaction of the Sn(IV) monomer with the nitrogen defects on the N-rGO.

5. References

1. Yin, Y.; Zhang, Y.; Gao, T.; Yao, T.; Zhang, X.; Han, J.; Wang, X.; Zhang, Z.; Xu, P.; Zhang, P., Synergistic phase and disorder engineering in 1T-$MoSe_2$ nanosheets for enhanced hydrogen-evolution reaction. *Adv. Mater.* **2017,** *29* (28), 1700311.

2. Gao, D.; Xia, B.; Wang, Y.; Xiao, W.; Xi, P.; Xue, D.; Ding, J., Dual-native vacancy activated basal plane and conductivity of $MoSe_2$ with high-efficiency hydrogen evolution reaction. *Small* **2018,** *14* (14), 1704150.

3. Lai, F.; Yong, D.; Ning, X.; Pan, B.; Miao, Y. E.; Liu, T., Bionanofiber Assisted Decoration of Few-Layered $MoSe_2$ Nanosheets on 3D Conductive Networks for Efficient Hydrogen Evolution. *Small* **2017,** *13* (7), 1602866.

4. Jia, L.; Sun, X.; Jiang, Y.; Yu, S.; Wang, C., A novel MoSe2–reduced graphene oxide/polyimide composite film for applications in electrocatalysis and photoelectrocatalysis hydrogen evolution. *Adv. Funct. Mater.* **2015,** *25* (12), 1814-1820.

5. Pramoda, K.; Servottam, S.; Kaur, M.; Rao, C., Layered nanocomposites of polymer-functionalized reduced graphene oxide and borocarbonitride with MoS_2 and $MoSe_2$ and their hydrogen evolution reaction activity. *ACS Appl. Nano Mater.* **2020,** *3* (2), 1792-1799.

6. Zheng, D.; Cheng, P.; Yao, Q.; Fang, Y.; Yang, M.; Zhu, L.; Zhang, L., Excess Se-doped $MoSe_2$ and nitrogen-doped reduced graphene oxide composite as electrocatalyst for hydrogen evolution and oxygen reduction reaction. *Journal Alloys Compd.* **2020,** *848*, 156588.

7. Zhang, L.; Sun, L.; Huang, Y.; Sun, Y.; Hu, T.; Xu, K.; Ma, F., Hydrothermal synthesis of N-doped RGO/$MoSe_2$ composites and enhanced electro-catalytic hydrogen evolution. *J. Mater. Sci.* **2017,** *52* (23), 13561-13571.

8. Liu, H.; Guo, H.; Liu, B.; Liang, M.; Lv, Z.; Adair, K. R.; Sun, X., Few-Layer $MoSe_2$ Nanosheets with Expanded (002) Planes Confined in Hollow Carbon Nanospheres for Ultrahigh-Performance Na-Ion Batteries. *Adv. Funct. Mater.* **2018,** *28* (19), 1707480.

9. Zhang, Y.; Shi, Y.; Wu, M.; Zhang, K.; Man, B.; Liu, M., Synthesis and surface-enhanced Raman scattering of ultrathin $SnSe_2$ nanoflakes by chemical vapor deposition. *Nanomaterials* **2018,** *8* (7), 515.

10. Tonndorf, P.; Schmidt, R.; Böttger, P.; Zhang, X.; Börner, J.; Liebig, A.; Albrecht, M.; Kloc, C.; Gordan, O.; Zahn, D. R., Photoluminescence emission and Raman response of monolayer MoS_2, $MoSe_2$, and WSe_2. Opt. Express 2013, 21 (4), 4908-4916.

11. Hidayah, N.; Liu, W.-W.; Lai, C.-W.; Noriman, N.; Khe, C.-S.; Hashim, U.; Lee, H. C. In Comparison on graphite, graphene oxide and reduced graphene oxide: Synthesis and characterization, *AIP. Conf. Proc.* AIP Publishing LLC: 2017; p 150002.

12. Huang, L.; Zhu, P.; Li, G.; Lu, D. D.; Sun, R.; Wong, C., Core–shell SiO_2@ RGO hybrids for epoxy composites with low percolation threshold and enhanced thermo-mechanical properties. *J. Mater. Chem. A.* **2014,** *2* (43), 18246-18255.

13. Kukreja, A.; Kang, B.; Han, S.; Shin, M.-K.; Son, H. Y.; Choi, Y.; Lim, E.-K.; Huh, Y.-M.; Haam, S., Inner structure-and surface-controlled hollow MnO nanocubes for high sensitive MR imaging contrast effect. *Nano. Converg.* **2020,** *7* (1), 1-11.

14. Dai, Q.; Tang, J., Magnetic properties of CoO nanocrystals prepared with a controlled reaction atmosphere. *RSC adv.* **2013,** *3* (24), 9228-9233.
15. Tian, C.; Wu, J.; Ma, Z.; Li, B.; Li, P.; Zu, X.; Xiang, X., Design and facile synthesis of defect-rich C-MoS_2/rGO nanosheets for enhanced lithium–sulfur battery performance. *Beilstein. J. Nanotechnol.* **2019,** *10* (1), 2251-2260.
16. Lee, J. E.; Jung, J.; Ko, T. Y.; Kim, S.; Kim, S.-I.; Nah, J.; Ryu, S.; Nam, K. T.; Lee, M. H., Catalytic synergy effect of MoS 2/reduced graphene oxide hybrids for a highly efficient hydrogen evolution reaction. *RSC adv.* **2017,** *7* (9), 5480-5487.
17. Liu, Y.; Xu, Y.; Han, Y.; Zhang, Z.; Xu, J.; Du, Y.; Bao, J.; Zhou, X., Facile synthesis of $SnSe_2$ nanoparticles supported on graphite nanosheets for improved sodium storage and hydrogen evolution. *J. Power Sources* **2019,** *436*, 226860.

6. Supplementary information

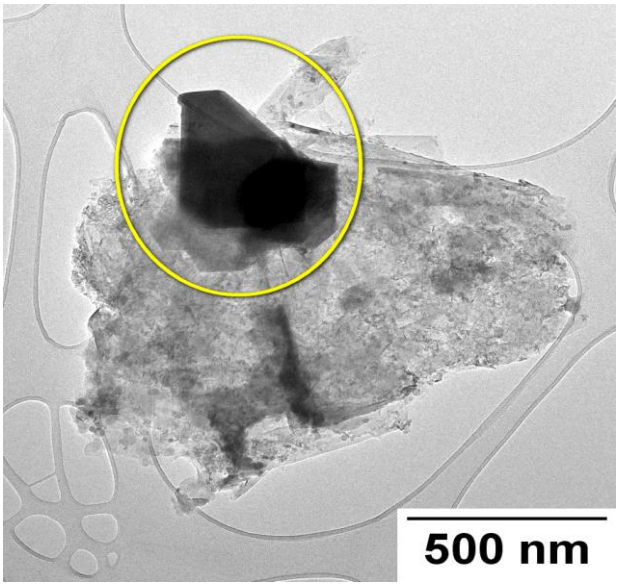


Figure S1: TEM image of $SnSe_2$ nanoplates on N-rGO nanosheets.

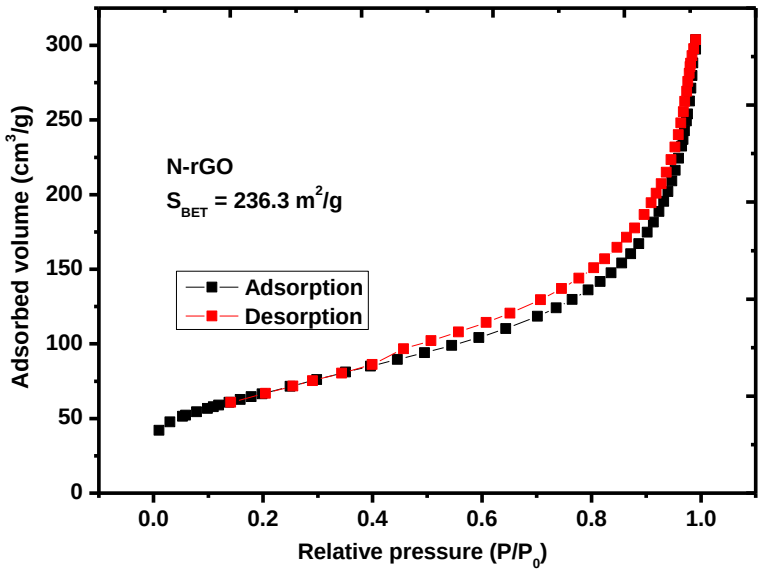


Figure S2: Adsorption- desorption isotherms of N-rGO.

Chapter 7: Catalytic activity of potassium doped $SnSe_2$ nanostructures towards the hydrogen evolution reaction

1. Introduction

The hydrogen economy has emerged as one of the most attractive clean and low polluting energy systems that could potentially reduce the world's dependence on fossil fuels and tackle climate change. This energy system would use hydrogen gas as opposed to fossil fuels as an energy carrier. Unfortunately, one of the major disadvantages of using hydrogen as an energy carrier is the relatively high cost of producing hydrogen gas. This high cost is normally attributed to the use of the expensive and precious metal platinum (Pt) as the catalysts used in the electrocatalytic production of hydrogen gas.[1] The hydrogen gas is normally produced using an electrocatalytic reaction called the hydrogen evolution reaction (HER) which is the half-reaction in water electrolysis along with the oxygen evolution reaction (OER). Several efforts have been made to study various alternative materials that can be used to replace platinum in the production of hydrogen gas.[2-3] Some of the materials that are currently being investigated are transition metal dichalcogenides (TMDs), which are a class of layered materials that exhibit exotic properties when in their monolayer or few-layer forms. Several of these nanomaterials have already been explored as potential electrocatalysts for the HER including MoS_2, $MoSe_2$, VS_2, and many others.[4-6] However, there has been very little work dedicated to exploring group IVA metal dichalcogenides such as $SnSe_2$. There have been several exceptional computational studies that have investigated the possible use of $SnSe_2$ as an electrocatalyst towards the HER.[7-9] The studies have alluded to the fact that $SnSe_2$ could possibly be used as an electrocatalyst in the HER but furthermore that there are various modifications one could make to $SnSe_2$ nanomaterials to improve the electrocatalytic activity. One such modification is the doping of $SnSe_2$ monolayer nanostructures with alkali metals such as sodium (Na), potassium (K), and calcium (Ca).[8] Doping has been shown to change the semiconductor nature of $SnSe_2$ to a more metallic character which seems to improve the electrocatalytic properties of the $SnSe_2$ monolayer nanostructures. Depending on the alkali metal used the active sites of the $SnSe_2$ can vary from being on the basal plane to being on the edge sites of the nanomaterials. Doping with K for instance activates the basal plane, where the basal plane becomes the most favourable H adsorption sites. K doping in $SnSe_2$ has also been shown to be a very effective electron-donating n-type dopant.[10] Unfortunately, work into evaluating the electrocatalytic activity of $SnSe_2$ nanostructures and their modified counterparts has been purely theoretical. In this work,

we seek to close that knowledge gap. Potassium doped $SnSe_2$ nanostructures were synthesized using colloidal synthesis and the electrocatalytic activity of the doped $SnSe_2$ nanostructures towards the HER was evaluated.

2. Experimental section

2.1 Chemicals

Tin(IV) chloride ($SnCl_4$) (98%), selenium powder (Se, 99.99%), oleylamine (70%), potassium chloride (99.99%) were purchased from Sigma-Aldrich and used as received without purification.

2.2 Synthesis of nanostructures

Synthesis of $SnSe_2$ nanostructures

Selenium powder (Se, 0.051 mmol) was added into a three-neck round bottom flask containing the solvent (20 ml) at room temperature. The temperature was increased to 220 ºC to thermally reduce the Se to Se^{2-} with the help of the solvent, which also acts as a reducing agent. Once all the Se was reduced, tin(IV) chloride ($SnCl_4$, 0.017 mmol) was added to the reaction mixture. The dopant was introduced by adding KCl into the reaction mixture. **$SnSe_2$-K1** was synthesized by introducing 0.0029 mmol of KCl into the reaction mixture. **$SnSe_2$-K2** was synthesized by introducing 0.0059 mmol of KCl to the reaction mixture. The temperature was then raised to 300 ºC and the reaction was run for 60 min. The nanoparticles formed were then washed with ethanol and toluene using a centrifuge and then left to dry.

2.3 Characterization techniques

The phase purity, crystallinity, and preferred crystal orientation of the products were examined using powder X-ray diffraction (PXRD) on a Bruker MeasSrv D2-205530 diffractometer using secondary graphite monochromated CuKα radiation (λ 1.5406 Å) at 30 kV/10 mA. Measurements were taken using a glancing angle of incidence detector at an angle of 2°, for 2θ values over 10 - 70° in steps of 0.026° with a step time of 37 s and at a temperature of 25 °C. The Raman spectra were obtained using the MacroRAM spectrophotometer which was fitted with a CCD detector that was cooled at -50 °C. All samples were measured after excitation with a laser wavelength of 785 nm. The XPS measurements of the powder samples were obtained using a Thermo ESCAlab 250Xi with Al kα photon source (1486.7 eV), X-ray power of 300W, X-ray spot size of 900 µm, pass energy (survey) of 100 eV, pass energy (20 eV), and pressure of $<10^{-8}$ mBar. The sample morphologies were determined using the transmission

electron microscopy (TEM) carried out on an FEI Tecnai T12 TEM microscope operated at an acceleration voltage of 120 kV The TEM samples were prepared by sonicating a spatula tip of the sample in ethanol and drop-casting that dispersion on a lacey carbon Cu grid. The SEM images were obtained using a Carl Zeiss mA 10 high-vacuum microscope, the SEM was operated at 20 keV. The concentration of potassium dopant was determined using a Bruker S2 ranger calibrated against a range of USGS and local (SARM) geological samples.

2.4 Electrochemical characterization

The electrochemical measurements were carried out on a BASi epsilon E2. All measurements were carried out in 0.5 M H_2SO_4 using a three-electrode system. An Ag/AgCl electrode was used as the reference electrode, a platinum wire was used as the counter electrode. A modified glassy carbon electrode with a 3 mm diameter was used as the working electrode. The ink or fresh dispersion of the sample was prepared by dispersing 5.0 mg of sample with 0.5 mg carbon black and 40 µl of Nafion solution (5 wt%) in a 1 ml mixture of water and isopropanol at a 3:1 ratio. The solution was then sonicated for 30 min and ~ 5 µl of the ink was drop-casted onto the glassy carbon electrode. The electrode was allowed to dry at room temperature. The linear sweep voltammograms were obtained at a scan rate of 2 mVs^{-1} and the cyclic voltammograms were obtained at a potential range of 0.2 – 0.6 V vs RHE at 100 mVs^{-1} scan rate. The measured potentials vs Ag/AgCl were converted to the reversible hydrogen electrode (RHE) scale according to the Nernst equation:

$$E_{RHE} = E_{Ag/AgCl} + 00059\,pH + E^{0}_{Ag/AgCl} \quad (1)$$

Where E_{RHE} is the converted potential vs RHE, $E^{0}_{Ag/AgCl}$ = 0.210 V at 25 °C. The Impedance spectroscopy studies were conducted on a Biologic SP 300, the measurements were done at a potential of -200 mV vs RHE and a frequency range between 0.1 Hz and 100 kHz.

3. Results and discussion

The phase, composition, and crystallinity of the nanomaterials were confirmed using powder X-ray diffraction (PXRD). The powder diffraction patterns confirm the formation of $SnSe_2$ (JCPDS card no: 01-089-0340) nanostructures. The powder diffractograms of the pristine and doped $SnSe_2$ nanostructures are shown in **Fig.1(a)**. The $SnSe_2$ crystallized in a hexagonal unit cell and a P-3m1 space group. The intense peak found at $2\Theta \approx 14°$, corresponds to the (001) lattice plane and is associated with the growth of the crystal along the c-axis.[11] A notable shift of the PXRD peaks was observed in the powder patterns of the doped $SnSe_2$. An example of this is shown **Fig.1(b),** which denoted the right shift of the (001) peaks of the doped $SnSe_2$.

This clearly indicates the incorporation of the K atoms in the structure of the $SnSe_2$ nanostructures.[12] Increasing the amount of dopant in the $SnSe_2$-K2 samples seems to introduce impurities that are not observed in the $SnSe_2$-K1 sample. These impurities have been identified to be from the KCl that was used as the dopant precursor.

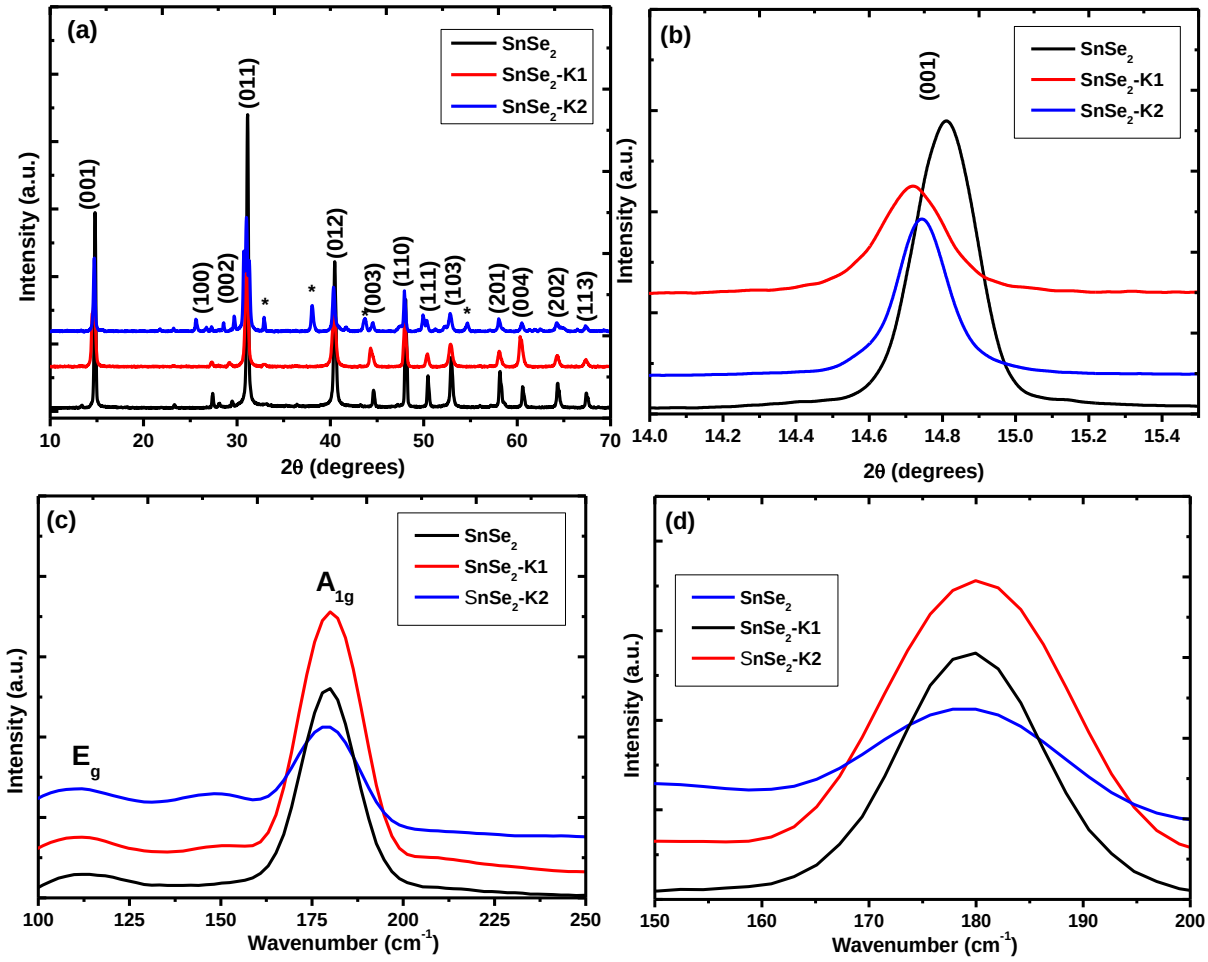


Figure 1: (a) PXRD patterns of pristine and doped $SnSe_2$ nanostructures, (b) Shift of the (001) peak after doping, (c) Raman spectra of the pristine and doped $SnSe_2$ nanostructures, and (d) the shift in the A_{1g} peak of the doped nanostructures.

Raman spectroscopy was also used to investigate the structural properties of the $SnSe_2$ nanostructures. The typical Raman spectrum of $SnSe_2$ has two characteristic peaks, the in-plane E_g vibrational mode, and the out-of-plane A_{1g} vibrational mode.[12] The position of the E_g can offer information about the polytype of the $SnSe_2$ (2H or 1T) as well the number of layers on the nanosheets. For 2H-$SnSe_2$ the position of the E_g is located at approximately 108 cm^{-1}. The E_g peak for the as-synthesized $SnSe_2$ was located at 114 cm^{-1} which suggests that the nanostructures crystallized in the 1T phase.[12] There seems to be no significant shift in the E_g

after doping which suggests that the polytype of the $SnSe_2$ nanostructures is not changed in the doping process. The location of the E_g peak is also associated with $SnSe_2$ nanoflakes of layer between 1-2 layers. The A_{1g} peaks seem to also blue-shift to higher wavenumbers as the concentration of the K dopant increases as shown in **Fig.1(d)**, this phenomenon has been reported in doped $SnSe_2$ nanostructures.[11]

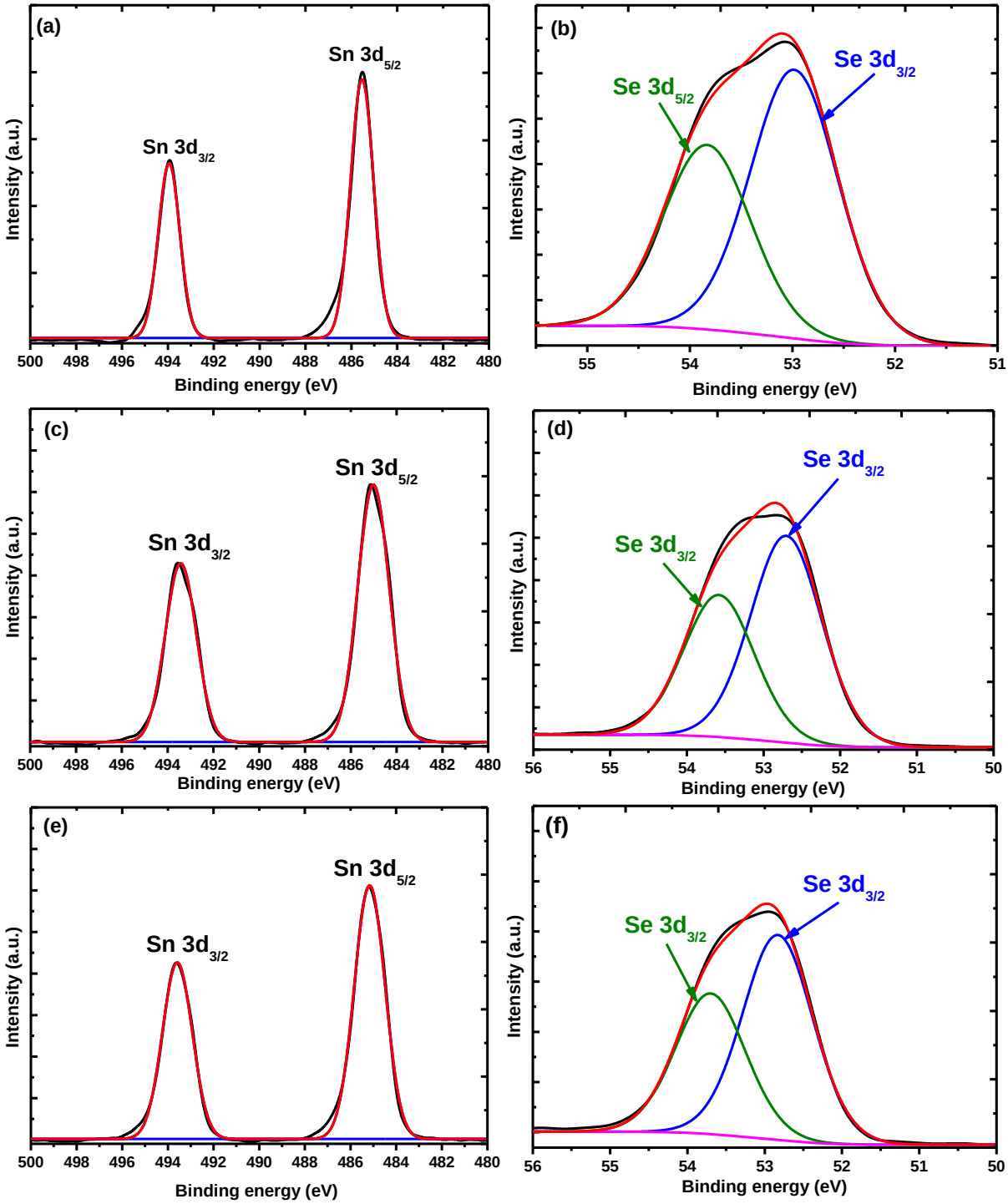


Figure 2: XPS spectra of Sn^{4+} and Se^{2-} respectively for (a-b) $SnSe_2$, (c-d) $SnSe_2$-K1, and (e-f) $SnSe_2$-K2.

X-ray photo-electron spectroscopy (XPS) was used to evaluate the bonding configuration and elemental composition of the pristine and doped $SnSe_2$ nanostructures. The peaks of interest which are the peaks for Sn 3d and Se 3d for the doped and undoped $SnSe_2$ are shown in **Fig.2(a)-(f)**. The characteristic core level peaks of Sn(IV) which are Sn $3d_{3/2}$ and Sn $3d_{5/2}$ are located at ~ 493.9 eV and 485.5 eV respectively. This shows that Sn is in the Sn^{4+} state.[13] The characteristic core level peaks of Se which are Se $3d_{3/2}$ and Se $3d_{5/2}$ are located at 53.8 eV and 53.0 respectively. This indicates that the Se is in the Se^{2-} state.[13] The doped $SnSe_2$ nanostructures have also been shown to have the characteristic Sn 3d and Se 3d peaks, as shown in **Fig.2(c)-(f)**. A summary of the peak binding energies and atomic compositions of the doped $SnSe_2$ nanostructures are shown in **Table 1**.

Table 1: Summary of the peak binding energies and atomic compositions of the pristine and doped $SnSe_2$ nanostructures

Sample	Element	Assignment	Binding energy (eV)	Atomic (%)
$SnSe_2$	Sn	Sn 3d	485.5	8.6
	Se	Se 3d	53.0	22.3
$SnSe_2$-K1	Sn	Sn 3d	485.3	7.9
	Se	Se 3d	53.1	23.3
$SnSe_2$-K2	Sn	Sn 3d	485.0	8.8
	Se	Se 3d	52.9	21.7

The Sn 3d and Se 3d peaks show a slight deviation to their positions in the pristine $SnSe_2$ which could be due to the potassium doping.[14] The XPS analysis did not show the presence of potassium in any of the doped samples. This was due to the existence of the Se Auger peak that masked the potassium K 2p peaks. X-ray fluorescence spectroscopy (XRF) was used to determine the percentage of potassium dopant on the doped $SnSe_2$ nanostructures. The XRF was able to determine that the $SnSe_2$-K1 and $SnSe_2$-K2 contained 0.93% and 1.54% of potassium. Since twice the amount of dopant precursor was used for $SnSe_2$-K2 as compared to $SnSe_2$-K1, it stands to reason that the $SnSe_2$-K2 would have nearly twice the dopant concentration of the $SnSe_2$-K2. This in accordance with the PXRD data confirms the doping of the $SnSe_2$ nanostructures with potassium, it also shows that increasing the dopant precursor concentration in the synthesis increases the dopant concentration in the nanostructures. However, increasing the dopant precursor concentration may also just lead to impurities.

Electron microscopy was used to further analyze the structure and morphology of the $SnSe_2$ nanostructures. The TEM and SEM images of $SnSe_2$ are shown in **Fig.3**.

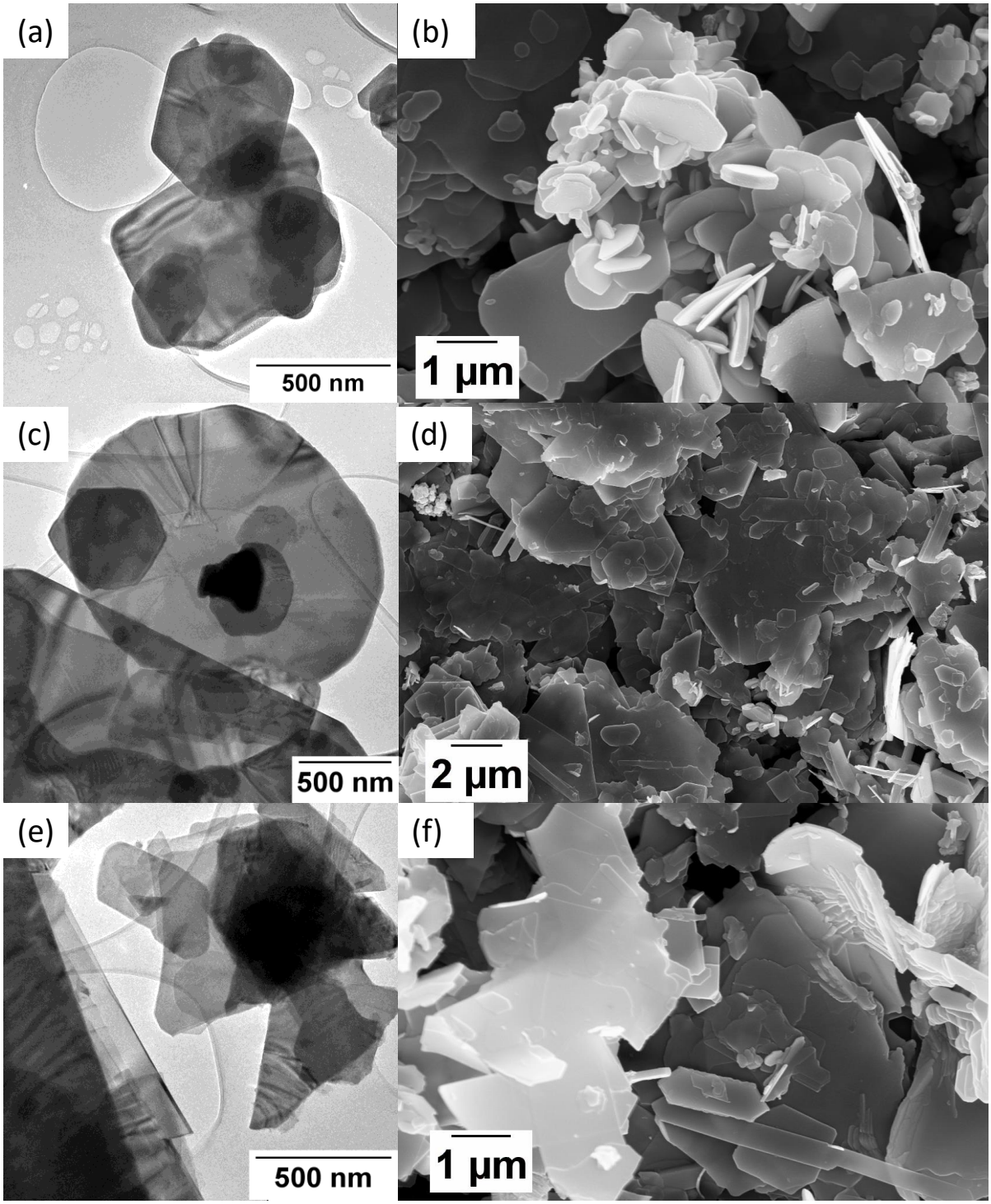


Figure 3: TEM and SEM images of $SnSe_2$ nanostructures (a-b) $SnSe_2$, (c-d) $SnSe_2$-K1, (e-f) $SnSe_2$-K2.

The SEM images show that the $SnSe_2$ nanostructures have formed in a mixed morphology. The images show that the $SnSe_2$ forms into 2D nanoplates of different shapes and lateral sizes. The

introduction of the K dopants at different concentrations does not result in any changes in the morphology of the $SnSe_2$ nanostructures which suggests that the K atoms have successfully incorporated into the existing structure of the $SnSe_2$ nanostructures. The electrocatalytic performance of the pristine and doped $SnSe_2$ nanostructures towards the HER was investigated using various electrochemical methods. The polarization curves of the doped and undoped $SnSe_2$ nanostructures are shown in **Fig.4(a)**.

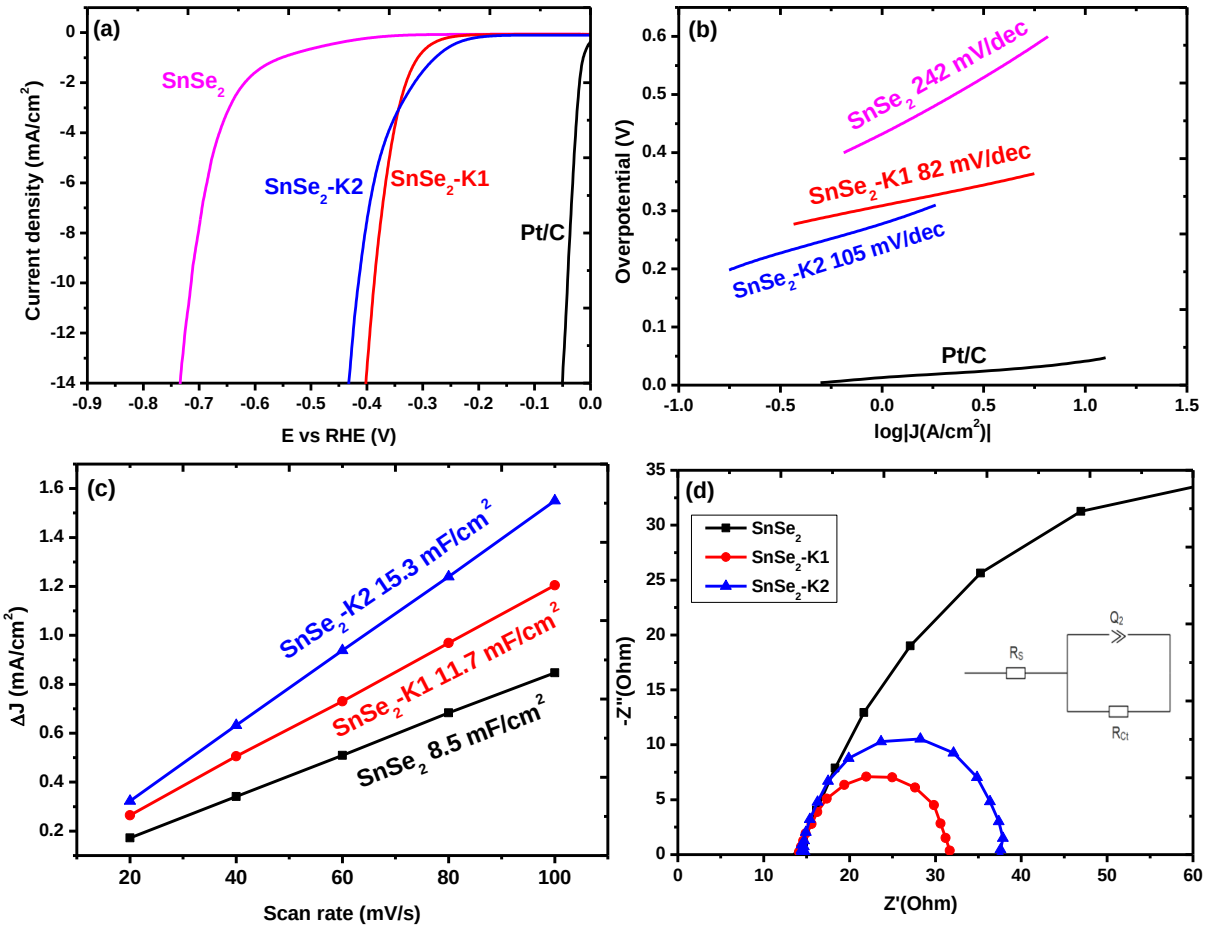


Figure 4: (a) Polarisation curves of the pristine and doped $SnSe_2$ nanostructures, (b) Tafel plots, (c) C_{dl} plots, and (d) Nyquist plots of the pristine and doped $SnSe_2$ nanostructures.

The first parameter which was evaluated was the onset potential which is the overpotential at which catalytic current is first observed. The highest onset potential was observed for the undoped $SnSe_2$ nanostructures at 390 mV. The $SnSe_2$-K2 had the lowest onset potential at 217 mV which was comparable to the onset potential of the $SnSe_2$-K1 at 265 mV. Another crucial parameter that was used to evaluate the catalytic activity of the pristine and doped $SnSe_2$ nanostructures was the overpotential at 10 mA/cm^2 (η_{10}), which is the operating current density

of the most cost-competitive photoelectrochemical cell system (PEC). The best performing catalyst would then have the lowest η_{10}. The $SnSe_2$-K1 had the lowest η_{10} which was measured at 385 mV, which was only slightly lower than the η_{10} of $SnSe_2$-K2 at 415 mV. The highest η_{10} as with the onset potential was from the pristine $SnSe_2$ nanostructures at 681 mV. The onset potential and overpotential suggest that the doping of the $SnSe_2$ with K seems to drastically improve the electrocatalytic properties of the nanostructures as suggested by the computational studies. Since doping with potassium has been shown to activate the basal plane by forming defects that act as active sites for the HER in $SnSe_2$. It can be surmised that the doping of the $SnSe_2$ nanomaterials increases the number of active sites on the basal plane, thus drastically increasing the catalytic activity of the nanostructures.[8] This is corroborated by the increase in catalytic activity with an increase in the K dopant concentration, which suggests that increasing the concentration of dopants increases the number of active basal plane sites on the $SnSe_2$ nanostructures.[8] However, there seems to be a bottleneck on how much the catalytic activity of the nanostructures can increase when the concentration of dopant is increased. When the dopant concentration is increased from 0.93% to 1.54%, the improvement of the electrocatalytic activity seems to be minimal. This can be further investigated using the Tafel plots of the nanostructures which were generated from the polarization curves. The Tafel plots are recorded with the linear region fitted to the Tafel equation ($\eta = b\log(j) + a$, where b is the Tafel slope and j is the current density). The Tafel slope can be defined as a measure of the sensitivity of the current density to changes in the applied potential. The Tafel slope can thus be used to gain an understanding of the mechanism by which HER occurs for a certain catalyst by determining the rate-limiting step of the reaction. The HER in acidic media can be described in three steps. The Volmer reaction is the primary discharge step in which protons are adsorbed on the surface of the catalyst. This step is followed by the Heyrovsky step which is the electrochemical desorption of the protons on the catalyst surface or by the recombination of protons followed by desorption of hydrogen gas from the surface of the catalyst which is called the Tafel step. The rate-determining step can be determined by obtaining the value of the Tafel slope. The Tafel slope of the pristine $SnSe_2$ was found to be 242 mV/dec which suggests that the Volmer step is the rate-determining step for this catalyst. The Tafel slopes of the $SnSe_2$-K1 and $SnSe_2$-K2 were found to be 82 mV/dec and 105 mV/dec respectively which suggest that the Volmer-Heyrovsky mechanism is the process by which HER occurs in these catalysts. An intrinsic measure of the catalytic rate of HER on a catalyst is the exchange current density. The higher the exchange current density, the better the catalytic performance. The exchange current

density can be determined from the Tafel plot by using $\log J_o = a$, where a is the intercept of the Tafel plot. As expected, the exchange current density of the $SnSe_2$-K2 was the highest at 0.526 mA/cm^2 which was comparable to that of $SnSe_2$-K1 at 0.490 mA/cm^2. The lowest exchange current density was that of the pristine $SnSe_2$ which was measured at 0.297 mA/cm. To confirm that the increased catalytic activity of the doped $SnSe_2$ is due to the increase in the number of active sites, the ECSA of the pristine and doped nanostructures was determined. The electrochemically active surface area (ESCA) can be estimated using the electrochemical double layer (C_{dl}) of the nanostructures which has been shown to scale with the ECSA. The C_{dl} has been determined by conducting cyclic voltammetry (CV) measurements at different scan rates. The CV curves are used to obtain ΔJ (J_{anodic}-$J_{cathodic}$) at a potential of 0.315 V vs RHE as shown in **Fig.S1**. The ΔJ is plotted against the scan rate which results in a linear plot that was used to determine the gradient, the gradient is equivalent to the C_{dl}. The C_{dl} plots are shown in **Fig.4(c)**. The ECSA of the pristine $SnSe_2$ was measured to be 8.5 mF/cm^2, while the ECSA of the doped nanostructures was found to be 11.7 mF/cm^2 and 15.3 mF/cm^2 for $SnSe_2$-K1 and $SnSe_2$-K2 respectively. The increase in the ECSA is attributed to the creation of new active sites on the basal plane of the $SnSe_2$. This is a consequence of the doping which has been shown to activate the basal plane and introduce new active sites.[8] The EIS results are represented as Nyquist plots as shown in **Fig.4(d)**. The equivalence circuit fitted to the data is shown as an insert in **Fig.4(d)**, the circuit components are shown as R_s (solution resistance), Q_2 (constant phase element), and the R_{ct} which is the charge transfer resistance. The R_{ct} of the pristine $SnSe_2$ was measured to be 90 Ω, while the R_{ct} of the doped $SnSe_2$ was measured to be 16 Ω and 22 Ω for $SnSe_2$-K1 and $SnSe_2$-K2 respectively. The doped $SnSe_2$ have shown lower charge transfer resistance compared to the pristine $SnSe_2$, this is due to the increased electrical conductivity offered by the K dopants on the $SnSe_2$. Studies have shown that potassium acts as an n-type dopant on $SnSe_2$. The potassium is able to donate electron density to the $SnSe_2$, this results in increased electrical conductivity which in turn reduces the R_{ct}.[9] The n-type behavior of K dopants can be determined by accompanying changes in the band-gap of the $SnSe_2$ nanostructures. Tauc plots of the pristine and doped $SnSe_2$ nanostructures are shown in **Fig.S2**. The band-gap of the pristine $SnSe_2$ was measured to be 1.33 eV, while the band-gap of the doped $SnSe_2$ was found to be 1.15 eV and 1.04 eV for $SnSe_2$-K1 and $SnSe_2$-K2 respectively.[9] The decrease in the band-gap was attributed to the charge transfer from the K to the $SnSe_2$. To determine the stability of the $SnSe_2$ in acidic media the nanostructures are normally subjected to numerous LSV scans in order to determine whether there is a huge deviation in the performance of the catalysts. The study was conducted on the doped and pristine $SnSe_2$ to

evaluate their stability in acidic media. Normally when stability studies are conducted, the LSV would only slightly shift to higher overpotential to denote a minimal decrease in the performance of the catalyst. However, in the case of the pristine and doped $SnSe_2$ nanomaterials show a gradual increase in the performance of the catalyst that is observed with an increasing number of LSV scans.

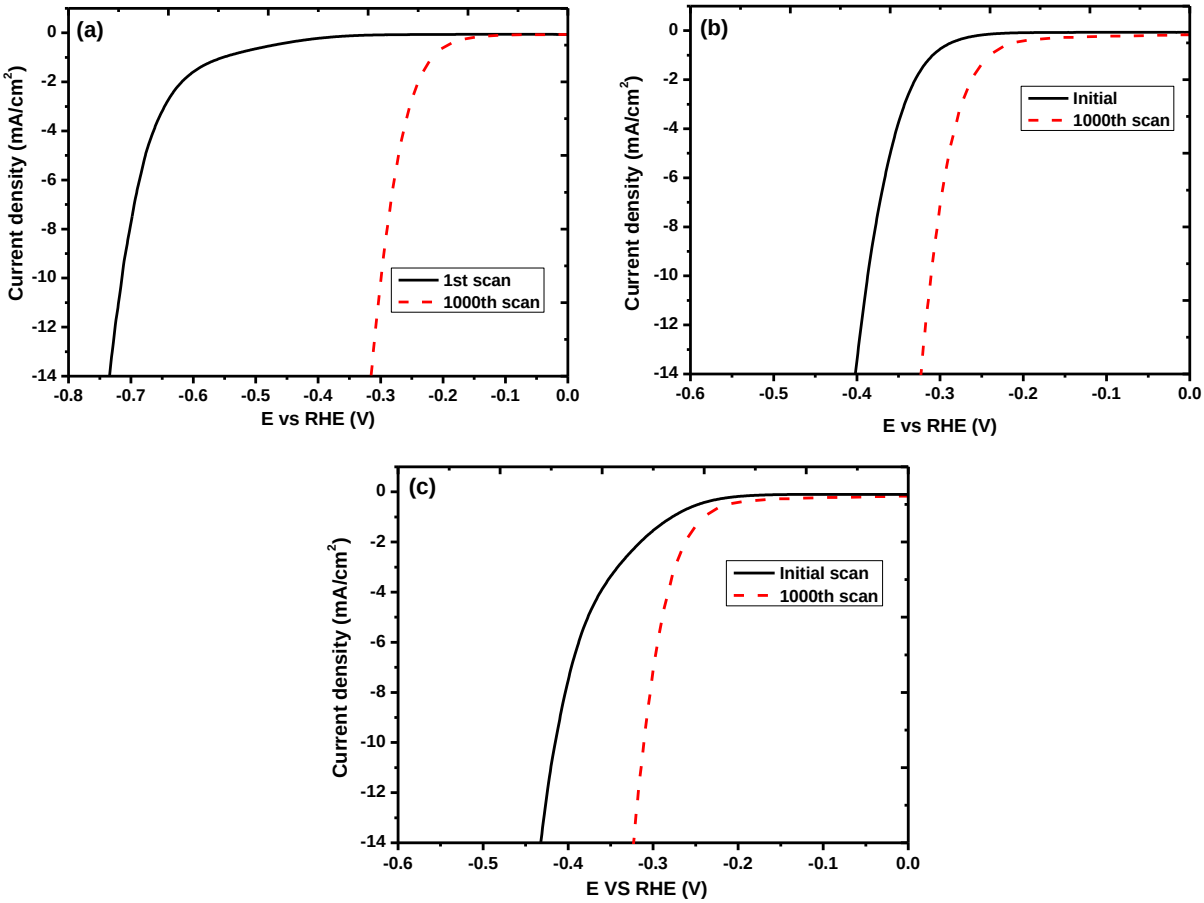


Figure 5: The stability studies of (a) $SnSe_2$ (b) $SnSe_2$-K1, and (c) $SnSe_2$-K2.

The increased number of scans results in a drastic improvement in the performance of the catalysts towards the HER. A table summarising the change in the values of the important electrochemical parameters before and after activation is shown in **Table 2**.

Table 2: Electrocatalytic parameters of the pristine and doped $SnSe_2$ nanoplates before and after electrochemical activation

Sample	Onset potential (mV)	η_{10} (mV)	Tafel slope (mV/dec)	J_0 (mA/cm^2)
$SnSe_2$	390	714	242	0.297
A-$SnSe_2$	141	289	79	0.607
$SnSe_2$-K1	265	385	82	0.490
A-$SnSe_2$-K1	154	310	69	0.640
$SnSe_2$-K2	217	415	105	0.526
A-$SnSe_2$-K2	136	312	70	0.632

The drastic reduction in the onset potential, overpotential, and Tafel slope represents a significant improvement in the catalytic activity of the $SnSe_2$ nanoplates. The in-depth study of this phenomenon conducted in **Chapter 4** revealed that the increase in catalytic activity is due to electrochemical activation via proton intercalation. The electrochemical activation seems to also occur in the potassium doped $SnSe_2$ nanostructures. The improvements in the electrocatalytic parameter shown in **Table 2** attests to this observation.

4. Conclusions

In summary, $SnSe_2$ was successfully doped with potassium atoms. The PXRD, Raman, and XRF analysis confirms the incorporation of potassium atoms in the structure of the $SnSe_2$ nanoplates. The XRF results have shown that increasing the dopant precursor concentration leads to an increase in the dopant concentration in the $SnSe_2$ nanoplates. The PXRD pattern shows that introducing large concentrations of the dopant precursor results in impurities in the $SnSe_2$ nanoplates. The electrochemical characterization revealed that the potassium-doped $SnSe_2$ nanoplates had higher catalytic activity towards the HER compared to the pristine $SnSe_2$. The superior catalytic activity of the doped nanostructures was attributed to the increase in catalytically active sites in the basal plane of the $SnSe_2$ nanoplates.

5. References

1. Wang, S.; Lu, A.; Zhong, C.-J., Hydrogen production from water electrolysis: role of catalysts. *Nano Converg.* **2021,** *8* (1), 1-23.

2. Penner, S., Steps toward the hydrogen economy. *Energy* **2006,** *31* (1), 33-43.

3. Yang, J.; Mohmad, A. R.; Wang, Y.; Fullon, R.; Song, X.; Zhao, F.; Bozkurt, I.; Augustin, M.; Santos, E. J.; Shin, H. S., Ultrahigh-current-density niobium disulfide catalysts for hydrogen evolution. *Nat. Mater.* **2019,** *18* (12), 1309-1314.

4. Ruiz, K. H.; Liu, J.; Tu, R.; Li, M.; Zhang, S.; Garcia, J. R. V.; Mu, S.; Li, H.; Goto, T.; Zhang, L., Effect of microstructure on HER catalytic properties of MoS_2 vertically standing nanosheets. *J. Alloys Compd.* **2018,** *747*, 100-108.

5. Najafi, L.; Bellani, S.; Oropesa-Nuñez, R.; Ansaldo, A.; Prato, M.; Del Rio Castillo, A.E.; Bonaccorso, F. Engineered $MoSe_2$-based heterostructures for efficient electrochemical hydrogen evolution reaction. *Adv. Energy Mater.* **2018**, *8*, 1703212.

6. Qu, Y.; Shao, M.; Shao, Y.; Yang, M.; Xu, J.; Kwok, C. T.; Shi, X.; Lu, Z.; Pan, H., Ultra-high electrocatalytic activity of VS_2 nanoflowers for efficient hydrogen evolution reaction. *J. Mater. Chem. A.* **2017,** *5* (29), 15080-15086.

7. Dong, S.; Wang, Z., Improving the catalytic activity for hydrogen evolution of monolayered $SnSe_{2\,(1-x)}\,S_{2x}$ by mechanical strain. *Beilstein. J. Nanotechnol.* **2018,** *9* (1), 1820-1827

8. Inamdar, A. N.; Som, N. N.; Pratap, A.; Jha, P. K., Hydrogen evolution and oxygen evolution reactions of pristine and alkali metal doped $SnSe_2$ monolayer. *Int. J. Hydrog. Energy* **2020,** *45* (37), 18657-18665.

9. Wu, Q.; Wei, W.; Lv, X.; Huang, B.; Dai, Y., Computational screening of defective group IVA monochalcogenides as efficient catalysts for hydrogen evolution reaction. *J. of Phys. Chem. C* **2019,** *123* (18), 11791-11797.

10. Xia, F.; Yang, F.; Hu, J.; Zheng, C.; Yi, H.; Sun, J., Enhanced visible light absorption performance of SnS_2 and $SnSe_2$ via surface charge transfer doping. *RSC advances* **2018,** *8* (70), 40464-40470.

11. Kim, J. T.; Hyeon, D. S.; Hanzawa, K.; Kanai, A.; Kim, S. Y.; Lee, Y. J.; Hosono, H.; Bang, J.; Lee, K., Role of fluorine in two-dimensional dichalcogenide of SnS_2. *Scientific reports* **2018,** *8* (1), 1-8.

12. Li, F.; Zheng, Z.; Li, Y.; Wang, W.; Li, J.-F.; Li, B.; Zhong, A.; Luo, J.; Fan, P., Ag-doped $SnSe_2$ as a promising mid-temperature thermoelectric material. *J. Mater. Sci.* **2017,** *52* (17), 10506-10516.

13. Mukhokosi, E. P.; Krupanidhi, S. B.; Nanda, K. K., Bandgap engineering of hexagonal $SnSe_2$ nanostructured thin films for infra-red photodetection. *Sci. Rep.* **2017,** *7* (1), 1-10.

14. Sezen, H.; Suzer, S., Communication: Enhancement of dopant dependent x-ray photoelectron spectroscopy peak shifts of Si by surface photovoltage. *J. Chem. Phys.* **2011,** *135* (14), 141102.

6. Supplementary information

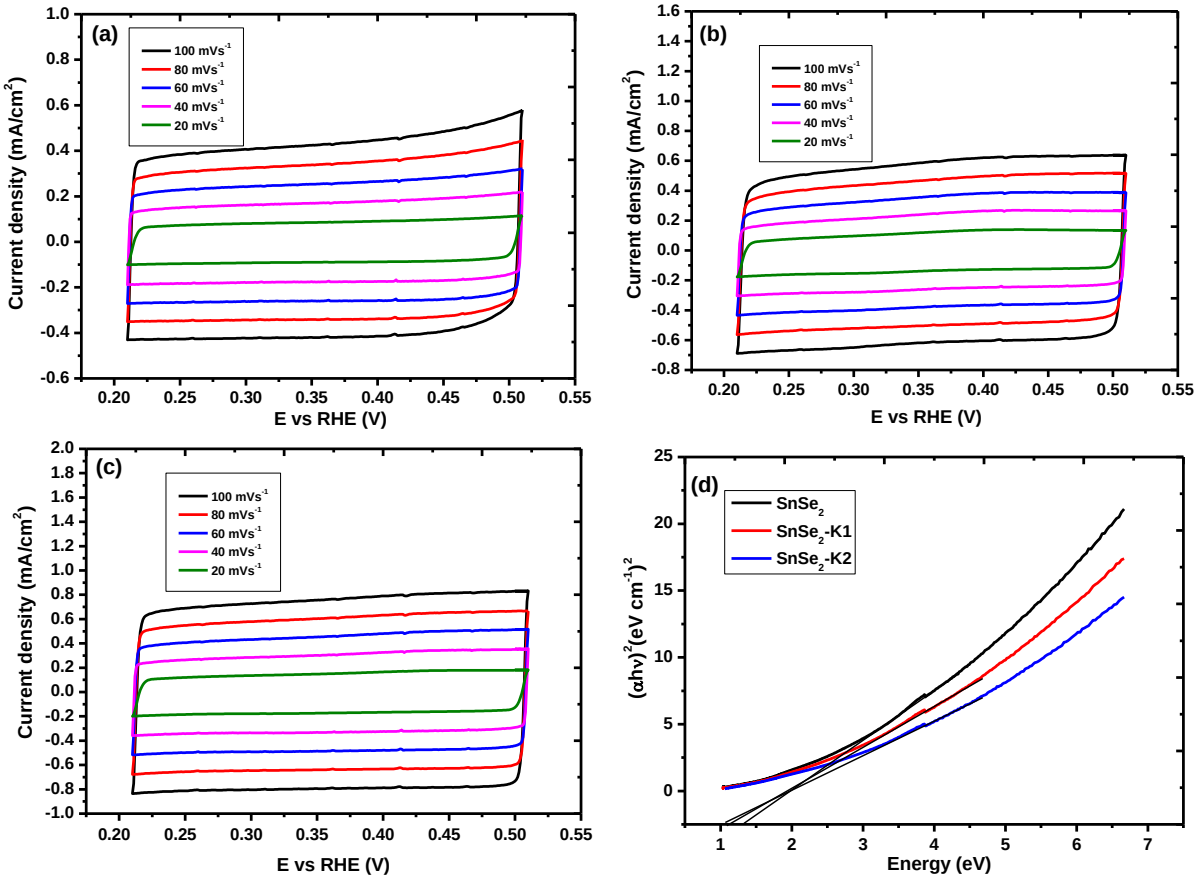


Figure S1: Cyclic voltammetry curves of (a) $SnSe_2$, (b) $SnSe_2$-K1, and $SnSe_2$-K2. (d) Tauc plot of the pristine and doped $SnSe_2$ nanostructures.

Chapter 8: Overall conclusions and recommendations

8.1 Conclusions

In summary, this thesis reports on the colloidal synthesis of metal diselenide nanostructures for HER applications. $MoSe_2$, $ReSe_2$, and $SnSe_2$ nanostructures were successfully synthesized using the colloidal method, and the catalytic activity of the nanostructures towards the HER was evaluated. The thesis demonstrated that the strategies used to improve the catalytic activity of TMDs could be fully utilized using the colloidal method. This work has shown that the choice of precursors in the synthesis of $MoSe_2$ and $ReSe_2$ plays a significant role in the structural and catalytic properties of the nanostructures. It was demonstrated that precise choice of the metal precursor can allow for the synthesis of TMD nanostructures with similar structural properties. The choice of metal precursor allowed for the synthesis of $MoSe_2$ and $ReSe_2$ flower-like nanostructures with comparable catalytic performance towards the HER. Additionally, using selenourea instead of selenium powder as the sulfur precursor in the synthesis of $MoSe_2$ can result in the introduction of Se vacancies in the $MoSe_2$ nanostructures. A change of sulfur precursor from selenium powder to selenourea in the synthesis of $ReSe_2$ nanostructures can lead to significant changes in the morphology of the nanostructures. The changes in the structural properties such as the introduction of Se vacancies and changes in the morphology affected the catalytic activity of the nanostructures towards the HER. For instance, the introduction of Se vacancies in the $MoSe_2$ nanostructures resulted in the improved catalytic activity of the nanostructures. The colloidal synthesis of $SnSe_2$ resulted in the formation of $SnSe_2$ nanoplates with rather poor catalytic activity towards the HER. However, the $SnSe_2$ nanoplates were shown to undergo electrochemical activation through proton intercalation that drastically improved the catalytic activity of the nanostructures. This was the first time this phenomenon was reported for $SnSe_2$ nanostructures.

Through this work, it has also been shown that the choice of solvent/surfactant used to synthesize the nanostructures plays a huge role in the catalytic activity of the nanostructures. Among three of the common solvents used in the colloidal synthesis of TMD nanostructures, namely OLA, OA, and TOPO. TOPO was identified as the best solvent to utilize in order to ensure the best catalytic activity. TOPO was shown to result in the smallest degree of passivation compared to OA and OLA, this was due to its bulky nature which ensured the lowest degree of interaction with the surface of the nanostructures. This meant that the TOPO

did not block the active sites of the nanostructures as well as the OA and the OLA, which resulted in the TOPO synthesized nanostructures having the highest catalytic activity across all the studied TMDs.

This work has also shown that it is possible to grow ReSe nanostructures on other carbon structures such as reduced graphene oxide (rGO) and nitrogen-doped reduced graphene oxide (N-rGO). This can effectively increase the catalytic activity of the $ReSe_2$ nanostructures, by improving the electron conductivity of the TMD nanostructures. The use of N-rGO was shown to result in a higher improvement in the catalytic activity of the $ReSe_2$ nanostructures compared to the rGO, this was attributed to the improved electron conductivity of the nitrogen-doped rGO. It was demonstrated that the interaction between the TMD nanostructures was essential to ensuring improved catalytic activity. The catalytic activity of the $MoSe_2$ nanostructures did not improve when the nanostructures were grown on N-rGO, the TEM images showed that the $MoSe_2$ grew independently from the N-rGO nanosheets which resulted in poor interaction. The $SnSe_2$ on the other hand was grown on the N-rGO and the catalytic activity of the nanostructures improved.

This work has also shown that colloidal synthesis can be used to dope TMD nanostructures to improve their catalytic activity towards the HER. $SnSe_2$ nanostructures were doped with potassium using colloidal synthesis. The doped nanostructures showed improved catalytic activity, this was attributed to the activation of the basal plane though doping. This results in an increase of the number of active sites.

Overall, this work shows that colloidal synthesis can be used to incorporate all the methods used to improve the catalytic activity of TMDs to produce TMDs with excellent catalytic activity. Moreover, the catalytic activity of these TMDs can surpass the catalytic activity of nanostructures synthesized using other methods. The $ReSe_2$ and $SnSe_2$ nanostructures synthesized in this work recorded catalytic activity towards the HER that was comparable or better to the best performing catalyst of identical nanostructures reported in the literature.

8.2 Recommendations

Future work would include but not be limited to:

- Further investigate the introduction of Se vacancies in the TMDs using various selenium precursors. Determine the possibility of increasing the number of Se vacancies using the reaction parameters.
- Computational studies to investigate the interaction of common solvents used in the colloidal synthesis with the basal plane of the TMDs. This could give information on the growth of the TMDs along the c-axis.
- Computational studies on how the interaction of surfactants and the surface of TMDs affects the ΔG_H.
- Substitutional doping of the $ReSe_2$ nanostructures with various metals to improve the catalytic activity.